

**A Measurement of the QED Compton Cross Section in Electron-Proton
Scattering with the H1 Experiment at HERA**

Dissertation

zur

Erlangung der naturwissenschaftlichen Doktorwürde
(Dr. sc. nat.)

vorgelegt der

Mathematisch-naturwissenschaftlichen Fakultät
der

Universität Zürich

von

Nicolas Keller

aus

Deutschland

Begutachtet von

Prof. Dr. Ulrich Straumann
Dr. Katharina Müller

Zürich 2003

Die vorliegende Arbeit wurde von der Mathematisch-naturwissenschaftlichen Fakultät der Universität Zürich auf Antrag von Prof. Dr. Ulrich Straumann und Prof. Dr. Peter Truöl angenommen.

Abstract

A measurement of the double differential leptonic QED Compton cross-section in positron-proton collisions is described. The kinematic range extends in x_l from $1.8 \cdot 10^{-5}$ to $1.78 \cdot 10^{-3}$ and in Q_l^2 from 1.5 GeV^2 to 85 GeV^2 . The data were accumulated with the H1 detector at the HERA storage ring in 1997, of which about 9.18 pb^{-1} of the integrated luminosity in that year were included in this analysis. The measurement focussed upon unambiguous particle identification, detailed detector understanding and a reliable determination of the interaction point. Both, the inelastic and the elastic channel were measured. The result is compared to theoretical predictions using the ALLM-97 proton structure function parameterisation, within the framework of the COMPTON-2.14 Monte Carlo generator.

Zusammenfassung

Die vorliegende Arbeit beschreibt die Messung des doppelt differentiellen, leptonischen QED Compton Wirkungsquerschnitts in Positron-Proton Kollisionen. Der kinematische Bereich der Messung erstreckt sich in x_l von $1.8 \cdot 10^{-5}$ bis $1.78 \cdot 10^{-3}$ und in Q_l^2 von 1.5 GeV^2 bis 85 GeV^2 . Die Daten wurden im Jahr 1997 am HERA ep Speicherring mit dem H1 Detektor aufgezeichnet, wovon ca. 9.18 pb^{-1} der integrierten Luminosität jenes Jahres für die Messung verwendet wurden. Ein besonderes Augenmerk der Messung lag bei der eindeutigen Teilchenidentifizierung, einem detaillierten Detektor Verständnis sowie einer verlässlichen Bestimmung des Wechselwirkungspunktes der betrachteten Ereignisse. Sowohl der elastische wie auch der inelastische Anteil der Reaktion wurde in der Messung berücksichtigt. Das Messergebnis wird verglichen mit theoretischen Vorhersagen unter Benutzung der ALLM-97 Parametrisierung der Proton Strukturfunktion im Rahmen des COMPTON-2.14 Monte Carlo Generators.

To Uzma, Saira and Zoha.

Contents

1	Introduction	1
1.1	The structure of the proton	1
1.2	Deep inelastic scattering	2
2	The QED Compton process	6
2.1	Radiative electron-proton interactions	6
2.1.1	Bremsstrahlung	7
2.1.2	QED Compton	8
2.2	Photon content of the proton	11
2.3	Objectives and outline of the analysis	16
3	Experimental Setup	19
3.1	HERA	19
3.2	The H1 detector	20
3.2.1	Layout and coordinate system	21
3.2.2	Calorimetry	21
3.2.3	Tracking	25
3.2.4	Time-of-flight system	29
3.3	Triggersystem and data acquisition	29
3.3.1	Luminosity measurement	30
4	Event selection	33
4.1	Monte Carlo	33
4.1.1	Compton signal	33
4.1.2	DVCS background	36
4.1.3	Di-lepton background	37
4.1.4	DIS background	37
4.2	Data basis 1997	39
4.2.1	Compton event selection criteria	39
4.2.2	Selection of the inelastic channel	41
5	Particle Identification	44
5.1	General conditions	44
5.2	Tracking in the backward region	45
5.2.1	Tracking with the Backward Drift Chamber	45
5.2.2	Validation of charged tracks with the CIP	46
5.2.3	CIP pad-clusters	47
5.2.4	Track reconstruction with the BST	48
5.3	Detection efficiencies	51
5.3.1	Efficiency in Compton	51
5.3.2	Selection of a DIS event sample	53
5.3.3	BST stability and efficiency	54
5.3.4	BST hit bank loss	55
5.3.5	CIP efficiency	56
5.3.6	BDC efficiency	63
5.4	Electronic noise	63
5.4.1	Noise measurement	65

5.5	Application to Monte Carlo	66
5.6	Vertex selection for Compton events	71
5.6.1	Vertex resolution	72
5.7	Photon conversion	72
5.7.1	Passive material in the backward area	73
5.7.2	Photon identification	75
5.7.3	Conversion between vertex and subdetectors	75
5.8	Electron–photon identification	79
5.8.1	Radial configurations	79
5.8.2	Identification algorithms	80
5.8.3	Reduced detector algorithm	84
6	Calibration	85
6.1	Subdetector alignment	85
6.1.1	Tilt of beams	85
6.1.2	Compensation of the electron deflection	86
6.1.3	SpaCal and BDC alignment	89
6.1.4	BST alignment	93
6.2	Cluster energy and dispersion	94
6.2.1	Non-linearity of energy measurement	94
6.2.2	Test of E_{DA} in Monte Carlo	96
6.2.3	Correction of non-linearity	99
6.2.4	Additional energy smearing in MC	102
6.3	Trigger	103
6.3.1	Compton trigger setup	103
6.3.2	Drift Chamber $r\varphi$ trigger on level 1	104
6.3.3	Topological trigger on level 2	108
6.4	Vertex weighting	110
7	Cross section	112
7.1	Definition	112
7.2	Kinematic range and acceptance	112
7.3	Control distributions	115
7.3.1	Vertex	118
7.4	Systematic errors	118
7.5	Cross section	120
7.6	Summary and prospects	122
A	Appendix	127
A.1	Computation of acoplanarity	127
A.2	Run selection	129
A.3	BST parameters	131
A.4	Encoding of the CIP cluster algorithm	133
	Tables	135
	Figures	136
	References	138

1 Introduction

The course of high energy physics has led to the development of a well established model describing the properties of and the interactions between microscopic elementary particles. This framework, the standard model of particle physics, came into being about thirty years ago and forms since then the theoretical basis of many experiments across the world. In this theory quarks and leptons are the constituents of matter, and the carrier of the known fundamental forces are the gauge bosons, namely the photon, W^\pm and Z^0 for the electroweak force, and the gluon g (in eight different strong colour charge combinations) for the strong force. While the quarks make up complex hadronic, *i.e.* strong interacting objects, leptons are found either as building blocks of the shells of atoms, which are the electrons; or they appear in electroweak interactions, such as the nuclear β -decay or as participants in the fusion processes in the cores of stars. The experimental attempt to understand the properties of the fundamental forces and to possibly discover new particles is reflected in the construction of increasingly complex particle acceleration and detection facilities over the last decades. Colliding two beams of particles, besides colliding one beam on a fixed target as well as the non-accelerator high energy experiments being run deep underground, has become the standard method. The principle of corresponding measurements is to gain cross sections, that is reaction probabilities, in dependence of the kinematic properties in the collisions. One of those facilities is the storage ring HERA set up in Hamburg where an electron beam and a proton beam are pointed against each other in order to inspect the structure of the proton by using the electrons as quasi point-like probes. As a characteristic kinematic measure to quantify the spatial resolution-power in this type of experiment serves the negative square of the Lorentz-invariant four-momentum change (Q^2) of the electron during the reaction. This quantity defines the equivalent wavelength $\lambda = h/\sqrt{Q^2}$ of the applied probe and thus the typical resolvable size of substructures of the object under investigation.

The topic of this analysis is the measurement of the QED Compton cross section in positron proton interactions as one of several reaction types being investigated in the H1 experiment. The Compton process probes the proton structure, as a consequence of its special topology, at very low values of Q^2 . After a general overview to the proton structure in this chapter and the relation to the Compton process in chapter two, a description of the experiment is given in chapter three. The used data samples and selection criteria are described in chapter four. The matter of particle identification in connection with a detailed treatment of the involved detector components follows in chapter five. Finally, the last two chapters discuss important calibration aspects and the cross section results, respectively.

1.1 The structure of the proton

The typical size of atomic nuclei was first determined by experiments of Geiger, Marsden and their interpretations by E. Rutherford in 1911 [1]. Nuclei were found to be amazingly small, namely about 10^{-5} in units of the size of atoms in general. This corresponds to a diameter of $\simeq 10^{-15}$ m. In the first decades after this discovery the natural question persisted whether nuclei were point-like or if there was some finer detail or substructure. Indications that the proton should have some internal structure were observed in the 1930s when the proton's magnetic moment was measured for the first time, which deviated from the value expected for a point-like Dirac particle [2]. A further milestone is the series of measurements on electron–nucleus scattering performed by R. Hofstadter [3] in the 1950s, using electron beam energies in the range of 190 to 600 MeV on fixed targets. These experiments gave a closer insight to the dimensions of different nuclei and in particular, by means of a hydrogen target, of the proton. In these (elastic) collisions the proton structure appeared as an extended object by showing an interference pattern in dependence of the electron scattering angle and momentum

transfer, respectively. It became possible to derive elastic form factors and nuclear charge densities, describing more detailed the structure of the proton, for the first time. The form factors were related to the elastic cross section like

$$\frac{d\sigma^R}{d\Omega} = \frac{4\alpha^2 E'^2}{Q^4} \frac{E'}{E} \cos^2 \frac{\theta}{2} \left(\frac{G_E^2(Q^2) + \tau G_M^2(Q^2)}{1 + \tau} + 2\tau G_M^2(Q^2) \tan^2 \frac{\theta}{2} \right) \quad (1.1)$$

utilizing $\tau = Q^2/4m_p^2$ with the proton mass m_p . This is the result of Rosenbluth's ansatz [4] for the hadronic current to describe the electromagnetic interaction of the beam electron on the unknown hadronic structure. In the above representation the deviation from the expected Dirac magnetic moment of the proton target is already incorporated in G_M . Experimentally, by cross section measurements at different scattering angles θ and final state electron energies E' , the form factors can be extracted, each of them as a function of Q^2 , and yield the dipole fits to $G_{E,M}(Q^2)$.

Then, with increasing electron energies towards the GeV-range the inelastic regime is reached. The shape of the proton passes through several excited states, the nucleon resonances, with increasing energy transferred to it in the collision. In more energetic collisions the proton breaks up and the process is accompanied by a multi-particle hadronic final state X of increasing invariant mass. For this domain the form factors $G^2(Q^2)$ are replaced by the structure functions W_1 and W_2 which are functions of the momentum transfer Q^2 and the energy transfer $\nu = E - E'$. The cross section is then described as

$$\frac{d^2\sigma}{d\Omega dE'} = \sigma_{\text{Mott}} \cdot \left(W_2(Q^2, \nu) + 2 W_1(Q^2, \nu) \tan^2 \frac{\theta}{2} \right). \quad (1.2)$$

The energy transfer ν (*i.e.* as measured in the lab frame) can be used to construct a quantity $x = Q^2/2m_p\nu$ which turns out to comfortably describe the type of the interaction with the target, as the case $x = 1$, or equivalently $\nu = Q^2/2m_p$, corresponds to elastic scattering while smaller values of x are found in inelastic collisions. Experimentally the observation of *scaling* of the above structure functions was made, that is their invariance against changes of Q^2 for a given fixed ratio of momentum transfer relative to energy transfer, x . This result, harmonized with Bjorken's algebraic findings that for $(\nu, Q^2) \rightarrow \infty$ and for constant x , a transition

$$MW_1(x, Q^2) \rightarrow F_1(x) \quad \nu W_2(x, Q^2) \rightarrow F_2(x), \quad (1.3)$$

towards structure functions independent of Q^2 (M represents the target mass) could be made, allowed to regard the proton (Feynman, 1969) as an object composed of smaller particles, called *partons*, acting as the true target objects in incoherent elastic collisions to sum up to the observed cross sections. In this picture Bjorken's x becomes a measure for the fraction of a parton's momentum of the proton's total momentum p , where $p \rightarrow \infty$ in the lab system. Furthermore, the interpretation of the structure functions can then be given as sums of partonic momentum distributions. Using the cross section results from experiments with different types of beams (made up either of neutrinos, anti-neutrinos, electrons or muons) and different targets (nucleons, nuclei) separate distribution functions could be isolated which are attributed to the existence of the constituent partons, *quarks* and *anti-quarks*. Together with further confirming observations these results were combined to the Quark Parton Model (QPM).

1.2 Deep inelastic scattering

In deep inelastic scattering leptons interact with protons by the exchange of electroweak bosons which are the photon and the high massive W^\pm and Z^0 . The fundamental Feynman graph in lowest order

is shown for electron-proton interaction in Figure 2.3. In this work the probing lepton is the electron (or positron) corresponding to the type of reactions investigated at HERA.

The kinematics in ep collisions is described in terms of the 4-momenta of the participating particles, using for example the following notation:

l	the incoming beam electron
l'	the scattered electron
P	the incoming beam proton
X	the proton remnant or (more general) the hadronic final state.

From these, further kinematic quantities can be derived to describe the interaction and to gain information about the hadronic initial state. To these quantities belongs the negative squared momentum transfer

$$Q^2 = -q^2 = -(l - l')^2, \quad (1.4)$$

which determines the invariant mass of the exchanged virtual boson and is thus a measure for the resolution scale applied to the object. Due to their high masses the charged bosons and the Z^0 do contribute significantly only at higher momentum transfers as their influence is suppressed due to the propagator $Q^2/(Q^2 + M^2)$. Thus, the interaction is dominated by photon exchange in the low Q^2 range; and only this kinematic range is considered here. Further, the Bjorken variable is defined as

$$x = \frac{Q^2}{2P \cdot q} \quad (1.5)$$

where the denominator can be written as $P \cdot q = m_p(E - E')$ for energies in the rest frame of the proton. The inelasticity of the reaction is given as

$$y = \frac{P \cdot q}{P \cdot l} \quad (= 1 - \frac{E'}{E})_{\text{r.f. proton}}. \quad (1.6)$$

Again, in the proton rest frame, y corresponds to the relative energy loss of the scattered electron through the virtual photon. Both Lorentz-invariant variables, x and y , assume values from 0 to 1. The center of mass energy squared in the ep collision is given by

$$s = (l + P)^2 \approx 2l \cdot P \quad (1.7)$$

where the last approximation holds for high collision energies where the electron and especially the proton mass can be neglected. Thus the above quantities can be combined in the (approximate) equation

$$x = \frac{Q^2}{sy}. \quad (1.8)$$

In the case of HERA with e, p beam energies of $E_e=27.6$ GeV and $E_p=820$ GeV (in the year 1997) the center of mass energy is $\sqrt{s} \simeq 300$ GeV setting the upper limit for any produced final state mass and $Q_{\text{max}}^2 \simeq 90000$ GeV². This configuration would equal a (hypothetical) fixed proton target experiment using electron beam energies of the order of 45 TeV.

The differential cross section description becomes in deep inelastic scattering, using the two structure functions F_1 and F_2 and neglecting the proton mass [5],

$$\frac{d^2\sigma}{dx dQ^2} = \frac{4\pi\alpha^2}{Q^4} \left[(1 + (1 - y)^2) F_1 + \frac{1 - y}{x} (F_2 - 2xF_1) \right] \quad (1.9)$$

where a third structure function F_3 is ignored since virtual Z exchange can be neglected. The second term represents the *longitudinal* structure function, now including the proton mass, given as

$$F_L(x, Q^2) = \left(1 + \frac{4m_p^2 x^2}{Q^2}\right) F_2(x, Q^2) - 2xF_1(x, Q^2) \quad (1.10)$$

which becomes equal to $(F_2 - 2xF_1)$ for $Q^2 \rightarrow \infty$. F_L represents the part of the structure function which is sensitive to the absorption of longitudinal virtual photons, whereas F_2 contains both longitudinal and transverse parts. With the Callan-Gross relation $F_2 = 2xF_1$, implying $F_L=0$, and its experimental verification it is understood that quarks have spin 1/2. The relation follows within the QPM, where transverse parton momenta are disregarded, from the consideration that spin-1/2 partons cannot absorb longitudinal polarized virtual photons. Thus, the deep inelastic scattering cross section is determined by F_2 .

QCD picture

As indicated by Eq. 1.9 the structure functions are allowed to also depend on Q^2 . This is a consequence of the observation that Bjorken scaling is only valid in some kinematic range of deep inelastic scattering. Furthermore, the QPM is not able to explain that quarks do not appear as single free particles but always seem to be enclosed in some hadron. This and other effects, like for instance the appearance of three ‘‘identical’’ quarks in the double positive proton-resonance Δ^{++} , can be explained in the theory of quantum chromodynamics, QCD: quarks are subject to the strong force, connected to their *colour* charges. The carriers of this force are the *gluons* which mediate the interaction by having colour charges themselves. Owing to these colours gluons can couple to themselves, and a special property can be attributed to the strong field, namely that its potential rises with increasing distance between colour charges (*i.e.* quarks). Figuratively, this behaviour causes the field energy to grow until some threshold for the production of one (or more) new quark-antiquark pair is reached from which new hadrons are generated, rather than just separating two quarks from a bound system into single free particles. While this describes the quark *confinement*, quarks seem to be asymptotically free when viewed at an increasing resolution scale Q^2 , which is described by a non-constant coupling $\alpha_s \propto 1/\ln(Q^2/\Lambda^2)$. With these considerations it is possible to qualitatively understand the structure function scaling violations which are not expected in the QPM: with increasing Q^2 the function $F_2(x, Q^2)$ rises at low x values and drops at high x values since it is more likely to find a quark when it just radiated off a gluon. This gluon carries away some amount of the original quark momentum (or: fraction of the proton momentum) such that it is observed at lower momentum fractions x . For the same reason it is less likely to encounter one of the three valence quarks (with relatively high mean values of $\bar{x}_{\text{QPM}} \simeq 0.3$) when probed at higher resolutions. This relationship between resolution scale Q^2 and the parton distribution functions is described by the DGLAP-formalism [6, 7, 8] which accounts for both the quark and the gluon content of the proton as determined by the splitting of quarks and gluons into quarks, gluons and sea quark-pairs.

In the context of the later described QED Compton scattering process, this aspect of the evolution of the particle momentum distributions, specifically those of the gluon, will be contrasted to the partonic photon content of the proton.

While the kinematic range of deep inelastic scattering above a few GeV^2 appears to be well understood by increasing precise measurements supporting perturbative QCD, where the proton structure function can be ostensibly regarded as the sum of partonic distribution functions, there is also interest in the low- Q^2 regime. In this area of ep interactions the parton picture cannot be used anymore. Instead the existing parameterisations are tested for their validity towards lower resolution scales and extended phenomenologically (*e.g.* [21]) to establish a connection between DIS and the photoproduction range, based on the combined data of several experiments. On the experimental side this

gap between HERA and fixed-target experiments can be touched and even accessed by different experimental and analytic techniques. To reach lowest possible Q^2 values three main methods can be mentioned:

- (i) the use of *shifted vertex* data in the ep experiments H1/Zeus, which extend the kinematic range using the same detector acceptance and allow the measurement of smaller scattering angles and thus smaller Q^2 . (S. Section 3.1 for a short description of this technique.)

Further by the analysis of scattering events of the radiative type which are

- (ii) the initial state radiation events, which lower the effective incoming beam electron energy by radiating off energetic photons moving collinearly to the beam, for the measurement of the structure functions F_L and F_2 at lower center-of-mass energies and momentum transfers, respectively, and
- (iii) the QED Compton scattering process giving access also to very low scales as two high energetic particles nearly balance their transverse momenta such that the total momentum transfer stays low.

While the first and second method has been used for corresponding analyses, the QED Compton event type, although suggested in earlier publications and used for luminosity control measurements [22], was applied for the detailed proton structure not before some sufficient amount of luminosity was recorded. A description of Compton scattering is given in the next section.

2 The QED Compton process

The QED Compton process (hereafter also denoted as QEDC) represents the scattering of electrons off protons accompanied by the emission of hard photon radiation under polar angles comparable to that of the scattered electron. It is one of a series of radiative interaction types present in ep scattering. In the following the different channels and their properties are discussed with a detailed focus on Compton scattering.

2.1 Radiative electron-proton interactions

The general description for radiative processes in electron-proton interactions is displayed in Figure 2.1. They appear topologically in different types. For a characterization of the corresponding kinematic regimes it is convenient to consider the following set of variables:

$$q_{e^*}^2 = \begin{cases} (p_\gamma - p_e)^2 \\ (p_\gamma + p_{e'})^2 \end{cases} \quad (2.1)$$

$$q_{\gamma^*}^2 = (p_X - p_p)^2, \quad (2.2)$$

where the 4-momenta of the incoming electron p_e , incoming proton p_p , scattered electron $p_{e'}$ and photon p_γ as well as the hadronic final state p_X are used. Both expressions are part of the propagator terms of the amplitude A for the reaction shown in Figure 2.1:

$$dA \propto \frac{dq_{e^*}^2}{q_{e^*}^2 - m_e^2} \cdot \frac{dq_{\gamma^*}^2}{q_{\gamma^*}^2} \quad (2.3)$$

The radiative processes can be classified by identifying the poles of both factors in Eq. 2.3: In the case of low virtual electron and photon masses, $q_{e^*}^2 \approx 0$ and $q_{\gamma^*}^2 \approx 0$, one obtains a high interaction rate which corresponds to the bremsstrahlung process. Looking on electron-proton collisions one can conclude from the smallness of both terms that the cross section peaks at small scattering angles, since one can write for example for the first factor:

$$\begin{aligned} q_{e^*}^2 &= (p_\gamma - p_e)^2 = p_\gamma^2 + p_e^2 - 2p_\gamma p_e = 0 + m_e^2 + 2\vec{p}_\gamma \vec{p}_e - 2E_\gamma E_e \\ &\simeq m_e^2 + 2E_\gamma E_e (\cos \theta - 1) \end{aligned} \quad (2.4)$$

where θ is the photon polar angle with respect to the incident electron direction. In fact, the HERA experiments make use of this process in order to measure the current beam luminosity.

Two further cases can be distinguished in which one of both factors in the denominator of Eq. 2.3 is close to ≈ 0 , while the other one has some finite value. This allows at least one particle, electron or photon, to be scattered under some angle relative to the direction of the incoming beam particles. With $q_{e^*}^2 \approx 0$ and $q_{\gamma^*}^2$ being finite the scattered electron is found towards higher angles. The momentum direction of the final state photon corresponds predominantly to the *incoming* electron momentum in the case of the left graph, and it is almost collinear to the *scattered* electron for the right graph of Figure 2.1. Both cases are known as Initial State Radiation, ISR and Final State Radiation, FSR respectively, in ep scattering and make radiative corrections to cross section measurements necessary.

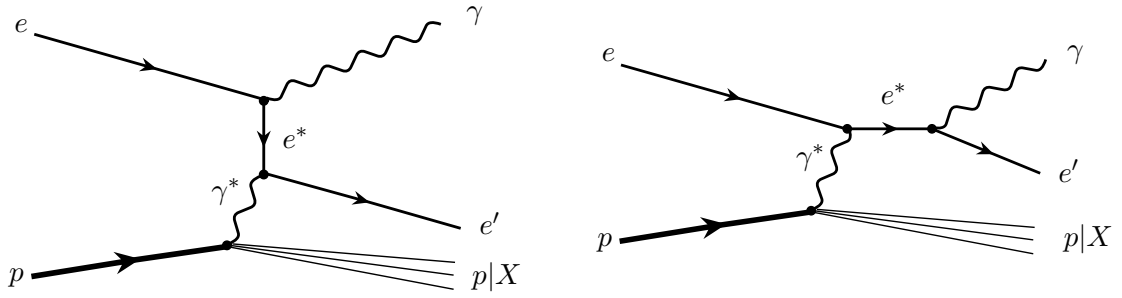


Figure 2.1: Lowest order Feynman graphs of radiative processes in ep scattering. The incoming particles are the electron ' e ' and proton ' p '. A real photon γ is radiated off the electron line in both graphs. ' $p|X$ ' denotes the final state depending on whether the interaction was elastic or inelastic.

On the other hand, when $q_{e^*}^2$ is sufficiently different from zero and $q_{\gamma^*}^2 \approx 0$, the pole in the expression leads to a topology with both particles emerging at significant higher scattering angles in comparison to the usual bremsstrahlung process. Therefore, this kinematic region is also denoted as “wide-angle bremsstrahlung” or “third peak” [17]. The equivalent denotation “QED Compton scattering” is motivated by the scattering of *quasi-real* photons γ^* on incoming electrons, by which the process resembles the classical Compton process

$$e + \gamma^* \rightarrow e + \gamma. \quad (2.5)$$

The separation into the mentioned sub-classes (summarized in Table 1) is somehow arbitrary since no observable parameter exists which would allow to strictly distinguish between them. They are defined by the different topologies found in typical high energetic particle collisions as well as by the detection acceptance of an appropriate experimental setup. A description of the mentioned event types is given in the following sections.

Table 1: Overview on photon and electron virtualities and the related radiative processes in ep scattering.

$ q_{e^*}^2 $	$ q_{\gamma^*}^2 $	type of process
≈ 0	≈ 0	bremsstrahlung
≈ 0	> 0	radiative DIS
> 0	≈ 0	QED Compton (“3 rd peak”)

2.1.1 Bremsstrahlung

This type of radiative processes is by far dominated by the elastic channel and therefore insensitive to the proton structure. This fact allows to use the process for the luminosity measurement. It is described more detailed in connection with the luminosity determination in the H1 experiment, in the next chapter, see Section 3.3.1.

2.1.2 QED Compton

Due to the smallness of the transferred momentum to the proton, $q_{T*}^2 \approx 0$, the QED Compton process involves a characteristic *back-to-back* topology, when viewed in the azimuthal plane into which the electron and photon are scattered. This means their both transverse momenta are nearly of the same amount but of opposite direction, such that the sum $\vec{p}_T = |\vec{p}_{T,e} + \vec{p}_{T,\gamma}|$ approximately becomes zero, s. Figure 2.2. Equivalently, the azimuthal angle difference $\Delta\varphi$ between these both particles is most likely found at $\approx 180^\circ$, which corresponds to a signed *acoplanarity*

$$A = 180^\circ - \Delta\varphi \quad (2.6)$$

peaking at a value of zero. The detailed acoplanarity calculation accounting for the sign is given in appendix A.1.

Compton scattering is generally described in terms of the different elasticity regimes of the reaction. The usual describing kinematic quantity is the invariant mass m_X of the hadronic final state. In the following an overview to the cross section formalism is given according to [9] in more detail.

Kinematic description

Compared to the usual describing variables of deep inelastic scattering the corresponding ones in Compton scattering have to account for the final state photon as it largely changes the kinematic situation. Using the extended four-momentum change $q_h = l - l' - k$, where l and l' refer to the incoming and outgoing electron and k refers to the scattered Compton photon, one defines:

$$Q_h^2 = -q_h^2 = -(l - l' - k)^2, \quad x_h = \frac{Q_h^2}{2P \cdot q_h}, \quad y_h = \frac{P \cdot q_h}{P \cdot l}. \quad (2.7)$$

Further, the mass of the hadronic final state is calculated as

$$m_X^2 = p_X^2 = m_p^2 + Q_h^2 \frac{1 - x_h}{x_h}. \quad (2.8)$$

The subscript ‘‘h’’ stands for the term ‘‘hadronic’’ as these variables are valid at the hadronic vertex and are thus of identical meaning as in the DIS case. This denotation will be used in the following to distinguish the variables from the corresponding leptonic variables discussed later on. In a measurement the hadronic final state mass could be calculated according to

$$m_X^2 = (l - l' - k + P)^2 = s - 2(l + P) \cdot (l' + k) + (l' + k)^2. \quad (2.9)$$

But because of $s \approx 2(l \cdot P)$ a subtraction of large numbers occurs in this formula and introduces large errors in the mass determination only from the momenta of the scattered electron and photon.

The presence of the photon in the process adds three further degrees of freedom, namely its energy, polar angle and its azimuthal angle with respect to the scattered electron. That means that the acoplanarity becomes a relevant additional parameter to completely describe the scattering. This is in contrast to the usual DIS process where the kinematics can be expressed in terms of the scattered electron alone or, alternatively, using the hadronic final state. As a consequence further parameters need to be introduced to describe the QED Compton differential cross section. The first one is the Lorentz-invariant quantity

$$x_\gamma = \frac{l \cdot q_h}{l \cdot P} = \frac{W^2 + Q_h^2 - m_e^2}{s - m_p^2 - m_e^2} \simeq \frac{W^2 + Q_h^2}{s}, \quad (2.10)$$

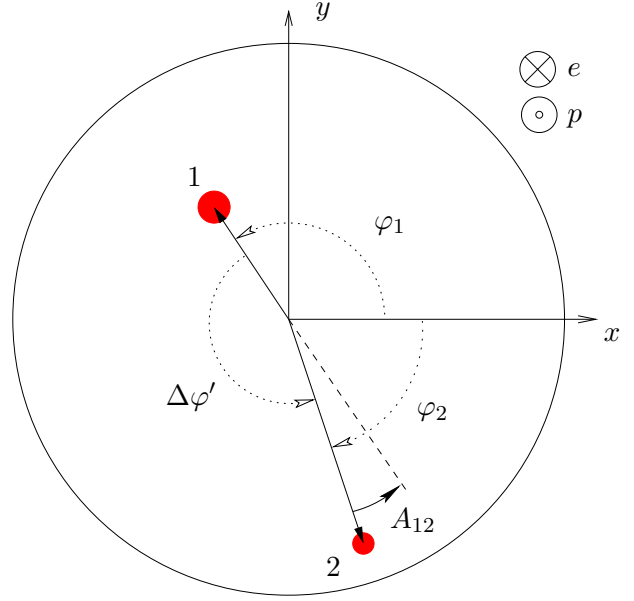


Figure 2.2: Definition of the acoplanarity A_{12} in QED Compton scattering. The distribution of the azimuthal angle difference of the two particles (dots 1 and 2) scattered through the SpaCal- xy -plane peaks at 180° . The beam directions of electrons and protons, perpendicular to the xy -plane, are indicated on the right side.

where W^2 is the squared invariant mass of the scattered electron and photon system, $(l+k)^2$. The second one is the solid angle element

$$d\Omega^* = du^* d\varphi^* = d(\cos\theta^*) d\varphi^*, \quad (2.11)$$

where θ^* and φ^* are the orbital and azimuthal scattering angles in the center-of-mass frame of the virtual Compton process $\gamma^*e \rightarrow \gamma e$, s. Figure 2.1. With these considerations the fourfold differential cross section can be written as

$$\frac{d^4\sigma^{ep \rightarrow e\gamma X}}{dx_h dx_\gamma dQ_h^2 d\Omega^*} = f_{\gamma^*/p}^T(x, x_\gamma, Q_h^2) \left[\frac{d\sigma}{d\Omega^*} \right]^T + f_{\gamma^*/p}^L(x, x_\gamma, Q_h^2) \left[\frac{d\sigma}{d\Omega^*} \right]^L, \quad (2.12)$$

using the subscript notation T and L for the transverse and longitudinal polarization of the virtual photon at the hadronic vertex. The factorization formula Eq. 2.12 clearly depicts the merging between the photon flux factor f and the virtual Compton process.

The virtual photon's polarization at the leptonic vertex is accounted for in the expressions

$$\left[\frac{d\sigma}{d\Omega^*} \right]^T = \frac{d\sigma_T}{d\Omega^*} + \epsilon \frac{d\sigma_L}{d\Omega^*} + \sqrt{2\epsilon(1+\epsilon)} \frac{d\sigma_{TL}}{d\Omega^*} \cos\varphi^* + \epsilon \frac{d\sigma_{TT}}{d\Omega^*} \cos 2\varphi^*, \quad (2.13)$$

$$\left[\frac{d\sigma}{d\Omega^*} \right]^L = \frac{d\sigma_T}{d\Omega^*} + \frac{1+\epsilon}{2\epsilon} \frac{d\sigma_L}{d\Omega^*} + \sqrt{2\frac{1+\epsilon}{\epsilon}} \frac{d\sigma_{TL}}{d\Omega^*} \cos\varphi^* + \frac{d\sigma_{TT}}{d\Omega^*} \cos 2\varphi^*. \quad (2.14)$$

The lower subscripts T, L, TL, TT denote the transverse and longitudinal cross sections, as well as the transverse-longitudinal and transverse-transverse interference cross sections of the virtual Compton scattering process. Furthermore, on the hadronic side the virtual photon spectra $f^{\gamma^*,L}$ equal

$$f_{\gamma^*/p}^{T,L} = \frac{1-x_h}{4\pi^3 x_h x_\gamma} g^{T,L}(x_h, x_\gamma, Q_h^2) \sigma_{\gamma^*p}^{T,L}, \quad (2.15)$$

with the functions $g^{T,L}$ given by the expression

$$g^L = g^T - \frac{x_\gamma^2}{2x_h^2} = \frac{(1 - \frac{x_\gamma}{x_h})Q_h^2 - x_\gamma^2 m_p^2}{Q_h^2 + 4x_h^2 m_p^2}, \quad (2.16)$$

they also define the virtual photon polarization parameter $\epsilon = g^J/g^T$. Finally, the different polarization cross sections $d\sigma/d\Omega^*$ of Eqs. 2.13 and 2.14 are simple but longer functions of W and Q_h^2 , [9].

The above calculations do not involve any approximations in describing the cross section of the process as represented by the Feynman graphs in Figure 2.1. They enter as the theoretical basis of the COMPTON event generator used in this analysis.

The photo-absorption cross sections $\sigma_{\gamma^*p}^{T,L}$ contained in the fluxes f of Eq. 2.15 depend on the basic type of the interaction, whether it is an elastic, resonant-inelastic or continuum-inelastic ep process. The different cases together with their γ^*p cross sections are discussed in the following paragraphs.

Elastic scattering

This case corresponds to an intact proton as the single particle in the hadronic final state, $m_X = m_p$. Its momentum is nearly the same as before the interaction and so the movement continues only under a small deflection angle from its original direction. In ep collisions this corresponds to a straight proton trajectory nearly parallel within the beam pipe to the incoming proton direction, no other hadronic particle is observed. But since a photon is produced in the final state, besides the electron and the proton, this channel is also denoted as *pseudo-elastic* (the pure elastic process would have only e and p in the final state). The photon-absorption cross section is calculated according to

$$\sigma_{\gamma^*p}^T = \frac{4\pi^2\alpha}{Q^2} G_M^2(Q^2) \frac{\delta(1-x)}{1-x}, \quad (2.17)$$

$$\sigma_{\gamma^*p}^L = \frac{16\pi^2\alpha m_p^2}{Q^4} G_E^2(Q^2) \frac{\delta(1-x)}{1-x}. \quad (2.18)$$

These formulae are the common description for the elastic scattering using the proton's elastic form factors

$$G_E(Q^2) = \frac{G_M(Q^2)}{2.79} = \frac{1}{(1 + \frac{Q^2}{Q_0^2})^2} \quad \text{with} \quad Q_0^2 = 0.71 \text{ GeV}^2. \quad (2.19)$$

Note that Bjorken- x in Eqs. 2.17 and 2.18, as implemented by the corresponding delta functions $\delta(1-x)$, does not enter the final cross section as a "varying" parameter. Instead, the notation reflects the situation that the virtual photon interacts with the proton as a whole but not with partonic substructures, thus analytically only the value $x = 1$ contributes to the cross section integral.

Resonance-inelastic scattering

This kinematic regime of ep collisions is featured by excitation energies high enough to bring the proton into the subsequent decaying resonant states $\Delta(1232)$, $N^*(1520)$ and $N^*(1680)$. Their final states are $N\pi$ and $N\pi\pi$. The decay widths of these most pronounced resonances are of the order of 10% of their masses due to the very short lifetimes in their hadronic decays. The domain spans in m_X from roughly $(m_p + m_\pi)$ as production threshold for $\Delta(1232)$ up to ≈ 1.8 GeV corresponding to the outer tails of the $N^*(1680)$. An approximate description of the total cross section can be given as a sum of Breit-Wigner shaped parameterisations of each resonance using experimental data of these well investigated states:

$$\sigma^T = \sum_R \sigma_R \frac{m_R^2 \Gamma_R^2}{(m_X^2 - m_R^2)^2 + m_R^2 \Gamma_R^2} \cdot \frac{1}{(1 + \frac{Q^2}{Q_R^2})^2}, \quad \sigma^L = 0, \quad (2.20)$$

where m_X is the final state mass, with the parameters m_R (resonance masses [27]), Γ_R (widths) and Q_R^2 (constants, typical size $\approx 3 \text{ GeV}^2$), and σ_R are the resonance cross sections as listed in [9], based on [28] and [29]. They are 550, 280 and 220 μb for increasing mass of the above resonant states.

Continuum-inelastic scattering

With further increasing momentum transfer to the proton the inelastic continuum with a hadronic mass of more than 1.8 GeV^2 is reached where only a few resonances are present. Their peaking is less pronounced so that they can be absorbed in the following structure description. The ratio of elastic and inelastic cross section drops rapidly due to the very different Q^2 dependence, Eq. 2.18. In the inelastic case both virtual photon absorption cross sections can be related to the structure function F_2 as

$$\sigma_T = \frac{4\pi^2\alpha}{(1-x)Q^2} F_2(x, Q^2), \quad (2.21)$$

$$\sigma_L = \frac{4\pi^2\alpha}{(1-x)Q^2} \frac{4x^2 m_p^2}{Q^2} F_2(x, Q^2). \quad (2.22)$$

On the other hand the structure functions must vanish in the limit $Q^2 \rightarrow 0$, such that the real-photon production cross section is obtained,

$$\sigma_T \simeq 100\mu\text{b} \quad \sigma_L = 0. \quad (2.23)$$

The question how to model the transition between the DIS regime and the photoproduction regime as $Q^2 \rightarrow 0$ is usually answered by multiplying to F_2 a damping factor of the form

$$\phi(x, Q^2) = \frac{Q^2}{Q^2 + F_2(x, Q^2)}. \quad (2.24)$$

The actual structure function parameterisation used for this analysis will be discussed later in the context of the Compton event generator, Section 4.1.1.

2.2 Photon content of the proton

The flux of quasi-real photon met in QED Compton scattering can be treated in a somewhat simplified way. It is an usual method to consider a fast moving charged particle as an equivalent ray of photons, the spectrum of which is given by the so called Weizsäcker-Williams approximation [12, 13]. This approach is a widely used method of calculating charged particle scattering processes, and also ep scattering. In this field the corresponding treatment is also called *collinear approximation* (CA) which denotes its essential property, the neglect of transverse momenta of virtual photons originating from the proton. This analogy to the parton model view on quarks and gluons, where the same assumption about the transverse momenta is made, allows to understand photons also as partonic constituents of the proton. This means the scattering process with a virtual photon is regarded as a probe on a part of the proton structure which is quite different to the usual concept. The theoretical interest can be summarized in the following points:

- firstly, the full description of the proton structure at current available c.m.s. energies;
- secondly, the comparison of different Q^2 evolution behaviour of the distribution functions of photons and gluons within the proton;

- thirdly, for the understanding of photon induced processes in ep and pp collisions at high energy, for example those expected at the LHC. There the partonic photon distribution $\gamma(x, Q^2)$ should become increasingly important, *e.g.* contributing to the production of heavy charged particles as in the fusion process in $pp \rightarrow \gamma\gamma \rightarrow H^+H^-$ (see for example [14, 15] where calculations show that other far more competitive processes exist, like Drell-Yan production).

From these points of view the QED Compton process has been mentioned in several publications to be used as a sensitive tool for the measurement of the photon content of the proton [16]. A comparison between Compton and usual deep inelastic scattering, as proposed in [10], is shown in Figure 2.3. The virtual photon is regarded as a partonic object, the scattered real photon becomes part of the hadronic final state in analogy to the production of a jet in DIS. The Compton hadronic final state might be the proton or some inelastic remnant. The spot at the leptonic vertex in the Figure (right graph) denotes the $e\gamma \rightarrow e\gamma$ subprocess of Figure 2.1, the photon content is probed by a virtual electron. Therefore, in this picture, the Compton process is also referred to as Deep Inelastic Compton Scattering (DICS). As a consequence the usual DIS kinematics has to be used, which is given by the *leptonic* variables

$$Q_l^2 = -q_l^2 = -(l - l')^2 \quad x_l = \frac{Q_l^2}{2P \cdot q_l} \quad y_l = \frac{P \cdot q_l}{P \cdot l_l}. \quad (2.25)$$

Thus, within the collinear approximation it is assumed to be sufficient to describe the interaction with two variables, x_l and Q_l^2 , in contrast to the complete kinematics in Compton where the additional Lorentz-invariant quantity x_γ is used, Eq. 2.10. The identity $x_l = x_\gamma$ holds due to the assumptions in the collinear approximation, as used for example in [10].

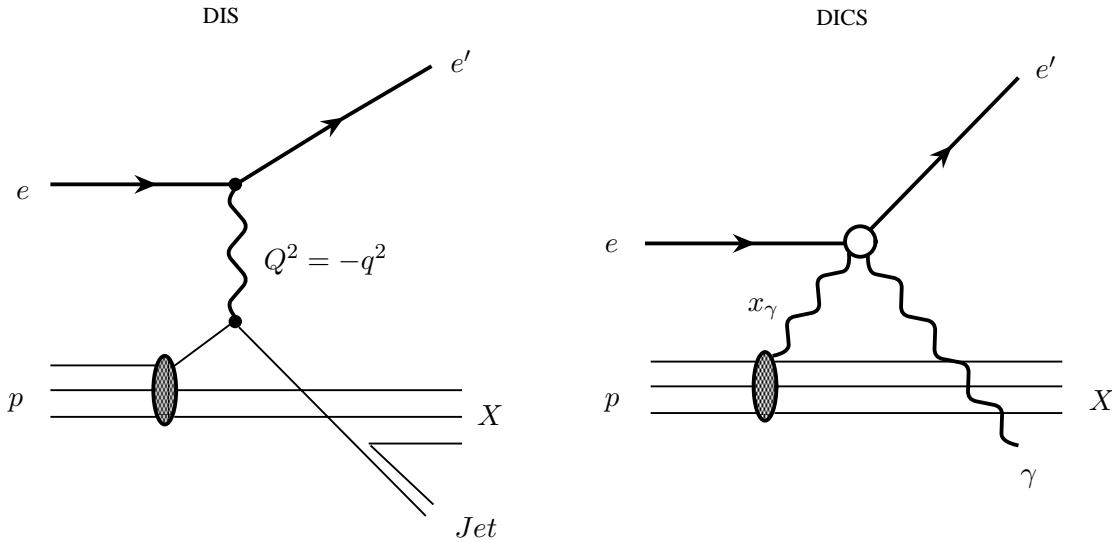


Figure 2.3: Analogy between standard deep inelastic scattering (left graph) and QED Compton scattering (right graph). While in the DIS case the virtual photon probes the partonic structure of the proton, it can be regarded in Compton itself as a partonic object; the idea (and drawing) based on a publication of De Rujula/Vogelsang [10].

Whereas the distinction between the elastic and inelastic channel in DIS clearly separates two rather different physical appearances, it is in DICS considered to be artificial as the real photon is always present. As pointed out in [37] the x_l plays (again) the role of the momentum fraction carried by the partonic photon of the proton momentum in which the photon is observed. This means, in a frame

of high proton momenta – and only there – the photon four-vector components are approximately given by

$$-q_h \simeq x_l P, \quad (2.26)$$

where P is, as usual, the proton four-momentum vector. But this relation does not hold for the squared photon momentum: $Q_h^2 \neq x_l^2 m_p^2$. This difference between collinear approximation and the precise calculation can also be seen according to the following analytic consideration: The squared invariant mass of the Compton electron and photon can be written in the CA as

$$\begin{aligned} W^2 = \hat{s} &= (p + l)^2 && \text{with } p = x_l P \\ &= x_\gamma^2 m_p^2 + m_e^2 + 2x_\gamma P \cdot l \\ &\simeq x_\gamma^2 m_p^2 + x_\gamma (s - m_p^2) \\ &\simeq x_\gamma s, && \text{since } s \gg m_p^2. \end{aligned} \quad (2.27)$$

In contrast to that, the exact calculation according to Eq. 2.10 yields

$$x_\gamma^{\text{exact}} = \frac{W^2 + Q_h^2}{s}. \quad (2.28)$$

This means that x_γ , as defined in the CA, comes closer to the true value only for very small hadronic momentum transfers Q_h^2 . These correspond in most of the cases to elastic events, while the inelastic channel is represented by $Q_h^2 = \mathcal{O}(\text{a few GeV}^2)$ which is nearly the same order of magnitude as the range of the invariant mass W^2 .

In analogy to deep inelastic scattering in DICS a *photon density* $\gamma(x_l, Q_l^2)$ can be defined which represents the probability to find a photon inside the proton. For the calculation of the double differential cross section one can write down the following convolution [16]:

$$\frac{d^2\sigma}{dx_l dQ_l^2}(x_l, Q_l^2) = \int_0^1 \frac{dz}{z} \gamma(z, Q_l^2) \frac{d^2\hat{\sigma}(e\gamma \rightarrow e\gamma)}{d(x_l/z) dQ_l^2} \quad (2.29)$$

using

$$\frac{d^2\hat{\sigma}(e\gamma \rightarrow e\gamma)}{d(x_l/z) dQ_l^2} = \frac{2\pi\alpha_{\text{em}}^2}{\hat{s}} \frac{1 + (1 - y_l)^2}{1 - y_l} \delta(1 - x_l/z). \quad (2.30)$$

As these expressions depend only on two kinematic variables they represent the collinear approximation in DICS. In this form one can regard the corresponding cross section as a measure for the photon distribution as a partonic density within the proton.

Elastic and inelastic description

For a theoretical description of the photon density in collinear approximation the elastic and inelastic ep channels have to be considered. The elastic part of the γ -function can be calculated as [18, 10]:

$$\gamma_{\text{el}}(x_l) = \frac{\alpha}{\pi x_l} \int_{Q_{h,1}^2}^{Q_{h,2}^2} \frac{dQ_h^2}{Q_h^2} \left[\left(1 - x_l - \frac{x_l^2 m_p^2}{Q_h^2} \right) \frac{G_E^2(Q_h^2) + \tau G_M^2(Q_h^2)}{1 + \tau} + \frac{x_l^2}{2} G_M^2(Q_h^2) \right]. \quad (2.31)$$

Here the proton electric and magnetic form factors $G_{E,M}$ are used and $\tau = Q_h^2/4m_p^2$ (Eq. 2.19). The integration limits are analytic functions of s, x_l and m_p (see [10]). They can be simplified via small- m_p expansion in writing

$$Q_{h,1}^2 \simeq Q_{h,\min}^2 = \frac{x_l^2 m_p^2}{1 - x_l} \quad \text{and} \quad Q_{h,2}^2 \simeq Q_{h,\max}^2 = s(1 - x_l). \quad (2.32)$$

As a result in the elastic case the density function $\gamma(x_l, Q_l^2)$ does not depend on Q_l^2 . The inelastic part γ_{inel} requires the incorporation of the usual proton structure functions as shown by Blümlein *et al.* [16]:

$$\gamma_{\text{inel}}(x_l, Q_l^2) = \frac{\alpha}{2\pi} \int_{x_l}^1 dz \int_{Q_{h,\min}^2}^{Q_i^2} \frac{dQ_h^2}{Q_h^2} \frac{z}{x_l} \left(\frac{1 + (1 - z)^2}{z^2} F_2(x_l/z, Q_h^2) - F_L(x_l/z, Q_h^2) \right). \quad (2.33)$$

The structure functions have to be defined in a way that they vanish with $Q_h^2 \rightarrow 0$. For the resonance region the corresponding parameterisations for the virtual photon cross sections are inserted to obtain the structure functions and thus a definition for γ_{inel} .

Evolution ansatz

A slightly different approach in building up the photon density was attempted in [10]: Instead of introducing the structure functions directly, as in Eq. 2.33, the function γ_{inel} can also be expressed directly in terms of an evolution equation in analogy to the Q^2 -evolution of quark and gluon distribution functions in perturbative QCD. According to [10] this is justified by the possibility to factorize the QED Compton process, as for instance in Drell-Yan scattering, production of high- p_T photons or jets in hadronic collisions. This allows to define a 'QED evolution'-equation for the photon density in the proton, written as:

$$\frac{d\gamma(x_l, Q^2)}{d \ln Q^2} = \frac{\alpha_{\text{em}}}{2\pi} \int_{x_l}^1 \frac{dy}{y} \sum_q e_q^2 P_{Aq} \left(\frac{x_l}{y} \right) [q(y, Q^2) + \bar{q}(y, Q^2)], \quad (2.34)$$

where the sum runs over all quark-types q, \bar{q} and their momentum distribution functions $q(x, Q^2)$, while e_q denotes the corresponding quark electric charge. (Note that for the momentum distributions the scale is that of Q_h^2 while for the evolution it plays no role, since for the result the leptonic notation Q_l^2 becomes valid.) A splitting function P_{Aq} is introduced which represents the probability to find a photon in a quark parton,

$$P_{Aq}(z) = \frac{1 + (1 - z)^2}{z}. \quad (2.35)$$

The corresponding Feynman graphs are shown in Figures 2.4 and 2.5. The latter shows the usual splitting processes P_{gq} and P_{gg} for the gluon density $g(x, Q^2)$ of the DGLAP-formalism, describing the scale evolution of the gluon:

$$\frac{dg(x, Q^2)}{d \ln Q^2} = \frac{\alpha_s}{2\pi} \int_x^1 \frac{dy}{y} \left[\sum_q \frac{4}{3} P_{gq} \left(\frac{x}{y} \right) [q(y, Q^2) + \bar{q}(y, Q^2)] + P_{gg} \left(\frac{x}{y} \right) g(y, Q^2) \right] \quad (2.36)$$

The QED evolution is performed under the assumption $\gamma = \gamma_{\text{el}} + \gamma_{\text{inel}}$ and starts at a scale $Q_0^2 = 0.25 \text{ GeV}^2$ using a set of parton distributions according to Glück, Reya, Vogt [11]. The result of the photon evolution is displayed and compared to the gluon evolution as $x\gamma/\alpha_{\text{em}}$ in Figure 2.6 for several bins in x_l versus increasing Q_l^2 . The graphs show a very different behaviour of the corresponding

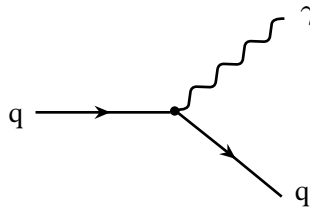


Figure 2.4: A quark radiates off a photon, the 'QED splitting' process as assumed in [10] contributing in the photon (γ) evolution.

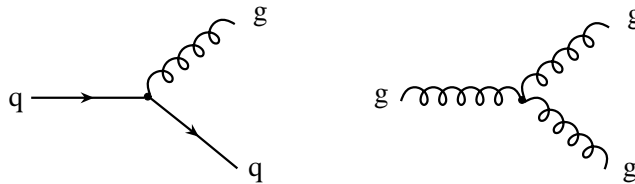


Figure 2.5: The QCD splitting processes contributing to the gluon (g) evolution. Left: quark \rightarrow gluon (P_{gq}), right: gluon \rightarrow gluon (P_{gg}).

density functions. This is expected as a consequence of the fundamentally different interactions: non-Abelian QCD involves gluonic self-interaction, while in QED such a type of interaction does not exist. The different evolution equations 2.34 and 2.36 are in accord with this expectation.

By a direct integration [37] of the elastic and inelastic γ functions, once in the CA based calculations of [10] and once in the ALLM-97 parameterisation used in the COMPTON Monte Carlo (also used in this analysis, s. 4.1.1), it could be shown that the elastic part γ_{el} is in very good agreement in both cases. Also the inelastic part γ_{inel} differs only by the order of 4% when comparing both frameworks. But on the other hand it was ascertained that the corresponding cross sections, derived in both cases for the same topological and kinematic event selection criteria, were different in the inelastic case by up to $\simeq 25\%$ in individual bins. The elastic cross sections still were found in agreement.

The effect of the different structure functions parameterisations as given by GRV-98 and ALLM-97, and also of the varying evolution starting scale values Q_0^2 could be used to conclude that they have only small impacts on the cross sections. Thus, it was reasoned that the collinear approximation does not describe the kinematics in the process with sufficient precision. As an instructive indicator the distributions for Bjorken- x_l and x_γ are shown for the total and for the three sub-selections (elastic, resonant-inelastic and continuum-inelastic, respectively) of the used MC event selection in Figure 2.7. In fact, it can be realized that x_γ^{MC} , *i.e.* the exact generated value, is not matched very well in the inelastic channel by the CA assumption that x_l should equal x_γ : both distributions in $\log x$ are clearly shifted w.r.t. each other. The resonant-inelastic distribution shows a small shift as well, while the elastic distribution appears virtually identical for both x .

Further, by applying additional kinematic cuts in order to select some more appropriate part of the phase space, no better agreement between both variables could be achieved. Also it could not be ruled out that corresponding cuts do exist. Therefore, the conclusion was drawn that the measurement of the leptonic double differential cross section in QED Compton events was not adequate to allow a determination of $\gamma(x, Q^2)$ out of it.

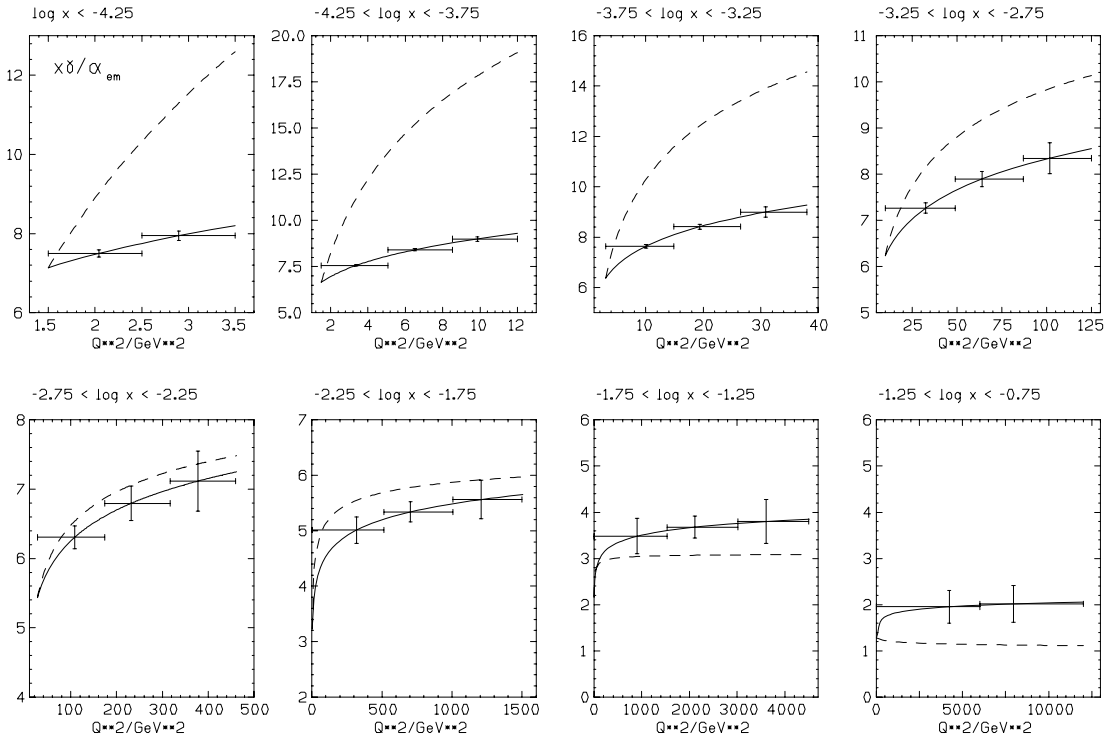


Figure 2.6: Comparison of the expected Q^2 evolution of the gluon density (dashed line) and the photon density (full line), in bins of x_l versus Q^2 . Both functions have been normalized as to coincide at the lowest Q^2 value. Calculation and diagrams from [10].

2.3 Objectives and outline of the analysis

As discussed above a measurement of the leptonic cross section corresponds to the QED Compton process measured as DICS (Deep inelastic Compton scattering), see again Figure 2.3. But as shown in [37] the interpretation of such a measurement in terms of the photon density seems, up to now, not reliable enough. As explained this observation is due to a problematic behaviour of the Monte Carlo numerical cross section integrations.

On the other hand a measurement still can be carried out until new progress about these issues has been made. As a first step towards the QED Compton cross section such a measurement also requires to figure out the individual identity of two electromagnetic particles found in a Compton scattering event. This allows to access the kinematics described in leptonic variables. Furthermore, such a procedure offers the possibility to get insight into and control about systematic error sources, as well as a better understanding and suppression of background sources. Then it becomes possible as well to perform a test about the correct description of the Monte Carlo on the total cross section.

These aspects are valuable requirements for a F_2 measurement at very low Q^2 using QED Compton. The kinematic plane given in Figure 2.8 localizes, in hadronic kinematic variables (x_h, Q_h^2), the inelastic part of the Compton process.

For such a purpose the hadronic final state in QED Compton would have to be measured, partially in the very forward region at very low y . This poses a demanding task due to the low acceptances in this part of the detector with a solid angle coverage of near to 4π , but with limitations due to the beam pipe holes. The phase space region between high c.m.s. (HERA) and fixed target experiments can, thus, be completed with additional data. A first step towards this aim has been performed in [38]

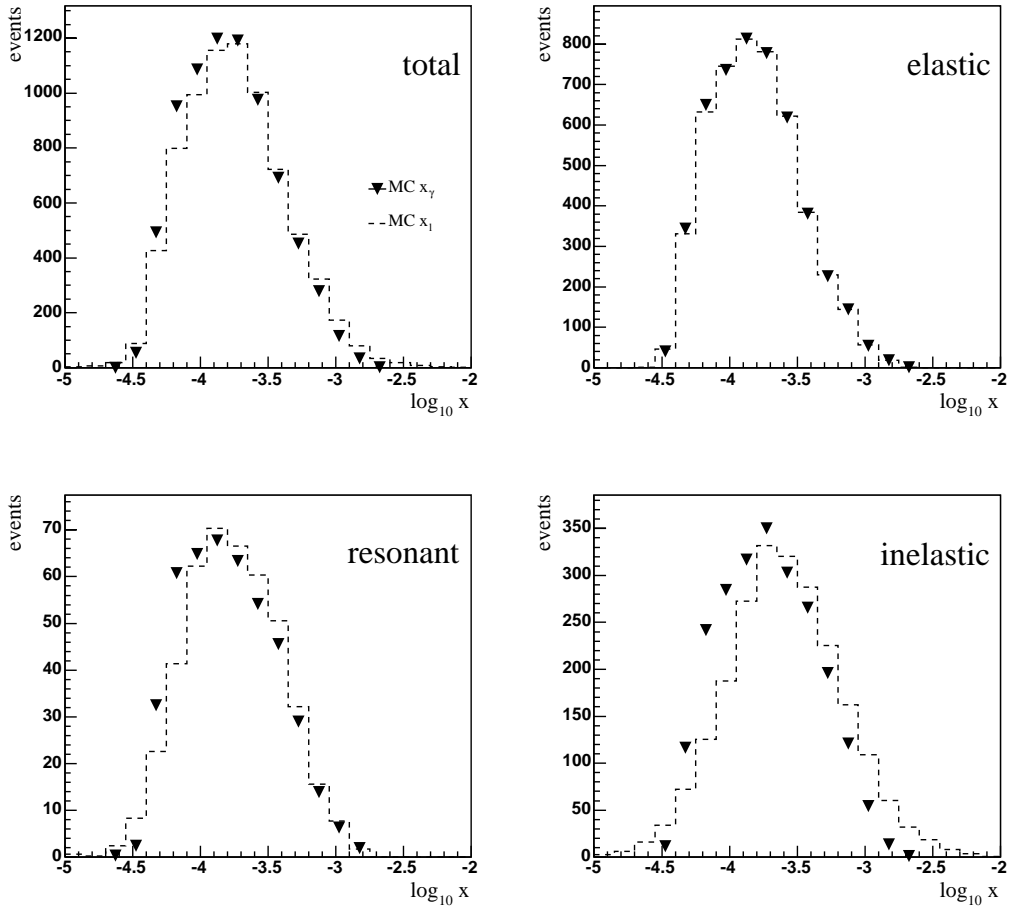


Figure 2.7: Comparison between x_l^{MC} and x_γ^{MC} in the collinear approximation as given by a Monte Carlo event selection in COMPTON. The diagrams display the exact x_γ^{MC} value as calculated by the generator. Left top: total event selection. Right top: elastic selection only. Left lower: resonant-inelastic only. Right lower: continuum inelastic only.

connecting these regimes, with one of them so far unmeasured at HERA.

To summarize, besides the identification of the electromagnetic final state (electron and photon) in order to obtain the leptonic cross section, a special interest lies on the inelastic contribution to the total leptonic cross section. Thus, it will be an additional aspect to distinguish between elastic and inelastic contributions.

The following chapters will discuss the experimental setup and some of its essential features for the cross section measurement, as well as the selection of the Compton events from the bulk 1997 data set, some control data samples, the Monte Carlo for the Compton signal and backgrounds. In chapter 5 the required particle identification strategy together with the involved critical experimental preconditions will be discussed. The aim of this part is to determine the event kinematics as precise as possible. This point is related also to the calibration chapter which treats a variety of corrections to geometrical and energetic quantities, taking partly advantage of the particle identification from the chapter before. Afterwards the cross section measurement in connection with the influence of systematic errors is presented in the last chapter. The results are discussed and summarized finally.

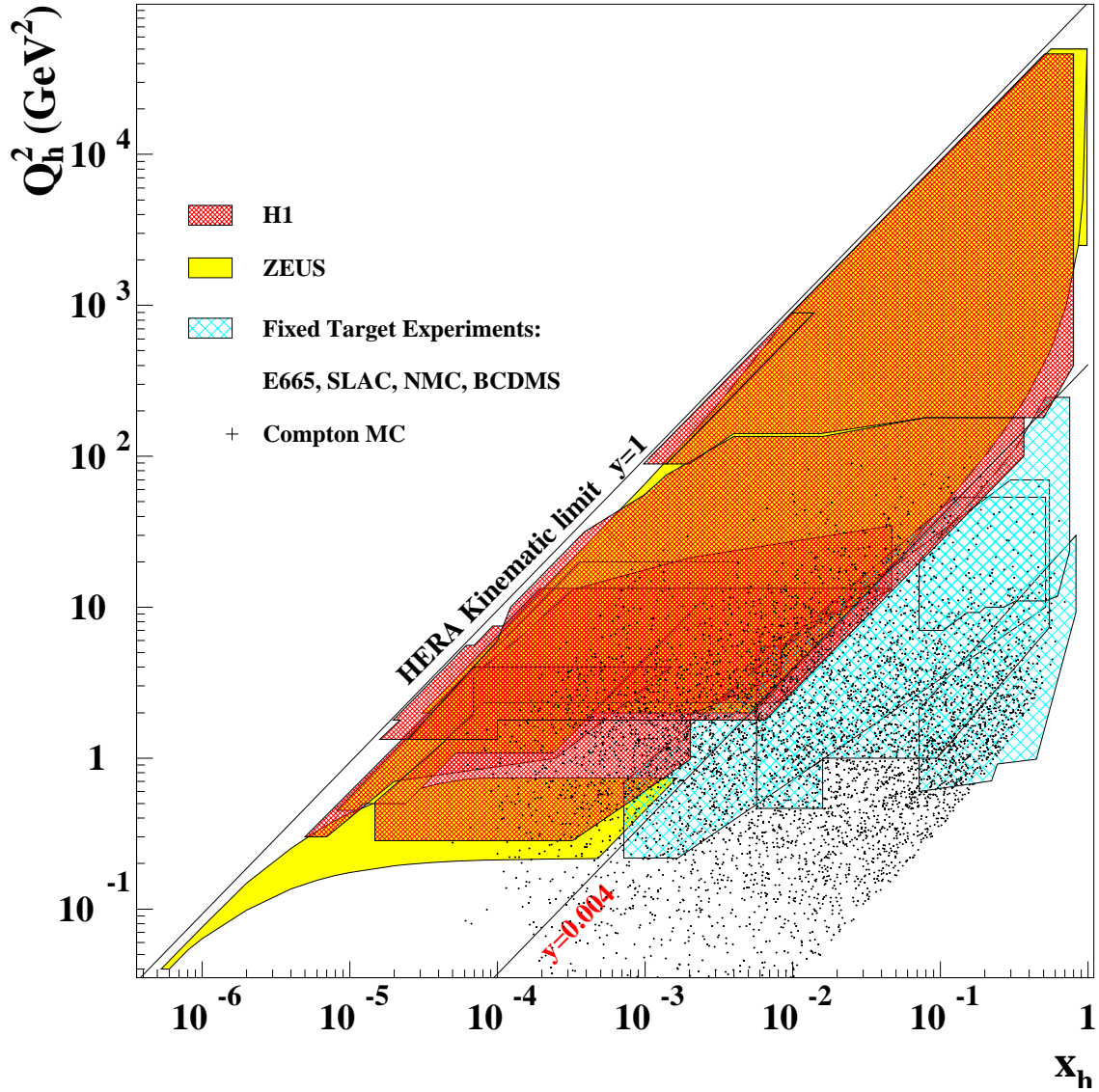


Figure 2.8: The coverage of the kinematic plane Q_h^2 versus x_h in HERA ep scattering and fixed target experiments. The transition between these two kinematic ranges is given by a straight line of constant y around 0.004. A set of inelastic Compton Monte Carlo events are shown as distribution of dots (“+”). The lower left border of this distribution represents a lower limit of constant hadronic final state mass m_X of about 1.8 GeV.

3 Experimental Setup

H1 is one of the four big experiments being performed at the Hamburg electron proton storage ring HERA. Together with the ZEUS experiment it was commissioned for the year 1992 when the first data from ep collisions were recorded. The HERMES experiment was ready for data taking in 1995 and the planned measurements on proton spin physics. HERA-B followed as the fourth experiment completing their installations in 2000. All experiments are dedicated to the measurement of the structure of the proton, the simplest atomic nucleus and the most abundant hadronic system, focussing on slightly different aspects. While ZEUS and H1 are similar types of experiments constructed for the detection of interactions in colliding electron and proton beams, the HERMES experiment makes use of a quasi-fixed and polarized target of hydrogen atoms to study the spin dependent structure properties. This is achieved by utilizing the polarization of the electron beam. HERA-B is dedicated to the measurement of CP-violation in B-meson decay ($B^0 \rightarrow J/\psi K_s^0$) occurring in the final state of proton-nucleus collisions; the experiment uses a movable set of wires each of them representing a fixed target near the proton beam.

The following sections describe the main functional principles of the particle acceleration, of the storage ring and of the components of the H1 experiment with a dedicated view on those parts which are essential for this analysis.

3.1 HERA

A schematic overview of the storage ring HERA (“Hadron Elektron Ringanlage”) is shown in Figure 3.1. Both e and p beams are produced in small linear accelerators with energies of 500 and 50 MeV, respectively. The proton beam starts as a H^- beam in this first stage and is converted, by stripping the ions while traversing a special foil filter, into a beam of bare protons. As next, electrons and protons are injected to the accelerator rings DESY II/III with final energies around 7 GeV and start into the pre-final stage of the PETRA accelerator ring. In this phase the overall bunch structure is already established. In total there are 210 particle bunches of both, electrons and protons, in the HERA storage ring, each bunch separated to the next by $\simeq 30$ m. The injection energy from PETRA to HERA is 12 GeV for electrons (positrons) and 40 GeV for protons. Protons bunches circulate clockwise (seen from above) and electrons in the opposite direction. Some fraction of the bunches is not filled and those without colliding bunch as a counterpart, called *pilot*-bunches, are used for background measurements as interaction in these bunches can only originate by collisions with residual gas in the beam pipe. The acceleration to the final HERA beam energies of 820/27.6 GeV (1997) is achieved by superconducting RF-cavities working at 52 and 500 MHz, respectively. For the protons beam bending is achieved by superconducting magnets producing the necessary fields of 4.7 T. Due to the large mass difference to protons, electrons radiate off about 127 MeV per HERA turn requiring a much higher total accelerating RF-power than protons. The HERA bunch clock of 10.4 MHz corresponds to a bunch separation of 96 ns.

The bunches of the beams have typical widths of $\sigma_z \simeq 10$ cm and they are brought into collision only at the center of the respective experiments by a corresponding winding arrangement of both beam pipes, Figure 3.2. Due to the acceleration scheme the e beam bunches are accompanied by so called *satellite* bunches with a distance (in z) of about one wavelength of the radio frequency ($\simeq 60$ cm). They appear shifted by this distance from the nominal interaction regions and produce additional contributions to the continuously recorded luminosity; this means their impact has to be accounted for (see also Section 3.3.1).

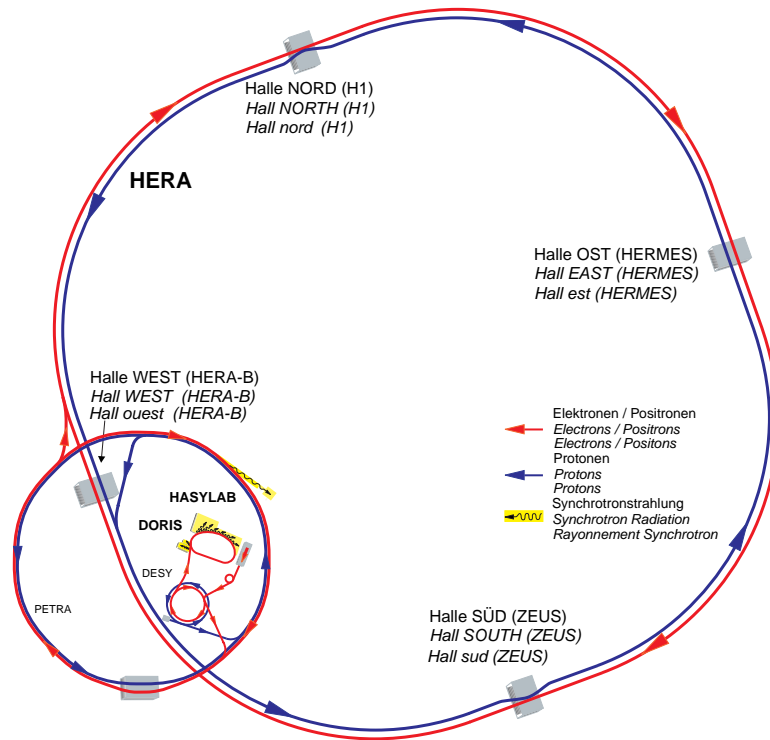


Figure 3.1: Schematic plan view of the electron proton storage ring HERA. The straight segments around the four interaction zones are 360 m long, the curvature radius of the arcs measures 780 m. The left lower part shows the pre-accelerators together with the PETRA ring.

The accelerator system can be adjusted in order to allow a positional shift in z of the electron bunches by one wavelength of the cavity frequency. In this way the nominal interaction point is shifted by this length along the beam line. This technique is called “shifted vertex” and opens the possibility to access an extended kinematic region in ep scattering. Much smaller electron deflection angles can be detected then without modifying the detector with respect to geometrical acceptance.

3.2 The H1 detector

The H1-detector is installed in the northern experimental hall of the HERA beam line ring about 20 m below ground level. The detection systems, also shortly denoted as *subdetectors*, are distributed over three main areas, namely the central components around the interaction point in the hall itself, the proton and proton-remnant detectors in the tunnel part of the outgoing proton beam, and the electron/photon detection devices placed in opposite part of the tunnel (towards HERMES). The subsequent detector descriptions refer to the setup in the data taking period of the year 1997. Before and since then modifications and upgrades have taken place continuously in order to take advantage of increased detector understanding, to gain performance and to extend the accessible kinematic range. Further detailed technical information about the detector layout can be found in [31].

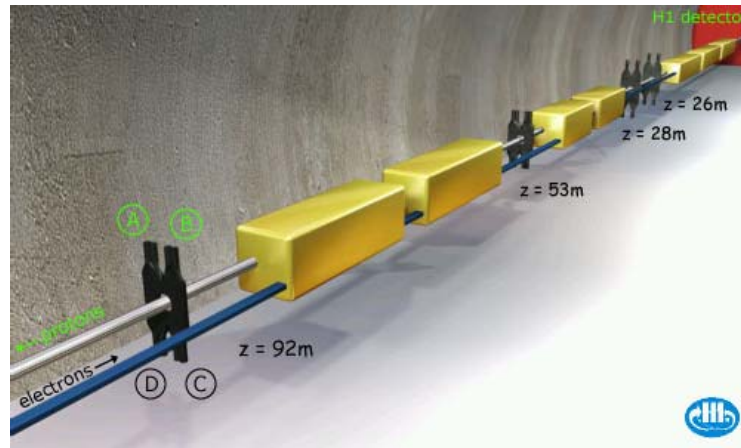


Figure 3.2: Schematic and simplified 3D-model of the $+z$ -tunnel area (“northwest”), [33]. Illustrated are the positions of the scintillating counter stations of the FTS system (black). Also the gradually decreasing distance and twisting between the proton- and electron-beampipe as they merge towards the interaction region is shown.

3.2.1 Layout and coordinate system

The principal structure of the central component is conceived as to meet the main determining kinematic property of ep interactions at HERA, namely the high boost of the center of mass along the proton direction with $\gamma_{c.o.m.} = 2.86$ corresponding to $\beta_{c.o.m.} = 0.93$. As a consequence most of the hadronic final state is collimated along the proton direction *i.e.* to the $+z$ -direction synonymously called the “forward” direction. Therefore, the main calorimeter and the forward tracking system are highly segmented and oriented as to allow an optimized detection of the (hadronic) final state. The common H1 coordinate system is oriented with the z -axis identical to the cylindric axis of the central tracking chambers, the x -axis points parallel to the hall floor and towards the center of the HERA ring, while the y -axis points vertically upwards from the hall floor. The origin is located in the center of the central tracking chambers. The following sections describe important technical properties of the components of the main apparatus of which an overview is shown in Figure 3.3.

3.2.2 Calorimetry

The calorimetric system in the H1-detector comprises as most important one the Liquid Argon Calorimeter (LAr) enclosing the forward and central tracking detector system (FTD and CTD), while the Spaghetti Calorimeter (SpaCal) covers the backward side. This detector part is basically defined by the opening left over by the shape of the LAr cryostat to allow insertion, supply and maintenance of the central tracking devices. A few thousand lines of high voltage cables for the sense wires, low voltage cables for preamplifier cards, signal and cooling and gas pipes are fixed to the inner cryostat wall. These lines and pipes are lead through to the outside at $z \approx -2.5$ m where the cryostat ends and where a variety of connector types establish connections to a multitude of 30 m long cables. They provide the transmission of raw or (by zero-suppression) preprocessed detector signals to the three-floor trailer bearing all readout electronics. This trailer rests next to the main detector and is mechanically connected to the main calorimeter support structure which is the lower part of the iron

HERA Experiment H1

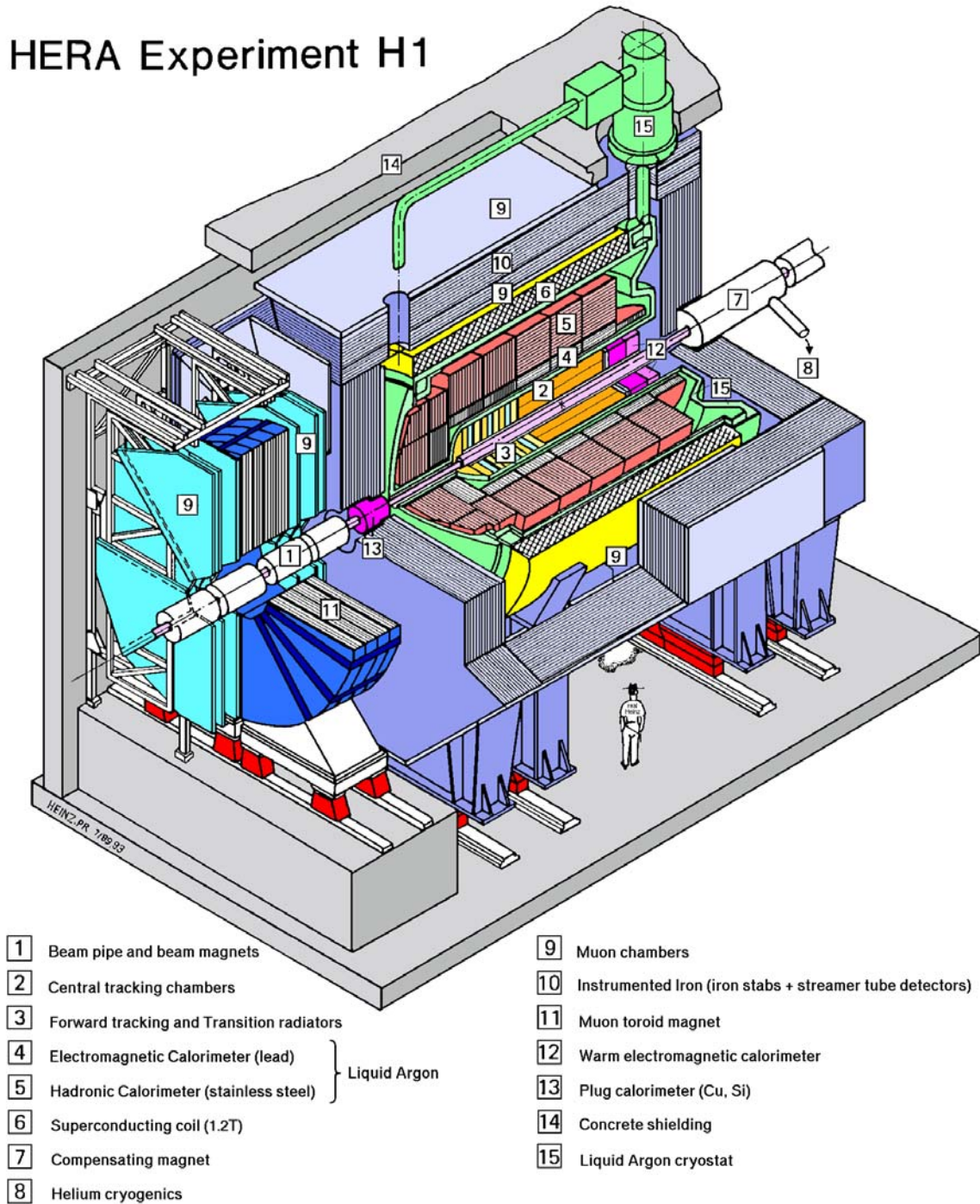


Figure 3.3: A view into the H1 detector with its most important components. Electrons (or positrons) enter from the left lower side, protons from the upper right side.

yoke (see below). Both parts are movable on rails mounted on the ground floor of the experimental hall.

The two main calorimeters are equipped with an inner (w.r.t. the interaction point) electromagnetic and an outer hadronic absorber section. Two smaller sized calorimeters are placed in the near beam areas, namely the PLUG in the very forward region and another one in the very backward region (BPLUG).

Liquid Argon Calorimeter

The main calorimeter constitutes the central and forward part of the detector. Its absorbers are contained in a big stainless steel, pot-shaped vessel filled with 53 m³ of *liquid argon* (“LAr”). The inner walls (see Figure 3.3) are made of aluminum alloy for minimization of passive material that could cause pre-shower effects and degradation of energy resolution. Calorimetry is achieved by using stacks of steel plates within the outer part of the vessel for detection of hadronic particles. A stack of G10-lead-G10 plates is used for the detection of electromagnetic particles (G10 is a mixture of epoxy and glass fibre). Eight stacks consisting of an inner e.m. and an outer hadronic part form a wheel that is placed concentrically around the beam axis. In total seven wheel structures make up the complete calorimeter. The orientation of the absorber plates in the different wheels was set to be either parallel (in the central detector part) or perpendicular (in the forward and very forward parts) to the beam axis in order to have jets or rays of particles from the interaction point traversing the absorber plates at a steepest possible angle. In the backward part there is an additional e.m. absorber stack (BBE) with a vertical orientation closing the gap in polar angle between the main LAr system and the backward calorimeter (see this Section). The signal detection is realized in between the layers of each stack. These layers are segmented in Cu-pads to form cell areas which collect the charge from a shower of secondary particles generated in the absorber plates.

Backward Calorimeter

This calorimeter was designed for a precise measurement of the energy and position of the scattered electron in *ep* interactions. Like the LAr it is made of two sections, an electromagnetic and a hadronic one. The electromagnetic part consists of 1192 cells each viewed by an own photomultiplier-tube, their size is 4.05 x 4.05 x 25 cm³. The hadronic part is made of 15x15x25 cm³ sized cells, *i.e.* of greater front face area than the e.m. part to accommodate for the larger transverse extension of hadronic particle showers. The detection principle is similar for both sections: layers of 0.8 mm thin lead sheets are stacked on top of each other to form a two-cell unit. Each sheet has a multi-groove profile to carry about 100 scintillating fibres. The corresponding lead-to-fibre ratio gives a Molière radius for electromagnetic particle showers of 2.5 cm. The cell size was designed accordingly. With a radiation length of 0.9 cm a longitudinal shower development is contained completely in one cell. This cannot be achieved for hadronic measurements since the hadronic part of the calorimeter contains only one nuclear interaction length (together with the e.m. section the value increases to $\approx 2\lambda$) due to the limited available space for the complete calorimeter. Due its fibre based construction principle it is called the Spaghetti Calorimeter (SpaCal).

Each geometrical cell is represented by a bundle of fibres which collect the scintillation light of secondary particles produced in a shower, the light being focussed onto to one PM tube and thus converted in an electric pulse signal. The so called Inclusive Electron Trigger (IET) represents a specific mechanism to detect electromagnetic energy depositions by combining the signals from neighbouring cells. As the energy of one particle can either be spread over a few cells or be concentrated almost in one cell only, it would not be adequate to set detection thresholds on single cells – instead it would

cause the detection efficiency to largely depend on a particle's impact point across one cell front surface and also on the impact angle. Therefore, the principle of *gliding sums* was applied to achieve an uniform calorimetry. It is realized by adding the analog signals of neighbouring 2×2 cell groups to one pre-sum signal. The signals of four of such 2×2 units are added to one IET cluster sum. This sum is subject to three adjustable trigger levels; a typical set is 2, 6 and 12 GeV. If one of these thresholds is exceeded, a corresponding IET-cluster bit (numbered 0, 1 or 2) is set to indicate an energy deposition. The central property of this trigger is that neighbouring IET cluster bits are formed with an overlap of two 2×2 cell units in each direction, that is x and y , of the calorimeter surface to the next cluster bit. In this manner a highly efficient trigger for particle detection and energy measurement is realized. Further details of the IET trigger specific to this analysis are discussed in Section 6.3.1.

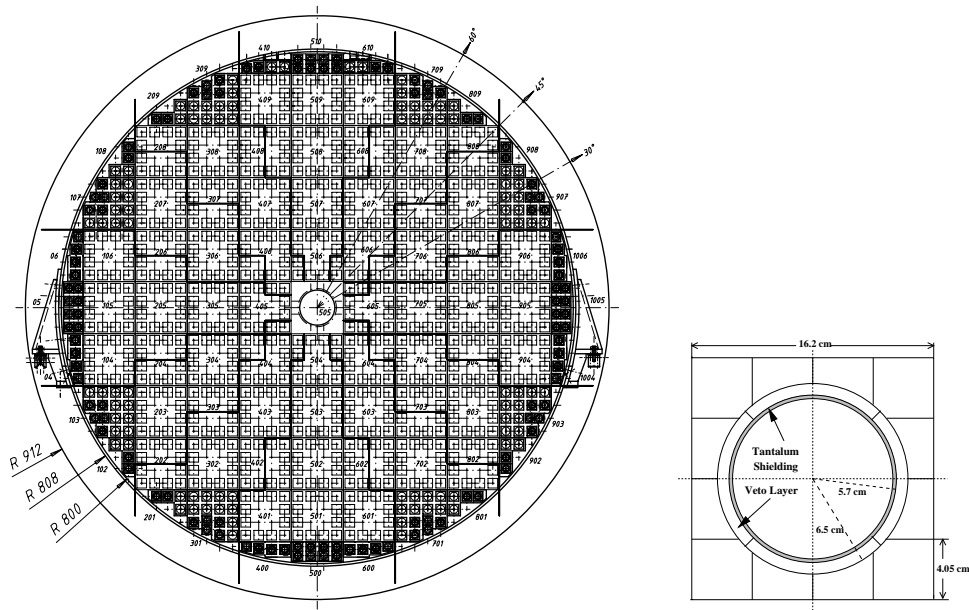


Figure 3.4: Technical drawing of the SpaCal surface, viewed in xy coordinates (radii in mm on the lower left). Squares correspond to separate e.m. cells. The drawing on the right shows the inner most cells near the beam pipe (insert with veto layer cells).

Main Magnet/Tail Catcher/Muon System

A solenoid magnet surrounds the LAr calorimeter with its cylindric axis parallel to the beam. The magnet on the other hand is enclosed in an octagonal iron yoke with flat end caps. The yoke serves the homogenisation of the magnetic flux within the solenoid volume.

The construction principle with the spectrometer magnet outside the main calorimeter differs from other detectors which have their magnets between the hadronic and e.m. absorbers (like the LEP experiments ALEPH and DELPHI) or even inside the e.m. part (ZEUS). It improves the energy resolution of the main calorimeter due to a reduced amount of passive material between the interaction point and the absorber plates. In H1, the four superconducting coils of the solenoid have a total length of ≈ 22.5 km and are mounted in a separate cryostat cooled with liquid helium. The magnet generates a nearly homogeneous field of 1.15 T (maximum deviations are $\pm 4.5\%$), this corresponds to an integrated bending power of 8.32 Tm.

The iron yoke is constructed in such a way as to allow two additional purposes besides shaping of the magnetic field. A part of the hadronic final state can leak through the LAr calorimeter and the solenoid cryostat. To reconstruct the energy flow involved in a collision event limited streamer tubes are placed in the layers between the iron plates. Furthermore, they serve for the reconstruction of tracks and thus provide additional information about the event topology. Especially muons, either from the event or produced by atmospheric cosmic particle showers, are detected by this system. Additional plate electrodes are installed to complete the energy measurement. This functionality defines the tail catcher (TC) system.

3.2.3 Tracking

The central tracking device consists of a set of six independent drift and proportional chamber volumes, constructed as concentric cylinders. The separated volumes are necessary because each chamber is supplied with its own gas mixture to fulfil each chamber's specific requirements in terms of gas composition and amplification as well as electrical stability. Figure 3.5 displays a radial view of the complete setup.

Jet Chambers

The two largest chamber volumes are the central jet chambers, named CJC1 (inner) and CJC2 (outer). Both are equipped with 30 and 60 drift cells, respectively. Each cell is oriented radially but tilted by an angle of 30° (Lorentz-angle) in azimuth with respect to straight tracks coming from the vertex. The value of this tilt angle has been chosen in order to achieve an optimum spatial hit resolution for straight tracks that are traversing the central tracking detector. It depends on the strength of the magnetic field permeating the tracking volume and the drift velocity of ionization electrons since the latter are deflected by the Lorentz force of the magnetic field. For this reason both magnetic field (solenoid current) and gas composition have to be kept constant in time. Additionally the reconstruction of tracks is simplified, since hit-ambiguities are resolved by sorting out those track-element orientations which do not point to the vertex or for which no connection between the two jet-chambers can be made to form a continuous track.

The drift volumes are defined by two outer cathode planes and by a sense wire plane in the middle of both cathode planes. These planes as well as the radially inner and outer cell boundaries are realized as parallel arrays of gold coated tungsten wires. In total there are four different types of wires: cathode and field wires to form the surrounding boundaries of a cell, as well as potential and sense wires being connected to ground and positive high voltage, respectively. The voltages, especially those between cathode and sense wires, are chosen according to their distances to achieve a drift field as uniform as possible and thus constant drift velocities over the cell volume. The hit resolution in the (r, φ) -plane has been determined to be 0.17 mm. The determination of the hit z -coordinate is achieved by measuring the difference of the signal pulse height between both end points of a sense wire. This method, also called "charge division", offers a z -position resolution of 2 cm.

The chamber concept is based on the central tracking chamber of the JADE experiment which has been performed at the former PETRA collider [42].

z -Chambers

The inner and outer central z -chambers (CIZ and COZ) allow to increase the precision of the z -position measurement of tracks in the central part of the detector. For these chambers the drift paths are parallel to the beam axis which requires the sense wires to be oriented perpendicularly to it. The

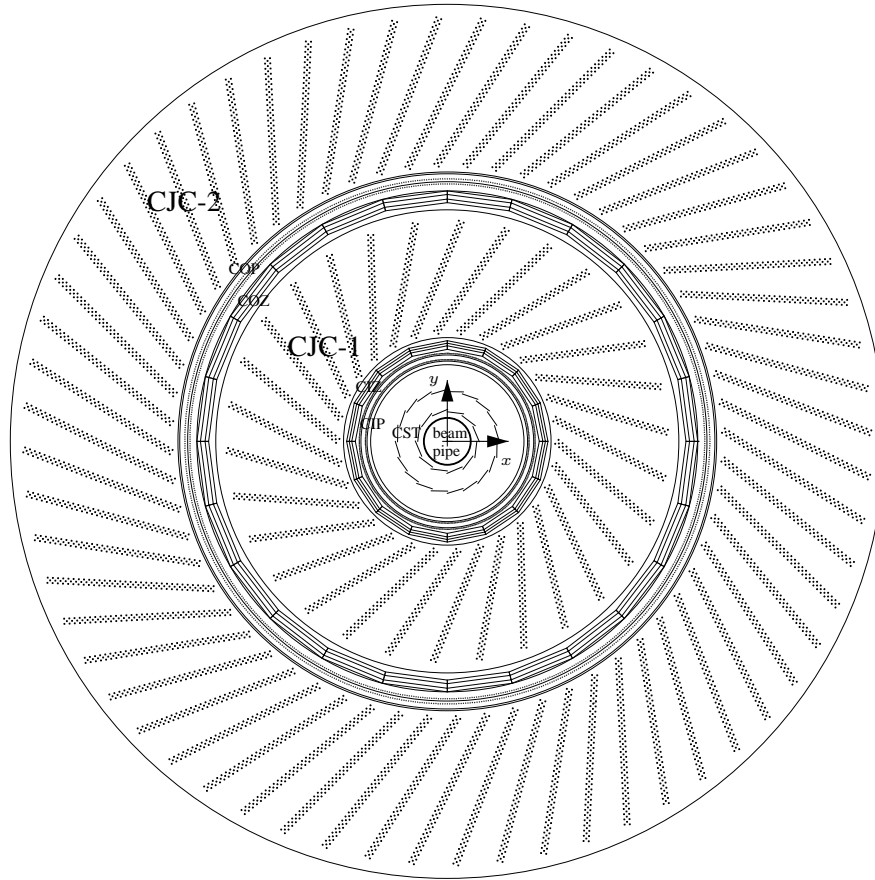


Figure 3.5: Radial view of the H1 central tracking chambers (full diameter about 1.6 m), seen in the direction of the electron beam. Each dot in the jet chambers represents a single wire (shown are the anodes and a part of the field wires). The radial position of the silicon tracking devices is indicated by the two inner circles next to the beam pipe circle.

segmentation in azimuth is a 16-fold (CIZ) and a 24-fold (COZ) polygonal cell array. A CIZ cell is dimensioned in $(z, r\varphi, r)$ as $12 \times 7.5 \times 2 \text{ cm}^3$. Each cell contains four sense wires for the measurement of drift times in z . The wire array follows a special setup: they are not parallel between the cell's two cathode-walls in z -direction. The sense wire plane is tilted by 45° , inclined roughly towards the interaction point and thus opposite for $z > 0$ and $z < 0$. This design avoids hit ambiguities and the effect of a too strong varying, and θ -dependent spatial resolution. The latter was determined to be 0.3 mm [43].

Proportional Chambers

Several proportional tracking chambers have been implemented in the forward, central and (in the beginning of the experiment) backward part of the H1 detector. The forward tracking detector (FTD) is a compact array of drift and proportional chambers in order to measure particle tracks in the forward direction on the $+z$ -side of the central tracking devices. They allow to gain information about part

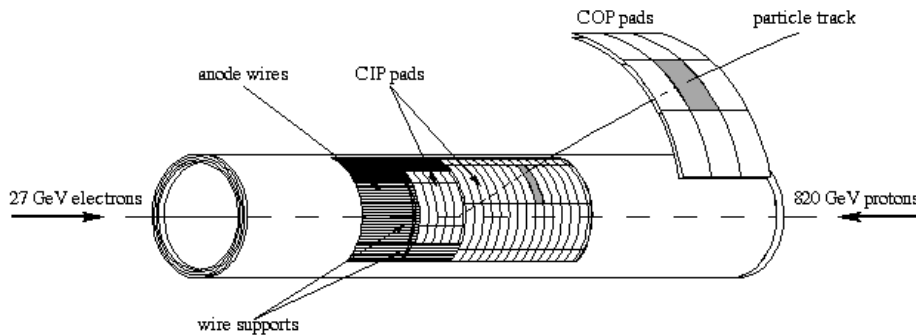


Figure 3.6: The pad sensor structure of the Central Inner Proportional Chamber (CIP) and part of the outer chamber. The position of the wire supports is indicated at one third from the $+z$ -end of the chamber. Corresponding wire supports are mounted at the lower third on the $-z$ -side.

of the hadronic final state (“jet”) in an ep interaction and also to support the reconstruction of the interaction point.

Important for this work is the inner one of the two central multiwire proportional chambers CIP and COP. Both are sketched in Figure 3.5 and Figure 3.6, showing their radial positions within the CTD and their pad structure, respectively. In case of the CIP the layout of the pads, used for the electronic readout of track signals, is a 60-fold segmentation in z in each of eight φ -sectors per layer. This ratio between longitudinal and azimuthal segmentation creates a striped shape of the pads. As the chamber is made up of two layers the pad stripes in the inner and outer layer are aligned in z , but they are shifted by $45^\circ/2$ w.r.t. each other. The anode wires, 480 per layer, reach from one end of a chamber to the other. In order to avoid mechanical instabilities of the wires two supporting rings, made of glass fibre epoxy, were attached at the first and second third division along z to fix the wires at these positions. Many detailed constructional and electronic characteristics are described in [31, 54].

Backward Drift Chamber

In 1995 the original main backward devices, namely the Backward Proportional Chamber (BPC) and the Backward Electromagnetic Calorimeter (BEMC), had been replaced by new components in order to achieve an improved resolution in both polar angle (via tracking) and energy measurement (via calorimetry) of the scattered beam electrons. The new tracking chamber BDC (Figure 3.7) is positioned between the central tracker barrel and the new calorimeter SpaCal. The BDC is made of eight layers in z grouped in four double layer modules. The active area of the drift cells ranges in r from 6 to 71 cm (measured in a cell’s middle), contained in independent segments each covering an angle $\frac{\pi}{4}$ in azimuth. A double layer is made of two wire planes which are radially shifted against each other by half a wire-to-wire distance in order to resolve the usual mirror hit ambiguities found in single drift chamber planes. The drift direction is radial to achieve an optimum resolution for the polar angle measurement. The wire-cathode distances are 0.5 cm for the inner cells and 1.5 cm for the outer cells. A transition between the inner cells and the outer cells is located at the chamber radius range of about 21 to 25 cm. For this position a special *transition cell* was designed with an asymmetric drift space in r . This allowed a smooth coverage of the whole backward plane, but it also introduced technical difficulties in terms of HV-operation and track reconstruction in this part of the detector.

The four double layers are staggered in azimuth in steps of 11.25° which allows a measurement of the φ -component of a hit, while the radial component is determined using the measured drift time. The

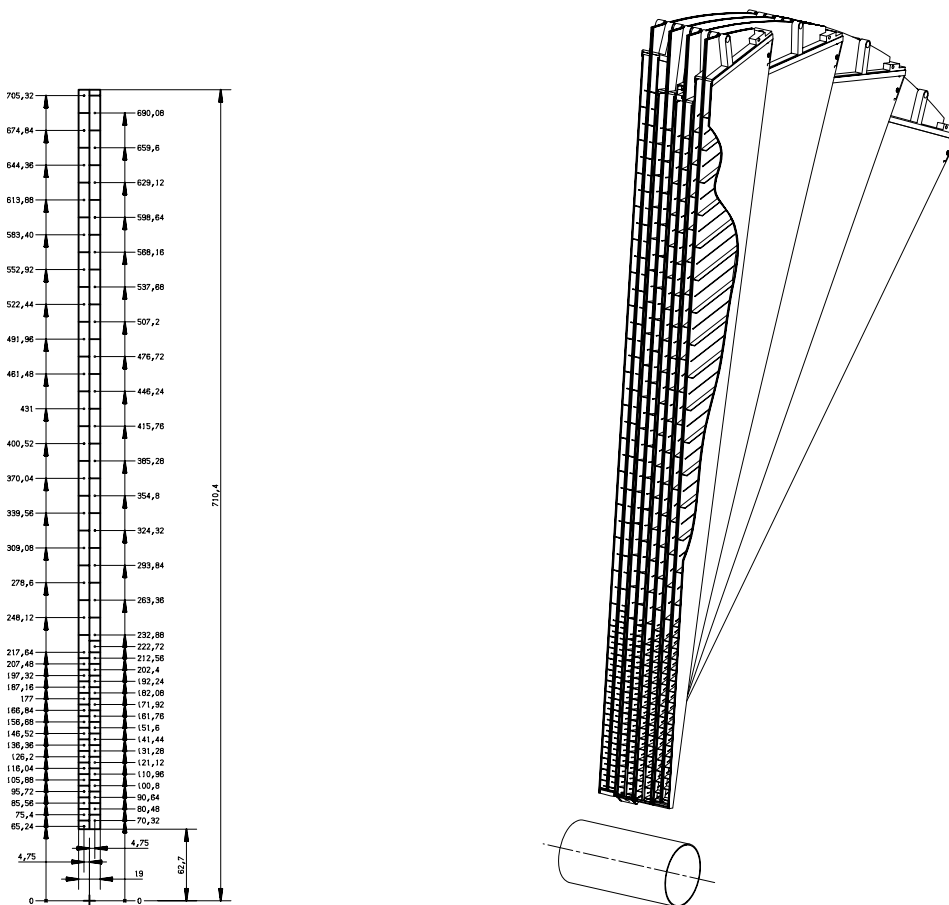


Figure 3.7: Left: side view of one Backward-Drift-Chamber double layer module (of four in total) with wire distances to the beam axis in mm. Right: cutout 3D-view of the chamber with its double layer modules staggered along z by $\pi/16$ ($=11.25^\circ$) steps in φ .

uncertainty in azimuth corresponding to the module-sector extension of 45° is resolved by forming tracks of hits from different double layers. In fact, the drift time information gives back only the position of a straight line parallel to the sense wires or a *secant* with respect to the chamber's discoidal shape. This means that the true hit or track segment position in r and φ needs to be calculated by intersecting those "hit lines" in a projection along z through the φ -stepping of different layers. After having expanded all hits and mirror-hits into one global hit bank, the reconstruction program produces from these data the space points of the corresponding particle trajectory. Further related details on track reconstruction algorithms are described in Section 5.2.1.

Silicon Tracking Detectors

For improved track and vertex reconstruction as well as extension of the kinematic range silicon pad based tracking detectors were added to the experiment near to the beam pipe. These are the central silicon tracker (CST) and the backward silicon tracker (BST), respectively. The BST is made of silicon pads suited for angle measurement in polar and azimuthal coordinates. The segmentation type is given by 16 pads in azimuth, this structure is repeated four times along z with layers located in a distance between 73 cm and 95 cm backwards of the center of the interaction region. The tracking algorithm of this subdetector will be discussed in detail in Section 5.2.4.

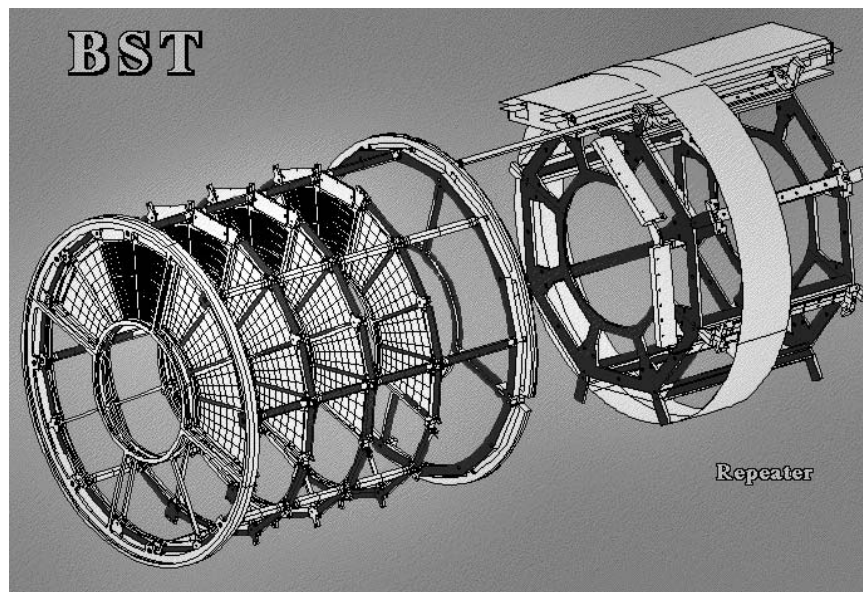


Figure 3.8: The backward silicon tracker BST, sensors (left) and repeater support (right). For tracking the silicon pads are faced towards the interaction region to the left. Only a part of the sensors is displayed. (Picture by [34].)

3.2.4 Time-of-flight system

Several arrays of scintillators and hodoscopes are positioned within and outside the central part of the experiment to identify potential background signatures in a collision event. Interactions between beam and residual gas molecules in the beampipe or between beam particles and the wall of the beampipe (or other structures there in, like collimators against synchrotron radiation) upstream the proton beam can generate particle tracks and energy depositions in the central detector which do not have their origin in the nominal vertex region. Therefore, the time-of-flight system (ToF) serves as an indicator for a proper event timing and allows to distinguish efficiently between background and regular ep interactions. Corresponding signals are logically combined with most of the event trigger elements to achieve this.

3.3 Triggersystem and data acquisition

The H1 trigger system [35] is made of a multi-level decision scheme in order to identify and recognize reliably a multitude of different event types and topologies. Subdetector signals from the experiment are collected by their respective subsystem control units under synchronisation to the HERA bunch clock indicating the proper arrival time of a electron and proton bunch, and thus of a collision event as well, each 96 ns corresponding to the bunch clock of 10.4 MHz. The coordination principle is displayed in Figure 3.9. Within the first trigger stage (“level-1” or L1) signals from sense-wires, calorimeter-cells, etc. are allowed to enter a digital or/and analog branch to be stored for signal pattern recognition or for signal shaping. Digital information, like for example “signal > threshold” can be stored in an electronic shift register, one per physical signal channel, which is synchronously clocked to the bunch arrival times. This *pipeline* scheme is identical for all readout components and

it provides a virtually deadtime free first trigger level because the signal information can be kept for some time period for further evaluation. Only if the trigger-logic has received a specific and valid signal combination from one or more subdetectors, a common L1KEEP-signal is generated which immediately stops the clocking of all pipeline registers for readout and subsequent further analysis on higher trigger levels for more complex signal evaluation.

The second trigger stage (“level-2” or L2) aims on detecting *topological* properties of an event, as for example the simultaneous presence of a track together with a calorimetric energy deposition both pointing into a similar direction of the detector could indicate the transit of a charged particle of a certain energy. In this way it is possible to collect events for physics analyses based on such specific informations. In addition level-2 owns a *Neural Network* based branch for signal evaluation. The third trigger stage (L3) performs no direct decision on whether some event is taken or not, in contrast to the fourth stage (L4) where more precise event information is gained, after an almost complete event reconstruction, and used for the final trigger decision.

The event rates measured at the respective stages decrease considerably towards the final event decision. The biggest reduction is achieved on the first level where a high background rate ($\simeq 100$ kHz) has to be suppressed. The L1 output rate is of the order of 100-200 Hz and it is further reduced until a typical L4 input rate of about 50 Hz is reached. Finally, properly classified events are written to tape/disk storage devices at a rate of 5 to 10 Hz. The typical overall dead time is about $\leq 10\%$.

The stream of accepted event data is divided into portions called *runs*, each of which a number (the “run number”) is assigned to, which is unique for *all* years of H1 data taking. Each run corresponds to a real data taking period of a few minutes up to two hours at maximum. The upper limitation is necessary to accommodate trigger settings to the changing beam and background conditions during one beam fill. Especially trigger prescale factors, which are applied to keep the computing load to the L4 trigger stage below a certain limit, have to be lowered as the corresponding event rates fall down proportional to the beam currents. The electron (or positron) beam quality and the beam current strength define the duration of most of the beam fills. Typically, one luminosity period lasts for about ten hours.

A few hours after their recording and transmission to the DESY computer center, the collected run data sets are input to the last full reconstruction stage from which a reduced set of data banks, relevant for all analyses, is written into a second data stream. The data banks of this stream contain, among many other information, lists of tracks and cluster energies. All these data structures (called “DST”-files) are the most important basis for typical analyses like the present one. In the data taking of the year 1997 a set of about $38.4 \cdot 10^3$ events were processed into this data format. The data of the second cycle of re-processing (“DST-2”) is used in the present work*. Details of the event selection are described in Section 4.

3.3.1 Luminosity measurement

The group of detectors forming the luminosity system is shown in Figure 3.10. They are located far away from the main H1 apparatus and consist of three calorimetric subsystems, two of them belonging to the photon branch (Photon Detector, PD, at $z = -103.1$ m with associated Veto Counter in front of it) and one for the electron (Electron Tagger, ET, at $z = -33$ m). The principle of the measurement of the current luminosity is based on the detection of bremsstrahlung which is radiated off by beam electrons when encountering the electric field of beam protons, $e p \rightarrow e p \gamma$ (see also Chapter 2.1.1). The typical photon energy ranges from a few GeV to nearly the nominal electron beam energy. The

*This cycle number corresponds to the sum of $31 \cdot 10^6$ events in *standard* running plus $7.4 \cdot 10^6$ events in *minimum bias* running.

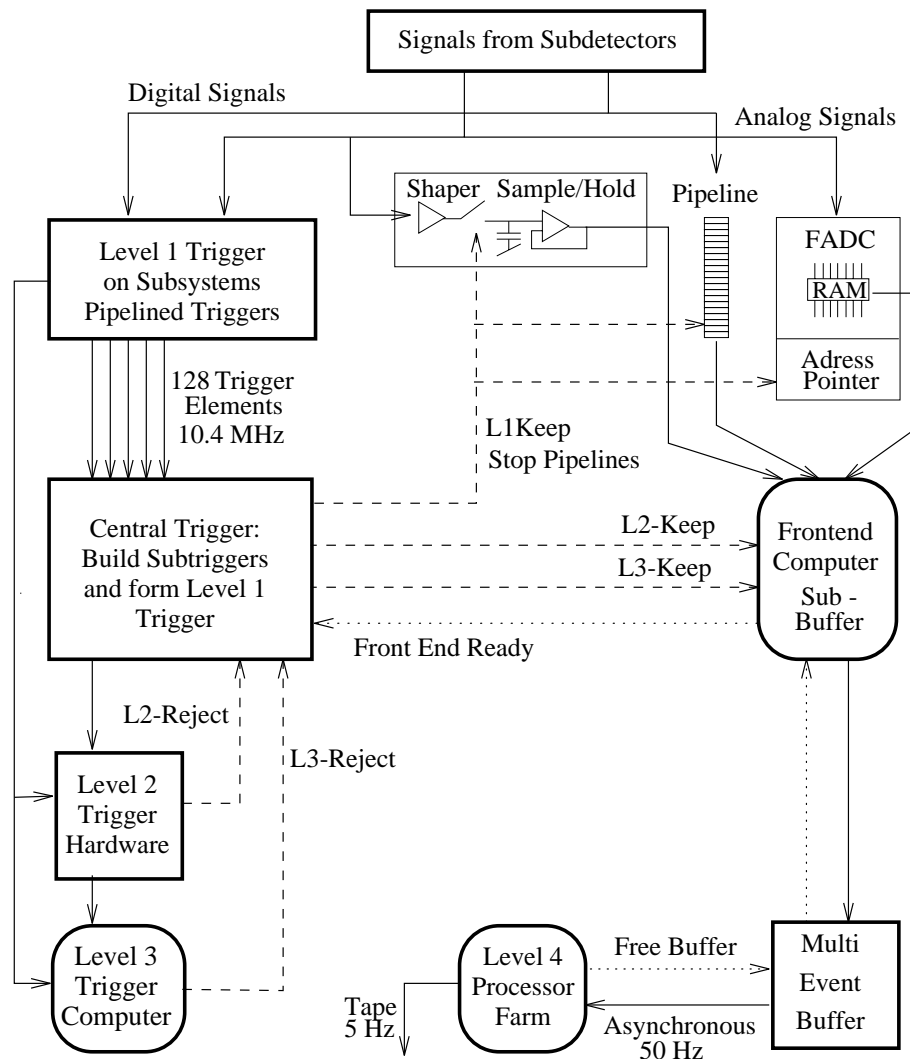


Figure 3.9: Block diagram of the H1 trigger system and data flow from the sub-components of the H1 detector to the final storage (from [62]).

energy loss of electrons undergoing a bremsstrahlung interaction bends their trajectories, by means of the magnet system, towards the center of the nominal (roughly circular) orbit such that they hit the ET.

There are two main sources of background which can be treated in appropriate ways. The first concerns low energetic synchrotron radiation originating from the last magnetic deflection of electrons before they reach the interaction region. A part of this radiation cannot only affect the detector parts in the interaction region but also the photon detector. For the measurement of the photon and electron energy the PD and ET use (TlCl+TlBr)-crystal in arrays of 5x5 and 7x7 elements each with attached photomultipliers. Čerenkov light is received by them and converted into corresponding energy values.

Bremsstrahlung from interactions between electrons and residual gas from imperfect vacuum in the beampipe contribute to the ep luminosity measurement. The background contribution is corrected by the subtraction of the luminosity accumulated in electron pilot bunches which have no complementary proton bunch partner and can, thus, only interact with residual gas molecules depending on the quality of the vacuum. A correction factor is gained by an extrapolation of this background rate to all

colliding electron bunches proportional to their total electric current [31]. This important procedure is imposed because of the high bremsstrahlung cross section in residual gas interactions.

The luminosity system serves also the localization of the current electron beam position, which is monitored as an important parameter for the beam steering procedure itself, especially in the phase of beam tuning at the beginning of the luminosity run. The beam position is determined by the average cluster position of bremsstrahlung photons, since their direction is identical to the incoming e -beam.

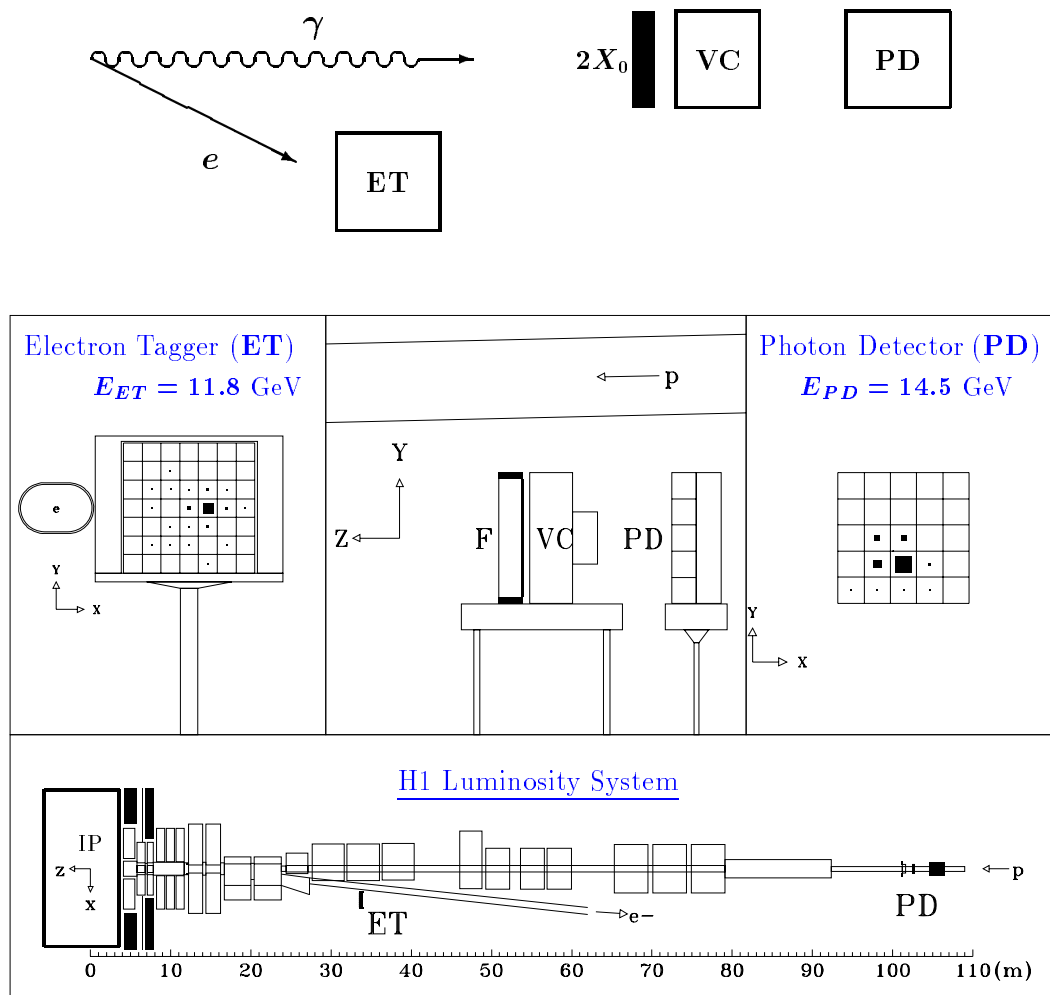


Figure 3.10: Overview of the luminosity measurement system: detection principle (upper part) and electron tagging calorimeter (lower part). ET = electron tagger; VC = Veto-Counter against synchrotron radiation, with a $2X_0$ lead filter F in front; PD = photon detector. The lower graphic shows the $-z$ magnet systems using a highly magnified scale for the x coordinate.

4 Event selection

In this chapter the selection of various data sets which enter the analysis is described. The first part discusses the Monte Carlo data sets derived from different generator programs. The second part describes details of the experimental data set taken during the HERA luminosity-operation of the year 1997, which included a special trigger setting period following the end of the standard data taking. In addition selection criteria for the Compton analysis are listed and discussed. Positrons were used as lepton beam particles in 1997, they are synonymously referred to as electrons throughout this text.

4.1 Monte Carlo

The simulation of high energy particle collisions can be resolved into two major steps. The first one is the generation of the physical process according to the common or new theoretical understanding of the forces as well as the principles of secondary particle production. The second step is the simulation of the generated set of particles as they pass through the experimental apparatus and interact with its compounding materials, parts and their specific spatial arrangements. This latter part is performed by the standard H1 simulation program which is continuously accommodated to current setup details and their changes. The output of this program are event sets which are identical in their bank structure to the data of the real experiment. In addition, generator specific banks are contained in them in order to have access to the original quantities, allowing to monitor any differences between generated and reconstructed quantities. In the following the MC generators for the signal and background are described as well as their simulated event samples.

4.1.1 Compton signal

The QED Compton generator produces event data according to the kinematic description given in Section 2.1.2. All three sub-processes, *i.e.* (pseudo-) elastic, resonances and continuum inelastic, are calculated at the same time. Compared to the original version of the program [9, 19] several improvements have been implemented [37] up to version 2.14 used in the present analysis. Some of them are shortly summarized here.

The generator produces internally events of higher absolute acoplanarities A , *i.e.* far from the Compton peak where the azimuthal angle difference between electrons and photons is getting smaller[†]. The program steering allows to set an upper limit for $|A|$ of the output events. Because the reconstructed acoplanarity is subject to smearing caused by the detector simulation an artificial event loss at this limit could occur if the same cut value of A is used in the selection of *reconstructed* events. In order to avoid such an effect in the analysis a limitation $A < 50^\circ$ is chosen for the generator steering, while $A < 45^\circ$ is required equally in the selection of simulated and experimental events (s. also Section 4.2.1). The kinematic range of the generated Compton events is shown in Figure 4.1 for the momentum transfer Q_h^2 and Bjorken x_h .

Since its first implementation the Compton generator has undergone recently many important improvements: up to version 2.0, the hadronic final state in inelastic Compton scattering was not

[†]The reliability of cross sections in this high- $|A|$ range has not been checked so far for the mentioned generator version.

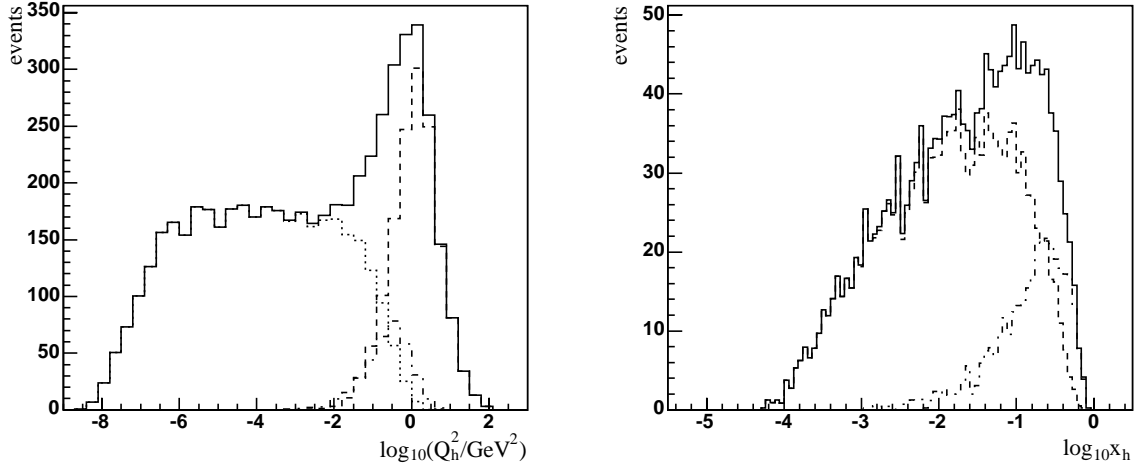


Figure 4.1: Kinematic range of COMPTON generated events in the hadronic variables Q_h^2 and x_h . The dotted lines correspond to the elastic part, the dash-dotted line to the resonance region, and the dashed line to the inelastic contribution. The full line represents the sum of all three parts, except for the right graph where the elastic peak at $x_h = 1$ is not included. The distributions are created according to the full set of event selection cuts.

generated, and also the applied F_2 parameterisation had to be updated (s. [37]). The original choice of the structure function was of a scale invariant type [9, 20]

$$F_2^p(x) = \frac{35}{32} \sqrt{x} (1-x)^3 + 0.2 (1-x)^7, \quad (4.1)$$

to which an additional interpolation term $\phi = Q^2/(Q^2 + F_2^p)$ was multiplied to obtain the correct behaviour at $Q^2 = 0$. As more data became available improved fits could be applied to describe the F_2 measurements especially in the range of low Q^2 . In the version 2.14 of the generator F_2 is implemented according to the results of the ALLM-97 parameterisation (Abramowicz, Levin, Levy, Maor, s. [21]). These are based on a Regge motivated approach and do also describe the high Q^2 region very well. The fit to F_2 is of the form

$$F_2(x, Q^2) = \frac{Q^2}{Q^2 + m_0^2} \left(F_2^{\mathcal{P}}(x, Q^2) + F_2^{\mathcal{R}}(x, Q^2) \right), \quad (4.2)$$

where the two functions represent contributions by the exchange of a Pomeron \mathcal{P} and a Reggeon \mathcal{R} , respectively,

$$F_2^{\mathcal{P}}(x, Q^2) = c_{\mathcal{P}}(t) x_{\mathcal{P}}^{a_{\mathcal{P}}(t)} (1-x)^{b_{\mathcal{P}}(t)} \quad (4.3)$$

$$F_2^{\mathcal{R}}(x, Q^2) = c_{\mathcal{R}}(t) x_{\mathcal{R}}^{a_{\mathcal{R}}(t)} (1-x)^{b_{\mathcal{R}}(t)}. \quad (4.4)$$

t is a slowly varying parameter of Q^2 , and $x_{\mathcal{R}/\mathcal{P}}$ are modified Bjorken- x variables which reach x for high values of Q^2 . The fit parameters (23 in total) were calculated by data from ZEUS, H1, SLAC, BCDMS, E665 and NMC.

Furthermore, the resonance region up to $m_X = 1.8$ GeV was improved: instead of the sum of Breit-Wigner resonance fits, a more refined parameterisation for the virtual photon absorption cross section was applied according to Brasse et al. [24]. The resonances are found in a x -range of $\simeq 0.3 \dots 0.8$.

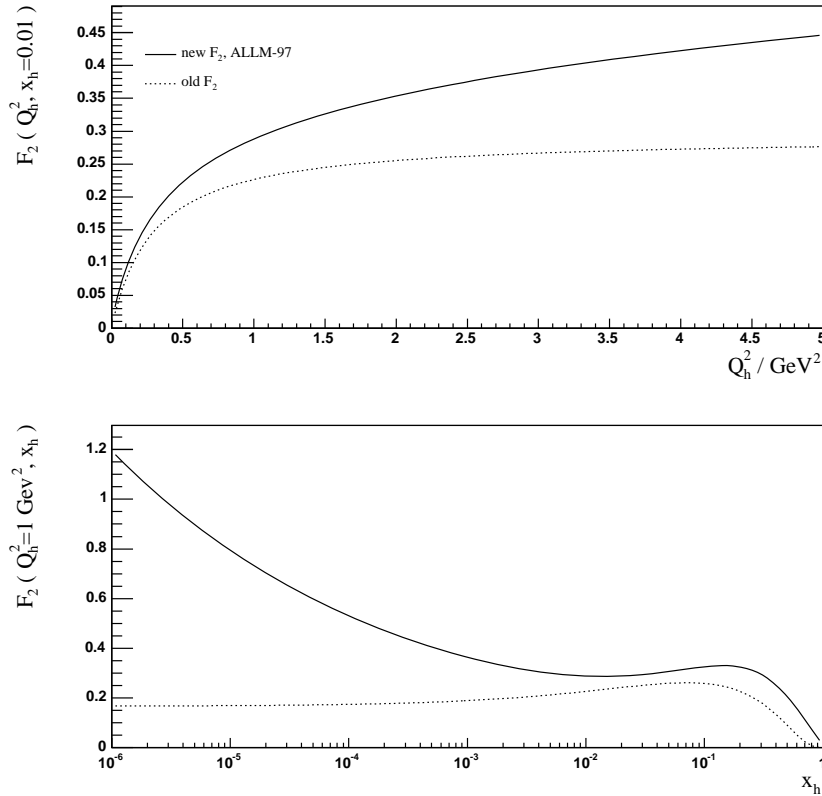


Figure 4.2: The new F_2 parameterisation, ALLM-97, as used in version 2.14 of the COMPTON event generator, in comparison with the old one of [9], illustration based on [37]. The upper plot displays $F_2(Q_h^2)$ for fixed $x_h = 0.01$, the lower one displays both functions in x_h -dependence for fixed $Q_h^2 = 1 \text{ GeV}^2$.

In Figure 4.2 the F_2 parameterisation differences between Eq. 4.1 and the ALLM-97 fit is shown. The upper graph demonstrates the Q^2 dependence in the range from 0. . . 5 GeV^2 for a fixed x value of 0.01. As pointed out in [37] the discrepancy between the old and the new parameterisation can be explained by the inclusion of $x^{-\lambda}$ terms in the more recent F_2 which were not present in the old one. These terms cause a rise at low x of $F_2^{\text{ALLM-97}}$ visible in the lower graph. The newer version is expected to give a better description at low x values. The comparison made in the lower graph using the x -dependence for fixed Q^2 at 1 GeV^2 shows that both structure functions have similar shapes. They converge towards zero in the limit $Q^2 \rightarrow 0 \text{ GeV}^2$. The peaking structure of F_2 (x -dependence), as expected from the resonant contribution in the medium to high x -range, is not displayed in Figure 4.2.

Radiative corrections to QEDC

The description of QEDC so far was in 1st order α_{em} only. Higher order contributions come from radiative corrections to the Compton process itself. They affect the kinematics and consist, as most important ones, in the radiation of an additional photon from the incoming electron line; this can be viewed as analogue to the usual corrections in the deep inelastic case as initial state radiation. The graphs for ISR in QED Compton are displayed in Figure 4.3.

In cross section calculations the *peaking approximation* [9, 30] is applied for the description of

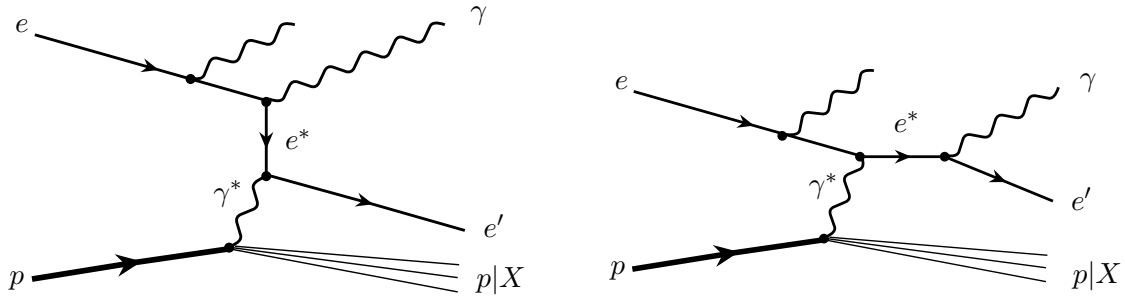


Figure 4.3: Initial state radiation process in QED Compton scattering. An additional ISR-photon is radiated off from the incoming electron line.

the ISR photon spectrum. The ISR radiation is equivalent to an energy loss of the beam electron, it is described according to the probability function

$$dP(k) = \beta k^{\beta-1} \left(1 - k + \frac{k^2}{2}\right) dk \quad (4.5)$$

using

$$\beta = \frac{2\alpha}{\pi} \ln \left(\frac{2E_e}{m_e} - \frac{1}{2} \right) \quad \text{and} \quad k = \frac{E_\gamma}{E_e}, \quad (4.6)$$

with E_e being the incident electron energy and E_γ the ISR photon energy. Technically the detached application of the electron energy loss is justified by the very different angles of the two final state photons since interference effects are suppressed in this configuration. The same calculation is used in the Compton generator.

4.1.2 DVCS background

A topological similar process to the QED Compton in ep scattering is the Deeply Virtual Compton Scattering (DVCS). This process represents the diffractive scattering of a virtual photon off a proton, illustrated by the two graphs in Figure 4.4 in lowest order QCD. The process corresponds to vector meson electro-production where in place of a meson a final state photon is observed. The final state particles are the same as in QED Compton scattering such that in principle interference effects have to be accounted for. Measurements on energy and polar angle, which are needed for the determination of differential cross sections, are not affected within the leading-twist approximation in DVCS. This allows to operate with two separate Monte Carlo event sets for both, QEDC and DVCS, and treat them as independent for background subtraction.

In the graphs the hadronic final state is denoted by the proton indicating that only the elastic part in the process has been measured so far [41]. For theoretical comparison in that publication the corresponding Monte Carlo generator TINTIN [40] was used. It produces only the contribution by elastic ep scattering. Due to the yet unmeasured inelastic part and the typical statistical and systematic uncertainties of the elastic cross section measurement, a total normalization uncertainty of 50% is attributed to the Monte Carlo prediction. The relative inelastic contribution in DVCS was estimated to be of the same order as the one found in vector meson production. As DVCS represents the strongest

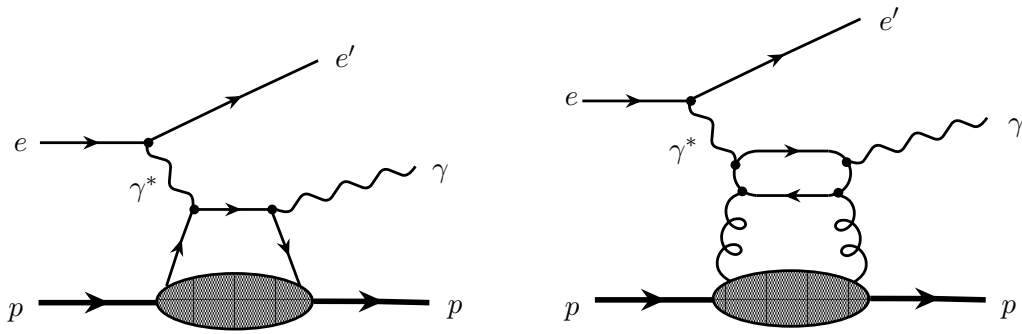


Figure 4.4: Deeply virtual Compton scattering, QCD lowest order feynman graphs. The outgoing proton in both graphs accounts for the fact that only elastic events are calculated in the corresponding background Monte Carlo as only the elastic contribution has been measured so far.

background contribution to Compton scattering it is desirable that the generator will be extended to the inelastic region accordingly. In fact, corresponding studies are being performed [63].

4.1.3 Di-lepton background

A further background process to Compton scattering is given by two-photon interactions which produce a lepton pair (di-lepton). Thus, one observes in total three leptons in the final state, one being the scattered beam lepton, while a lepton pair appears in addition. The corresponding graphs for the production of an e^+e^- pair are shown in Figure 4.5. The program GRAPE-Dilepton [23] is chosen for the generation of an event set of this di-lepton type. Because there are three electrons in total appearing in the final state of this di-lepton process it is likely that one of them escapes through the beampipe, if scattered under a sufficient small angle, or that it falls out of acceptance in other parts of the detector. In such cases, events with only two reconstructed e.m. clusters from a di-lepton process appear in the data sample as candidates for a QED Compton cluster pair. Particle identification applied to the Compton cluster pair ensures that corresponding di-lepton contributions are suppressed. Thus, di-lepton events can contribute after this selection step only by detector inefficiencies (as this can imitate an Compton electron/photon pair, s. Chapter 5), and their relative contribution to the final signal sample should be of an order of magnitude of not more than typical detection inefficiencies or mismatch rates in the particle identification, respectively.

The GRAPE di-lepton generator produces resonant and continuum inelastic events in addition to the elastic channel. The same parameterisations as in COMPTON are used for this purpose, namely the ALLM-97 for the continuum and the resonance fits by Brasse et al. [24].

4.1.4 DIS background

Events generated with the DJANGO program can be used in two ways: firstly, in connection with a corresponding DIS event selection from the experiment for verification of efficiencies and other detector properties as calculated in the Monte Carlo, and secondly as a background Monte Carlo sample. When used as for background studies it is necessary to exclude the Compton events generated by DJANGO in order to avoid double counting, as they already contribute through the COMPTON

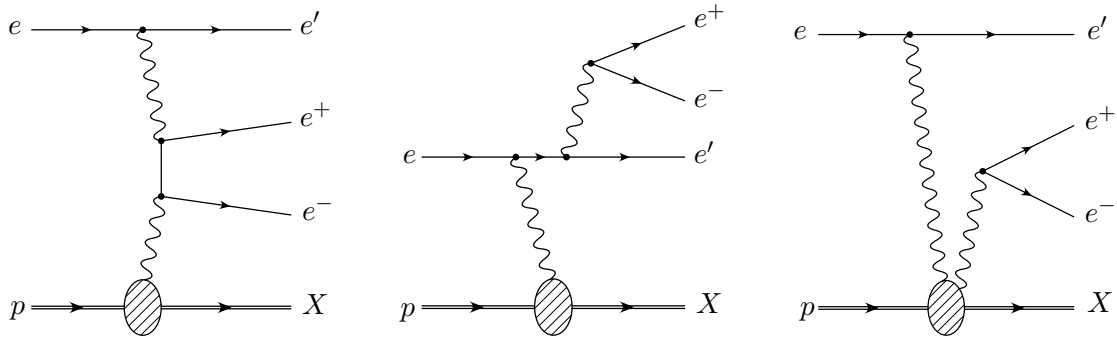


Figure 4.5: Di-lepton scattering in ep collisions. “Two photon” reactions, left: $\gamma\gamma$, middle: γ radiated by the electron, right: γ radiated by the proton.

generated event sample. This represents an important measure because the QEDC selection carries out a specific search for two high energetic clusters and thus enriches especially this event type in the final selection from the DIS background simulation.

This simulation of DIS events in the kinematic range of low Q^2 was found to give unexpected high event rates. This could be traced back [37] to an unexplained property of generated events where a single pion were scattered into the backward region, *i.e.* into the direction of the incoming lepton. The consequence was that the background rate would have become a substantial fraction of the Compton signal which seemed very unlikely compared to the data. Indeed, a closer look into the output of the event generator showed that these events are of singular nature responsible for the observed high hadronic final state masses due to the pion. The solution was to cut off this type of events and to rescale the DJANGO Monte Carlo with the help of the measured rates of backward scattered π and η meson peaks in the data. The result was that the typical DIS background contribution is about 1% of the Compton signal. This number will be assumed in this analysis without repeating the procedure. As the DIS background is, thus, much smaller compared to the dominant DVCS background, of which the simulation is dominated anyway by large normalization uncertainties as introduced by its not very well studied inelastic channel, it will be neglected in the analysis and in subsequent histogram representations of physical quantities.

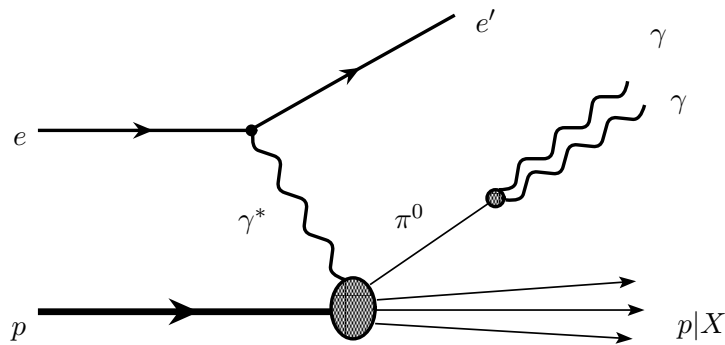


Figure 4.6: Deep inelastic ep scattering with a backward scattered π^0 and its subsequent decay into two photons. Both photons can leave either two separate e.m. clusters or only a single one in the backward calorimeter.

4.2 Data basis 1997

4.2.1 Compton event selection criteria

Starting from the full data sample of the 1997 standard running period a sub-selection of QED Compton events is performed, and used as the primary basis for this analysis. The principal run range corresponds to the numbers 177500...200444. The event selection is based purely on calorimetric criteria to detect the characteristic Compton event topology of two electromagnetic particles. The trigger setup for recording these events, as established for the 1997 data taking, is discussed later in Section 6.3.1.

General run selection criteria

Before any refined selection cuts are applied to an event, the run in which it was recorded is required to have a minimum data quality. The corresponding information depends on the experimenters' rating of the overall data quality of a given run, based on the monitored stability of the subdetectors and the data acquisition system as well as on the beam conditions and background rates. In general, each run is marked with a quality label which is either *poor*, *medium* or *good*. Only the last two cases are considered for the present selection of QED Compton events.

Especially in the first phase of a luminosity run high prescaling factors (Section 3.3) may be present in the data for individual subtriggers. Because very high prescales introduce correspondingly high statistical uncertainties, when applied later as event weights, one aims generally on avoiding them for the event analysis. For this purpose a *trigger phase* (TP) number higher than "1" is demanded for each run. The values of TP range from 1 to 4 and indicate periods of different subtrigger prescale settings within one luminosity fill. A value of 1 corresponds to the beginning of a luminosity run. Using different TPs was necessary to optimize the acquisition and processing of the event data stream delivered by the H1 detector because in this scheme the rates of different physics processes are better balanced w.r.t. each other. Also, since not all subdetectors can be switched on as long as the HERA beam steering continues for luminosity optimization or the background rates vary considerably, events belonging to the first phase were excluded from the further analysis.

In addition it is checked during the Compton event selection whether the correct subdetector high voltage settings were in agreement with a filter mask formed according to those components required for the event analysis. Also the respective branches of the data acquisition readout system were required to be active. This bundle of criteria defines largely the overall luminosity available for the analysis. Further run restrictions arise from the standard set of rejected runs and run ranges of the ELAN working group [46], where runs of bad quality or very low efficiencies or subdetector failure are compiled. The run list is given in the appendix, Table 10. Finally, another set of runs is added to this list, which is determined in the subdetector stability analysis of this work. This run *deselection* is based on periods of problematic detector performance and it is discussed in detail in the Sections 5.3 and 5.4. The full list of rejected runs and run-ranges is used as input to the luminosity calculation (carried out with an independent program) using identical requirements for high/low voltage settings, readout branches and trigger phase.

Cluster based selection

For each event a search for electromagnetic energy depositions (*clusters*) over the corresponding data banks of all calorimeters is performed by the standard H1 electron finder program *QESCAT* [45]. Depending on the specific purposes of any analysis several parameters can be adjusted to narrow or

open the selection criteria, such as for example the maximum number of clusters to be searched for, energy range, and cluster size.

Like all event relevant properties also the electromagnetic clusters in the backward calorimeter SpaCal are calculated by the event reconstruction program. SpaCal clusters are created by selecting a group of neighbouring calorimeter cells each containing some minimum amount of energy. A basic calibration procedure, that is converting photomultiplier signal levels into energy values, is used in this calculation. Several algorithms have been tested which differ mainly in the type of how cells are weighted in order to determine both, the cluster barycenter and its lateral extension (the cluster *radius*). Basically a choice can be made between linear, square root and logarithmic weighting techniques. As shown for example in [25] with MC simulations, for the spatial localization of a cluster the logarithmic method is advantageous in comparison with the others. The barycenter ζ of a cluster's x or y coordinate is calculated with this algorithm by forming the weighted sum of all active calorimeter cells related to the cluster as

$$\zeta_{\log} = \frac{\sum_i x_i w_i}{\sum_i w_i} \quad (4.7)$$

where

$$w_i = \max \left(0, W_0 + \ln \frac{E_i}{\sum_i E_i} \right). \quad (4.8)$$

The cutoff parameter W_0 has a typical value of 4.8 as determined by other studies. The E_i are the cell energies and the x_i are the cells' central coordinates along the calorimeter front face measured in H1 coordinates.

The maximum number of electromagnetic clusters to be searched for in an event was set to a high value. To be considered as appropriate a cluster has to have an energy $E_{\text{cluster}} > 2$ GeV and a radius $\sigma_{\text{cl}} < 6$ cm. The first and the second cluster in an event (*i.e.* the ones with highest and second highest energy) have to fulfil the conditions

$$E_1 > 10 \text{ GeV} \quad E_2 > 4 \text{ GeV} \quad 20 \text{ GeV} < E_1 + E_2 < 35 \text{ GeV}. \quad (4.9)$$

These numbers are motivated by the generator distributions shown in Figure 4.7 and are also usual in earlier studies. The lower limit of the energy sum serves the reduction of radiative influences, while the upper limit is justified by the expectation value of the simulation. At this point no cluster-track links are required to decide about the particle identities (electron/photon) of the cluster candidates. This task of the analysis will be described later.

A typical QED Compton candidate event in the H1 detector is shown in Figure 4.8 as side-view and radial projection in proton beam direction (right). The event display shows two electromagnetic clusters in the SpaCal while the remaining calorimeters are empty. A small amount of energy has leaked into the hadronic section of the backward calorimeter. Both clusters have associated track elements of the backward drift chamber BDC and the backward silicon tracker BST, the latter pointing to the vertex region.

Final selection

The last part of the selection is made on the event sample left over from the above run and cluster treatments. A list of the applied event cuts is given in the following:

- acoplanarity between photon and electron $A < 45^\circ$
- SpaCal residual e.m. energy $E_{\text{tot}}^{\text{e.m.}} - E_1 - E_2 < 1 \text{ GeV}$

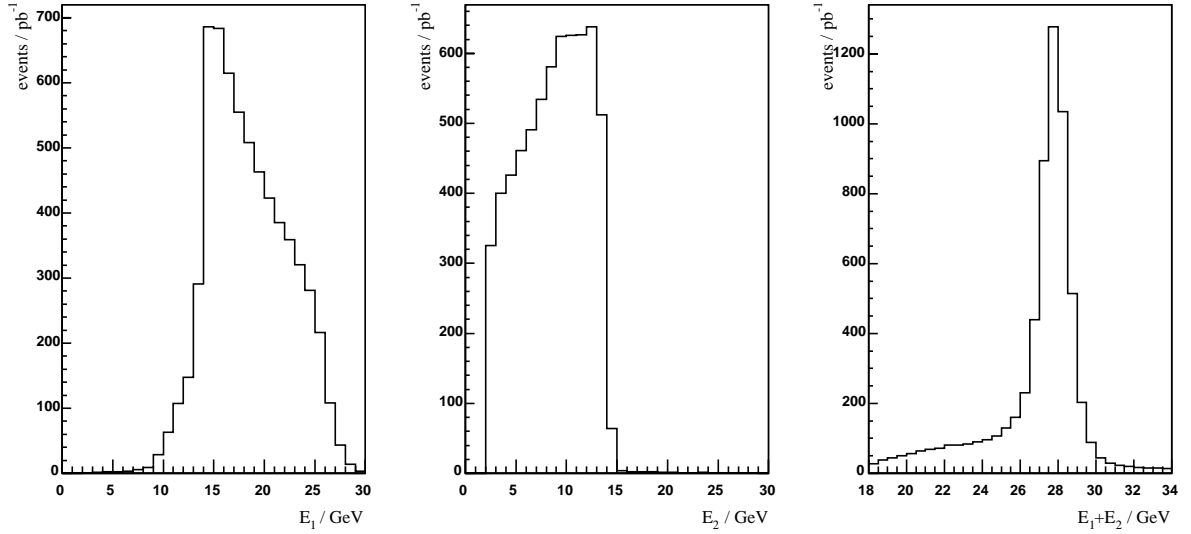


Figure 4.7: Reconstructed cluster energies from a simulation of COMPTON generated events. Left, middle: first and second cluster energy; right: energy sum of both clusters. The distributions are plotted without detailed cuts of the event analysis and thus contain a large fraction of radiative events. The peak-to-tail ratio (tail: $E_1 + E_2 < 25$ GeV) is therefore lower than in the final distribution.

- SpaCal residual hadronic energy $E_{\text{tot}}^{\text{e.m.}} < 0.5$ GeV
- SpaCal veto cell energies of each cluster $E_{1,2}^{\text{veto}} < 1$ GeV
- cluster radius $\text{ECRA}_{1,2}(\log) < 4$ cm
- actual L1 subtrigger s_{13} on
- limit LAr cluster $\theta < 30^\circ$
- position of event vertex is restricted as $|z_{\text{vtx}}| < 30.8$ cm
- cut on event energy-momentum balance $E - p_z < 60$ GeV

The total integrated luminosity of the data sample after exclusion of all low quality run ranges – including those determined later in the hardware stability analysis – was calculated to $\mathcal{L}_{\text{data}} = 9.178 \text{ pb}^{-1}$. The integrated luminosities of the background samples are: $\mathcal{L}_{\text{DVCS}} = 31.0 \text{ pb}^{-1}$ and $\mathcal{L}_{\text{di-lepton}} = 46.3 \text{ pb}^{-1}$. The luminosities of the individual Monte Carlos are used to reweight their events accordingly by a factor $1/\mathcal{L}_{\text{MC}}$ in all distributions of physical quantities shown in the following chapters where Compton data and Monte Carlo (signal with backgrounds) are compared.

4.2.2 Selection of the inelastic channel

The inelastic part in any ep reaction is characterized by the invariant mass of the hadronic final state m_X . But especially in the region of very low masses this quantity cannot be measured precisely enough. As discussed in [26] the selection of the inelastic channel in QED Compton can be realized

by a combination of cuts on the acoplanarity between Compton electron and photon, and on the total $e\gamma$ transverse momentum. Because the acoplanarity is applied in this analysis for important calibration studies it was not used as a property to cut on. Instead a simpler indicator for the presence of an inelastic Compton event was chosen using the total measured electromagnetic and hadronic energy deposition in the Liquid Argon calorimeter. For this purpose the energies of all reconstructed LAr clusters, with each single energy above 0.5 GeV, have been added as

$$E_{\text{LAr,total}} = \sum_i^{\text{N}_{\text{clus}}} (E_{\text{LAr-e.m.}} + E_{\text{LAr-had}}). \quad (4.10)$$

All events with $E_{\text{LAr,total}} > 2$ GeV are classified as inelastic. Since the separation between the elastic and inelastic channel is, in any case, a compromise between the required efficiency and purity of the resulting sample of one of the channels, this method was chosen. The main purpose is to give an approximate impression and reference of the fraction of inelastic QED Compton events in the distributions of the relevant physical quantities. Due to the expected small acceptance for inelastic events (resonance and continuum) as a consequence of the limitations given by the beam pipe, numbers of the cross section measurements will be calculated only for the total Compton sample.

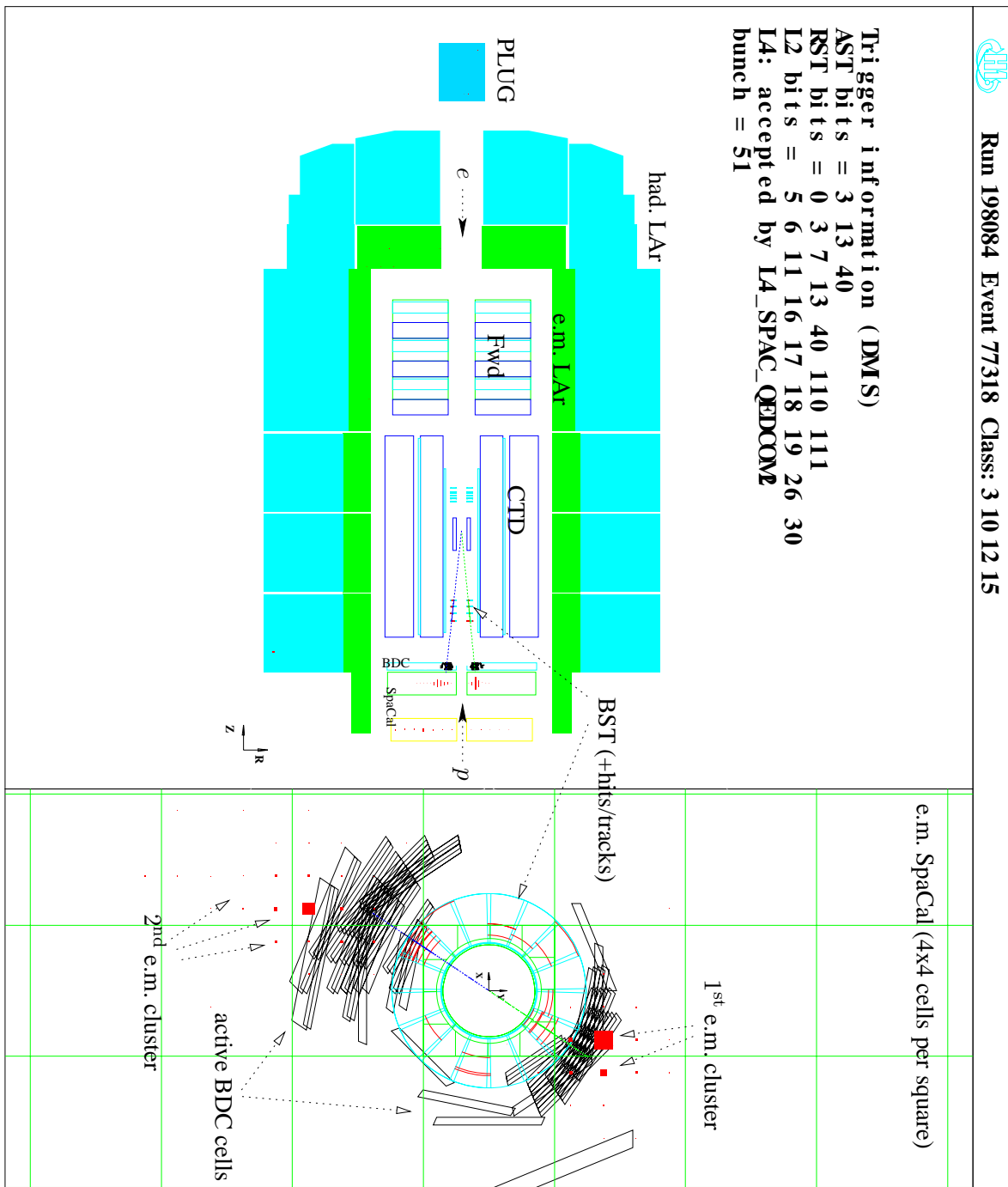


Figure 4.8: A typical elastic Compton candidate event in the H1 detector display. The LAr calorimeter has no significant energy depositions. All stages of the trigger system accepted the event. Here, the adverse situation is found that both SpaCal clusters have associated track signals from both, BDC and BST, inhibiting the particle identification. The event was discarded by an anti-background criterion requiring less than 0.5 GeV hadronic energy in the SpaCal (2 GeV measured). It would have been rejected by the particle identification as well.

5 Particle Identification

As a consequence of the event kinematics the Compton photon and electron are mainly scattered into the H1 backward calorimeter SpaCal. For the identification of the two leading electromagnetic clusters the backward tracking devices play a decisive role. In the following sections detailed descriptions are given on the techniques of forming tracks or corresponding space points from subdetector signals in order to gain information about particle trajectories and to verify links between the vertex and the cluster position. Like before, the term 'electron' will be used to denote the positron used as lepton type, as it was the case in the HERA beam collision mode of 1997.

5.1 General conditions

As discussed in the introduction to the Compton kinematics it is a central question how to distinguish between the most prominent particles in a QEDC scattering event, the electron and the photon. Because the analysis aims on measuring the leptonic cross section, it is necessary to identify the electron, or equivalently the photon. While in a typical deep inelastic scattering measurement the identification of the electron is reduced in many cases simply to its verification, namely by proving that a track or track piece exists between the event vertex and the electron's energy deposition, the same procedure in QEDC is hampered by a series of preconditions and effects specific to this type of interaction. They form a complex bundle of questions whose decomposition needs careful considerations.

I) *Photon*: The additional electromagnetic (e.m.) final state particle, which is very similar to the electron in its calorimetric properties, makes it difficult to distinguish between them. The energy depositions in the e.m. calorimeter part are nearly of the same shape as the elementary physics processes are of identical nature, namely subsequent bremsstrahlung and/or conversion processes induced by the incident electron or photon. Thus, it is necessary for the purpose of particle identification to apply track criteria on both particles, according to the expectation that the scattered electron should leave a track behind it while the Compton photon should have no track signature in most of the events. But due to *conversion* a track can originate, in fact, from a photon which appears identical to an electron. The same effect occurs when there is *electronic noise*. Finally, another source of misidentification can be the *inefficiencies* of tracking devices spoiling the verification of the electron trajectory.

II) *Event vertex*: Two cases can be distinguished in the analysis of QED Compton events. In an elastic Compton event *no* hadronic final state (HFS) particles are present in the main detector which could be used for the reconstruction of the vertex position. The standard event reconstruction program ("H1REC") requires at least one charged track that points to the vertex region to do this. This means that either the electron or the photon (after conversion in front of a tracking device) has to be used in order to determine the vertex position.

The second case concerns inelastic events in which at least one charged track can be found in the central tracking chambers. When HFS particles are present they have to have high enough polar angles to allow a sufficient precision of the vertex position measurement. In general this means, even for an inelastic event, that a well determined vertex is not guaranteed as the hadronic momentum transfer in QEDC is low and also the invariant mass of the hadronic final state and thus the average polar angle is predominantly low.

To circumvent the limitations related to an unreliable or non-existing standard vertex due to low quality forward tracks a different approach is chosen instead of using tracks or track elements from

the standard reconstruction. This is made in order to determine the vertex position uniformly for all event topologies.

III) *Trigger*: Events with tracks in the acceptance range of the outer central jet chamber (CJC2) are partially suppressed by the Compton subtrigger setting of the 1997 data taking period. This is due to the fact that, at this time, the trigger was constructed as to be sensitive primarily to elastic Compton scattering, as this class was considered for calibration purposes. As the finite bandwidth of the data acquisition system has generally to be shared among the different physics analyses their corresponding subtrigger rates have to be limited. This is achieved either by an appropriate set of subtrigger conditions or by the choice of reduction counters applied to individual subtriggers. In the case of QED Compton the trigger rate was kept low by a suppression of inelastic events using a trigger element of the Drift Chamber $r\varphi$ trigger which signals three (or more) central tracks above some minimum transverse momentum. The details related to this and the track subtrigger settings are described in Section 6.3.1.

It is the aim of the following sections to scrutinize the individual effects for those detector parts relevant for the event selection described in Chapter 4. The studies are introduced by descriptions of the tracking principles and algorithms applied for the backward tracking devices, which are the BST, CIP and the BDC. This is followed by a study on detector performance, *i.e.* their stabilities and efficiencies over the data taking period. Electronic noise as well as photon conversion effects are discussed after that. The tracking related parts are concluded by a discussion on the procedure to localize the event vertex z -position using the measured track elements. The chapter ends with a description on the electron/photon identification process and possible optional algorithms.

5.2 Tracking in the backward region

5.2.1 Tracking with the Backward Drift Chamber

For the Backward Drift Chamber (BDC) two different reconstruction schemes were developed for standard use in any type of analysis. The software routines are the original “HDREC” [55, 56] and the later “BDCLEV” [57]. The main difference between both methods is that the first one explicitly reconstructs tracks considering from the beginning all hits available per event, while the second one uses preselected hits. In HDREC, a Kalman-filter delivers a list of track-candidates. The intention to select the optimum track candidate from this bunch of candidates emerged to be a very difficult task [56]. This is related to the distribution of passive material located in the interspace between CTD and BDC causing increased particle multiplicities by pre-showering, as well as to some imperfections of the reconstruction procedure. For example, the code ignores the common origin of a hit and its mirror-hit (see Section 3.2.3). Furthermore, to harmonize experimental and MC-simulated BDC data a difficult extension of the simulation would have been necessary [60].

The BDCLEV code aimed for an improvement of the polar angle θ_e resolution. It uses a beforehand reconstructed z -vertex position and the space point of the scattered electron in the backward calorimeter. Only those hits can contribute to the final track segment which match the input track hypothesis best. Performance aspects of the strategies in both programs were compared in [60].

It was observed that the radial distribution of electron tracks crossing the BDC-plane show a pattern reflecting the BDC drift cell structure, see Figure 5.1. These so called “migrations” [58] were suspected to have several origins, as there is, for example, the BDC transition-cell positioned at $r \approx$

22...25 cm which could cause distortions by its specific construction and hardware problems (high voltage, s. also Section 3.2.3). In addition, the same radial range corresponds to the projection of BST- and CIP-related, discontinuously distributed passive material on the BDC plane. As a consequence these effects could not be detached easily, until, in fact, a wrong treatment of the asymmetric transition-cell in the reconstruction code was found [59].

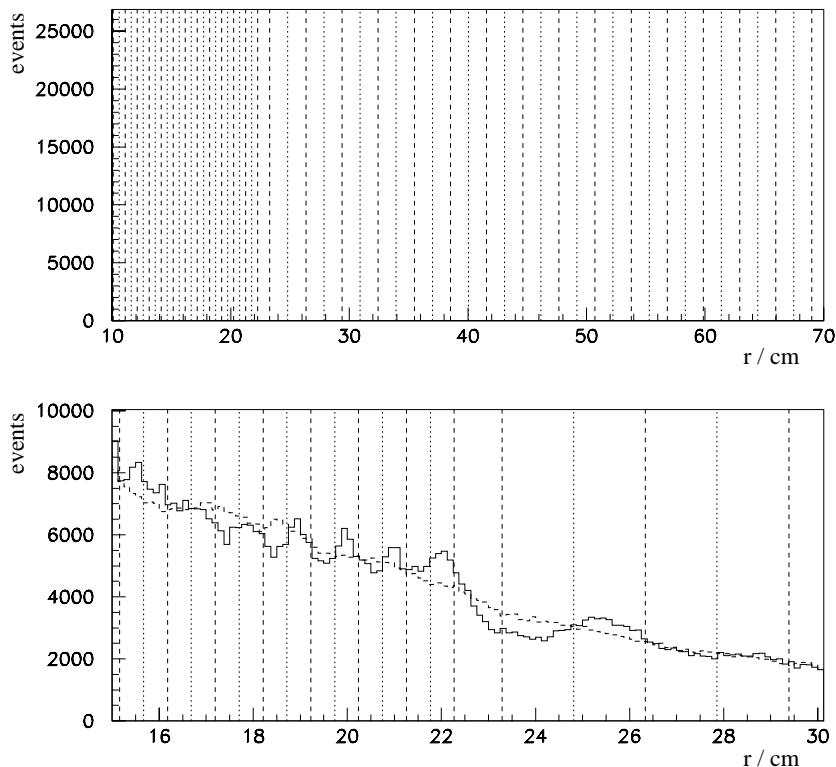


Figure 5.1: Distributions of radial track positions in the BDC as measured with the old BDC reconstruction using electrons of a high statistics DIS event sample. Top: full BDC radial range, bottom: detail view on the transition cell region. The vertical lines indicate the positions of the BDC drift cell limits. A strong deviation from the expected steady decrease was observed especially in the range of $r = 22...25$ cm. A corresponding Monte Carlo distribution is shown as dashed curve in the lower histogram which runs smoothly in contrast to the data. (Original graphs from [59].)

5.2.2 Validation of charged tracks with the CIP

The two sensitive layers of the Central-Inner-Proportional Chamber (CIP) can be used to determine a charged particle's trajectory, or a part of it, originating from the interaction point. Although the other central chambers could also contribute to the tracking procedure in the backward area, in this analysis only the CIP was used for the following reasons: since the CTD acceptance volume decreases quickly with increasing polar angle θ_{H1} where track finding becomes more and more unreliable and for reasons of simplicity the analysis was restricted to the use of the CIP. Also, the jet chambers were affected by a strong efficiency loss for some part of the azimuthal range during the 1997 running.

Active pads, at least one in each chamber layer, are searched for in a limited z -range along the CIP surface. The range follows from a projection of a vertex range $z = -50\dots +50$ cm onto the CIP surface in direction of the considered SpaCal cluster position, see Figure 5.2. This excludes possible CIP signals, in an earliest possible phase of the track search, caused by particles not related to the ep vertex. The requirement of an active pad in each layer suppresses random noise signals which otherwise could mimic accidentally a particle track. As shown in the figure the allowed z -ranges on their respective CIP layer surfaces are determined accurately according to their different cylinder radii.

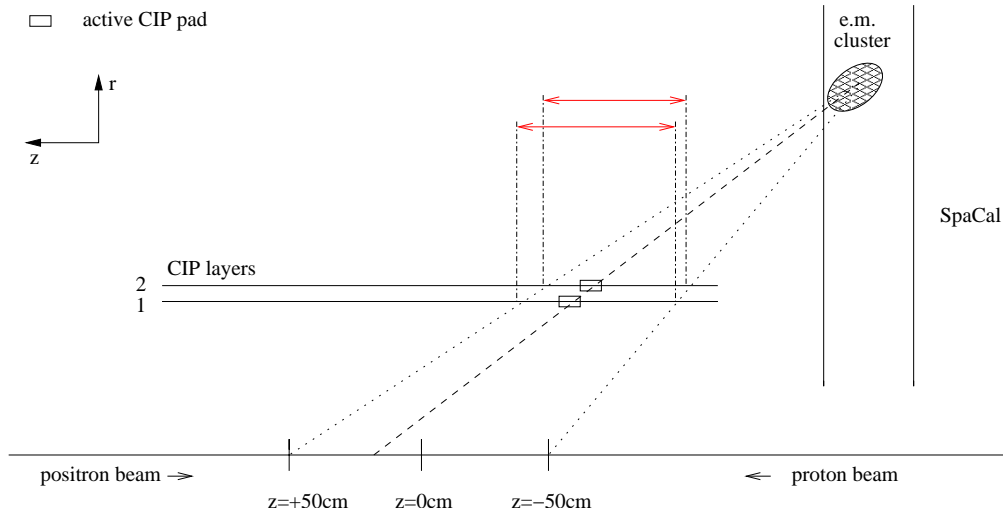


Figure 5.2: Vertex reconstruction using the CIP. The schematic side view of beam axis, CIP and SpaCal indicates those regions (horizontal double arrows) in which active CIP pads are searched, while the vertex position is unknown.

5.2.3 CIP pad-clusters

The experimental data show that in a significant fraction of events additional active pads are present near to the one pad per layer required at minimum. The question arises how to combine their positions into one space point (per layer) and for a complete track, respectively. The discrete array of pads constituting the CIP with a z -width of 3.65 cm is not suited for precise track reconstruction, as a single active pad can be regarded only as an approximate space point of a passing charged particle. This means that combining the center points of two pads (one from each layer) into one trajectory would result in a corresponding discrete polar angle reconstruction. Therefore, a different method was chosen in which the CIP pads have to form a contiguous *cluster of pads*. The geometrical barycenter of all valid pads, belonging to such a pad-cluster, within the z -ranges of Figure 5.2 is calculated and considered as second space point in addition to the position of the SpaCal cluster. Both space points together define then particle trajectory.

Starting from the list of valid active pads a pad-cluster is required to be shaped as to “point” from the vertex region towards the SpaCal energy deposition. This is achieved by the application of corresponding cluster growth rules as one pad after the other is added to an initial *seed pad*. Thus, the final pad association is defined using a

CIP pad-cluster formation algorithm:

- Single pads, which do not have directly adjacent pads in r (across layers) and z (no gap allowed within one layer), are removed from the initial list of valid pads in order to avoid that separate and unrelated signals are combined.
- Additional pads contributing to the pad-cluster are required to be immediate neighbours, in r or z , to at least one of those which were already collected.
- For a pad in the outer layer at least one additional active pad must be located either (i) on its $+z$ -edge, or (ii) below it in the inner layer, or (iii) one pad position in $+z$ -direction in the inner layer.
- For a pad in the inner layer the conditions are the same, except that all directions are inverted. This allows in addition the reconstruction of an extended pad-cluster where one inactive pad is located in between active pads of the pad-cluster.

The algorithm rules are used to carry out a search for active pads, starting from the negative z -end of each CIP layer shown in Figure 5.2. Figures 5.3-a,b illustrate the removal of pads having no neighbours in r or z , or of combinations which do not have the expected track inclination towards the backward calorimeter. In the example a cluster of three pads is kept according to the selection rules listed above. The appendix A.4 presents a code implementation of these rules. Typical final pad-cluster shapes as found in the data are shown in Figure 5.3-c.

In every event and for each observed SpaCal cluster a pad-cluster (if present) is stored with all its assigned pads. This information is used in the calculation of a z -vertex position. If an additional piece of the track can be reconstructed using BDC hits, the BDC track position at $\mathfrak{z}_{\text{BDC}}$ replaces the SpaCal cluster position as the reference space point used for extrapolation to the beam axis. A flag is set to indicate that the particle was CIP validated. This flag is used later in the particle identification step.

The resulting pad-cluster width distribution in z is shown for deep inelastic scattering events in Figure 5.4 (for description of DIS event selection see Section 5.3.2). The width is defined for one layer as difference of the z -coordinates of both ends of the cluster. Thus, for only one active pad per cluster the width in a layer corresponds to the pad z -size of 3.65 cm, or multiples of it for more than one pad. The total cluster width is then defined as the difference of the maximum and minimum z of the pad edges, irrespectively of the layer (Figure 5.4-right). In simulated events the pad-cluster is found to be narrower than for data.

5.2.4 Track reconstruction with the BST

This paragraph summarizes the algorithm for the reconstruction of BST tracks which has been developed in an earlier work [32]. The present analysis uses this method to find BST track-links to electromagnetic SpaCal clusters and for the vertex determination.

Two different methods exist depending on whether the vertex position is known in advance or not. In the first case, with a vertex reconstructed from central tracks, the algorithm uses the position error of the considered SpaCal cluster. This together with the vertex uncertainty defines a corridor between the cluster and vertex position. The width of this corridor is calculated for each BST plane, called

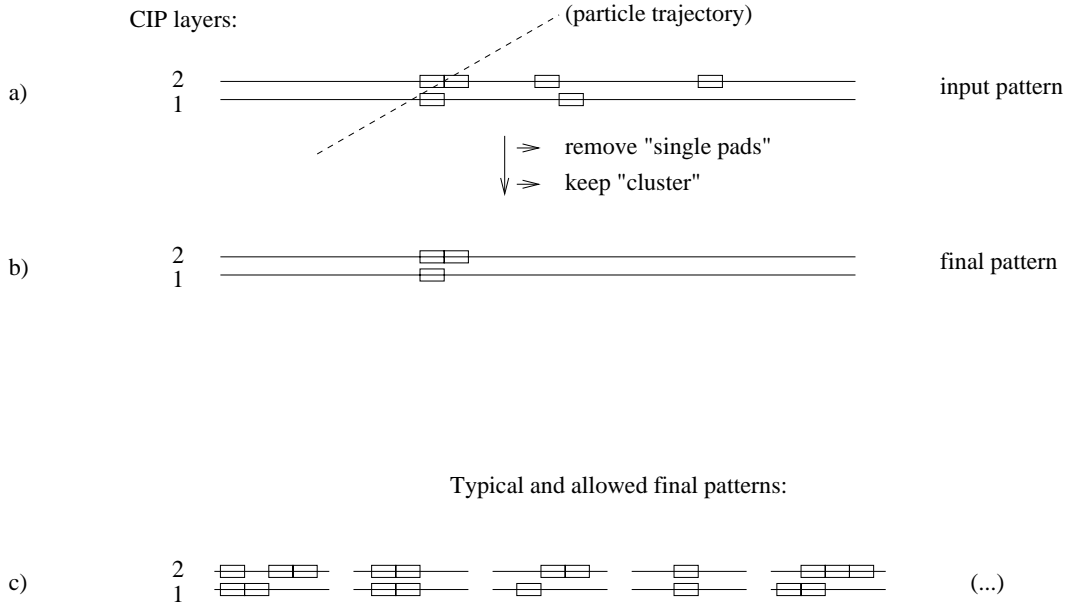


Figure 5.3: CIP pad cluster search algorithm. a) example for an input pad distribution, b) after application of the algorithm. c) a few typical examples for cluster shapes found in the data.

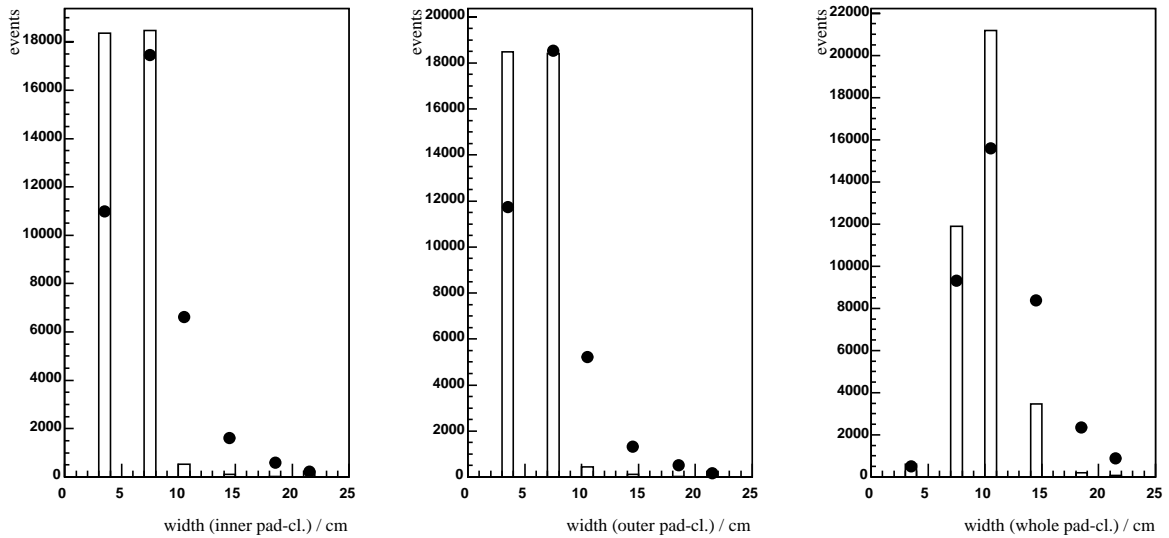


Figure 5.4: CIP pad-cluster widths measured with DIS events for both inner and outer CIP layer (left and middle) and for the whole pad-cluster. Experimental (full dots) and simulated data (histogram) are not normalized w.r.t. each other.

σ_i^{corr} for plane number $i = 1 \dots 4$. BST hits are collected which are the nearest within $3\sigma_i^{\text{corr}}$ around a line defined by the polar angle of the SpaCal cluster. An eccentricity correction is applied for each of these hits accounting for the different oriented axes of BST and beam. If at least two hits are found within the corridor a preliminary validation flag is signalled which enters a next step in which a straight line fit is applied to the hits. The fit assumes for each hit a Gaussian error using the ratio of the deviation to the expected spatial position to the known BST radial resolution of $16 \mu\text{m}$ ([32]). In the last step a new corridor is formed using a fixed width of $300 \mu\text{m}$ and the slope of the fitted straight line. This procedure additionally singles out those hits which do not belong to the particle track due to their large deviation, see also Figure 5.5. The remaining set of hits enters a final re-fitting in which the mentioned BST spatial resolution is used only. This ensures that all selected hits have the same weight in the fit.

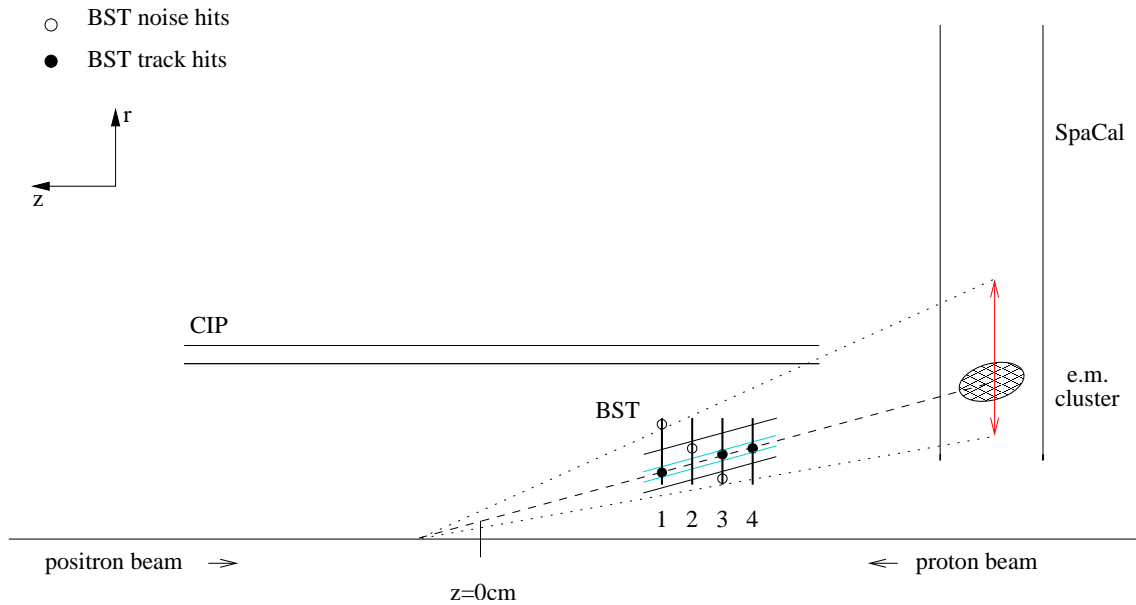


Figure 5.5: Schematic side view of beam axis, BST and SpaCal. The dotted lines and the vertical arrow respectively mark the BST acceptance range for track reconstruction requiring at least two planes to be crossed. The BST silicon planes are shown as vertical lines, numbered from one to four. The traversing parallel lines represent the two corridors used in the two steps of the hit finding algorithm, see text.

In the second case the vertex and the track pointing to a cluster have to be determined from BST information only. The approach is realized by linking each reconstructed BST-hit within the same φ -sector of the e.m. cluster with the cluster position. The algorithm starts with a hit search from the most backward plane near to the SpaCal (plane “4” in Figure 5.5) in order to propagate a straight line towards the vertex region through the remaining BST planes. When a hit was found it is extrapolated onto the next plane using the cluster position, a new hit search is started within a corridor width of $5\sigma_{ij} = \sigma_{r(\text{Cluster})} \Delta z_{ji} / \Delta z_{i,\text{SpaCal}}$, where Δz_{ji} , $\Delta z_{i,\text{SpaCal}}$ are the distances of plane i to j and the distance of plane i to the SpaCal z -position respectively. The energy dependence of the SpaCal spatial resolution is taken into account. As soon as a second BST-hit is found in the corridor in one of the next planes the cluster position can be dropped, such that the continued search for more hits can take advantage of the high BST radial resolution, independent of the cluster position uncertainty. For this reason a constant corridor width of $100 \mu\text{m}$ is used for the subsequent hit search. The result is typically a number of one to three track candidates, which are subjected to further consistency checks (for example not being horizontally oriented). Finally the track with the highest number of

hits is chosen as the best candidate. A straight line fit returns the track slope, polar angle and a solely BST-determined z -vertex position.

5.3 Detection efficiencies

To achieve an equivalent discrimination of electrons and photons in QED Compton in experimental and simulated data, a measurement of the individual subdetector efficiencies is necessary. As will be shown in Chapter 5.8 these efficiencies are especially important for the quality of the particle identification.

The probability for a given Compton cluster to have an associated track signal in one of the tracking subdetectors can be separated into the determination of electron track-efficiencies and photon conversion-probabilities. Since the identity of the two clusters is initially unknown (a consequence of the event selection purely based on calorimetric information) both properties – efficiency and conversion-probability – are treated equally as “*detector-response-probabilities*”. This is justified because a track signal caused either by an electron or a converted photon cannot be distinguished, even if more detailed properties of the signal are used (like number of hits per track, χ^2 of track fit, charge deposition, etc.).

For the determination of response probabilities two data sets are available: a sample of elastic QEDC events (see Chapter 4) and a selected sample from the large set of standard deep inelastic scattering events. Because only the Compton sample contains photons it is indispensable for the measurement of conversion induced detector responses.

The elastic Compton process is characterized by the absence of hadronic final state particles in the backward calorimeter region which can be present in inelastic events. In principle it would be possible to use the elastic sample for efficiency measurements. But considering the very different numbers of available events in both samples, QEDC and DIS, the second one seems much more appropriate for this type of measurement. The same statement holds for the determination of detector noise levels. Alternatively, the use of elastic Compton events for detector efficiency determinations has been realized in [37]. There, the precise calculability of the elastic Compton part is exploited by fixing the efficiency in the data such that the total event rates in data and simulation agree. However, the procedure does not account for the influence of detector noise. This aspect will be included in an independent measurement of the noise level in Section 5.4.1. But before turning to this point and to actual efficiency measurements the following paragraph describes the effect of the photon on detector efficiencies when derived from the Compton sample.

5.3.1 Efficiency in Compton

Using the elastic Compton sample the measurement of the electron track efficiency needs the identity of both SpaCal clusters to be known. The particle identity can be assigned to both clusters by requiring that one cluster has an associated BDC-track (the electron), while the remaining cluster has none (the photon correspondingly):

$$\text{BDC-ID} = \begin{cases} \text{e.m. cluster A : with BDC track link} \\ \text{e.m. cluster B : no BDC track link} \end{cases} \quad (5.1)$$

This section discusses the implications of using the BDC for the definition of a reference event sample with this simple e/γ identification for efficiency measurements on the detectors BST and

CIP. The backward drift chamber is particularly suited because it covers the radial range of the whole backward calorimeter in contrast to BST and CIP which do not offer full acceptance in the polar angle range as covered by the backward calorimeter.

Note that the BDC is placed behind these tracking detectors as seen from the vertex, such that the identification method is appropriate for probing their acceptances and efficiencies as they are within the vertex–BDC volume. Because the condition BDC–ID defines a reference event sample it is not necessary to determine the BDC efficiency at this point (although the assumption $\mathfrak{B}_{\text{BDC}}(r, \varphi) \simeq \text{const}$ is made). A measurement of the BDC efficiency is performed by using DIS electrons (Section 5.3.2).

In the Compton sample the above BDC track/no-track requirement reduces the available (already not very high) statistics considerably, because, as known from earlier analyses, photons traversing the backward region of the H1 detector have a significant probability to convert into e^+e^- pairs (s. also next sections). Therefore, a substantial fraction of electron-photon pairs have an associated BDC-track for *both* clusters due to conversion, such that they are rejected according to the BDC requirement. With the remaining sample of events one can probe how many electrons of all BDC-validated electron-photon pairs have a corresponding track signal in the BST and CIP, respectively.

Assuming that the pure detection efficiency of a *reference* detector is high, *i.e.* close to 100% for a charged particle passing the respective detector (like a drift chamber), such a method can yield in general approximately the electron efficiency of another subdetector probed in the above manner. The reason for the necessity of this assumption is that a very low electron efficiency of the reference detector would also lower the amount of *detected* photon conversions, thus degrading the quality of the e/γ identification. The rate of e/γ misidentification within the BDC-defined sample introduced by conversion of the Compton photon is considered more closely in the following. The calculation is in general applicable to other subdetectors as reference detector as well.

The response probabilities of a chosen reference subdetector are denoted p_e for the electron and p_γ for the photon. Every event can be categorized in one of four possible, separate classes in which either of the particles causes a track signal ($s = “+”$) or not ($s = “-”$). The probability to detect one of the corresponding cases will be denoted as $p^{s_e s_\gamma}$ which is the product of the response probabilities for the electron and the photon:

$$\begin{aligned} p^{+-} &= p_e \bar{p}_\gamma \\ p^{-+} &= \bar{p}_e p_\gamma \\ p^{--} &= \bar{p}_e \bar{p}_\gamma \\ p^{++} &= p_e p_\gamma, \end{aligned} \tag{5.2}$$

where the probabilities to observe no track signals are given as

$$\bar{p}_e = 1 - p_e, \quad \bar{p}_\gamma = 1 - p_\gamma. \tag{5.3}$$

Then the total fraction of events which are selected due to their track/no-track signature is equal to $p^{+-} + p^{-+}$, because the case for p^{-+} cannot be distinguished from the case for p^{+-} using the above identification method. In the case of p^{+-} the particle identities are assigned correctly, whereas the case p^{-+} corresponds to the situation where the electron has no visible track due to some inefficiency, and the photon induced at the same time some charge deposition in the tracking chamber due to conversion within the passive material. The relative contribution ρ_{mis} of misidentified cluster pairs to the total number of selected events in the reference sample is then

$$\rho_{\text{mis}} = \frac{p^{-+}}{p^{+-} + p^{-+}}. \tag{5.4}$$

With an estimated photon conversion rate of $p_\gamma \approx \bar{p}_\gamma \approx 50\%$ which is a typical value for photon trajectories between the vertex and the BDC, these two probabilities nearly cancel out, and therefore:

$$\rho_{\text{mis}} = \frac{1}{\frac{p^{+-}}{p^{-+}} + 1} = \frac{1}{\frac{p_e \bar{p}_\gamma}{\bar{p}_e p_\gamma} + 1} \approx \frac{1}{\frac{\bar{p}_e}{p_e} + 1} = \bar{p}_e. \quad (5.5)$$

This example shows that an average BDC electron track efficiency of 95% translates into a content of mismatched cluster identities for all $e\gamma$ -pairs of the order of 5% in a corresponding reference sample. This uncertainty enters the final electron efficiencies when determined from the Compton sample directly.

To summarize, the strong systematic effect of the BDC identification on the efficiency measurement makes the Compton sample less favourable. For this reason the DIS event selection will be used for the final electron detection efficiency since the result will be, in addition, of much higher statistical significance compared to the Compton case. In DIS it is an advantage that the scattered electron can be easily determined, because its cluster stands out prominently. This is in contrast to QED Compton where the accompanying photon cluster resembles very much the electron in terms of energy and cluster shape, such as for example the transverse dispersion. Thus, the DIS selection is better suited for electron efficiency measurements.

5.3.2 Selection of a DIS event sample

In the last section it was demonstrated that using the Compton sample the difficulty of e/γ separation can clearly affect the quality of an efficiency measurement. A more robust and independent result is achieved by using electrons from a deep inelastic scattering event selection which is described below. For the coverage of conversion effects the use of the Compton sample is still mandatory since only in this event class a photon is present. The influence of ambiguities due to conversion probabilities on the cluster identification will be discussed later in the corresponding sections.

The selection of DIS events is performed by applying the following series of basic criteria on the standard as well as the minimum bias data sets from the luminosity period of 1997. Each event is required to have

- proper hardware conditions (such as high voltage 'on', inclusion in the data acquisition-readout, *medium* or *good* run quality),
- at least one SpaCal electron candidate cluster, using the standard H1 electron-finder program *QESCAT* [45],
- an electron candidate cluster energy of larger than 10 GeV,
- a minimum cluster-beam distance (SpaCal radial position) of > 9 cm.

The preselection results in a total number of about $8 \cdot 10^6$ events of which a varying sub-selection is subject to further conditions on the analysis level. Depending on the required statistical precision every n^{th} event ($n = 5, 10$ or 20) of the original data set is selected (also for reasons of data handling performance). These conditions require

- a minimum electron candidate energy E_e of 15 GeV,
- a reconstructed event vertex $|z| < 35$ cm, with a vertex error $\Delta z < 0.5$ cm,

- a cut on the remaining energy in the calorimeter: $|E_e - E_{e.m.}| < 1 \text{ GeV}$,
- $E_{\text{had}} < 0.4 \text{ GeV}$,
- a limited amount of e.m. or hadronic energy within some isolation cone,
- energy-momentum balance $45 \text{ GeV} < E - p_z < 65 \text{ GeV}$,
- a SpaCal veto cell energy below 1 GeV (if present),
- a maximum transverse cluster dispersion of below 4 cm,

where $E_{e.m.}$ and E_{had} correspond to the total energy deposited in the electromagnetic and hadronic part of SpaCal. The cuts related to these energies ensure that there is only one large energy deposition in the e.m. section and only a small leakage of electron energy into the hadronic section. The $(E - p_z)$ -cut is imposed to suppress background events in which not all particles are contained in the detector, most important photoproduction events where the electron escapes along the beampipe. The following sections discuss subdetector stability, acceptance and efficiency using the described selection of DIS events.

5.3.3 BST stability and efficiency

Since the Backward Silicon Tracker covers the high polar angle region into which most of the Compton electrons and photons are scattered, a good knowledge of the efficiency of this detector is mandatory. As a first step the event rate is monitored over the whole data set versus run/fill number without any run restrictions. For this purpose the event rate is defined as the number of BST track validated electrons divided by the number of electron candidate events, both accumulated over constant intervals of run or luminosity fill numbers respectively. Events fulfilling the DIS selection criteria are used for this procedure (Section 5.3.2). An event satisfies the BST-validation if

- the track validation flag was set 'active' by the BST reconstruction program
- the reconstructed track lies within BST acceptance
- the radial distance between the reconstructed track and the center of the e.m. cluster is below 1 cm, as measured after back-extrapolation of the track to the SpaCal plane.

A particle is considered to be within acceptance if its track traverses the two inner BST planes. This case is tested geometrically by a projection of the SpaCal cluster position onto the BST planes as seen from the well defined vertex position of deep inelastic scattering events. Thus, by requiring that the BST track has a distance to the z -axis of

- r_{track} greater than 5 cm at z_2 (second BST plane)
- r_{track} lower than 12 cm at z_3 (third BST plane),

it is ensured that each of at least three planes can produce a hit signal for the event vertex range of interest (for plane numbering see Figure 5.5). Also more relaxed or restrictive conditions could be applied by allowing a trajectory to cross 'any two neighbouring planes' or to force it to cross 'all four planes'. The chosen condition above was found to be a reasonable compromise between sufficient safety against too high noise contributions ('any-2-planes') and too low statistics ('all-planes'). The

last point has to be considered especially in the view of the low overall statistics of the Compton sample.

To extract the acceptance range the radial position of the cluster is used as a parameter which is measured in the (x, y) -plane of the backward calorimeter. Since this radial position (for some given values of the event kinematics) depends on the vertex position a comparison between different acceptance ranges is made. For this purpose the vertex is chosen to be located predominantly at high, medium or low z -positions, *i.e.* the vertex position is restricted to $z = (20, 0, -20) \pm 5$ cm. The probability, in DIS data and Monte Carlo events, to find an active acceptance flag for a radial cluster position r is shown in Figure 5.6 separately for the three different vertex regions. Both event sets appear in good agreement with some discrepancies at very low radii r .

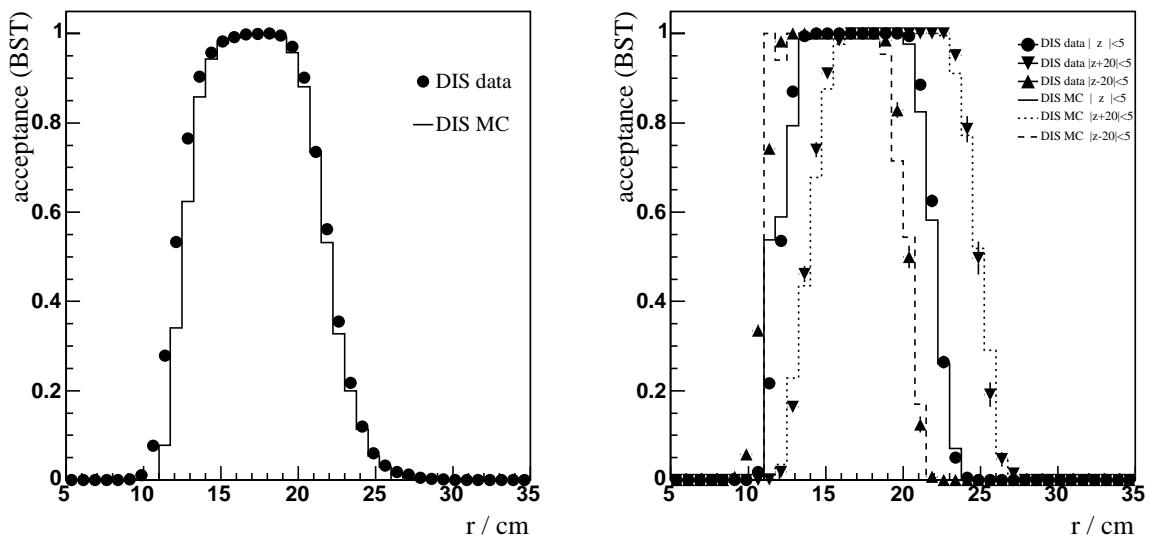


Figure 5.6: *BST* acceptance as a function of *SpaCal* radial position of *DIS* electron clusters, left: for all vertices, right: for three different vertex ranges. Curves from left to right in the right histogram: $z = (20, 0, -20) \pm 5$ cm.

Inspecting the whole available range of the 1997 run set one can observe several periods with a lower rate of *BST* validated electrons compared to the otherwise higher plateau level of around 90% in average, as shown Figure 5.7. In a further step all those runs are excluded from the data sample which belong to a commonly unused set of runs and run ranges for the H1 data taking period in 1997, s. Section 4.2.1 and [46]. Different reasons have been identified for those low quality runs which do not only concern instabilities of the *BST* but also of other components. A list of this set of rejected runs is given in the appendix. However, the resulting new validation rate changes only slightly with these additional run restrictions.

5.3.4 *BST* hit bank loss

A closer look during the first analysis phase revealed that a big difference was visible between the experimental and simulated *BST* acceptance as function of the electron radial position in *SpaCal*. The corresponding acceptance flag was taken in this case directly from the output of the reconstruction

code. The reason for the unexpected high difference was that a BST hit bank was missing in some fraction of the events in the experimental data. Due to its internal structure the BST reconstruction program [32] caused the acceptance flag to be left unset. Since the hit bank represents a fundamental input to the track reconstruction code run periods of data readout problems – especially coherent losses – can be detected this way just by monitoring the bank loss rate. The method can be regarded as a sensitive tool because the readout data of a silicon tracking device, such as the BST, with many thousand channels should always contain at least a few noise hits in each event such that there always should be a regular hit bank.

By a small code change the flag was constructed as to indicate, whether the hit bank was missing or not during event preselection. The rate of occurrence of this special flag value, again relative to the number of DIS electron candidates per run range, is shown in Figure 5.8. The external acceptance is required to be fulfilled for this test by using the known DIS central z -vertex position and by selecting only very well localized vertices (see above). The histogram shows an extended luminosity fill range with high loss rates or for some smaller ranges even complete loss.

These losses are directly correlated to drops and gaps in the BST stability as a function of time, as displayed in Figure 5.7. For an improved run selection those luminosity fills are discarded for the further analysis in which the hit bank loss rate is above 2.5%. The final total remaining loss rate is $\approx (0.7 \pm 1)\%$, averaged over the whole run range.

The stability curve shows that not all of its variations can be explained with missing hit banks. For example, the stability shows a reduced level between the luminosity fill numbers 1390...1430, but there is neither a visible counterpart in the hit bank loss-rates nor in the noise-rates (for its measurement see Section 5.4 and 5.5, respectively). In order to avoid a too high quality degradation of the analysed data samples due to periods of a low or varying stability an additional cut is imposed on the data, requiring the stability rate to be greater than 84%. As a consequence the mentioned fill-number range is not accepted anymore for the further analysis. But also very few periods with exceptionally high validation rates above 99% (*i.e.* significantly above the plateau) are excluded as there is no reason for such high values except low bin entry numbers.

Figure 5.9 displays the total BST efficiency as measured with the DIS event selection versus the radial position of the corresponding SpaCal cluster. The histograms show that the simulated efficiency is significantly above the experimental numbers. In the medium r -range of the data distribution the mean ε is slightly below 90%. This can be expected from and is in accord with the estimated average of the stability curve of Figure 5.7 after all low quality periods have been cut out.

The efficiency distribution at its lower and upper end is dominated by a decreasing acceptance (see Figure 5.6). Because the histogram shows only mean values in r , possible azimuthal efficiency variations of the BST were checked as well. In fact, the result of this test showed that there are large differences among the 16 azimuthal sections of the BST. The corresponding numbers and their application in a MC resimulation are presented in Section 5.5 together with the results of sector-wise noise measurements.

5.3.5 CIP efficiency

The CIP layers are tested for possible unstable periods by a procedure analogous to the BST. Deeply inelastic scattered electrons are considered as to be in CIP acceptance if the line between vertex and cluster center crosses both layers at a z -coordinate of greater than $z = -112.5$ cm. The acceptance is displayed as function of the SpaCal cluster radius in Figure 5.10, again for the full vertex range as well as for three different vertex sub-ranges. A small acceptance variation is observed using different vertex ranges and there is a good agreement between the experimental data and the simulation.

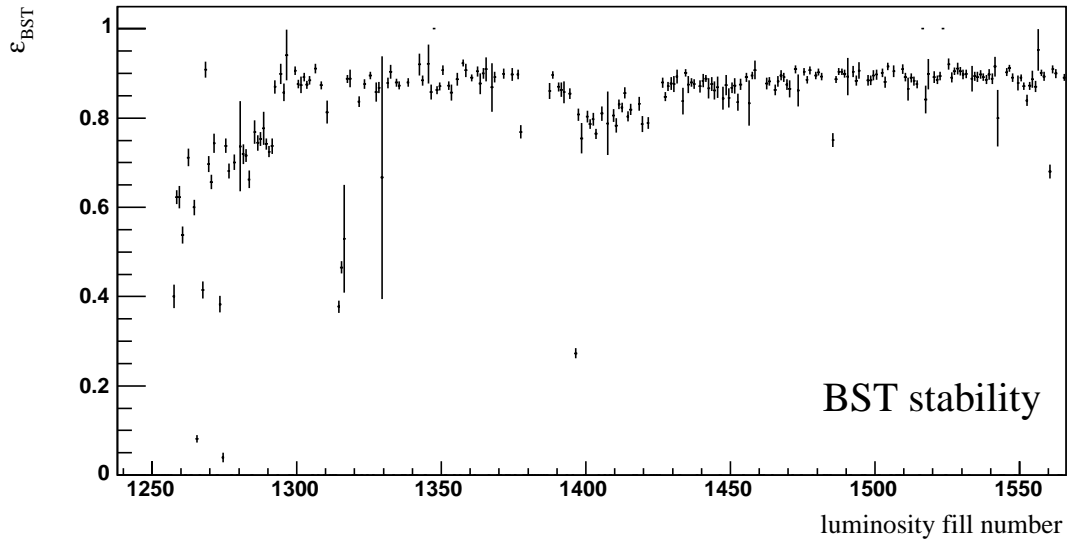


Figure 5.7: *BST validation rate of DIS electrons versus luminosity fill number in 1997, displaying stability changes over time. Only stable phases contribute to the final selection; periods like fill number ranges up to 1290 are deselected for the further analysis. The period at the beginning shows correlations with the hit bank loss rate shown in Figure 5.8.*

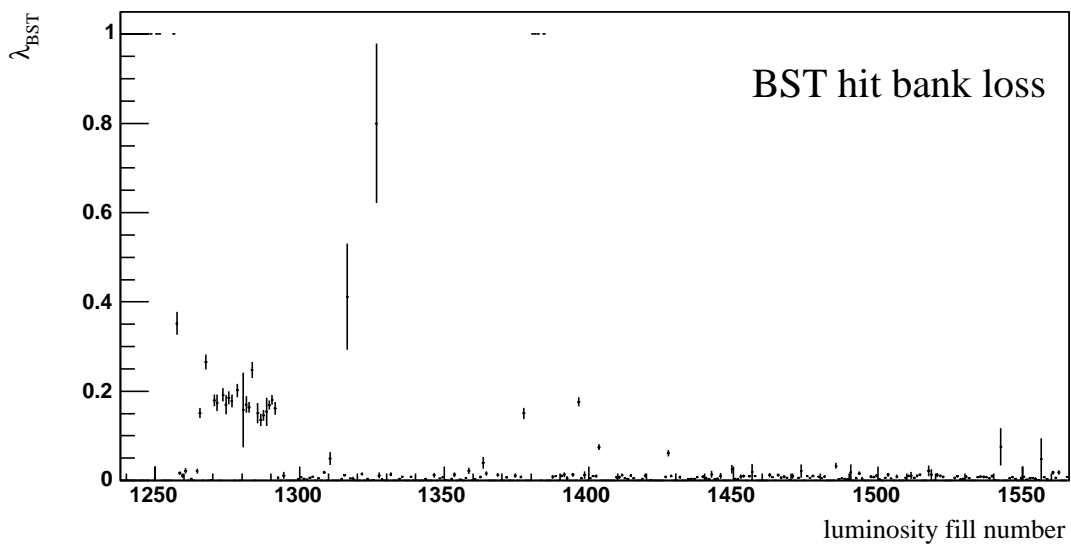


Figure 5.8: *Relative rate of BST hit bank loss, λ_{BST} versus luminosity fill number in 1997. Periods of increased loss rates are used for the definition of the final data run selection.*

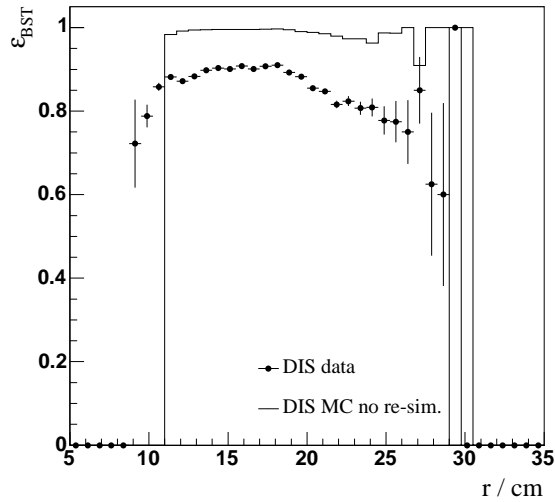


Figure 5.9: *BST* efficiency as function of radial position of the DIS electron in SpaCal. Dots: DIS data, full histogram: DIS Monte Carlo. In the radius range higher than 25 cm acceptance effects dominate and ε becomes unreliable. The high MC-levels in this range have no meaning.

The stability is measured as the probability to find a CIP pad-cluster pointing from the SpaCal cluster to the allowed z -vertex range. The corresponding histogram is displayed in Figure 5.11. The plot demonstrates a stable overall performance of the CIP chamber during the whole data taking period. Only in a very small number of luminosity fills the measured stability rate is identical to 1. As these high rates could be associated to noisy periods they are excluded from the further analysis. Finally, Figure 5.12 shows the CIP efficiency for DIS electrons measured as a function of the SpaCal radial position.

However, a detailed inspection of the CIP efficiency along the chamber's z -coordinate showed that there is also a variation among the pads' individual efficiencies. Especially in the region $z \approx -40$ cm both CIP layers show exceptionally low efficiencies, plotted in Figure 5.13 once versus pad number and once versus the barycenter of the reconstructed pad-cluster. In these distributions a sharply restricted z -vertex error turned out to be mandatory in order to establish reliable efficiency values. Again, this is due to the predominantly flat crossing angle of the electron track w.r.t. the planes of the pads. Small uncertainties of the measured vertex position or of the SpaCal cluster position are sufficient to shift the calculated crossing point on the CIP surface and thus the assigned reference pad position. Therefore, also the position of the associated BDC track had to be used instead of the comparatively worse defined SpaCal cluster barycenter.

The most outstanding feature of the efficiency is a drop observed at around $z \approx -40$ cm. It is *not* described by the original Monte Carlo simulation where a uniform pad efficiency is observed. (Figure 5.13 uses a resimulation of this MC which is described below.) In fact, the true detailed chamber geometry and material is not exactly accounted for in the detector simulation: In the original standard simulation the electronic responses of the pads were imitated by artificially varying the thresholds for input signals in different areas of the CIP. Such a procedure brought the simulated efficiencies into agreement with the experimental data available at that time [52, 53]. These studies focussed on much steeper crossing angles of particle tracks w.r.t. the CIP pads. This could be one reason for the differences between data and simulation found in the present analysis.

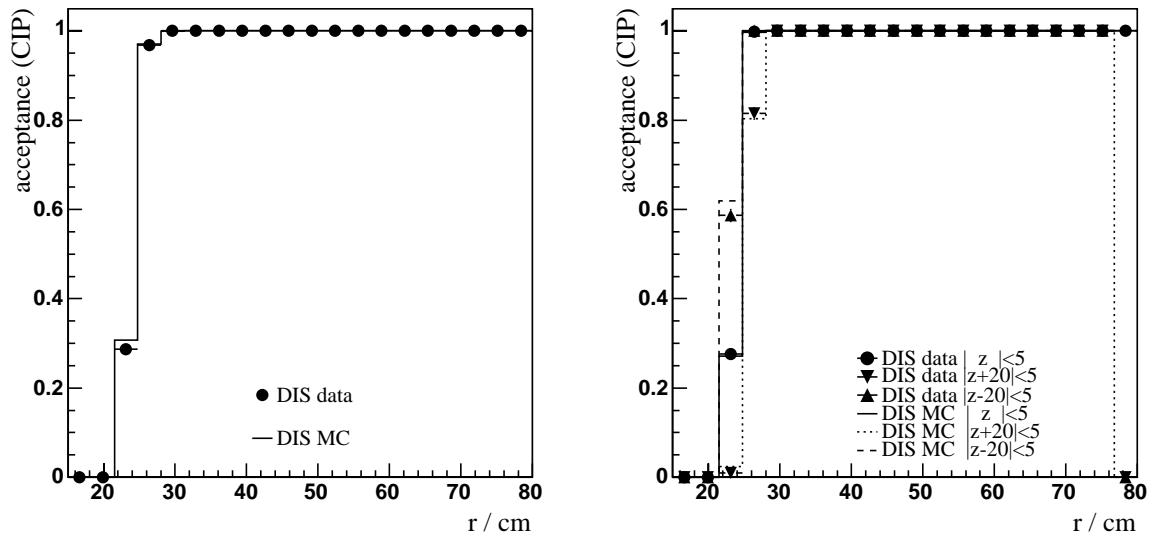


Figure 5.10: CIP acceptance as function of the SpaCal radial position of the electron cluster candidate. Above the transition range the acceptance is fulfilled for each cluster position in data and MC. Right: acceptance under variation of the vertex range.

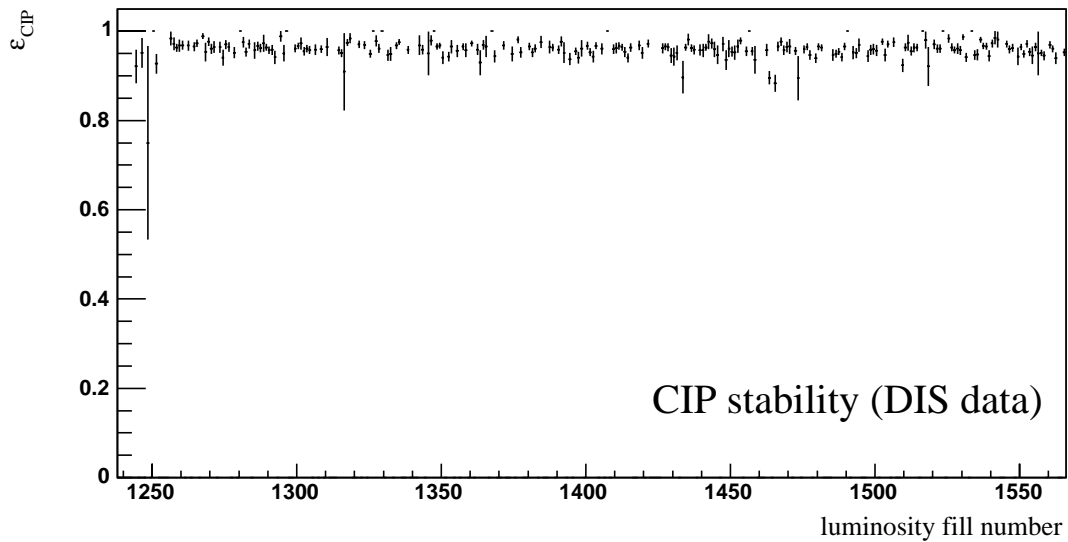


Figure 5.11: CIP validation rate of DIS electrons versus luminosity fill number in 1997, displaying stability changes over time.

An explanation for the observed efficiency drop could be the CIP structure comprising *wire supports* in between two pad pairs with the numbers “19/20” and “39/40”, respectively, s. Figure 3.6. The numbering starts with “0” as the first pad on the $-z$ -end side of the chamber. The wire supports are made out of a combination of the materials Araldit and Stesalit, shaped in a small block of about 5 mm width in z . These blocks separate the pads at the positional numbers given above and they support the anode wires [54]. This means that the wire support at the first pad pair (19/20) could affect the electric field shape, charge distributions and by that the charge detection at this position of the chamber. The efficiency loss as measured in [53] is comparable to the drop visible in Figure 5.13.

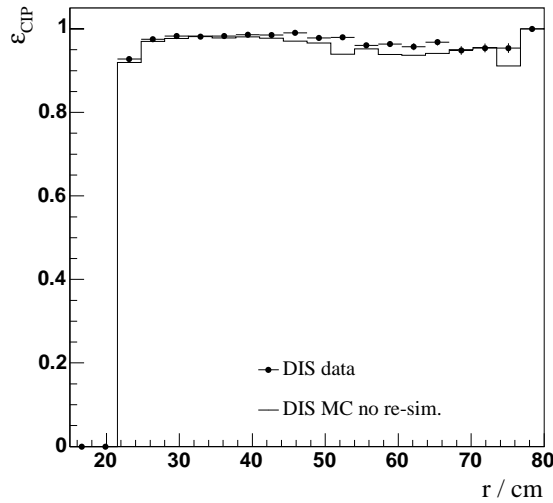


Figure 5.12: CIP efficiency as function of the SpaCal radial position of the electron cluster candidate.

Correlated efficiencies

This previous finding leads to an investigation on *correlated efficiencies* between pads adjacent in the z -coordinate. The method is to ask for one active pad before one adjacent pad is tested for its signal probability (or its efficiency). The correlated efficiencies $\kappa_{i\pm 1,i}$ are defined as

$$\text{if pad } i - 1 \text{ active, then : } \quad \kappa_{i-1,i} = \begin{cases} 1 & \text{if pad } i \text{ active} \\ 0 & \text{if pad } i \text{ inactive} \end{cases} \quad (5.6)$$

$$\text{if pad } i + 1 \text{ active, then : } \quad \kappa_{i+1,i} = \begin{cases} 1 & \text{if pad } i \text{ active} \\ 0 & \text{if pad } i \text{ inactive} \end{cases} \quad (5.7)$$

The averaged rates of $\kappa_{i\pm 1,i}$ are histogrammed for each layer in Figure 5.14. In both cases a straight line, given by a precise vertex position and a BDC-track, is required to cross the pad with the positional number i . The event is used for the efficiency measurement if either pad $i - 1$ or pad $i + 1$ is active. If this is the case pad i is probed whether it was active or not. The result (0 or 1) yields the event’s contribution to the (averaged) κ . In this way a sensitive test is performed on differences in correlated pad activity in data and MC, which is *independent* of the different mean pad-cluster widths in data and MC; refer again to Section 5.2.3 or Figure 5.4. A sharp efficiency drop of pad number 19

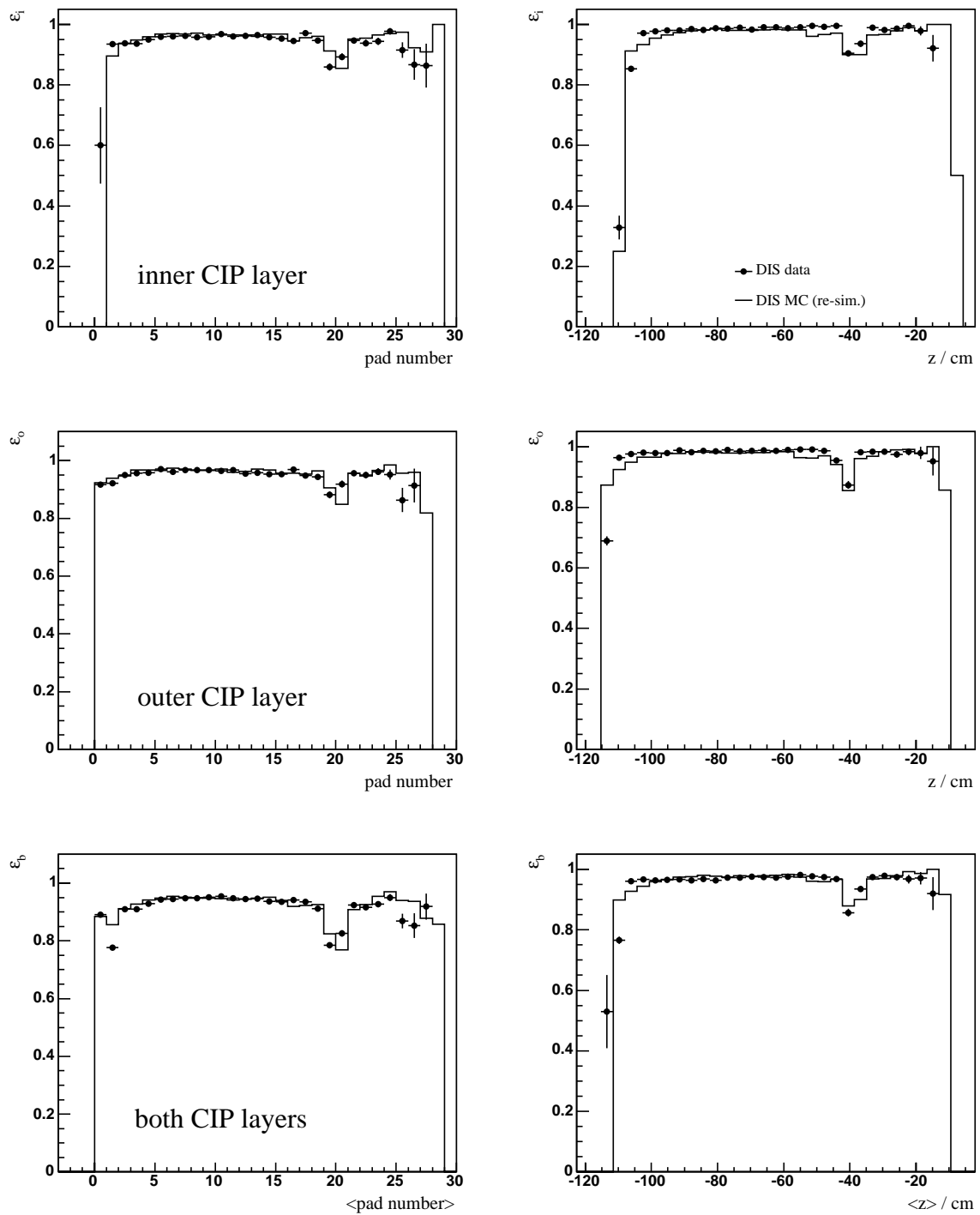


Figure 5.13: CIP efficiency as function of pad number (histograms left column) and pad-cluster barycenter in z (right column) corresponding to the position where the DIS electron trajectory crosses the CIP surface. Pad numbers are counted from the negative chamber end starting with number 0. The behaviour of individual CIP pads has been resimulated after the standard simulation to match the data efficiency drop around pad 20.

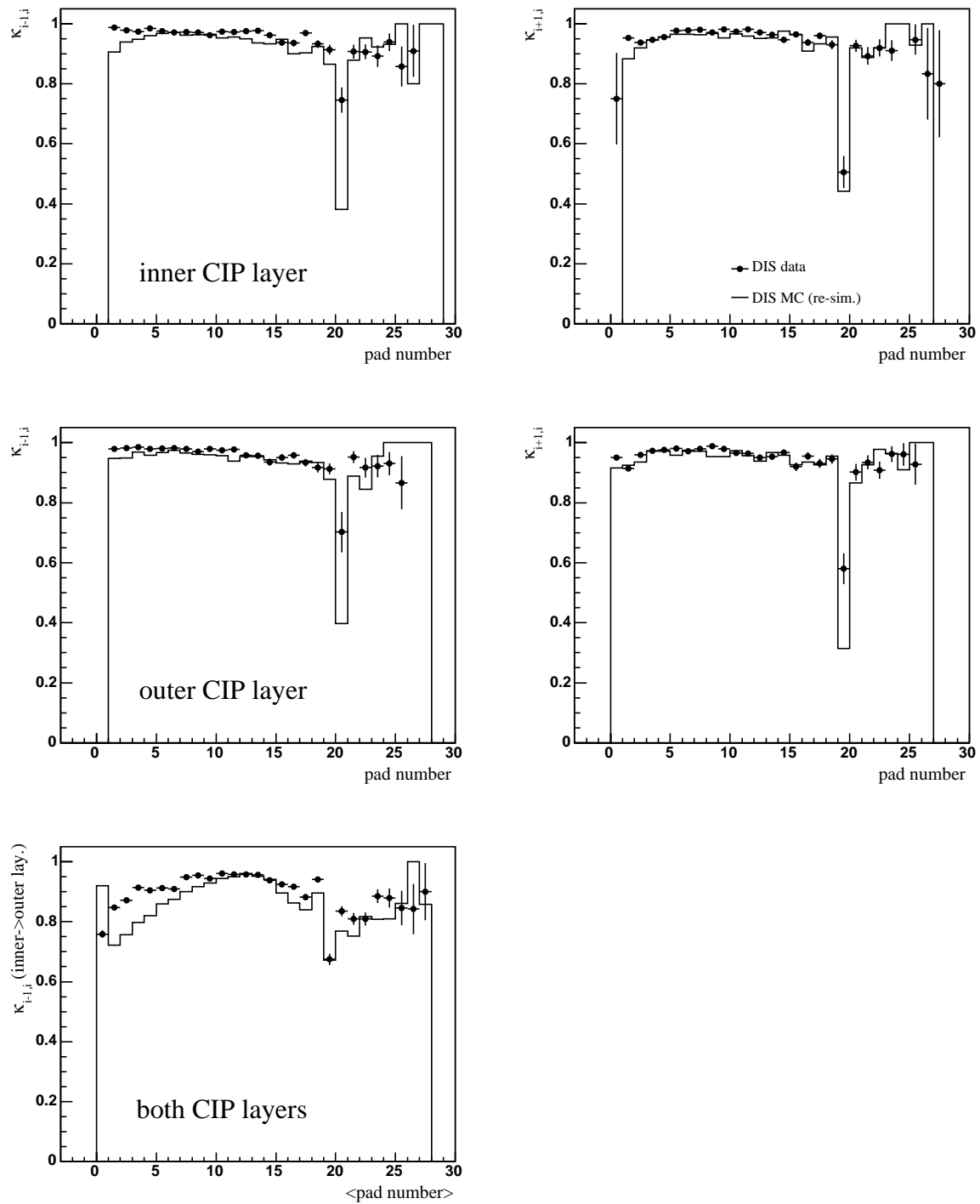


Figure 5.14: Correlated CIP pad efficiencies as function of pad number corresponding to the position where the DIS electron trajectory crosses the CIP surface (explanation see text). Pad numbers are counted from the negative chamber end starting with number 0. Individual CIP pad efficiencies have been resimulated in the MC.

is observed for $\kappa_{i-1,i}$ down to values of 50. . .60%, and also a smaller but still significant reduction is present in pad number 20 for $\kappa_{i+1,i}$. This result demonstrates again that the wire support material effectively reduces activity correlation between these pads.

In order to achieve the same result for the Monte Carlo a resimulation has to be performed on the analysis level applying the measured correlation values for $i_{\text{pad}} = 19, 20$. For this purpose the generated and, thus, exact particle track vector is taken from event generator information (stored in parallel with the reconstructed event variables) and it is extrapolated precisely to the CIP surface. In this calculation the linear system $\vec{r}_{\text{CIP}} = \vec{v} + \lambda \cdot \vec{u}_e$ has to be solved for the parameter λ , where the simulated vertex position \vec{v} and the unity vector \vec{u}_e of the electron momentum are used. \vec{r}_{CIP} is constrained to point onto the CIP surface using the respective CIP radius. The vertex (x, y) -components (0.3 and 0.4 cm) cannot be neglected but have to be included in \vec{v} .

Provided the track crosses the volume of the wire support block within its z -width of 5 mm, the signal of the pad being traversed by the particle is set to *inactive* in the simulation. In fact, this treatment effectuates a similar pad- and pad-cluster-efficiency in data and Monte Carlo. But still some differences remain especially for the correlated efficiency of pad number 20.

5.3.6 BDC efficiency

The whole radial range of the BDC can be regarded as acceptance area. The active drift cell volume of the chamber begins at the inner radius of 6.3 cm which is well below the BST radial acceptance essential for the vertex determination and particle identification in this analysis. The outer radius ends at 71 cm by which the full backward calorimeter front side is covered. Again, the DIS event selection serves as input to this efficiency measurement. For this purpose it is tested whether a BDC track element has been reconstructed as a link between the vertex and the cluster in the backward calorimeter. As an essential track property it is required that

$$N_{\text{hits,BDC}} \geq 4 \quad (\text{condition 1})$$

associated track hits, out of eight at maximum, are found in one track link. These data are taken from the reconstruction program BDCLEV (Section 5.2.1). In addition, in an alternative cut the minimum hit number has been raised to tighten the condition:

$$N_{\text{hits,BDC}} \geq 6 \quad (\text{condition 2}) .$$

The result of both tests is displayed in Figure 5.15. The comparison shows that the weaker condition gives a high and quite smooth efficiency distribution, while the second condition suffers a strong discontinuous shape ranging around $r = 24. . .32$ cm. In addition, for the outer position radii a 10% efficiency reduction is observed compared to the inner drift cells. For these reasons the first condition is chosen for all further measurements. With this criterion only around $r = 25$ cm a small deviation between data and Monte Carlo remains which is attributed to the problems related to the transition cell as discussed in Section 5.2.1. The stability is monitored in Figure 5.16, it demonstrates a steady overall performance.

5.4 Electronic noise

Subdetector noise can have different sources such as cross-talk from the diverse surrounding electronic components, especially in the very first stages of the signal path. It can also be induced by the

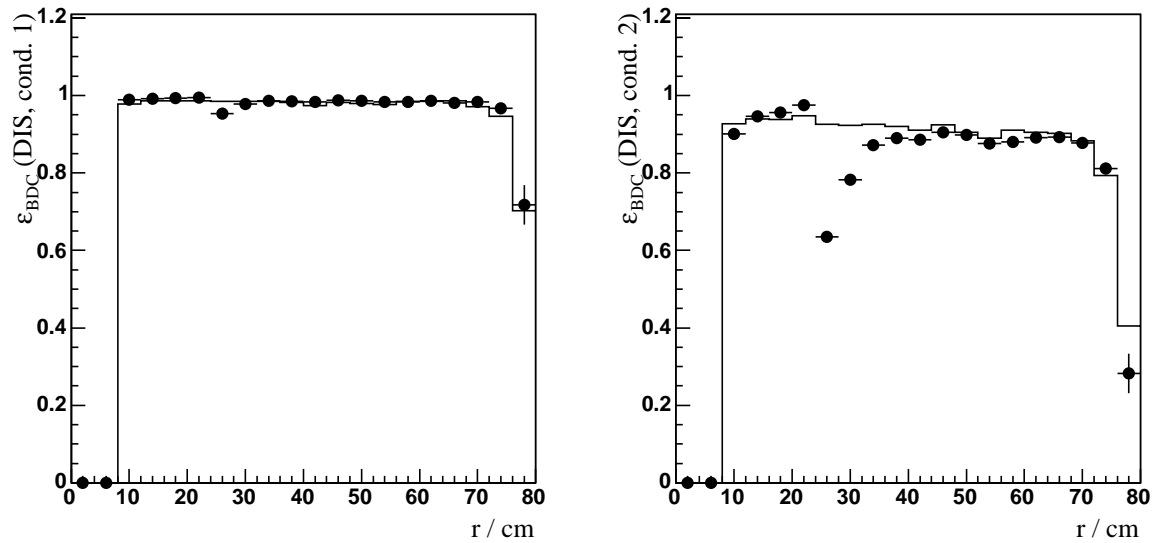


Figure 5.15: BDC efficiency measured versus radial position r in SpaCal using DIS electrons. Left: with “ ≥ 4 hit” condition, right: with “ \geq hit 6” condition. A strong efficiency drop is observed in the range of the BDC transition cell at $r = 25$ cm.

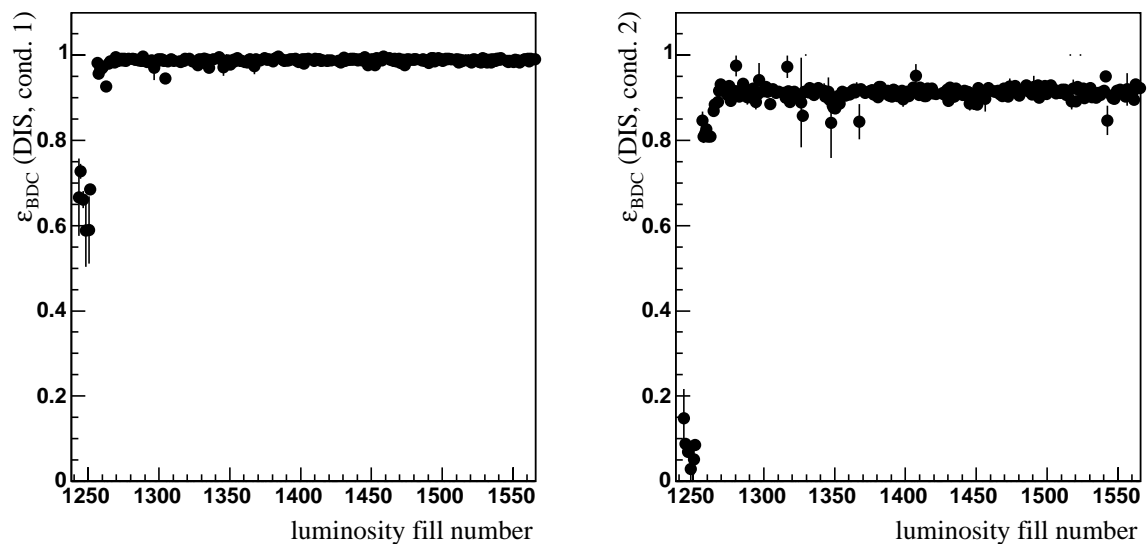


Figure 5.16: BDC stability measured versus run number during the 1997 data taking. Left: “ ≥ 4 hit” condition, right: “ \geq hit 6” condition. The low values during the start-up phase are caused by usual chamber instabilities which can be caused by high voltage, gas-mixture or data readout problems.

subdetector’s own amplifiers due to electronic noise or possible instabilities of the supply voltages. In fact, during the last one and a half years of the BDC operation (ending with data taking of 2000) several failures of the chamber’s power supplies were discovered. The consequence was in most of the cases a 50 Hz noise on the low voltage power lines due to thermal overload of capacitors and the appendant rectifiers. These signals overlaid directly quasi as “common mode”-noise to all readout channels of the corresponding double layer modules, *i.e.* a quarter of all readout channels (one channel is understood as one wire in the digital readout branch or a set of eight wires in the analog readout branch, see Section 3.2.3). The effect was clearly visible in the low level data quality diagrams (“L4-histograms”), regularly checked during the data taking, such as in overall channel maps where large groups of channels faked increased numbers of hit entries. Also for the other relevant subdetectors periods of increased noise level occurred, *e.g.* in the beginning of the 1997 data taking period for the BST including coherent noise effects.

5.4.1 Noise measurement

Besides the exclusion of known low-quality runs as assigned by subdetectors experts and analysis groups, a separate test for possible noise affecting this analysis has been carried out. Again, the high statistics DIS event selection over the whole standard 1997 data set has been used for this purpose. The method of the noise level determination is realized by constructing a new artificial cluster-position different from the original high energy DIS electron e.m. cluster. Then this position is transferred to the standard search for tracks and active-pads (CIP). These data are stored in parallel to the first selected DIS electron as it would be the case for a real second cluster. Any track- or hit-signals which are recorded for this pseudo-cluster, for which no signal is expected, are interpreted as an effect of any kind of noise source. This principle is applied to all relevant subdetectors of the Compton analysis.

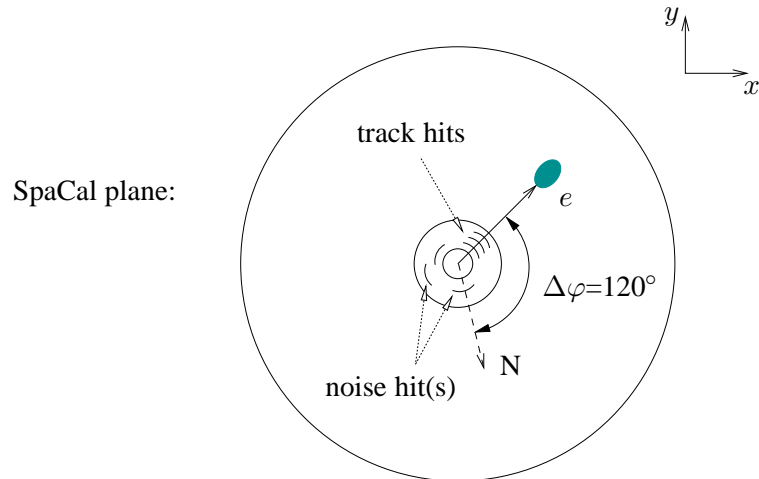


Figure 5.17: Principle of the noise measurement: the position of a DIS electron in the SpaCal azimuthal plane is rotated by 120° in order to obtain a new artificial cluster position “N”. The new coordinates define the reference position from which track signals are searched for. Regular track hits of a BST electron as well as noise hits are indicated as segmented arcs in this radial view.

The new position N of the virtual cluster is defined by a rotation of the DIS electron coordinates around the z -axis by

$$\Delta\varphi = 120^\circ,$$

while the original electron polar angle is kept. The shift in azimuth is chosen high enough in order to avoid possible overlap with track signals caused by the true electron along its trajectory. This could be the case, for example, due to the large angles covered in azimuth by a subdetector's φ -segmentation. This is especially important for the CIP, while the BDC is less concerned in this context since tracks can be reconstructed with a φ -resolution much better compared to the size of azimuthal segmentation.

Secondly, the azimuthal shift was set to a value different from 180° to avoid signal detection in spurious back-to-back topologies, such as for example in a Compton event which – because of its similar calorimetric appearance with a high energetic cluster – could still enter the DIS sample. Such a possibility is already suppressed by the DIS event selection implying that only a very small calorimetric energy is permitted besides the actual electron candidate.

The result of this study is shown in Figure 5.18 for the relevant subdetectors. There is an increased noise level for the BST in the first run number range (up to 184000) of the order of 20%. For the remaining data set a lower plateau of 5% is visible. The CIP noise is of the order of 2-3% at maximum. For the BDC the discussed method cannot be applied for noise level measurements. The reason for this is the complex structure of the cluster finder program (*QESCAT*) which requires a true reconstructed SpaCal cluster. A corresponding procedure would require major program code modifications in order to let it accept the parameters of a user-defined artificial cluster.

5.5 Application to Monte Carlo

The measured subdetector properties are now implemented to resimulate the existing Monte Carlo event by event. Technically this is achieved by using a set of boolean variables which represent track signal *flags* assigned to each of the e.m. cluster candidates. The flags are initially set according to the reconstructed subdetector signals depending on whether a track- or pad-cluster signal has been detected or not. For experimental and simulated data the values for all flags are determined from the same set of reconstructed variables which passed the same calculations of the analysis chain. The raw signal flag $S_{d,0}^i$, produced from a subdetector d and assigned to a SpaCal cluster i , is set to the boolean value TRUE if the particle is regarded as electron-like, *i.e.* if a track signature was found. This can occur for both a true electron or a converted photon. If there is no such signal the flag default value FALSE is kept. In simulated events these signal flags are overwritten by new random (boolean) variables which are generated according to the measured differences between data and simulation. The calculation of the probabilities which are fed in to software random generators producing the random variables is described in this section.

For the BST and the CIP different procedures have to be applied. While the BST reconstruction returns fixed, geometrical tracks, the CIP response is made up of a list of active pads, which are combined to pad-clusters only in a late phase of the analysis chain. At this point BST tracks cannot be modified anymore without going back to the “hit level”. Thus, to account for some inefficiency a given BST track validation is negated, whereas single CIP pads are marked randomly as inactive *before* the pad-cluster formation takes place. The opposite, namely switching the track signal flag to TRUE, is applied to resimulate the effect of detector noise.

The complete resimulation of the original track signal $S_{d,0}^i$ for a cluster i can be written in the boolean equation

$$S_d^i = S_{d,0}^i \wedge E_d^i \vee \bar{S}_{d,0}^i \wedge N_d^i \quad (5.8)$$

where E_d^i and N_d^i represent the random flag variables for efficiency and noise, having the default values TRUE and FALSE, respectively. In the case of the BST the variations of the azimuthal efficiency

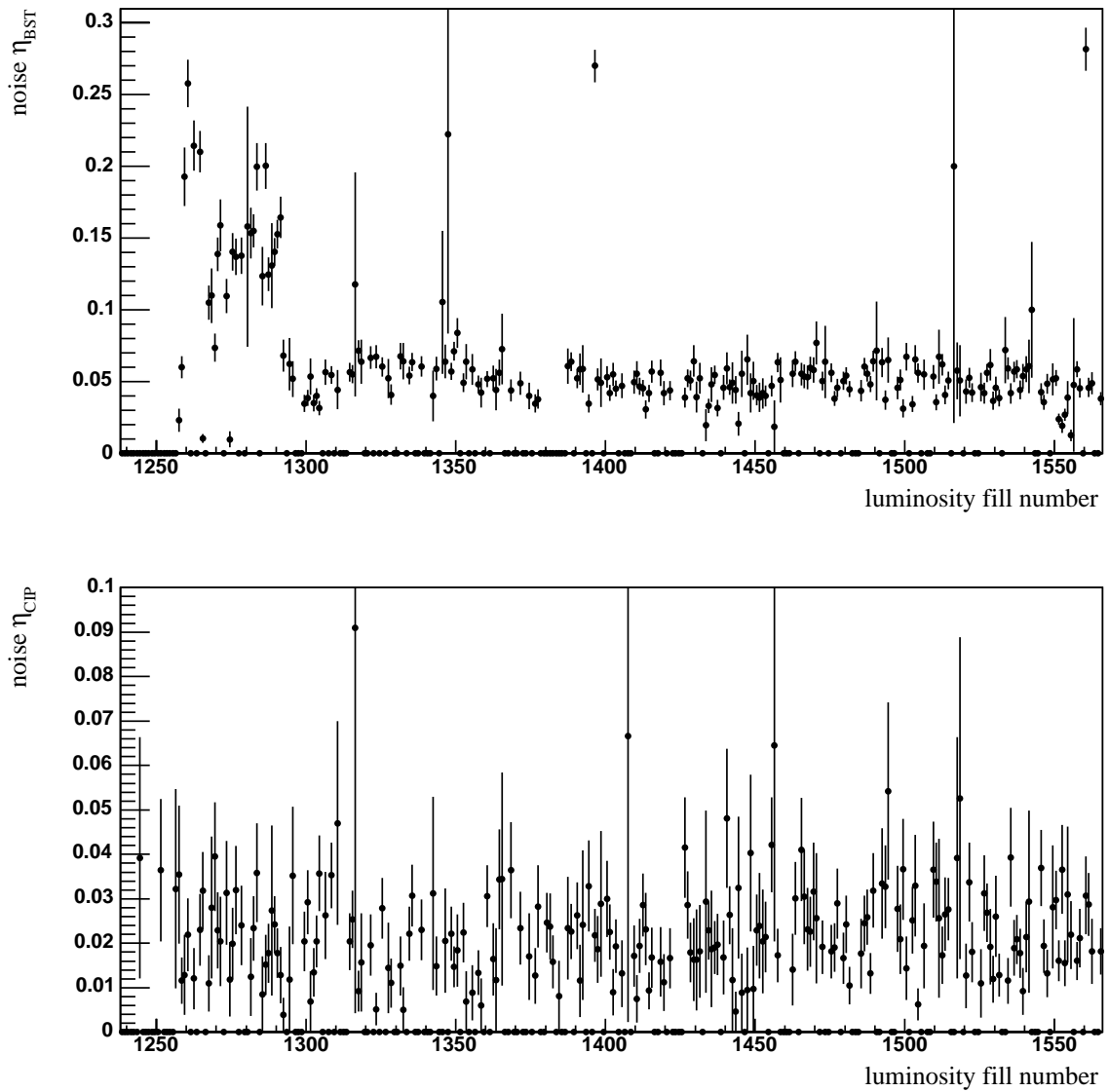


Figure 5.18: Total noise rates for the subdetectors *BST* (upper plot) and *CIP* (lower plot) as a function of luminosity fill number in the year 1997. The *BST* noise diagram reveals strong peaks and bursts at low fill numbers and otherwise a nearly constant level of 5%. The *CIP* shows a constant behaviour over the whole period.

values are resimulated according to the efficiency $\varepsilon(\varphi_i)$, where the argument φ_i is taken from the original calorimeter coordinates of cluster i .

According to Eq. 5.8 a subdetector signal $S_{d,0} = \text{TRUE}$ appears in the effective signal S_d as FALSE if the efficiency flag E_d is reset. The probability for setting E_d randomly to FALSE, accounting for the different measured efficiencies ε in data and MC, is calculated like:

$$p_{E \rightarrow \text{FALSE}} = 1 - \frac{\varepsilon_{\text{data}}}{\varepsilon_{\text{MC}}} . \quad (5.9)$$

On the contrary, when $S_{d,0}$ is FALSE, *i.e.* if no track was reconstructed, noise could still contribute by generating $N = \text{TRUE}$. N is randomly switched into the active state with a probability determined by the measured noise probabilities η as

$$p_{N \rightarrow \text{TRUE}} = 1 - \frac{1 - \eta_{\text{data}}}{1 - \eta_{\text{MC}}} . \quad (5.10)$$

In this case an artificial track is created which points on the z -axis to a random value z_{Noise} in the nominal z -vertex range. The z_{Noise} of these generated tracks have a flat distribution.

In Figures 5.21 and 5.22 the Monte Carlo values of ε_{BST} and η_{BST} before and after the resimulation are displayed together with the experimental values for each BST φ -sector in DIS events. The plots illustrate for the experimental data the distinct efficiency changes from sector to sector as well as the varying amounts of noise. The measurements suggest that there is no obvious correlation between sector-wise changes in inefficiency and noise.

The corresponding measurements for the CIP did not reveal any large azimuthal variations. Therefore, the small inefficiency difference between data and Monte Carlo was accounted for in the resimulation by a global probability-factor applied independently of geometrical parameters. The CIP efficiency drop of the CIP pads “19/20” was discussed earlier in Section 5.3.5; the inefficiencies are corrected according to the above equations. A summary of the overall noise rates for BST and CIP with and without resimulation are shown in Figure 5.19. The BST sector-wise efficiencies during the data taking are presented in Figure 5.20.

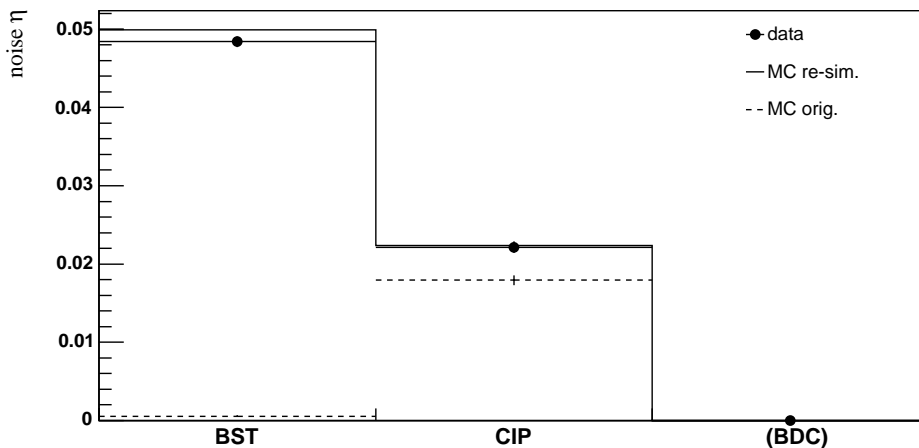


Figure 5.19: Total noise rates for the three tracking detectors, determined from the DIS event selection. Only for the BST the noise has to be added in a MC resimulation. The method of the noise measurement (see text) cannot be applied in the case of the BDC. The dashed histogram indicates the noise generated by the original standard simulation.

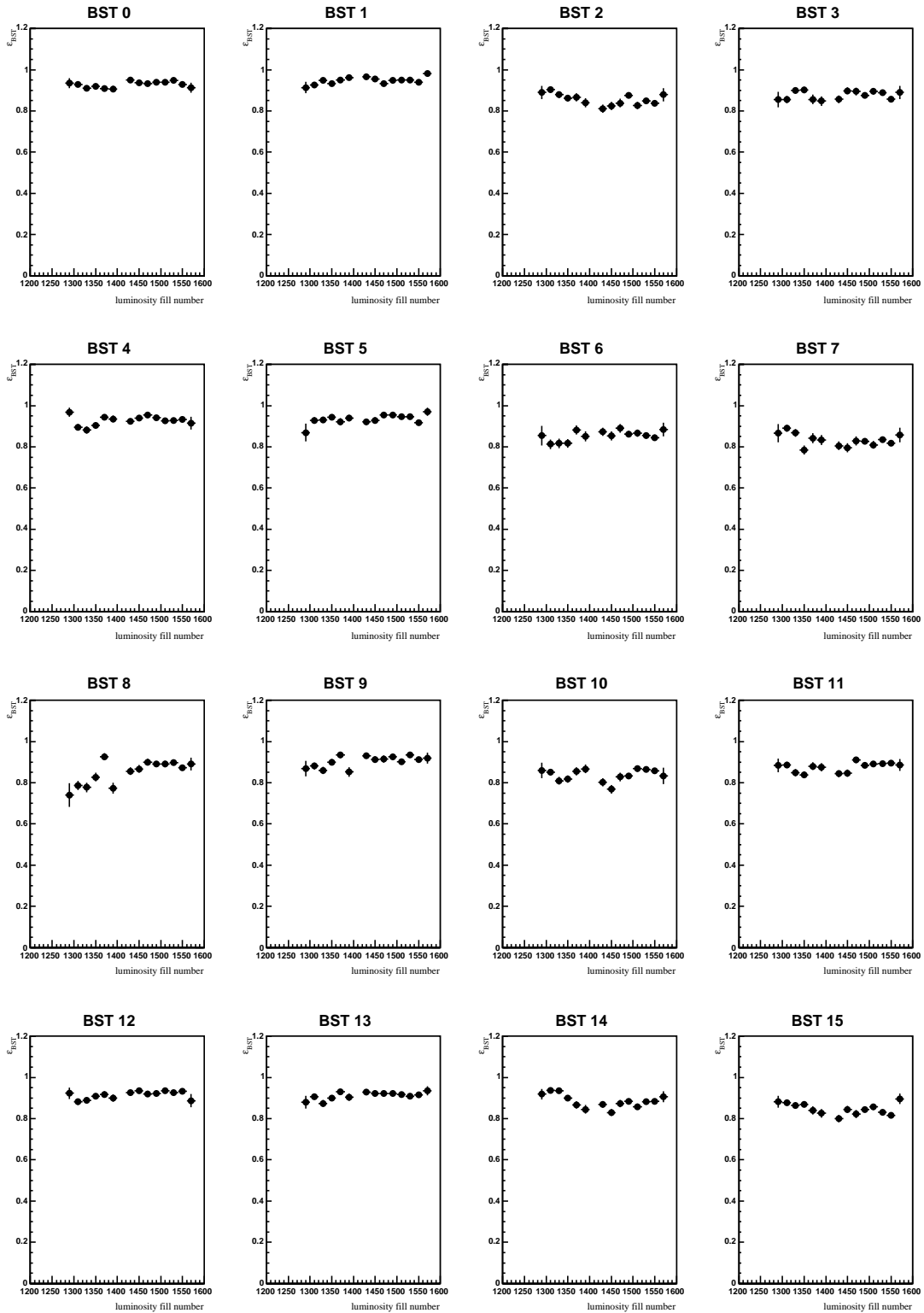


Figure 5.20: *BST efficiency measured for each of the 16 BST φ -sectors versus luminosity fill number, using all run deselections explained in the text.*

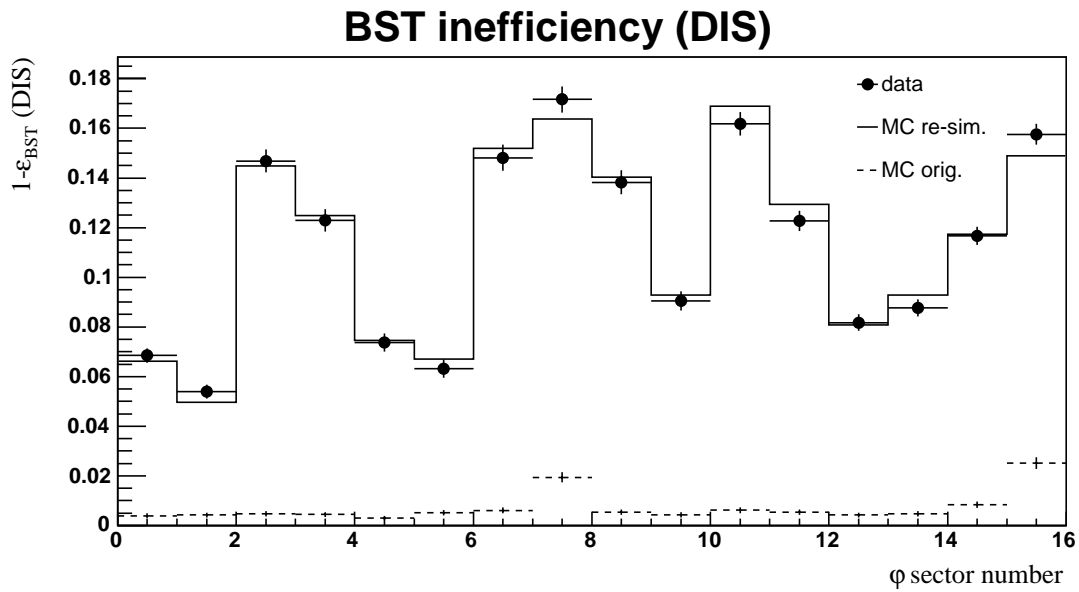


Figure 5.21: *BST inefficiency* $1-\epsilon_{\text{BST}}$ in φ -sectors ($0 \dots 15 = 0 \dots 2\pi$). The original MC values (dashed histogram) are nearly zero or small. Agreement with data levels is achieved by resimulating the sector-wise inefficiencies according to Eq. 5.9.

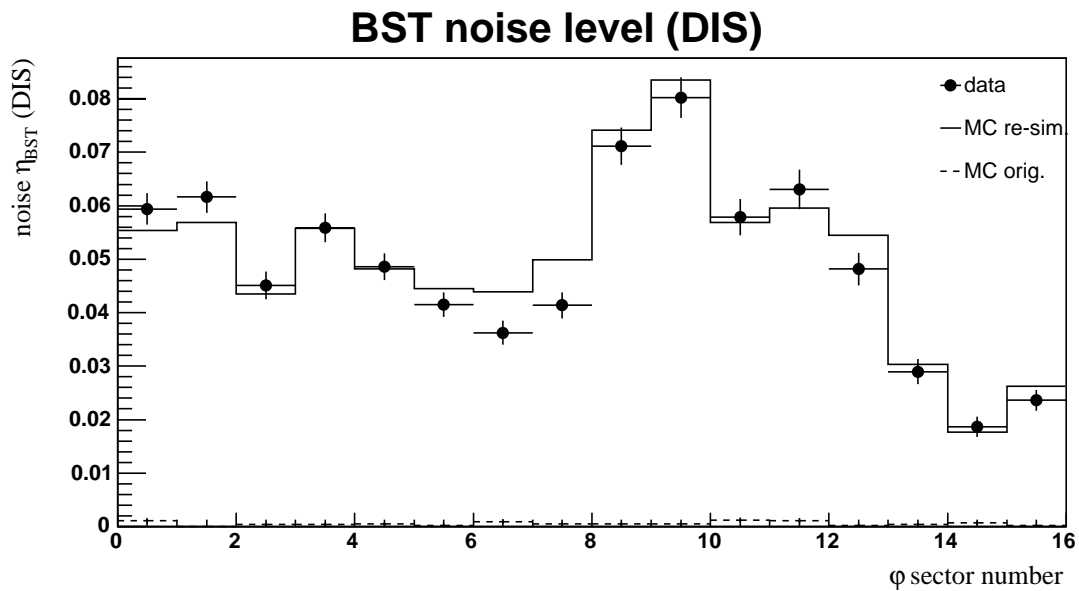


Figure 5.22: *BST noise* η in φ -sectors ($0 \dots 15 = 0 \dots 2\pi$). The original MC contains no noise contributions (dashed histogram). Data–MC differences are resimulated sector-wise according to Eq. 5.10.

5.6 Vertex selection for Compton events

In contrast to deep inelastic scattering events the vertex position in QED Compton events has to be calculated with an own scheme because of a potential unreliably reconstructed *standard* vertex. To allow a consistent transition between the elastic and inelastic channel, the vertex is determined in all events using the Compton-electron. As long as the electron identity is not yet fixed during the analysis of one event both Compton particles can, in principle, deliver the z -vertex position. This means that all possible ep vertex positions have to be kept until the identification decision, acting as the final cut, has been made for the event.

The vertex position is determined either by the BST reconstruction which returns the z -vertex by extrapolation of the corresponding track link of the SpaCal cluster towards the beam axis. Or by the CIP where the vertex is derived by an extrapolation of the associated pad-cluster position towards the beam line. In the linear equation $\vec{x}_{\text{CIP}} = \vec{v} + \alpha(\vec{c} - \vec{v})$, where \vec{x}_{CIP} points to the CIP crossing of the particle trajectory, \vec{v} is the vertex with its x, y components fixed by their known average values for each run, and \vec{c} represents the cluster position. All vectors are measured in H1 coordinates. Thus, the (x, y) -components of \vec{x}_{CIP} are constrained by the given CIP radius $r_{\text{CIP}}^2 = x_{\text{CIP}}^2 + y_{\text{CIP}}^2$ since the CIP is part of the central tracking device and its internal coordinates are automatically H1 coordinates. The vertex solution v_z follows then together with the parameter α and the azimuth of x_{CIP} and y_{CIP} .

As an essential analysis prerequisite it was required that as long as there is no decision about the final vertex position, “double” vertices must be separated by not more than $\Delta z = 10$ cm. In any case it is mandatory that *mutual* vertex compatibility among the two clusters is fulfilled: this means that at least one combination must exist in which one cluster is in the acceptance range of some subdetector under the assumption that the z -vertex position calculated with the other cluster is *the* z -vertex of the considered event. If none these conditions is fulfilled the event is rejected from the further analysis as well as from the photon conversion rate measurement. Figure 5.23 shows the difference distributions of $\Delta z = z_{c0} - z_{c1}$ in case two vertex positions could be reconstructed using the clusters c0 and c1, one of which being in the acceptance of BST and CIP.

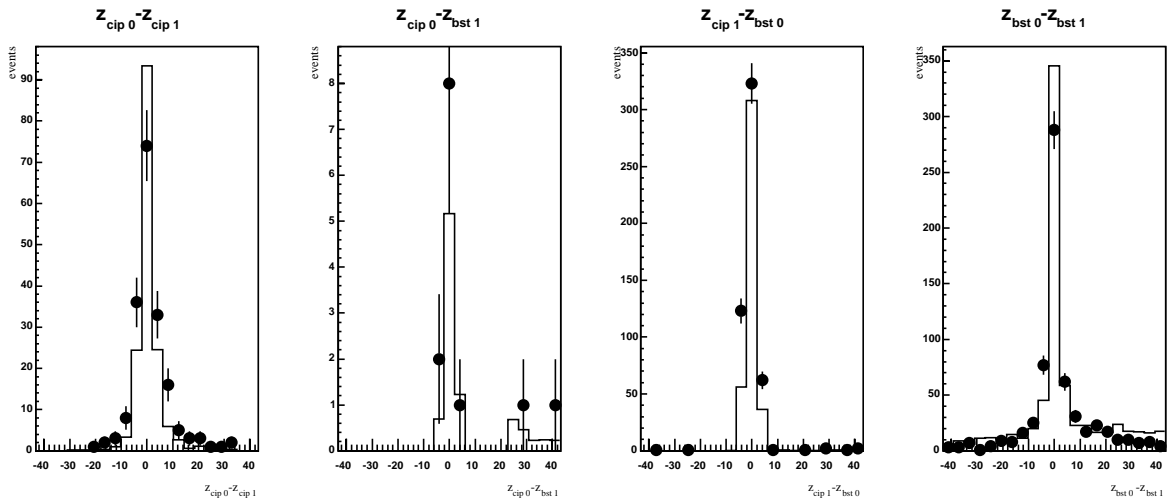


Figure 5.23: Distributions of the difference of the z -vertex positions between the two Compton clusters for each subdetector combination (index 0 means first cluster with highest energy, index 1 means second cluster). A cut is imposed requiring $|\Delta z| < 10$ cm.

5.6.1 Vertex resolution

The vertex resolution was measured using the event vertex of the DIS sample as reference. The distributions of its difference to the vertex position, as determined by using subdetector track information, are shown in Figure 5.24. The CIP determined vertex demonstrates a lower resolution than the BST based vertex, as one expects due to the CIP pad width; the corresponding distribution for the BST is considerably narrower. As rough estimators Gaussian fits are applied in both distributions, resulting in the widths

$$\text{CIP: } \sigma_z^{\text{MC}} \approx 1.3 \text{ cm, } \sigma_z^{\text{data}} \approx 2.2 \text{ cm} \quad \text{BST: } \sigma_z^{\text{MC}} \approx 0.45 \text{ cm, } \sigma_z^{\text{data}} \approx 0.6 \text{ cm.} \quad (5.11)$$

The clear deviation of the shape between data and MC in the case of the CIP again shows, again, the difficulty to reconstruct a backward track with only two sensitive pad layers present in the CIP. On the other hand, as the influence of unrelated tracks of the hadronic final state to the pad-cluster algorithm or simulation details is hard to estimate, both data and MC resolutions are still of comparable orders of magnitude. The width in the CIP data distribution will be used to estimate the systematic error to the final results. In order to achieve a better agreement between data and MC, the corresponding efficiencies or part of the algorithm in the H1 detector simulation program would have to be adjusted.

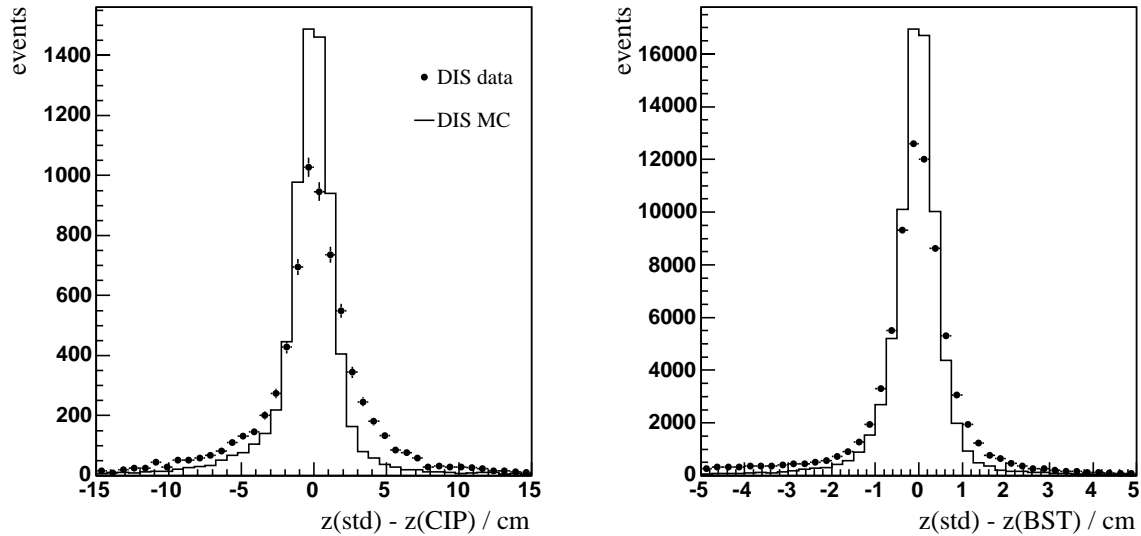


Figure 5.24: Resolution of z -vertex for the subdetectors CIP (left) and BST (right). The distributions are measured by using the DIS event vertex as reference (dots correspond to data, histograms to MC; MC has been normalized to data).

5.7 Photon conversion

With an ideal detector without passive material where photons would not convert into electron-positron pairs the identification of the two QED Compton clusters could be easily achieved by the detection of only one track associated to one of the clusters. In the real experiment only a part of

the events have a signature in which a clear track based distinction between an electron and a photon cluster can be made. In the remaining events conversion takes place such that both clusters are accompanied by a track signal. In order to correct for this possible effect equally in data and Monte Carlo a measurement has to be made of how many photons interact by conversion in the space between the event vertex and the calorimetric detection of the photon. This is studied in the following sections by comparing simulated and experimental events of the Compton selection described in Section 4.2.1. The final run selection as determined in the efficiency studies with DIS data of the previous sections applies now.

As pointed out in the beginning of this chapter the simulation of the backward region had been improved in an earlier study [36] with a detailed implementation of passive material like electronic readout devices, cables, support structures and cooling devices. Especially the inhomogeneity of these different materials was refined representing much better the actual spatial distribution of the material. In simulated events the identity of all generated particles is known. This allows to determine the level of conversion by Compton photons to be expected in the experimental data. The study mentioned above indicated that the amount of passive material is still not completely accounted for in the current standard simulation. Therefore, it is necessary not only to rely on the simulation but also to probe the amount of conversion from real data for comparison. Possible differences of such a measurement between experimental and simulated data can then be used accordingly for a resimulation of the simulated data. In such a case the hit- or track-variables, associated with the Monte Carlo photon cluster, have to be modified using random variables on a calculated fraction of the events.

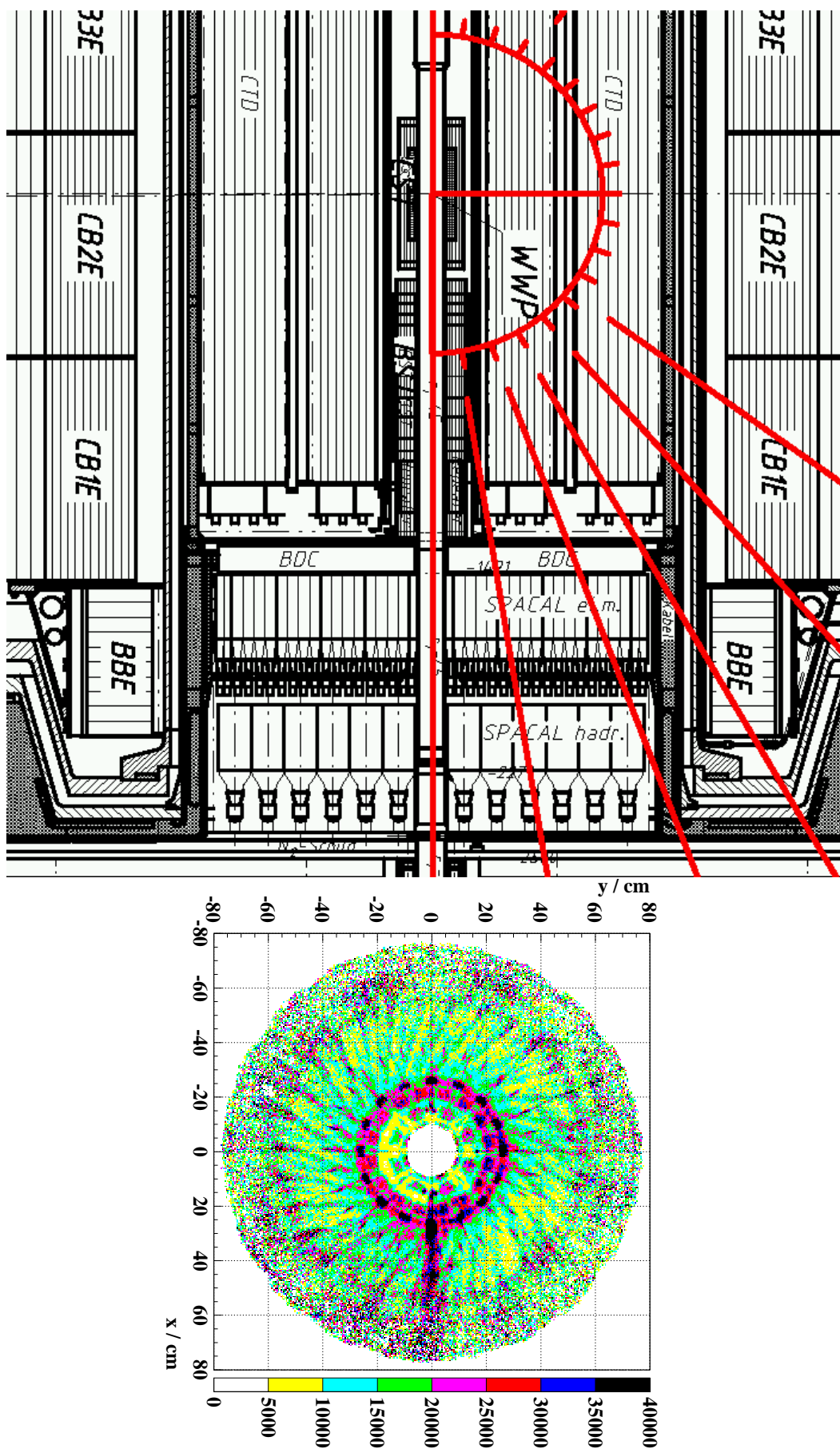
5.7.1 Passive material in the backward area

The backward region of the H1 detector contains subdetectors for the accurate measurement of the polar angle and energy, especially that of the scattered electron. At the same time the space between the sensitive parts of the detector also contains *passive material* for the supply of central components as described in Section 3.2.2. A cutting view through the detector is shown in Figure 5.25 to illustrate the arrangement of the components. It also indicates the density of passive material located especially at the $-z$ -ends of the central tracking devices. In fact, a former study by H1 ([44]), aiming at an improvement of the energy measurement in the backward calorimeter, demonstrated that details of the structure of the passive material distribution are visible in the BDC charge depositions resulting from pre-showering processes of DIS electrons passing the material in front of the BDC. As Figure 5.25 shows, such a projection reflects several structural elements, such as φ -symmetric arrays of preamplifier cards from the CJC, end flanges and electronic boxes from CIP and COP. In addition structures can be seen which represent projection images of the cooling pipes of the silicon trackers CST and BST, as well as cable channels for CIZ around $\varphi \approx 0$. In the figure the BDC charge is measured and displayed in arbitrary ADC[‡] units.

The first implementation of passive material in the detector simulation did not account for all the different materials. At that time the major components were integrated using averaged values of radiation lengths. Structural details were largely disregarded. In a further study [36] the situation was re-evaluated and the detector simulation was extended in 1998 by additional amounts of material. The simulation contains the detailed structure of the subdetectors as well as their support and supplying parts, especially for the $-z$ -wall of the CTD and the multi-layered chamber walls of the BDC.

[‡]Analog-to-digital converter.

Figure 5.25: A side-view of the HI detector backward region from a technical drawing (left part), the lines indicate the polar angle in steps of 10° . The right side represents a map of the averaged electric charge deposited by DIS electrons traversing the BDC plane at $z = -146$ cm. The coloured scale gives a measure for the charge deposition in an arbitrary unit [44].



5.7.2 Photon identification

An unequivocal identification of the photon in reconstructed data is hampered by the fact, that it is impossible to distinguish between a track caused by an electron and one (or more) close tracks originating from photon conversion or pre-showering. This means that a more reliable and independent criterion is required for the decision about which of the two clusters is the electron. The absence or presence of a track signal associated with one cluster cannot be used since this is the property one wants to measure also with the remaining cluster (the photon).

One criterion could be for example to demand well determined track elements from two different subdetectors along a trajectory of one cluster in order to identify it as an electron and the other cluster consequently as a photon. The quality of the result will then depend directly on the amount of misidentification introduced when the decision for the electron fails due to the fake signal from a photon that converted already in front of both subdetectors of which the track elements were taken. The rate of mismatching the identity of both clusters with this method is difficult to estimate. But at least for comparison such an attempt is made and corresponding results for BST and CIP are given below.

Alternatively, if only global corrections are desired for each separate subdetector, averaging the measured conversion rates over geometrical properties like the photon polar angle and azimuth is acceptable. This allows an important control of the first method which aims at and relies on explicit particle identification. Instead, the second type of measurement is realized by determining the number of events in which both Compton clusters 1 and 2 give a track or hit signal (S) relative to the number of events in which at least one cluster has a track or hit signal:

$$\varepsilon_{\gamma} = \frac{N(S_1 \wedge S_2)}{N(S_1 \vee S_2)}. \quad (5.12)$$

The quantity ε_{γ} is assumed to measure the response probability for photons. This method does not rely on particle identification and yields an integrated conversion rate. In fact, with such an approach a distribution of the conversion rate can be extracted from the event sample without losing too much spatial information (*e.g.* the SpaCal radial position), provided both cluster positions have been scattered into a similar range of the polar angle. However, such an additional requirement reduces the resulting statistical reliability sizeably.

5.7.3 Conversion between vertex and subdetectors

The event samples used for the conversion measurement are the same as established for the complete Compton analysis. Only the final identification decision separating electrons from photons is not performed at this point. This is clearly necessary because after some identification procedure the fraction of converted photons in the selected events will be very low; the remaining fraction of converted photons would not reflect an absolute conversion rate. The results of the efficiency and noise level measurements are included and applied to the boolean signal flags of both Compton particles in Monte Carlo events.

Another input condition for this study is the exclusion of inelastic events by applying the corresponding cuts discussed in Section 4.2.2. This is done to ensure that as few as possible (charged) particles of the hadronic final state overlay by chance to the measured rates. However, the magnitude of this effect is expected to be low.

BST

Two approaches for the BST conversion rates are plotted in Figure 5.26 as function of the SpaCal radial position. In the left plot events are selected with one cluster within the CIP acceptance range and the other cluster within the BST acceptance. For the CIP-accepted cluster an electron-like validation is asked for while the BST response is left open. The average validation rate for the BST-accepted cluster is drawn versus its SpaCal radial position. This type of “mixed” rate-definition (*i.e.* using BST and CIP) implies that also converted photons might be present on the CIP side while there is an electron which traverses the BST. Hence, tracks of true electrons or noise effects can contribute to the observed rate on the BST side as well. The order of magnitude of both effects can be estimated by the difference from the Monte Carlo rate to the rate observed by the true photon overlaid as light coloured histogram in Figure 5.26. The information about which SpaCal cluster in the MC event represents the true original photon is, in this case, taken from the generator. The reconstructed rates in MC and data exhibit similar values which are for both systematically above the generator determined conversion rate. Two adjacent data bins between 16 and 18 cm remain a bit higher, while the two bins around them do agree well. This is attributed to unsettled BST noise-effects because neither one of the MC graphs nor the passive material distribution (beam pipe) between vertex and BST give reason to assume a discontinuous distribution of the conversion in r_{cluster} . The overall conversion rate differs by $\approx 5\%$ between data and MC.

In the next step a “pure” BST rate is calculated and depicted according to Eq. 5.12 in the histogram of Figure 5.26-right. In this case only BST-accepted SpaCal clusters can contribute. The input condition is, as explained, that at least one of both clusters has been validated. Then, if both clusters are validated the current event is considered as one with conversion. The event is filled twice with half the event weight for each particle at its radial position. This procedure causes a smearing in r so that possible radial features are broadened and appear less pronounced. Again, since a continuous rate characteristics from the detector point of view is a reasonable expectation the method seems justified. The reconstructed conversion rates of data/MC as well as the true conversion rate (obtained by selecting the true photon directly from generator information) agree quite well taking into account the statistical significance. Also, the total conversion rate measured with this method is quite close, as data and MC do not differ by more than 2%. To summarize, the presented approaches do not indicate major differences between MC and data.

CIP

Conversion in front of the CIP chamber is measured via the same two strategies which have already been applied in the case of the BST: In the *mixed* method a cluster within BST-acceptance has to be electron-like, while the remaining cluster has to be in the acceptance of the CIP only. On the other hand, the *pure* method requires both clusters in the CIP acceptance, at least one of them has to have a pad-cluster signature. The corresponding histogram is filled for this case twice with both particle radii, each receiving the half event weight. Both results can be viewed for Figure 5.27.

Again, the rate distributions indicate for both methods a good agreement for data and MC, regarding both r -dependency and the integrated conversion rate. This can be noticed especially in the pure “CIP-CIP” case.

BDC

The backward drift chamber is treated slightly different compared to the other detectors. In fact, two approaches exist for the conversion measurement. The pure method can be applied obviously in the same manner. But the mixed method offers the possibility to realize explicit particle identification

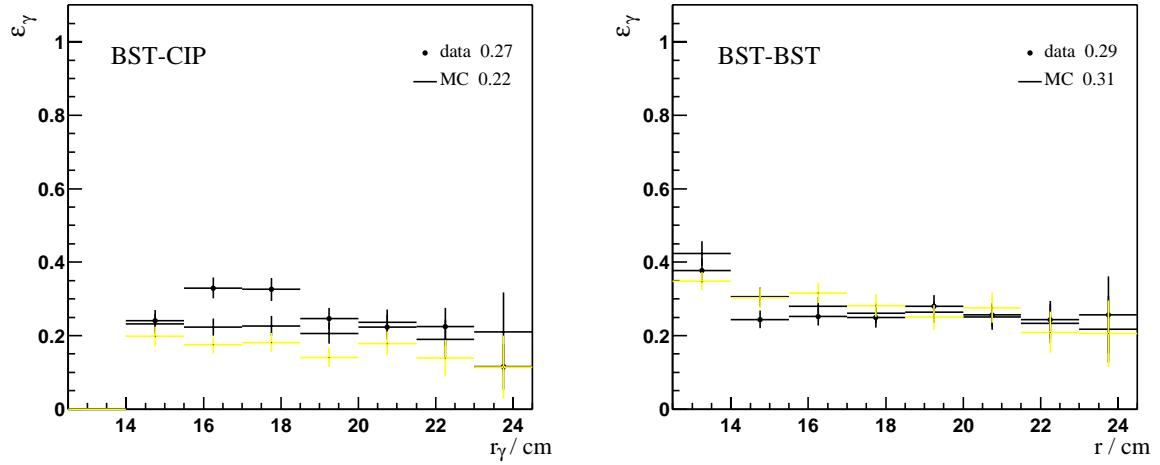


Figure 5.26: Photon conversion probability ε_γ in front of BST versus SpaCal radial position, left: combined method BST-CIP, right: BST-only. The total conversion rate is given as a number for data and MC. The light coloured histogram represents the MC conversion rate of the true (generated) photon.

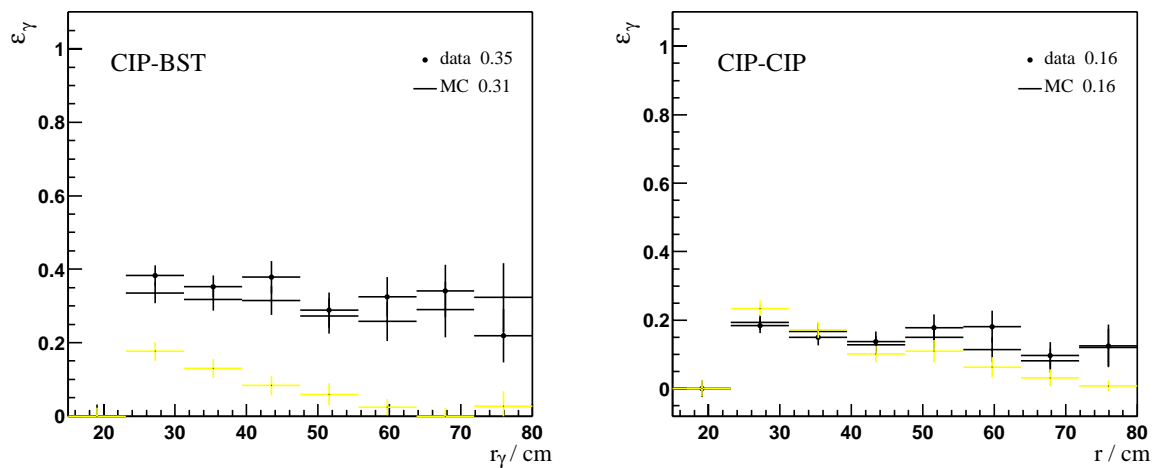


Figure 5.27: Photon conversion probability ε_γ between vertex and CIP versus SpaCal radial position, left: combined method CIP-BST, right: CIP-only. The total conversion rate is given as a relative number for data and MC in each histogram. The light coloured histogram shows the MC conversion rate determined with the generated photon.

before both Compton particles reach the BDC, namely by asking for opposite track signals in BST and/or CIP depending on the actual event topology.

It can be expected that the two methods measure different response probabilities. In the pure method (“BDC_{pure}”), which uses exclusively the BDC no difference is made about *where* the photon converted along its path from the event vertex up to the chamber’s front side where tracking starts. In the other case the particle identification itself takes place much closer to the vertex where already a part of the total radiation length has been traversed by the photon. Since BST-/CIP-identified events define this way an event sub-sample in which the photon cannot have converted up to one of these detectors, any conversion measured afterwards must have occurred between the first two tracking devices and the BDC. In other words, the measured rate is caused by the passive material distribution in the CTD-BDC interspace only. As such it is expected to be lower in comparison to the BDC_{pure} rate.

The results of the respective methods are shown in Figure 5.28-left (mixed) and right (pure). While the MC reconstructed and ‘generated’ rates behave nearly identical in dependence of the cluster radius, a systematic and – in the lower r -bins – a significant difference can be asserted for the photon conversion in data. This can be regarded as an indication for a still incomplete implementation of passive material in the CTD–BDC interspace. While the different measurement methods give similar results concerning the pronounced deviations between data and MC the overall rate is, in fact, higher for the BDC_{pure} measurement. The distributions indicate a typical increase of up to 10. . .15% in this case.

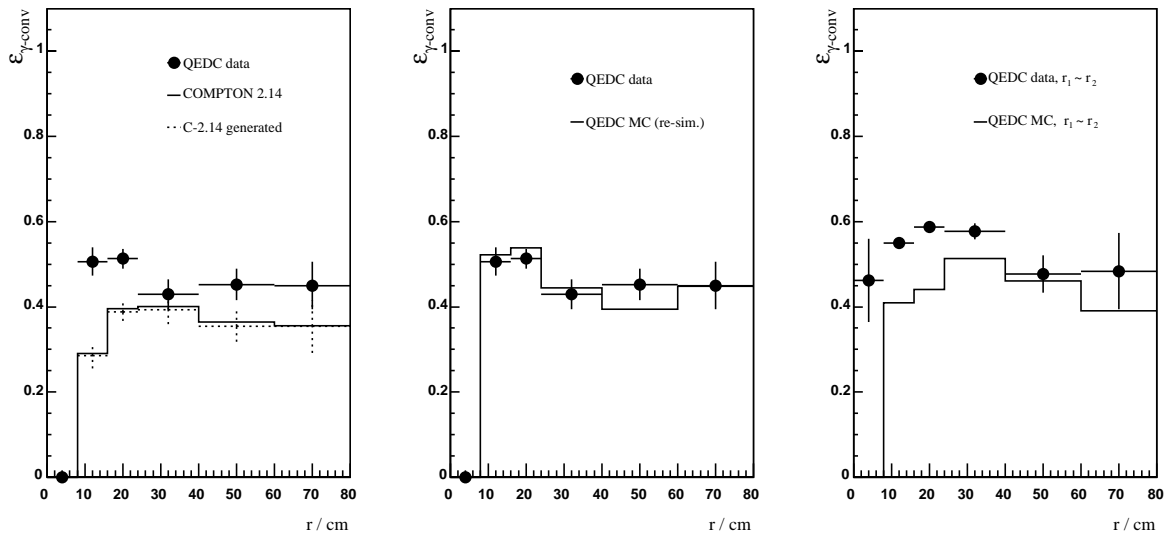


Figure 5.28: Photon conversion probability displayed versus SpaCal radial position. Left: Measured between BST/CIP area and the BDC. The dashed histogram represents the true rate conversion extracted from generator information. Electron/photon identification was imposed by using track information of both particles only in front of the BDC. Middle: same as left after applying a resimulation to the MC. Right: Conversion between event vertex and BDC (without resimulation of MC) measured by requiring that the SpaCal radial positions of both clusters do not differ by more than 10 cm. Radial features become identifiable with both methods.

5.8 Electron–photon identification

The determination of the leptonic event kinematics in QED Compton interactions requires the identification of the electron among both leading electromagnetic clusters. After the measurement of individual subdetector efficiencies and photon conversion rates in front of them, these results can now be used to test different identification schemes against each other in terms of their efficiency and degree of purity of the identified electron photon pairs.

5.8.1 Radial configurations

In the first approach aiming on particle identification in QED Compton events it seemed reasonable to divide the event selection into separate samples according to the radial position r_i of each Compton cluster i within the SpaCal calorimeter, *i.e.* $r_i = r_i(z_{\text{clus}})$. This method is motivated by the experimental setup: neither CIP nor BST offers acceptance over the full backward calorimeter radial diameter. Instead, there is an acceptance transition between BST and CIP around $r_i \approx 25$ cm above which the BST acceptance steeply decreases while that of the CIP increases. This situation suggested to introduce a rough criterion for classifying the event topology by checking whether r_i was below or above this threshold. The idea was supported by the irregularities of the backward chamber’s efficiency in exactly this r -range (“event migrations” [58]), and the specialties of the transition cell structure of the BDC, s. Section 3.2.3 and 5.2.1. For the first studies in this field the “transition region” in $r = 19 \dots 25$ cm (region “1”) was treated as a separate topological part. Together with the ranges below 19 cm (region “0”) and greater than 25 cm (region “2”) there were in total six topologically different sub-samples of the full Compton selection (two particles distributed in three different areas). However, this method neglects the finite vertex range such that the acceptance limits, measured as function of r , do strongly shift depending on where the event vertex z_{tx} is actually localized. In this way it is not possible to make meaningful statements about specific detector properties in different r -regions, especially concerning the intermediate region “1”.

In parallel it was found that the BDC, due to the total strength and uncertainties of the photon conversion just in front of this tracker, is not well suited for the use in the identification procedure. Both aspects, acceptance and conversion (near the BDC), changed the further study to not follow this way. Instead the number of regions were reduced to two:

$$\text{region 0 : } r_i < 25 \text{ cm} \quad \text{region 2 : } r_i > 25 \text{ cm} .$$

The regions correspond predominantly to the acceptance range of the BST and to that of the CIP, respectively. Although they are not used for probing acceptances these regions still classify roughly the event topologies and are applied for the identification process. They are also used for monitoring control distributions of several quantities in these regions.

The radial subdivision leads to three different *configurations* depending on the SpaCal cluster positions:

- configuration “c00” or “BST-BST”: first and second cluster in BST acceptance.
- configuration “c22” or “CIP-CIP”: first and second cluster in CIP acceptance.
- configuration “c02” or “CIP-BST”: one cluster in BST acc., the other in CIP acc.

5.8.2 Identification algorithms

For the decision about which of the Compton clusters is accepted as the validated electron – and thus which of them is the photon – the detector track signals are available. Because refined track properties (*e.g.* number of hits, etc.) do not carry decisive information only the presence or absence of a track is used. The corresponding boolean quantity is regarded as equivalent for both electron and photon. This means, a positive electron track indication (flag equals TRUE) has the same weight in identification decisions like the positive indication caused by one of the daughter tracks of a photon conversion process. The conditions for the flags assigned to a SpaCal cluster i are defined for the detectors as:

$$\text{BST}_i : \text{reconstructed track}(i) = \text{YES} \wedge \text{RSP}_i < 1.5 \text{ cm}, \quad (5.13)$$

where RSP is the radial distance (in the H1 coordinate system) between the SpaCal cluster barycenter and the BST track in the SpaCal plane at the cluster z -position. For the CIP the condition is

$$\text{CIP}_i : \text{reconstructed pad-cluster}(i) = \text{YES} \wedge n_{\text{pad},i} < 7, \quad (5.14)$$

where $n_{\text{pad},i}$ is the number of active pads contained within one layer of the reconstructed pad-cluster. All other pad-cluster related conditions discussed in the CIP track reconstruction section (geometrical cuts which define the cluster formation) apply as well. Finally, for some numerical considerations involving the BDC also the first of the discussed BDC hit conditions holds in the following.

As shown earlier in the example of the BDC-ID the *quality* of the particle identification is not only affected by detector efficiencies, but also by the probability that the Compton photon appears as an electron. This means, the expected probability of mismatching the identities of both particles (*i.e.* taking the true electron for the photon and vice versa) depends on the chosen combination of flags. Such a combination will be called an *identification-* or *ID-algorithm*. The question arises which algorithm offers the lowest possible mismatching rate.

The general situation is that one Compton particle, electron or photon, traverses two backward tracking detectors, these are: either BST and BDC, or CIP and BDC. In addition, there are three different main topologies found in Compton events, namely those previously defined as c00, c02, and c22. The quality of an algorithm can, thus, be calculated for each of these cases. The following paragraphs discuss alternative possible identification schemes. For better readability of the efficiency representations the tracking detectors are numbered using the subscripts 1, 2 or 3. The description of response probabilities, as applied already in the discussion about the BDC identification mismatch rate, is used again. Measured values for the particle response probabilities obtained in the previous sections will be used to estimate the total yield- and misidentification-rate for the schemes.

Algorithms for c00 and c22

Both Compton particles are in acceptance of the *same* two tracking detectors denoted as 1 and 2, where 1 is the label of the detector next to the event vertex (this is either CIP or BST), and 2 denotes the BDC.

I) “1 or 2”: This scheme tries at first detector 1 in order to give a definite decision on the particle identity by comparing its assigned flag variables, one for each Compton cluster. If both variables have *different* values the decision is accepted as final and the cluster with the active track signal flag is regarded as the electron, the other (flag equals FALSE) is assigned the photon identity. But two cases remain for which a decision cannot be made, namely if both flags are FALSE or both are TRUE.

Then, and only then, one proceeds to detector 2 which is probed in the same way as detector 1. This method, denoted here as “1 or 2”, has the advantage that the first tracker is less affected by conversion effects because it is closer to the vertex as compared to detector 2, the BDC. The total rate of $e\gamma$ validated events is given by the expression:

$$p_I = p_1^{+-} + p_1^{-+} + (p_1^{++} + p_1^{--}) \cdot (p_2^{+-} + p_2^{-+}), \quad (5.15)$$

where the indices 1 and 2 refer to the corresponding detectors and the signs follow the convention used in Section 5.3.1 and Eq. 5.2 (first sign indicates the electron signal, the second one the photon). Because of the special dependence imposed by this algorithm, probability correlations have to be kept in mind as two different photon conversion rates are involved: the total rate and the one measured between detectors 1 and 2. In each of the cases p_1^{++} and p_1^{--} the probability products p_2^{+-} and p_2^{-+} have to be resolved separately into terms which account for this effect:

$$\begin{aligned} p_I &= p_1^{+-} + p_1^{-+} + p_1^{++} \cdot (p_2^{+-} + p_2^{-+}) + p_1^{--} \cdot (p_2^{+-} + p_2^{-+}) \\ &= p_1^{+-} + p_1^{-+} + p_1^{++} \cdot (p_2^e \bar{p}_2^e + \bar{p}_2^e p_2^e) + p_1^{--} \cdot (p_2^e \bar{p}_2^\gamma + \bar{p}_2^e p_2^\gamma p_2^e), \end{aligned} \quad (5.16)$$

where the variable $p_2^\gamma = p_2^\gamma - p_1^\gamma$ has been introduced. The systematic misidentification δp_I is expressed by the terms containing the electron-like cases of the converted photon, *i.e.*

$$\delta p_I = p_1^{-+} + p_1^{++} \cdot \bar{p}_2^e p_2^e + p_1^{--} \cdot \bar{p}_2^e p_2^\gamma p_2^e. \quad (5.17)$$

II) “1 & 2 as one”: In this scheme all combinations of flag states are chosen in which one detector validates the electron and the other confirms the identity of the photon at one “significance level” lower. This means the significance of the photon identity is required to be “stronger” if the indication for the electron is “weaker”. In other words, the two detectors under consideration are regarded as one physical tracking device with a varying total track quality. The method also becomes clear in its algebraic notation of the total expected validation rate:

$$\begin{aligned} p_{II} &= p_1^e \bar{p}_2^e \bar{p}_1^\gamma \bar{p}_2^\gamma + \bar{p}_1^e p_2^e \bar{p}_1^\gamma \bar{p}_2^\gamma + p_1^e p_2^e \bar{p}_1^\gamma p_2^\gamma + p_1^e p_2^e p_1^\gamma \bar{p}_2^\gamma \\ &+ \{ \text{same terms with labels } e \leftrightarrow \gamma \text{ switched} \} \end{aligned} \quad (5.18)$$

The first two products require one track flag to be positive while those two flags assigned to the remaining cluster have to have negative flags. The misidentification rate δp_{II} is given by the second sum $\{ \dots \}$ in 5.18.

III) “1 eq 2”: The simplest and sharpest criterion for the $e\gamma$ identification using two tracking detectors is that a track signal has been reconstructed in both detectors associated to one SpaCal cluster, while for the other cluster no signal is permitted at all in any of the detectors. Thus, the flag combination must be *equal* for each tracker. The total fraction of events selected this way can be written as

$$p_{III} = p_1^{+-} \cdot p_2^{+-} + p_1^{-+} \cdot p_2^{-+}. \quad (5.19)$$

Again, the second term denotes the probability by which cluster pairs are mismatched.

In all above calculations I-III) the relative misidentification rate $\rho = \delta p/p$ characterizes the overall quality of the respective algorithm. For the full detection efficiency of converted photons the usual track efficiency has to be multiplied, in principle, with the conversion probability. This additional efficiency factor was neglected for the reason of simplicity: It is assumed that $\epsilon_{\text{track}}(\text{conv. } \gamma) = 1$ and

that only the conversion probability itself contributes. In this way conversion rates become slightly overestimated.

Algorithms in c02

In this type of event shape one SpaCal cluster is in the acceptance of the CIP and the other one is in the range of the BST. In contrast to the configurations c00 and c22 an assumption has to be made in c02 about through *which* detectors the electron and the photon are moving. This is necessary to assign the correct response probabilities to the algorithm. It means one has to distinguish between the two cases: a) “electron in CIP” and b) “electron in BST”, respectively. As a consequence of this separation the total validation rate as estimated from both cases together depend on the actual polar angle distributions of the Compton electron and photon, *i.e.* on the statistical weights of both sub-samples. But the two validation rates a) and b) can be roughly compared under the assumption that the polar angle distributions of both particles are not *too* different. Again, the BDC (now denoted with subscript 1) is taken into account *a priori* for the identification. CIP and BST are numbered as 2 and 3, respectively.

IV) “1,2 versus 1,3”:

a) “Electron in CIP”. The electron is required to leave positive signatures in the trackers 1 and 2, while the cluster to be identified as photon must have not more than one active flag: it has to have either one in 1 *or* in 3, or it has to have no active flags at all. Using such a scheme yields a validation rate for $e\gamma$ pairs given by

$$\begin{aligned} p_{\text{IV}}^{\text{a}} &= p_1^e p_2^e \cdot (p_3^\gamma \bar{p}_3^e \bar{p}_1^e + \bar{p}_3^\gamma p_1^\gamma p_1^e + \bar{p}_1^\gamma) \\ &+ p_2^e p_2^\gamma \cdot (p_3^e \bar{p}_1^e + \bar{p}_3^e p_1^e + \bar{p}_3^e \bar{p}_1^e), \end{aligned} \quad (5.20)$$

where $p_{1'}^\gamma = p_1^\gamma - p_3^\gamma$ was used. The first two factors represent the electron part while the following sum in parentheses describes the photon response probabilities. The second line gives the part of the misidentification when the photon fakes the electron signature by conversion while the electron completely fails to fulfil it.

b) “Electron in BST”. The formula describing the validation rate is nearly the same as Eq. 5.20 except that the CIP and BST indices are switched:

$$p_{\text{IV}}^{\text{b}} = p_{\text{IV}}^{\text{a}}(2 \leftrightarrow 3). \quad (5.21)$$

The index replacements in this formula also hold for $p_{1'}^\gamma$, which is then modified into $p_{1'}^\gamma = p_1^\gamma - p_2^\gamma$.

V) “1,2 versus 1,3”: In this algorithm the track signals are compared *detector-wise* one after the other, analogous to the scheme **I** in c00 and c22, and independent of whether a particle trajectory can cross a detector or not.

a) “Electron in CIP”. The validation rate can directly be written down according to

$$\begin{aligned} p_{\text{V}}^{\text{a}} &= p_1^{+-} + p_1^{-+} \\ &+ (p_2^{+-} + p_2^{-+}) \cdot (p_1^{++} + p_1^{--}) \\ &+ (p_3^{+-} + p_3^{-+}) \cdot (p_2^{++} + p_2^{--}) \cdot (p_1^{++} + p_1^{--}). \end{aligned} \quad (5.22)$$

Due to the limited acceptances of the BST and the CIP two factors vanish: $p_3^e = 0$ and $p_2^\gamma = 0$, followed by $p_2^{-+} = 0$ and $p_2^{++} = 0$, which is equivalent to using only one track indicator, associated

with a cluster, for the identification decision without looking on the signature of the other cluster. This increases in general the overall validation rate but can also cause large mismatching rates in sub-samples of this selection although the total mismatch rate might appear relatively low.

b) “*Electron in BST*”. The description is identical to the previous case:

$$p_V^b = p_V^a, \quad (5.23)$$

but instead the identities $p_2^e = 0$ and $p_3^\gamma = 0$ hold, implying $p_2^{++} = p_2^{+-} = p_3^{-+} = 0$. Like before the mismatch rates are given by the sums of all those products in Eqs. 5.22 and 5.23, respectively, containing probabilities with the “ $-+$ ” sign combination.

Numerical discussion

The formulae of methods I)-V) are used to estimate typical yield and mismatch rates using the known efficiencies and probabilities. Not all sources of misidentification are considered as for example the influence of electronic noise. Table 2 compares the quality of the different algorithms.

Table 2: Identification algorithms with BDC included. Listed are their yields p_i and mismatch probabilities as absolute and relative rates, δp_i^{abs} and $\rho_i = \delta p_i^{\text{abs}}/p_i$.

algorithm i	configuration	yield p_i	δp_i^{abs}	$\rho_i = \delta p_i^{\text{abs}}/p_i$
I	c00	0.7451	0.1117	0.1499
I	c22	0.5953	0.0307	0.0516
II	c00	0.4946	0.0577	0.1166
II	c22	0.4741	0.0066	0.0139
III	c00	0.2401	0.0024	0.0098
III	c22	0.4097	0.0001	0.0002
IV a)	c02	0.6479	0.0670	0.1034
IV b)	”	0.5228	0.0241	0.0461
V a)	”	0.9941	0.0257	0.0259
V b)	”	0.8908	0.1135	0.1274

The summary table shows that there are large variations among the different kinds of identification schemes. The worst quality in terms of $e\gamma$ misidentification is given by strategy I) in the c00 configuration which has an unacceptable high systematic mismatch of 15%. In general such high values cannot be considered as useful. The overall result is that the involvement of the BDC brings too high mismatch rates into the schemes due to the high total conversion rates in front of the chamber. Although there are examples, like the algorithm III) in c00 and c22, which show very low ρ values for the price of lowest yields, the majority of algorithms is more or less strongly affected by too many converted photons. The same is true even for the algorithms of c02 where all detectors are considered together. In this configuration, because of the *a priori* unknown statistical sizes of the sub-samples a) and b), *i.e.* the unknown polar angle distributions of photon and electron, an *overall* mismatch rate cannot be calculated for a)+b) together.

Table 3: Particle identification mismatch rates estimated for the three main detector combinations corresponding to the configurations *c00*, *c02*, and *c22*. The numbers are determined from Monte Carlo after its resimulation (eff. and noise) using the reconstructed particle identities in combination with the true ones from generator information.

	BST-BST	BST-CIP	CIP-CIP	total
MC	3.2%	1.4%	1.3%	1.6 %
expected	3.3%	–	1.1%	–

5.8.3 Reduced detector algorithm

The results of the previous section demonstrated the uncertainties introduced by using BDC track signatures for the electron-photon identification. Therefore, a much simpler concept was chosen for the final ID, allowing a better control and prediction of mismatching. In this ansatz the cluster related flag variables, of CIP and BST only, are probed against each other by requiring opposite flag values. That means, the flag definitions of Eqs. 5.13 and 5.14 apply in the elementary boolean tests

$$T_{c00} = (BST_0 \neq BST_1) \quad (5.24)$$

$$T_{c22} = (CIP_0 \neq CIP_1) \quad (5.25)$$

$$T_{c02} = \begin{cases} (BST_0 \neq CIP_1), & \text{if 1st cluster in BST} \\ (BST_1 \neq CIP_0), & \text{else} \end{cases} \quad (5.26)$$

These simplified selection rules allow to give expectation values for the relative misidentification on the basis of the discussed efficiencies and conversion rates. The expectation values are calculated again according to Eq. 5.4 and listed in Table 3 for comparison with the amount of the misidentification ρ_{MC}^{true} still contained in the final set of simulated events after all selection cuts have been applied. ρ_{MC}^{true} can be determined by making use of the true particle identity from generator information stored together with the usual event data. The identification efficiencies in the above scheme are of the order of 70...80%.

Summary: The previous study showed the difficulties in particle identification found in the different Compton topologies. The main problematic source of misidentification is the measurable level of photon conversion in front of BST and CIP which leads to *i*) a substantial rejection of Compton events since two track validated SpaCal clusters do not allow to discriminate the electron from the photon, and *ii*) misidentification as a result of the interplay of inefficiency plus noise plus conversion. Referring again to Table 2 one sees, that the BST is affected in particular by these effects (not accounting for noise). Nevertheless, the overall amount of mismatched cluster pairs is on a moderate level of 1.5-3% using the final $e\gamma$ -identification rules T_{c00} , T_{c22} and T_{c02} . They will be applied for all following analysis steps. In the majority of events the electron can be identified as the true electron which allows to study calibration aspects, like geometrical alignment and energy, separately for both Compton clusters. These questions will be scrutinized in the following chapter.

6 Calibration

This chapter describes various aspects of detector calibration such as the alignment of the relevant tracking devices and of the backward calorimeter. The Compton acoplanarity peak is exploited for this purpose. The analysis of these properties is followed by a study on the precision of the energy measurement of the Compton electron and photon. The last parts discuss the influence of the Compton trigger on the event selection and, finally, a event reweighting procedure based on different vertex distributions in experimental and simulated data.

6.1 Subdetector alignment

The central jet chambers define the fundamental H1 reference frame while all other components have to be aligned with respect to them in order to obtain consistent measurements. The subdetector alignment as required in this analysis affects mainly the backward calorimeter and backward drift chamber as their positions are not fixed relative to the CTD during H1 maintenance periods but moved in and out of the LAr detector independently. For the components CIP and BST two cases are distinguished: The CIP is regarded as fixed relative to the other central tracking chambers (but see [37] where some remaining misalignment could not be excluded). For the BST the alignment constants of [32] are applied. They comprise the five parameters for an external orientation of the cylindrical BST volume and further 64 parameters to fix the internal relative positions of all BST silicon-sensors, a list of these is given in the appendix, Table 12.

6.1.1 Tilt of beams

The electron and the proton beams are guided by the HERA magnet system through the H1 interaction region such that their bunches collide in a parallel orientation relative to each other. On the other hand, this beam orientation as measured in the H1 coordinate system is *not* parallel to the z -axis in H1. Usually the deviation between beams and z -axis, the *beam tilt*, is of the order of 1 mrad, varying slightly over the run periods. As the symmetry axis for the ep scattering process is given by the beam direction, and not by the H1 coordinate system, all particle coordinates have to be transformed into the beam system to obtain the correct kinematic quantities. This fundamental geometrical correction has to be applied to all coordinate variables. The tilt is defined by the slopes of the vertex x and y coordinates in the H1 system with respect to the z -coordinate. During the 1997 data taking the average beam slopes were:

$$\tau_x = \frac{\partial x(z)}{\partial z} \simeq -0.0016, \quad \tau_y = \frac{\partial y(z)}{\partial z} \simeq 0.0003 .$$

Using the mean beam coordinates $x_{\text{vtx}}, y_{\text{vtx}}$ at $z = 0$, any H1 space point coordinates $x_{\text{H1}}, y_{\text{H1}}, z_{\text{H1}}$, like cluster positions or track points, are transformed through

$$\begin{aligned} x_{\text{H1}} &\rightarrow x_{\text{H1}} - x_{\text{vtx}} - (z_{\text{H1}} - z_{\text{vtx}}) \tau_x - x_0 \\ y_{\text{H1}} &\rightarrow y_{\text{H1}} - y_{\text{vtx}} - (z_{\text{H1}} - z_{\text{vtx}}) \tau_y - y_0 \\ z_{\text{H1}} &\rightarrow z_{\text{H1}} . \end{aligned} \tag{6.1}$$

The additional offsets x_0, y_0 represent alignment corrections for the corresponding subdetector. The original coordinates $x_{\text{H1}}, y_{\text{H1}}$ returned by some part of the H1 reconstruction programs are approximate values only because small deviations of the subdetector positions from the design values are

unavoidable. In the simulation the offsets are zero because all detector positions are assumed to have their nominal values. The actual offsets are measured directly from the data using their relative spatial shifts. This measurement is discussed after the following treatment of the influence of the magnetic solenoid field.

6.1.2 Compensation of the electron deflection

The homogeneous magnetic field in H1, oriented parallel to the z_{H1} -axis, deflects charged particles within the H1 tracking area. The effect causes their original azimuth at the vertex, φ^{tx} , to be shifted by some amount to a new azimuth, φ^{rec} , depending on their momenta and the path length between vertex and their detection points. The same happens to Compton electrons and shifts the acoplanarity $A_{e\gamma}$ (defined in Eq. 2.6) between electron and photon accordingly, such that averaged over all events

$$\langle A_{e\gamma} \rangle \neq 0 .$$

Note that this shift of the peak does not occur in the alternative acoplanarity definition, A_{12} , where *unidentified* Compton SpaCal clusters are used and the azimuths of the first (highest energy) and second cluster enter. Compared to $A_{e\gamma}$ the peak of A_{12} is just wider if the first cluster is equally often found to be either the electron or the photon, because the electron is picked randomly as the first cluster and, thus, averages out the deflection in A_{12} . The A_{12} peak can also become asymmetric and *distorted* or it can even show two close peaks if the polar angle distributions of electron and photon are sufficiently different. This phenomenon can be caused either by the kinematic details of the QEDC process itself which determine how frequent the electron appears as the first cluster; but also because of some special event selection which could favour, for example, more electrons (relative to photons) at higher polar angles than at lower angles. Due to the strong kinematic correlation between cluster energy and polar angle in QED Compton a given event selection determines the (yet unmeasured) ratio of the numbers of electrons and photons, $N_e : N_\gamma$, found for instance as the first cluster. Then, because of the momentum dependency of the deflection, the A_{12} distribution is also affected by the selection and is, therefore, not suited for alignment measurements as much as $A_{e\gamma}$. These important interrelations underline the necessity of particle identification (allowing the calculation of $A_{e\gamma}$) and accurate considerations on geometrical aspects like the magnetic deflection.

The acoplanarities $A_{e\gamma}$ and A_{12} are shown as distributions as function of the azimuth of the electron and the first cluster, respectively, in Figure 6.1. One can observe in the histograms that in the $e\gamma$ case (left figure) a narrow band exists while in the case of unidentified Compton clusters (right figure) the same set of events forms a much broader band. Both bands have a wiggled shape due to the SpaCal misalignment w.r.t. the H1 coordinate system. The $e\gamma$ band is shifted to negative values due to the deflection as explained above, while the other band is centered around zero.

Since the analysis makes use of the $e\gamma$ acoplanarity peak at zero for the determination of the SpaCal alignment parameters Δx_{Sp} and Δy_{Sp} (for their measurement see paragraph below), the electron deflection, as contained in the measured azimuth, has to be compensated. This is equivalent to the determination of the electron azimuth *at* the event vertex where the magnetic field has not yet disturbed the electron trajectory. It must be kept in mind that the alignment procedure discussed in Section 6.1.3 is based on a χ^2 minimization method by which the alignment parameters could in principle also be obtained when the electron deflection is not compensated but kept in the kinematic variables, because the deflection does not directly influence the χ^2 minimum (see Eq. 6.3). This statement holds under the assumption that all selected Compton clusters are distributed symmetrically in φ across the SpaCal plane: the sine-wave structure is then a consequence only of the misalignment. Due the band's symmetry along the azimuth around some given mean acoplanarity (Figure 6.1-left)

the χ^2 minimum is obtained when the true SpaCal shift is subtracted from all cluster coordinates such that the sine shape shrinks to a straight band. This can be understood by considering the ratio ε of the sine amplitude, or elongation of any point on the curve, relative to the mean offset of the curve in A_γ from zero. By its symmetry one can always find two points on the sine curve with equal ε for which $\chi^2 \propto (1 - \varepsilon)^2 + (1 + \varepsilon)^2 = 1 + 2\varepsilon^2$, *i.e.* always > 1 .

But in principle it is possible that, for example, asymmetry effects in the cluster distributions along azimuth of the SpaCal plane affect the band shape. These could influence systematically the alignment result. Using the deflection compensation the absolute value of the χ^2 minimum, relative to its vicinity, is better pronounced and thus facilitates its determination. The main purpose of the compensation is, therefore, to lower possible systematic influences on the alignment procedure.

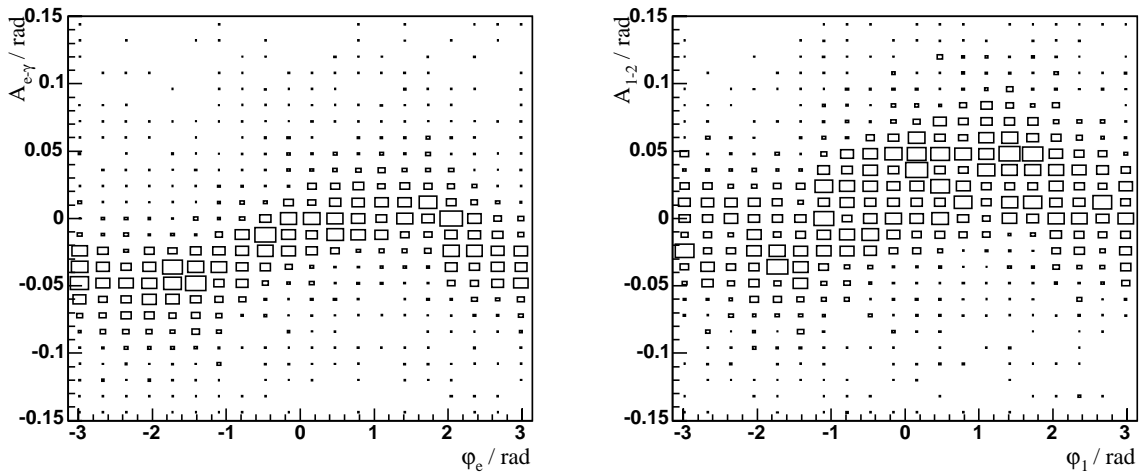


Figure 6.1: Comparison of acoplanarities $A_{e\gamma}$ (left) and A_{12} (right) in elastic Compton events, histogrammed versus the SpaCal azimuth of the electron and of the first cluster, respectively. The magnetic deflection of the electron trajectory manifests in the global shift to negative values of the band in the left histogram. This effect is not seen in the case of A_{12} for which no particle identification takes place.

The electron azimuth is reconstructed using the SpaCal calorimeter, φ^{rec} . As discussed in Section 5 the Compton electron track is reconstructed only in relatively short pieces of the whole trajectory, using CIP and BST, between event vertex and calorimeter. This means that the electron azimuth at the vertex, φ_e^{vtx} , which is relevant for the event kinematics, especially the acoplanarity, cannot be measured directly from a track curvature as it would be possible in principle using a track arc reconstructed with the CTD. Instead the momentum dependence of the deflection is used for the calculation of φ_e^{vtx} . The azimuthal deflection $\Delta\varphi$ of electrons with energy E_e can be parameterised like

$$\Delta\varphi(E_e) = \frac{s_0}{E_e - \Delta E} + \text{offset} \quad (6.2)$$

where the parameter s_0 accounts for the strength of the magnetic field and for the particle charge. As additional parameters ΔE and *offset* are provided to allow for an adjustment of small systematic effects. A distribution of $\Delta\varphi(E_e)$ from simulated events is presented as a two dimensional histogram in Figure 6.2-left. Since in the simulation the electron is subject to the solenoid field (implemented with equal strength as the experimental value), whereas the generated electron vector represents the momentum at the vertex (azimuth φ_e^{gen}), the energy dependent deflection can be made visible. The

histogram shows the electron deflection $\Delta\varphi(E_e) = \varphi_e^{\text{rec}} - \varphi_e^{\text{gen}}$ as a function of the generated electron energy. A fit using the function $\Delta\varphi(E_e)$ is applied to the distribution and gives the fit parameters

$$s_0 = -0.268 \frac{\text{rad}}{\text{GeV}}, \quad \Delta E = 0.138 \text{ GeV}, \quad \text{offset} = -1.02 \cdot 10^{-7} \text{ rad} .$$

This means that ΔE is small compared to typical electron energies and that the offset is practically negligible (as it should be). These fit parameters are used by default in data and MC for rotating the electron momentum vector using the reconstructed energy E_e such that the final electron azimuth φ_e^{final} becomes

$$\varphi_e^{\text{final}} = \varphi_e^{\text{rec}} - \Delta\varphi(E_e) .$$

A control distribution for MC in Figure 6.2-right shows that the compensated $\Delta\varphi^{\text{final}} = \varphi_e^{\text{final}} - \varphi_e^{\text{gen}}$ is centered at zero for all electron energies. In general the deflection reaches a few 10 mrad at lowest energies which is already too small for a reliable momentum/angle measurement from the track curvature, even if the track was measured in the jet chambers, but it is still high enough to cause a visible shift of the acoplanarity peak.

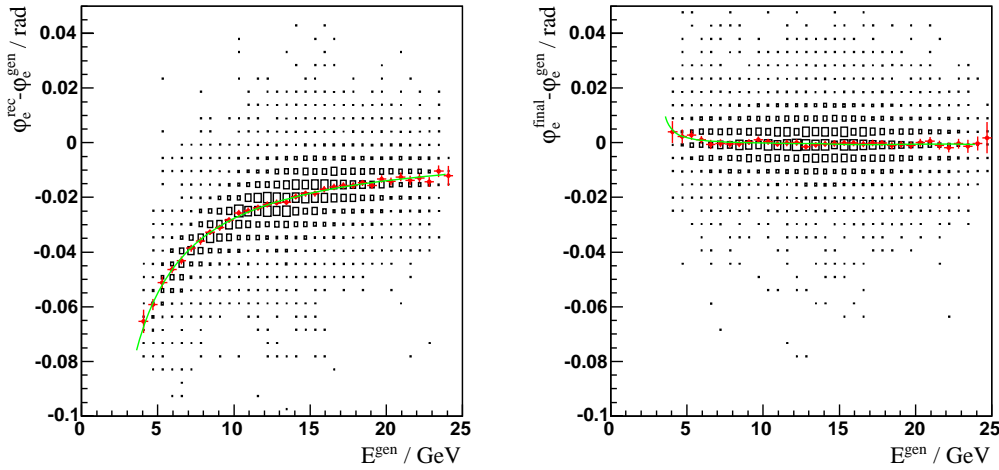


Figure 6.2: Compensation of the electron deflection in azimuth caused by the magnetic field of the H1 solenoid, using Monte Carlo events. Left: difference between azimuths of MC reconstructed and of generated electron. Right: difference between azimuths of final and of generated electron. Fit curves of Eq. 6.2 are overlaid in both pictures.

6.1.3 SpaCal and BDC alignment

The actual SpaCal position in the experiment is obtained by minimizing the deviation of the Compton acoplanarity $A_{e\gamma}$ from zero. This becomes possible after the beam tilts and the magnetic deflection of the electron have been compensated as one part of the coordinate transformation Eq. 6.1. The raw position coordinates of the photon and electron clusters are defined within the SpaCal internal coordinate system. A shift of the calorimeter relative to the H1 frame in x and y leads to a periodic variation of the measured acoplanarity as function of the azimuth. This is shown in Figure 6.3-left for electrons of the elastic Compton sub-sample. The acoplanarity $A_{e\gamma}(\varphi_e)$ is modulated sine-like as shown by a corresponding function fitted to the distribution. The oscillation in φ_e causes a deterioration of the acoplanarity resolution as evident when performing a projection along φ_e . Since the acoplanarity distribution in the picture contains a whole spectrum of different SpaCal radial positions $\eta_{1,2}$ of the clusters – there is no functional dependency between A and $\eta_{1,2}$ – a sine fit yields only the direction of the shift in azimuth but not its radial amount. Because of that, the extraction of the true calorimeter shift is carried out by means of a χ^2 method. For all N_{ev} contributing elastic Compton events a sum of acoplanarities

$$\chi^2(\Delta x_j, \Delta y_k) = \sum_{i=1}^{N_{ev}} \frac{A_{e\gamma}^2(x_{c1} + \Delta x_j, x_{c2} + \Delta x_j, y_{c1} + \Delta y_k, y_{c2} + \Delta y_k)}{\sigma_i^2} \quad (6.3)$$

is calculated as a function of N_{grid}^2 discrete displacements $\Delta x_j, \Delta y_k$ of the two coordinates of the SpaCal clusters in each event. The location of the minimum of χ^2 is expected to represent the deviation of the SpaCal from its nominal position:

$$\chi^2(\Delta x_{Sp}, \Delta y_{Sp}) = \chi_{min}^2(\Delta x_j, \Delta y_k)$$

The inverse event weight $\sigma_i^2 = (\sigma_{Sp}/r_1)^2 + (\sigma_{Sp}/r_2)^2$ is used [39], where the SpaCal spatial resolution $\sigma_{Sp} = 0.3$ cm for cluster positions applies. Thus, the weighting favours acoplanarities based on cluster positions in the outer SpaCal where the azimuth measurement for $A_{e\gamma}$ is of better precision ($\delta\varphi \propto \mathcal{O}(\text{radial resolution}/\text{radius})$). A grid of equidistant base points is established with the parameters

$$N_{grid} = 20 \quad \Delta x_j, \Delta y_k = -0.475 \dots + 0.475 \text{ cm} \quad (j, k = 1, N_{grid}).$$

The displacements $\Delta x_j, \Delta y_k$ are chosen to match roughly the expected range of the calorimeter shift. Note that their values represent the symmetrically arrayed bin centers of the histogram which is used to represent the χ^2 sum of Eq. 6.3. The resulting event acoplanarity is used to sum up χ^2 which is displayed as function of both shift parameters in Figure 6.3-right. The minimum position is determined not just from the position of the smallest bin entry on the discrete grid but instead by performing a two-dimensional fit on the histogram distribution using a function of the form

$$f(x, y) = a + b(x - \Delta x_0)^2 + c(y - \Delta y_0)^2 \quad (6.4)$$

which yields the final SpaCal misalignment parameters $\Delta x_{Sp} = \Delta x_0, \Delta y_{Sp} = \Delta y_0$. The minimum bin content of the histogram is subtracted from all bins before the fitting procedure is executed in order to avoid numerical difficulties in the fit because of big numbers. It turned out that a full compensation of the SpaCal shift could not be achieved in a single step: Applying the shift values $\Delta x_0, \Delta y_0$ from a first iteration as default alignment correction in a new χ^2 sum for the general coordinate transformation of data events (Eq. 6.1) a small shift remained. In an iterative procedure each residual shift amounts was added to the previous shift until constant values were obtained. This is meant to

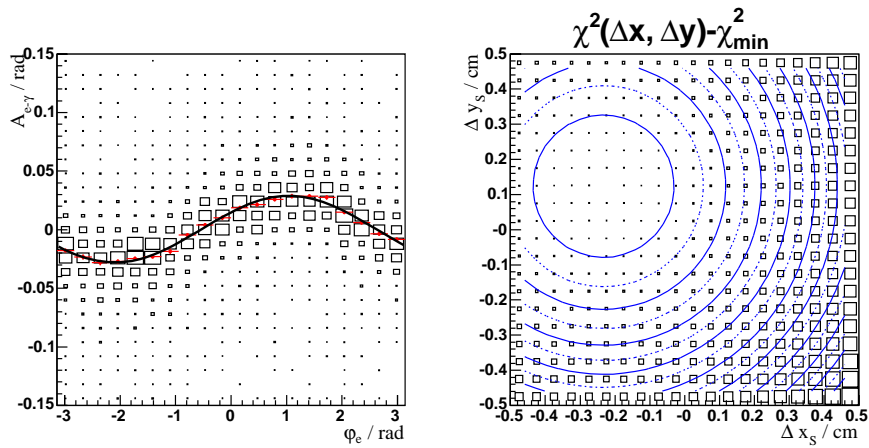


Figure 6.3: Measurement of the misalignment of the backward calorimeter using elastic Compton events. Left: Compton acoplanarity $A_{e\gamma}$ versus electron azimuth. Right: χ^2 distribution as function of the numerical calorimeter displacements Δx_S , Δy_S , and its curves of constant level derived from a paraboloidal fit.

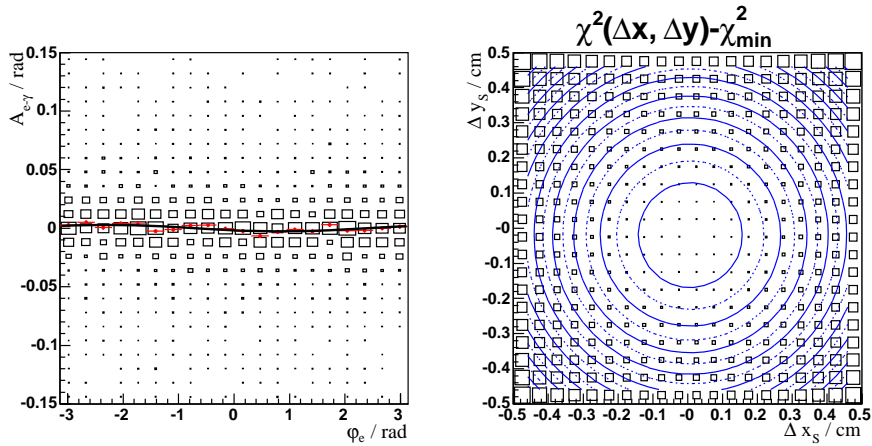


Figure 6.4: Control diagrams after the correction of the backward calorimeter misalignment for 1997 data using elastic Compton. Left: Compton acoplanarity versus electron azimuth. The fit of a sine function applied (as above) to the acoplanarity mean values in slices of ϕ_e shows only a small systematic remaining amplitude. Right: paraboloidal fit to the χ^2 distribution.

reduce systematic effects of the limited fit-range which is asymmetric with respect to the minimum of $f(x, y)$ as visible in Figure 6.3-right. After typically five to seven iterations the minimum position does not change anymore. The final SpaCal position results then in:

$$\Delta x_{Sp} = -2.70 \text{ mm}, \quad \Delta y_{Sp} = 1.45 \text{ mm}$$

The numbers are close to those of former analyses [37, 47]. While the y -shift seems to agree well with their results the amount of the shift in x is higher by ≈ 1 mm. Although the described iterative procedure converged in all cases starting from several different initial conditions, systematic effects cannot be excluded either due to the complex dependencies among the many involved quantities or due to the iteration procedure itself (degeneration of variables). The first χ^2 -summation yields as x -shift ≈ -2 mm which is noticeable closer to the cited previous finding of $x_{E\text{lan}} = -1.8$ mm. For this reason a systematic error of 0.7 mm is assumed for Δx_{Sp} .

Including both effects, the alignment correction and the magnetic deflection compensation, the final acoplanarity distributions, A_{12} and $A_{e\gamma}$, in data and Monte Carlo are compared in Figures 6.5 and 6.6 respectively, on linear and logarithmic scales.

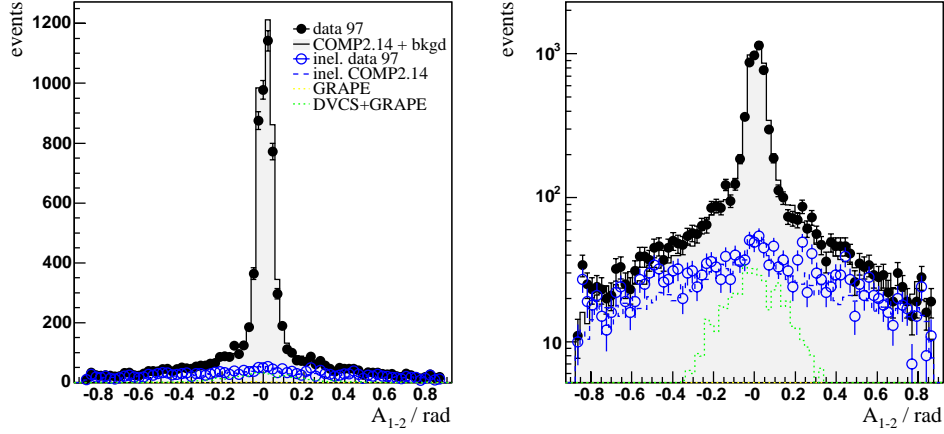


Figure 6.5: Acoplanarity between first and second cluster, linear scale (left) and logarithmic (right). The peak structure shows a small asymmetry which can be explained with different polar angle distributions of electron and photon. The background contributions and the inelastic Compton part (data: open circles, MC: dashed histogram) are shown as well.

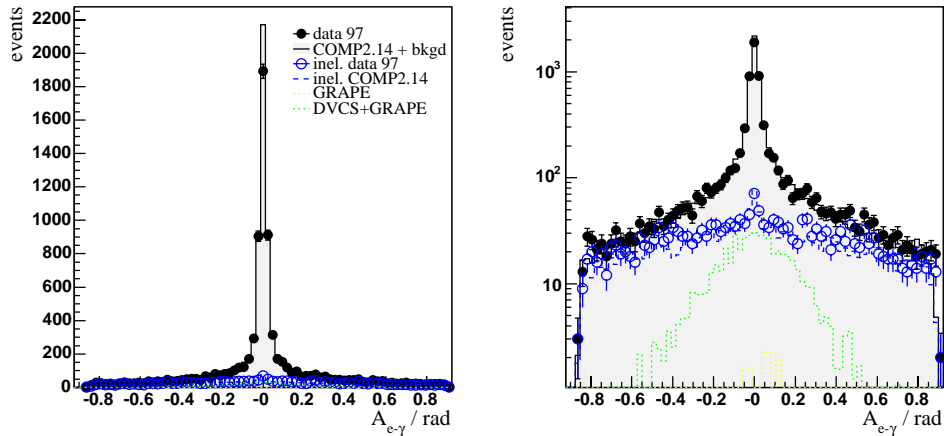


Figure 6.6: Acoplanarity between electron and photon, using φ -correction on electron azimuth, as well as tilt- and alignment-corrections on all coordinates. The peak width is smaller and higher than the one of A_{12} .

Positioning BDC

The BDC alignment in (x, y) -coordinates is carried out with respect to the SpaCal final position. This is a compromise because the drift chamber offers a better radial resolution compared to that of SpaCal, $\Delta r_{\text{SpaCal}} \approx 5$ mm, which also affects the SpaCal alignment shifts. A more direct and independent method would be to align directly the BDC with respect to the central jet chambers. Because the CTD was affected by an efficiency drop in some certain φ -range and for reasons of data manageability the alignment with respect to the SpaCal was chosen. The BDC misalignment is depicted in Figure 6.7-left using the polar angle difference between the BDC track and the SpaCal electromagnetic cluster for Compton electrons (elastic subset), the SpaCal shifts are included. The calculation of the chamber displacement is done by a minimization of the polar angle difference, by which for all events the following sum is computed:

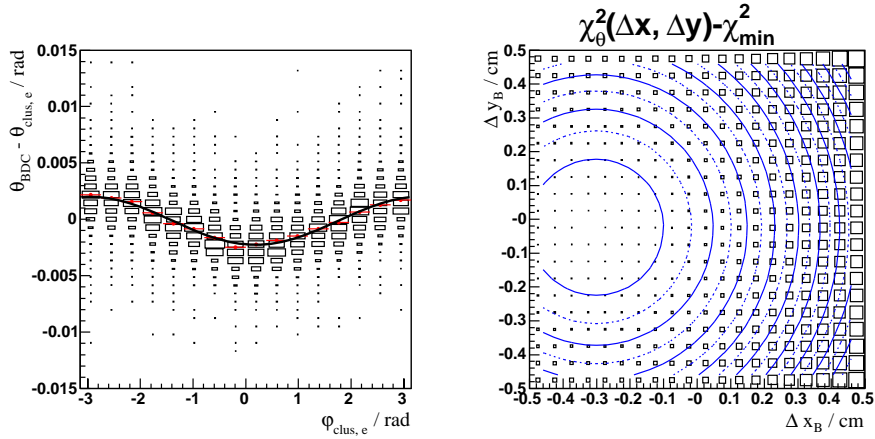


Figure 6.7: BDC misalignment before correction. Left: difference of electron polar angles in BDC and SpaCal versus electron azimuth. Right: χ_{θ}^2 as function of numerical chamber displacements $\Delta x_B, \Delta y_B$ and curves of constant level of the fit function.

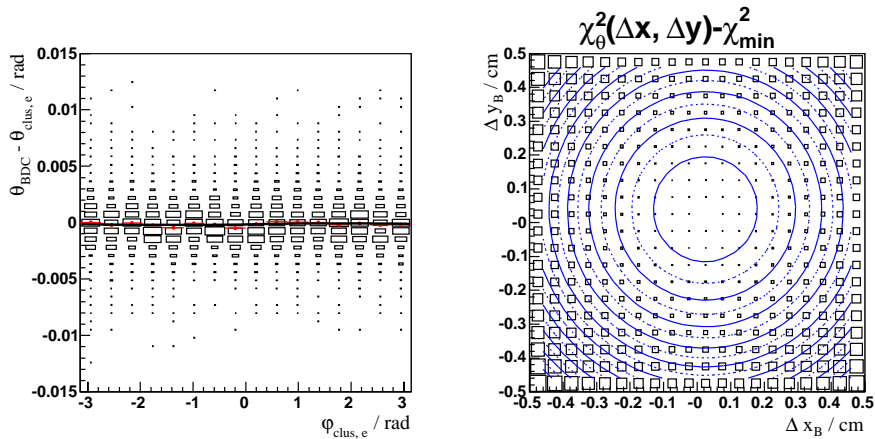


Figure 6.8: Control diagrams for BDC alignment after correction. Left: electron polar angle difference of BDC and SpaCal versus electron azimuth. Right: χ_{θ}^2 as function of numerical chamber displacements $\Delta x_B, \Delta y_B$.

$$\chi^2(\Delta x_B, \Delta y_B) = \sum_{i=1}^{N_{\text{ev}}} \frac{(\theta_{i,\text{BDC}} - \theta_{i,\text{SpaCal}})^2}{\sigma_i^2}. \quad (6.5)$$

The variation in $\Delta x_B, \Delta y_B$ shifts the electron track position, measured at the chamber center in z , by a small amount and thus modifies the θ_{BDC} calculation accordingly. A fit is applied to the χ^2 distribution using the function f of Eq. 6.4, the result is shown in Figure 6.7-right. The fit parameters point to the minimum of f which is given by the displacement

$$\Delta x_B^0 = -3.4 \text{ mm}, \quad \Delta y_B^0 = -0.34 \text{ mm}.$$

As a consistency check the numbers are added by default to the coordinates of every BDC track. Repeating the χ^2 calculation with these defaults results in a proper shift compensation as demonstrated by the flat fit curve and the centered χ^2 -distribution of Figure 6.8.

6.1.4 BST alignment

Although the BST alignment parameterisation has already been measured in [32] (s. appendix) and is used in the present analysis, the alignment relative to BDC and SpaCal was probed again. For this purpose the BDC and SpaCal alignment parameters determined in Section 6.1.3 are implemented and remaining differences to the BST measured polar angle of electrons are compared in Figure 6.9. As the histograms show the BST alignment parameters seem to be in accord with the positions of both, the backward drift chamber and the calorimeter. In addition one observes some irregular changes of the average θ differences as function of the electron azimuth. These do not appear to agree with the usual sine-like variations expected for a simple detector displacement in x and y w.r.t. another detector, such as found, for instance, in the alignment between BDC and the SpaCal. As similarly shaped structures are visible in both cases it seems likely that the source of these variations is related to the BST itself, and not to some specific problem with the reconstruction of clusters or backward tracks. The maximum mean deviation between expected and BST-measured polar angle is of the order of 1 mrad.

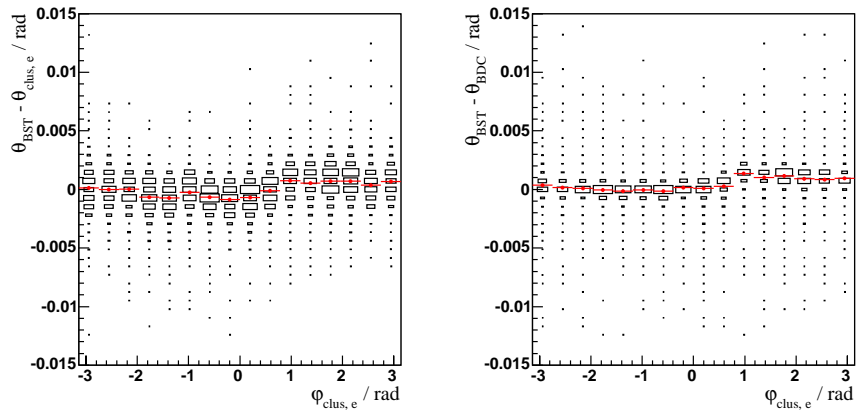


Figure 6.9: Difference of the BST measured polar angle of elastic Compton electrons to the polar angle of SpaCal (left) and BDC (right), plotted versus azimuth of electron SpaCal cluster in both histograms. The line of dots in each histogram indicates the mean values derived from Gaussian fits in slices of $\varphi_{\text{clus,e}}$. The better radial resolution of the BDC is demonstrated by the narrower width of the right distribution.

6.2 Cluster energy and dispersion

The calibration of the calorimetric cluster energies, as delivered by the standard reconstruction, is tested by comparing them to their corresponding *double angle* (DA) energies. In the case of an optimum calibration there should be no significant deviation of the mean energies. For this study the elastic Compton event selection is used again. The double angle energies E_a , E_b are computed for the two Compton particles a and b using the formulae

$$\begin{aligned} E_a &= E_0 \cdot \sin \theta_b \\ E_b &= E_0 \cdot \sin \theta_a \\ \text{with } E_0 &= 2 E_{\text{beam}} / (\sin \theta_a + \sin \theta_b - \sin (\theta_a + \theta_b)) \end{aligned} \quad (6.6)$$

where E_{beam} corresponds to the nominal electron beam energy. In this way the cluster energies can be determined only by measured polar angles and the electron beam energy, while effects of energy reconstruction and energy loss due to pre-shower interactions are suppressed. This assumes that there is only a weak correlation in the cluster reconstruction between the cluster barycenter (affecting θ_{cluster}) and the calorimetric cell-wise energy summation (affecting E_{cluster}).

The method of using the polar angles of Compton electron and photon for calibration purposes assumes that there are no other particles present in the event which could disturb the energy/momentum balance between the two leading e.m. particles. In other typical HERA analyses studying ep DIS events containing a hadronic jet representing the struck quark the double angle method can be applied for the jet and the scattered electron. In this case inelastic events are considered from the beginning and all final state particles are contained. However, the QED Compton event sample used in this analysis contains elastic as well as inelastic events, but the double angle method is only applicable in the sub-sample of elastically scattered $e\gamma$ pairs. In order to allow for an uniform treatment of particle energies in all Compton events the measured energies E_{rec}^0 have to be used for the measurement of the event kinematics instead of the double angle based energies. The E_{DA} will only be used for the extraction of calibration factors f_{DA} for rescaling of the reconstructed energies. Thus the final measured energies become $E_{\text{rec}}^{\text{final}} = f_{\text{DA}} \cdot E_{\text{rec}}^0$.

Figure 6.10 shows for elastic Compton events spectra of the relative deviation between reconstructed and double-angle energy in three ranges of E_{DA} . With increasing cluster energy the width of the relative deviation shrinks as a result of the improving resolution of the measurement of the reconstructed energy E_{rec} . This observation is in agreement with the SpaCal resolution function as measured in earlier studies [48].

6.2.1 Non-linearity of energy measurement

The reliability of the energy measurement is studied by calculating the double angle energies (Eq. 6.6) of the e.m. SpaCal clusters in elastic Compton events. The results of this study can be applied to all types of Compton events, *i.e.* elastic as well as inelastic collisions. The full $e\gamma$ -identification procedure is run through. Although an explicit identification is not necessary according to Eq. 6.6, it lowers the relative amount of events with (photon-) pre-showering within CIP/BST and, thus, reduces the average measured energy loss of the photon. Additionally, it allows to look on possible differences of the non-linearity behaviour between electrons and photons. In a first consideration the relative deviation between the reconstructed energy and the calculated double angle energy is compared for simulated and real events, respectively:

$$\Delta L = \frac{E_{\text{rec}} - E_{\text{DA}}}{E_{\text{DA}}}. \quad (6.7)$$

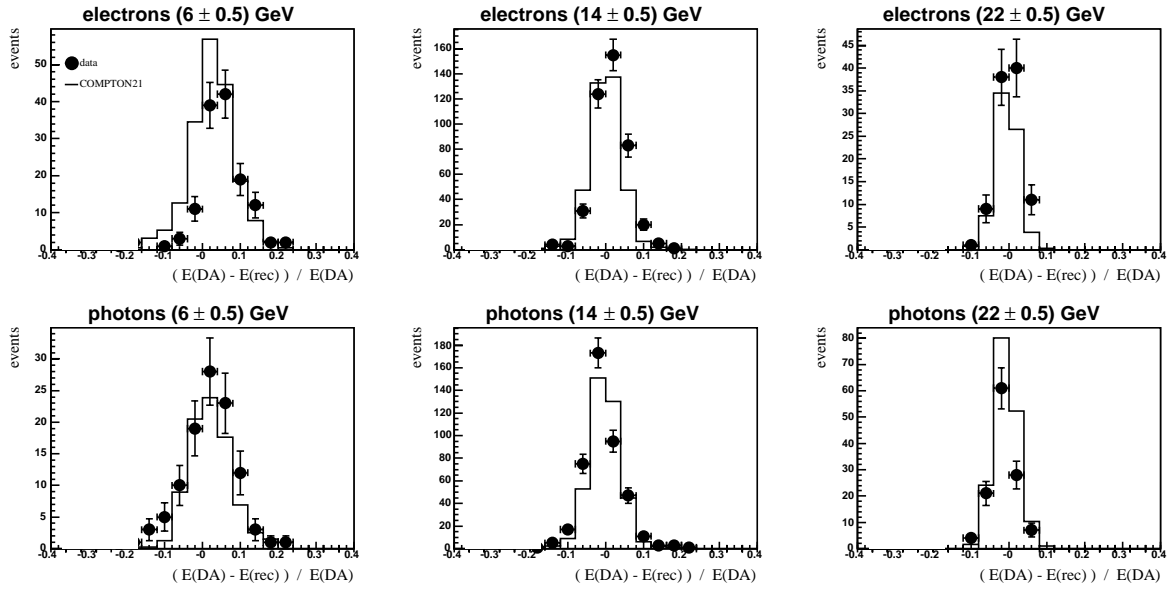


Figure 6.10: Distributions of the relative deviation between measured and double-angle calculated energy in elastic Compton events for electrons (upper row) and photons (lower row). The double angle reference energies are required to be within a range of $-0.5...0.5$ GeV around the center values of 6, 14, and 22 GeV (left to right).

This quantity defines the non-linearity[§] in energy and is viewed as function of E_{rec} and E_{DA} . For each of these arguments ΔL is plotted in Figure 6.11-A₀ and -A. As the diagrams show the slopes of the ΔL distributions are lower when changing from reconstructed to double angle energies on the abscissa for both particles. This can be understood as the consequence of migration of some fraction of events from one bin to another due to the finite resolution of the energy measurement and due to the deviation from linearity itself: Since, for example, clusters with measured energy values below the expected E_{DA} contribute partly to the next lower bin in E_{rec} , the mean of ΔL in that bin experiences a pull *downwards*. Assuming for this case a decreasing event distribution in E_{rec} the over-next lower bin cannot have enough events on average to compensate the pull.

While the measured energies, because of their limited resolution, have a wider spread around a given E_{rec} -bin, stronger migrations occur in $\Delta L(E_{rec})$ in contrast to the $\Delta L(E_{DA})$ distribution where the particle energy is more likely to be contained within the correct bin. Thus, the bin width for the non-linearity studies was chosen high enough in order to achieve

- > a better statistical significance, and
- > a reduction of overlap and migrations among adjacent bins, caused by the limited resolution.

After the transition to the abscissa E_{DA} the following observations can be made (Figure 6.11):

- a general rise of ΔL in data and MC for electrons and photons
- Monte Carlo non-linearities are above those in the data for electrons and below them for photons
- a significant rise to positive values is observed for photons with $E > 12$ GeV.

[§]The term denotes *any* deviation to double angle energies as non-linearity, also in the case that a constant $\Delta L \neq 0$ exists for all energies. In other works it is also denoted as *pull*.

The last two points indicate general differences between electrons and photons. It turned out that the occurrence of conversion or non-conversion of the photon is strongly correlated to the discrepancy between the non-linearity curves of data and Monte Carlo. The situation is demonstrated in Figure 6.11-B and -C where the experimental and simulated events are separated into two subsets of which the first one contains unconverted photons and the second one contains converted photons only. Conversion is detected by the presence of a BDC track signal in front of the photon cluster while the non-conversion case is indicated when there is no track along the photon path through the backward area. Since the $e\gamma$ identification does not make use of the BDC but is performed on track pieces much closer to the event vertex, namely by CIP and BST, conversion is generally restricted to occur behind these detectors.

The diagrams show that most of the discrepancy (compare right diagrams of row B and C) occurs in the data sample containing those photons which did not convert in front of the BDC. On the contrary the Monte Carlo distributions do not change very much. The question arises what causes the level difference of about 2-3% between converted and unconverted photons in the data, while the curves for electrons in both cases (left histograms) and the converted photon appear on similar levels. Also, the differences between data and MC appear small in these cases.

In general, two major effects contribute to the non-linearity: on the one side it is the calorimeter internal non-linearity, caused by imperfect cell/calorimeter calibration and cluster reconstruction effects concerning the cluster barycenter (on which the polar angle measurement depends) and the total cluster energy. On the other side there is energy loss caused by pre-shower processes in the backward region. Such an energy loss has the effect of lowering the measured energy and thus lowering the measured ΔL (Eq. 6.7) while reconstruction related effects can shift the pull, in principle, to lower or higher values.

For electrons reconstruction effects and pre-showering act both at the same time and the resulting pull is an average effect. Particularly, an electron pre-shower event producing a bundle of secondary particle tracks cannot be distinguished from one where the electron left a single track only. This explains that the electron curves do not change very much (Figures 6.11-B,C left) since there is always a *mixture* of events present with pre-showering and non-pre-showering electrons. Comparing that to converted photons in the experiment, one finds that their average energy loss (or: difference to MC) is lower. This can be explained by the fact that the tracks produced by conversion induced e^+e^- -pairs have a shorter mean track length as they start not before the point where the conversion took place, while a Compton electron can initiate a pre-shower process along its full path and, thus, loses more energy on average.

Only the unconverted photons behave completely different. Their ΔL is unexpected high and does not show the typical level of the electron non-linearity curve but appears significantly shifted upwards instead.

6.2.2 Test of E_{DA} in Monte Carlo

For Monte Carlo events the reconstructed energy of a particle is compared directly to the original energy carried by the generated particle. This is achieved by viewing the profiles of the histogram distribution of

$$\Delta L'(E_{\text{gen}}) = \frac{E_{\text{rec}} - E_{\text{gen}}}{E_{\text{gen}}} \quad (6.8)$$

as a function of the generated energy. This quantity allows to study possible effects on the energy reconstruction process. Furthermore, the reliability of the double angle reconstructed energy as a

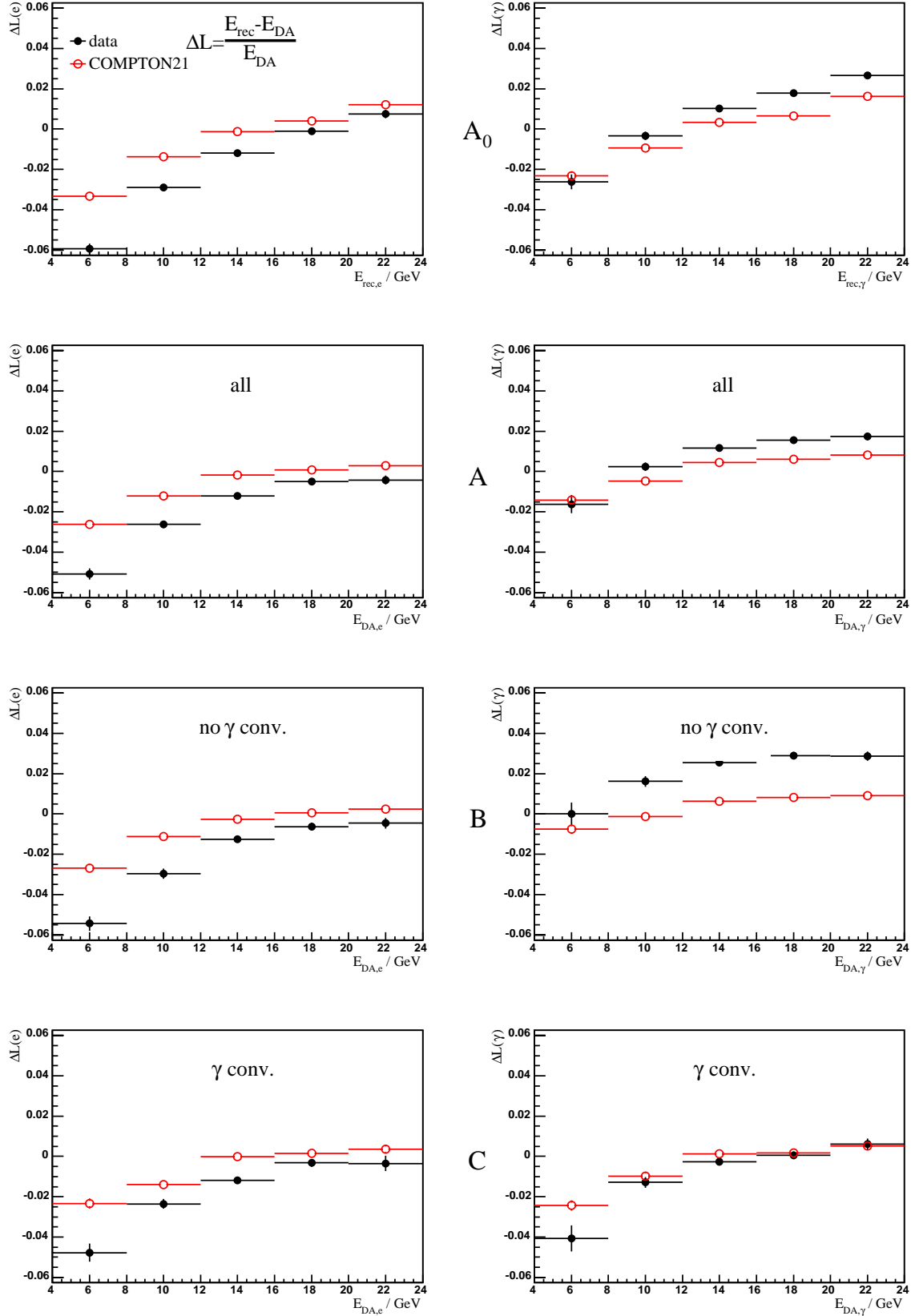


Figure 6.11: Non-linearities of energy measurement of SpaCal clusters using elastic Compton events, for electrons (left column) and photons (right column) versus energy. A_0 : as function of reconstructed energy E_{rec} , A...C: as function of double angle calculated energy E_{DA} . Sub-selections of the Compton sample are plotted in row B, unconverted photons only, and row C, converted photons only.

good reference is probed by comparing E_{DA} to the energy values on generator level:

$$\Delta D(E_{\text{gen}}) = \frac{E_{\text{DA}} - E_{\text{gen}}}{E_{\text{gen}}}. \quad (6.9)$$

The corresponding distributions are displayed in Figure 6.12, again for both electrons and photons. The $\Delta L'$ distributions indicate a similar shape as observed previously for ΔL . The curves serve the final energy calibration step (s. Section 6.2.3-IV). The double angle energy agrees well with the generated energy for all energies without systematic deviations. Only a few bins do not coincide with $\Delta D = 0$ due to too low statistics. Therefore, double energies are considered to be reliable references.

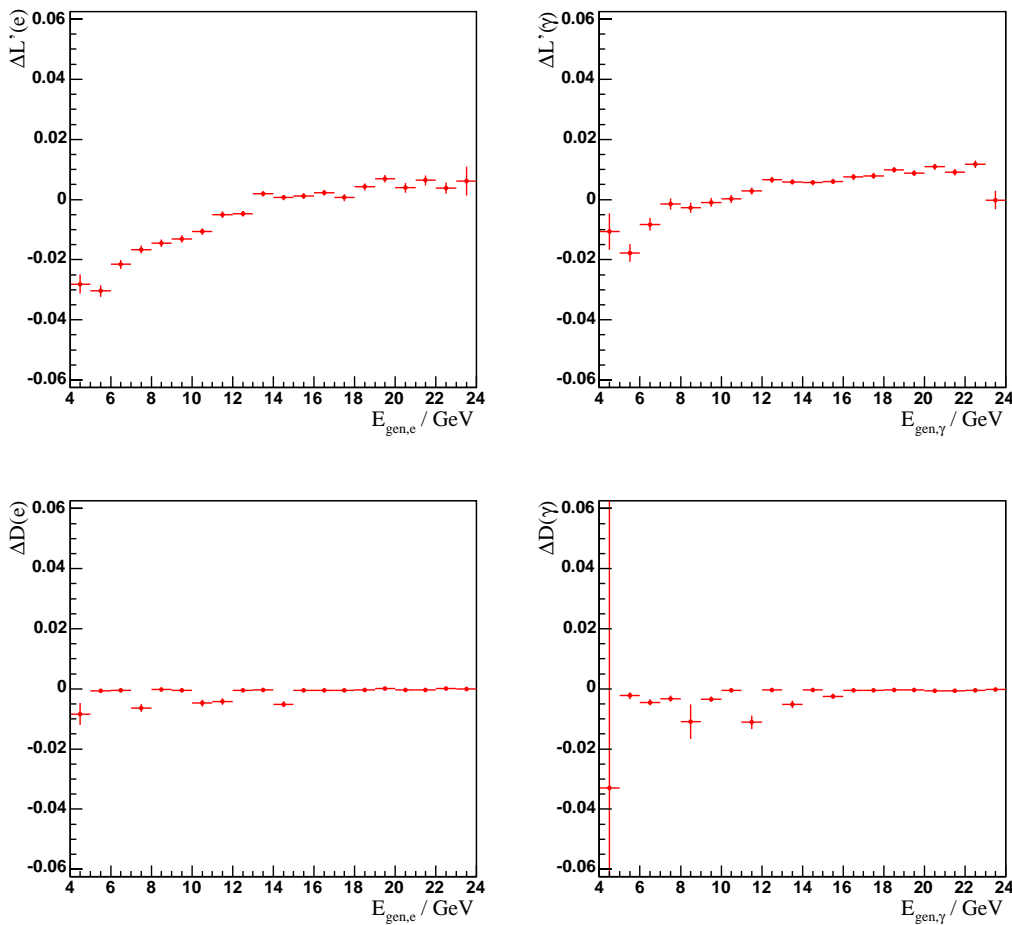


Figure 6.12: Energy reconstruction in Monte Carlo, upper row: relative difference ($\Delta L'$) between MC-reconstructed and generated particle energy for electrons and photons. Lower row: relative difference between double-angle energies and generated particle energies (ΔD). All plots are given as function of the MC-generated particle energy.

6.2.3 Correction of non-linearity

In the following the measured non-linearities are extracted to recalibrate reconstructed energies of electrons and photons separately. For this purpose the sub-samples of unconverted and converted photons, respectively, are used again. The aim is to let the non-linearities in data and simulation coincide as good as possible by shifting the experimental energy values (and thereby ΔL) to those yielded by the simulation. Taking into consideration the limited event statistics the number of variables in which ΔL can be differentially analysed is also limited, generally to one or two. Naturally these are the cluster energy and polar angle.

I) Calibration for electrons and converted photons

After the agreement of double-angle energies with generated energies has been verified it is possible to calculate and use double angle reference energies. The track-based polar angles of the electron and the (converted) photon are used for this purpose. The polar angle of the photon can be calculated from its associated BDC-track and, thus, the angle measurement for the photon is just as precise as that for the electron. This means especially that in this case no systematic spatial effects from the SpaCal cluster reconstruction can influence the polar angles as the method is purely track based.

II) Calibration for electrons and unconverted photons

For the unconverted case two alternative solution paths for the correction of the measured non-linearity are possible:

a). For electrons the ΔL in this sub-sample differs only slightly from the ΔL distribution of the sub-sample in step **I**), s. Figure 6.11. A strategy would be just to correct all electrons independently according to the correction procedure in the conversion case. However, this appeared to be a rather inconsistent treatment as it is a solely numerical correction neglecting other physical aspects. This leads to case

b). A second strategy is given by applying the correction for electrons from the conversion case and start a special treatment for those differences left over after the first step. These remaining differences between electron data and MC are then attributed to uncertainties of the photon polar angle entering the double angle formulae. Because of the absence of a photon-induced track only the calorimetric photon position is available. In addition to other known systematic effects of the SpaCal cluster reconstruction, the position of e.m. clusters is known to be reconstructed at systematically higher radial positions in the SpaCal compared to the true impact point [49]. The observation was made especially in the inner region of the backward calorimeter using electron clusters for which an alternative angle measurement exists through track information.

In the following the method of the correction of the photon polar angle is discussed. The angle is shifted by some small amount such that the remaining non-linearity difference for the *electron* vanishes. The amount of the correction can be extracted from the double angle equations. Using the definition $c(\vartheta_\gamma) = \Delta L_e = E_{\text{rec}}^e / E_{\text{DA}}^e - 1$, and respecting $\vartheta = \pi - \theta_{\text{H1}}$ for all polar angles, the following derivative is calculated using the angle dependencies of Eq. 6.7:

$$\frac{dc}{d\vartheta_\gamma} = \frac{E_{\text{rec}}^e}{2E_{\text{beam}}} \cdot \frac{\cos \vartheta_\gamma + \cos(\vartheta_e + \vartheta_\gamma) - (\sin \vartheta_\gamma + \sin \vartheta_e + \sin(\vartheta_e + \vartheta_\gamma)) \frac{\cos \vartheta_\gamma}{\sin \vartheta_\gamma}}{\sin \vartheta_\gamma}. \quad (6.10)$$

This formula yields the photon angle correction $\Delta\vartheta_\gamma$ which is required to shift the electron's ΔL_e by an amount equal to the (observed) difference $\Delta c = \Delta L_{\text{data}} - \Delta L_{\text{MC}}$:

$$\Delta\vartheta_\gamma(\vartheta_e, \vartheta_\gamma) = \frac{\Delta c}{\left(\frac{dc}{d\vartheta_\gamma}\right)(\vartheta_e, \vartheta_\gamma)}. \quad (6.11)$$

This angle correction can also be interpreted in terms of a shift of the photon cluster z -coordinate from the nominal value used in the cluster reconstruction. The amount of the shift follows as

$$\Delta z_\gamma = r_\gamma \left(\frac{1}{\tan \vartheta_\gamma} - \frac{1}{\tan(\vartheta_\gamma + \Delta\vartheta_\gamma)} \right), \quad (6.12)$$

where r_γ represents the radial position of the photon cluster in the calorimeter at the nominal z -coordinate of the cluster. The angle correction is histogrammed in Figure 6.13-left by the ratio $\Delta\vartheta_\gamma/\vartheta_\gamma$ as function of the photon polar angle θ_γ . As shown there, the correction is applied to θ_γ for the two highest bins only, while all other angles are left unchanged. The number of events affected by the correction is given by the box sizes in the histogram. The typical magnitude of the angle correction is of the order of 2-3% of ϑ_γ . At the average SpaCal cluster z -position (≈ -161 cm) this corresponds to a shift in the cluster radial position of about $\Delta r \simeq 8$ mm at maximum. For the alternative case that one interprets the angle displacement not by a radial position shift but by a shift of the cluster z -position the Δz of Eq. 6.12 is also plotted in Figure 6.13-right.

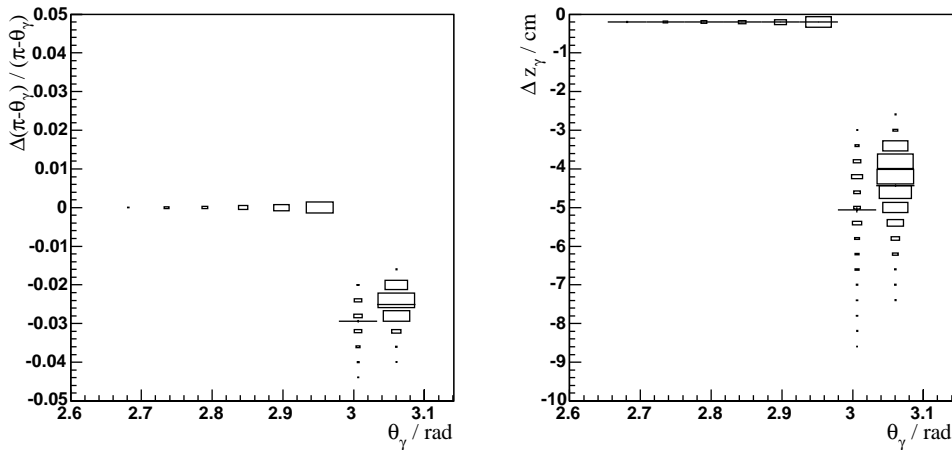


Figure 6.13: Left: Polar angle correction $\Delta\vartheta_\gamma/\vartheta_\gamma$ of the unconverted photon versus its polar angle θ_γ in data events as required for the electron calibration. The right figure shows the same set of events where the angle shift is interpreted as a cluster z -shift. In both histograms the mean value of the correction per polar angle bin is represented by a Gaussian mean from a fit along a bin slice. The number of events underlying the correction procedure is given by the box sizes.

Clearly the situation for unconverted photons is difficult because of both, the comparatively imprecise calorimetric polar angle information and the energy calibration. A study in which *converted* photons with a reconstructed BST track were probed for their calibration [50] showed that there is no major difference to electrons in terms of non-linearity or polar angle. This is in agreement with the measurements presented in this analysis. The precision of the calorimetric angle measurement can be checked for electrons and photons by comparing θ_γ of BDC and SpaCal. The maximum deviation between these angles is not exceeded by more than ≈ 1 mrad. However, as explained in Section 6.2.1 and above it does not seem justified to infer from these earlier findings [50] that the same still holds for *unconverted* photons.

The effect is in principle supported firstly by the observation of a systematically higher reconstructed SpaCal radial position (equivalent to a lower measured θ_{H1}) of electromagnetic clusters especially at low SpaCal radii. This means that the true θ is in fact higher than the measured one. And secondly, it is supported by the higher radiation length of photons of $9/7 X_0$ compared to the electron

value X_0 . This corresponds to a backward shift in z of the cluster barycenter[¶], which causes (photon) polar angles to be modified in the same direction as by the first effect. Because the standard cluster reconstruction cannot account for this effect and because a cluster's z -position cannot be measured directly and independently, the measurements fit well into the picture.

The average z_{clus} -shift values of 4-5 cm appear to be rather high compared to what one would expect from the consideration of the different radiation lengths between electron and photon. Also, the simulation of the electromagnetic shower development in the SpaCal should not be wrong by such an amount of a few cm (for detail aspects see for example [51]). Therefore, it seems much more likely that a larger fraction of the assumed positional uncertainties originates in the reconstruction of the radial position returned by the standard cluster reconstruction program.

III) Calibration of the unconverted photon

In the last energy calibration step the remaining differences observed for unconverted photons are compensated by shifting ΔL_{data} to ΔL_{MC} . Such a correction accounts for the general shift for this class of photons. These experience no energy loss due to the absence of any interaction with the passive material in front of the calorimeter. In other ep processes than QED Compton, used for calibration (as for example DIS with a single backward scattered electron), any energy loss in front of the calorimeter becomes integrated and averaged out in the basic calibration process. This yields the primary calibration constants entering any H1 data analysis. This could explain well why a significant shift is observed for non-interacting photons in QED Compton: the energy calibration constants applied to unconverted photons are the *same* as for electrons and tend to overcompensate the energy loss, because the reconstruction program has no information about the identity of the electromagnetic particle. A direct measurement of possible energy losses in front of the calorimeter was performed in [44, 60] using the backward drift chamber as a pre-shower detector for the SpaCal and, thus, establishing for (electron) pre-shower events a correlation between the difference of reconstructed to expected double angle energies on one side, and the total amount of electric charge, deposited by electrons and their produced secondary particles, on the other side. Although a slightly improved energy resolution was achieved in these studies, the method did not become a standard because of difficulties related to the simulation, especially to that of the BDC charge deposition.

IV) Absolute energy scale

Finally, after all ΔL have been brought onto the same levels in experimental and simulated data, the values are corrected according to the difference of MC-reconstructed to MC-generated energies, s. Figure 6.12, in order to bring the reconstructed energies onto an absolute scale. A correction function is extracted from the simulation by fitting a low-order polynomial which is applied to MC as well as to the data.

As argument for all the described recalibration corrections the reconstructed particle energies are used. Again, the reason for this is that the double angle energy calculation is not valid anymore in the inelastic process due to the different kinematic situation in these events: the presence of hadronic final state particles changes the scattering angles of the Compton electron and photon. This becomes drastically visible when one allows inelastic events only to pass the event selection the measured non-linearities are systematically shifted by unrealistic amounts of $\approx 10\%$ and beyond.

[¶]The effect is expected to be small as $2/7 X_0$ is only $\simeq 0.3$ cm.

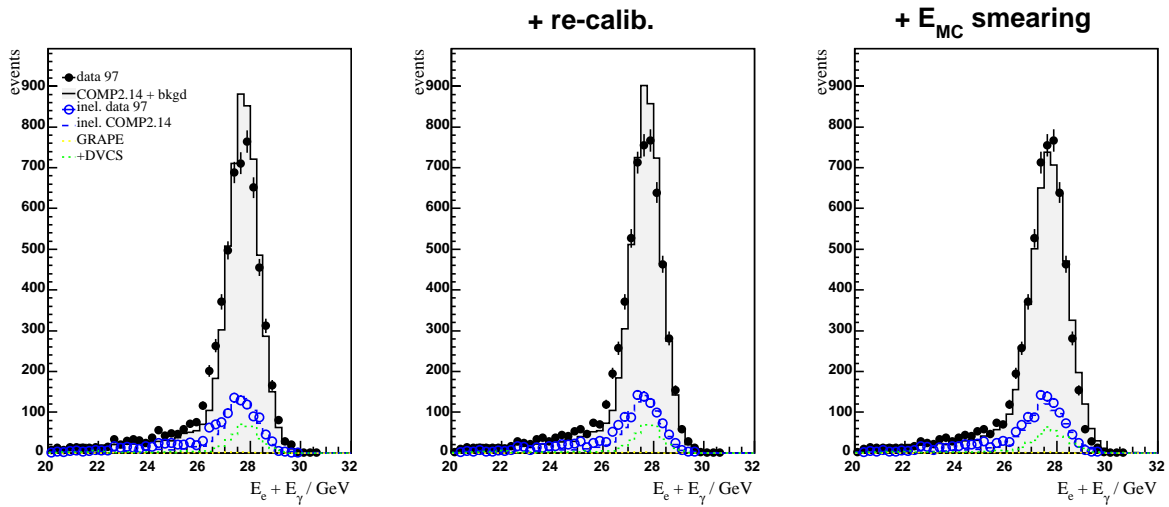


Figure 6.14: Energy sum of Compton electron and photon, left: raw reconstructed energies, middle: after recalibration as explained in the text, right: after recalibration and additional Gaussian smearing of the simulated energies.

6.2.4 Additional energy smearing in MC

After the preceding calibration procedure the simulated and measured mean energies are harmonized. This has been done in such a way that the energies exhibit an as similar as possible dependence on the kinematic variables, like cluster energy and polar angle. But the resolutions of Monte Carlo and data still might be different. Therefore, the energy sum of the reconstructed electron and photon energies was compared as well, for both event samples, data and Monte Carlo. The result is shown together with the background samples in Figure 6.14-left without application of the previously determined calibration constants on reconstructed energies. The total energy peaks, as expected from the kinematics in QED Compton, around the beam energy of 27.6 GeV. It is visible that the full Monte Carlo and the data distributions have slightly different widths in the kinematic peak. The middle histogram of the same Figure shows the energy sum after the recalibration process as discussed in the previous paragraphs. Although the full Compton energy shows no major shifts between the peak center positions in the uncalibrated case, the calibration brings both distributions closer in their shapes. The remaining differences near the peak centers and the lower flanges is ascribed a slightly better resolution in the simulation causing a smaller peak width. The effect is compensated by broadening the MC distribution using a Gaussian random function, by which each cluster energy is randomly smeared by 1.5% of its reconstructed value. The result is displayed in Figure 6.14-right. Finally, both data and MC agree much better than before this measure.

6.3 Trigger

This chapter describes the various trigger stages relevant for the recording of QED Compton events in H1 and their influence on the event selection efficiency. The principle mechanism of the multiple decision levels is explained in Section 3.3.

6.3.1 Compton trigger setup

The first level of the H1 event trigger during the 1997 ep collision period was set up in order to collect Compton events among other event types. The main trigger condition of the corresponding Compton subtrigger was constructed for this purpose according to a boolean combination of fundamental trigger elements available in the H1 data acquisition setup:

$$s_{13}^0 = (\text{SPCLe_IET}>2 \vee \text{SPCLe_IET_Cen_3}) \wedge \text{SPCLe_ToF_E_2} \wedge \overline{\text{DCr}\varphi_Tc} \quad (6.13)$$

where the first three trigger elements represent conditions on preset minimum energy depositions in the backward calorimeter to be signalled by the Inclusive Electron Trigger (IET). Their meaning and involved thresholds are listed in Table 4. Also listed in there is the fourth component of s_{13}^0 which denotes the *negated* central drift chamber (DC) trigger element T_c . The condition suppresses events in which at least three tracks occur with each having a minimum transverse momentum p_t of 420 MeV/c. In addition the DC track trigger provides two further elements, T_a and T_b , which ask for at least one track and two tracks, respectively, each element requiring the same p_t condition to be fulfilled.

Table 4: *The trigger element definitions of the Compton trigger and their corresponding physical conditions. The 'inner SpaCal' region is defined as all calorimeter cells placed within the range of $-16 \text{ cm} < x < +8 \text{ cm}$, $-8 \text{ cm} < y < +16 \text{ cm}$, the remaining area is denoted as the outer SpaCal.*

Name of trigger element	trigger type and location	condition/threshold
SPCLe_IET>2	electromagnetic cluster energy, outer SpaCal	$E > 6 \text{ GeV}$
SPCLe_IET_Cen_3	e. m. cluster energy, inner SpaCal	6 GeV
SPCLe_ToF_E_2	e. m. cluster(s) energy sum, full SpaCal	12 GeV
DCr φ _Tc	for each of $n \geq 3$ tracks in CTD, $r > r_{CJC-2}$	$p_t > 420 \text{ MeV/c}$

This combination of trigger elements accounts for the Compton event topology as it is sensitive to two clustered energy depositions. In comparison with the outer calorimeter range (Figure 3.4) the nomenclature is slightly different for the central region because in the inner SpaCal the thresholds were set to higher values. These were necessary to suppress high energetic photons originating from synchrotron radiation generated by the electron beam in conjunction with the last bending magnetic field on the $+z$ -side of the experiment. Since the photons have trajectories close to the beam and are thus able to hit the inner cells of the calorimeter the corresponding central Local IET surrounding the beam whole of the SpaCal is treated separately.

At last the main trigger component s_{13}^0 is combined to the pre-final s_{13} (*i.e.* before subtrigger prescaling is applied) including further anti-background trigger elements which are commonly used among many other level-1 subtriggers as well:

$$s_{13} = s_{13}^0 \wedge v_3 \wedge f_0 \quad (6.14)$$

using the definitions

$$\begin{aligned} v_3 &= \overline{\text{BToF_BG}} \wedge \overline{\text{VETO_inner_BG}} \wedge \overline{\text{VETO_outer_BG}} \wedge \overline{\text{SPCLh_AToF_E_1}}, \\ f_0 &= \text{ToF_IA} \vee \overline{\text{FToF_BG}}. \end{aligned} \quad (6.15)$$

The meaning of these trigger elements is:

$\overline{\text{BToF_BG}}$	suppress background signalled by the ‘‘backward, time-of-flight’’ scintillator
$\overline{\text{VETO_inner_BG}}$	suppress background signalled by the inner veto walls
$\overline{\text{VETO_outer_BG}}$	suppress background signalled by the outer veto walls
$\overline{\text{SPCLh_AToF_E_1}}$	suppress hadronic activity in the (had.) SpaCal exceeding some threshold
ToF_IA	require a general Time-of-Flight signal within ep -interaction time window
$\overline{\text{FToF_BG}}$	suppress background signalled by the forward ToF scintillator.

One further fundamental property of the Compton subtrigger on the first trigger level is that no cut on the Compton acoplanarity is imposed. This means that the construction of the trigger also allows topologically similar processes to contribute to the collected event sample, *e.g.* deep inelastic scattering events with final state radiation. The topology of these can resemble an inelastic Compton event where the azimuthal angle between electron and photon is very small. Such events are suppressed in the analysis chain by a corresponding cut on the acoplanarity although there is no physical quantity to strictly distinguish between both types of events.

Efficiency of the IET trigger

As a consequence of the high IET trigger efficiency measured for individual electromagnetic clusters a very high overall efficiency of the calorimetric trigger part can be expected in QED Compton events. This follows from the combined inefficiency

$$\begin{aligned} \varepsilon_{\text{calo-s13}} &= 1 - (1 - \varepsilon_{\text{IET}})^2 \\ &= \varepsilon_{\text{IET}} (2 - \varepsilon_{\text{IET}}), \end{aligned} \quad (6.16)$$

where ε_{IET} represents the single IET trigger efficiency. For the topological case with an outer and an inner Compton cluster, the efficiency amounts to $>99\%$ when the single trigger efficiency is assumed to be in the range of 95% or higher. Concerning the trigger part connected to the total SpaCal energy (SPCLe_ToF_E_2) it can be stated that the complete electromagnetic energy deposition is well above the threshold of 12 GeV. Furthermore, the threshold of the trigger efficiency curve is by far exceeded by both, the conditions on the 4th trigger level and the final analysis cut which asks for at least 20 GeV total energy measured in the calorimeter for the two leading e.m. clusters together.

6.3.2 Drift Chamber $r\varphi$ trigger on level 1

The track trigger uses hit information from the central tracking area to recognize particle track patterns in the narrow time window between two consecutive bunch crossings. For this purpose the DC $r\varphi$ trigger continuously compares incoming drift chamber hit signals with a multitude of pre-calculated patterns. Because the trigger requires a minimum number of layers of the inner and outer jet chambers (seven and three layers respectively), the polar angle acceptance range is limited by the radial position

of the outer sense-wire layer in CJC2 used for this trigger. This radial position is given by $r = 58.72$ cm. For the low angle range on the $+z$ end of the CJC such a radius corresponds to a track polar angle of $\theta \approx 28^\circ$.

The Compton subtrigger contains the track trigger element T_c which does not allow more than two of such tracks with transverse momenta above $420 \text{ MeV}/c$ in the hadronic final state. With higher track multiplicities than this, in the hadronic final state, $\overline{T_c}$ becomes inactive and, thus, no positive trigger signal can be generated anymore by s_{13} (s. Eq. 6.13).

This poses a problematic situation with respect to the selection of the inelastic channel. It is therefore necessary to figure out the suppression factor caused by the track component of the Compton trigger. This trigger is already demanded during the event recording and thus the efficiency cannot be extracted from the same event data. Instead, an independent Compton selection must be used which does not contain elements of the DC $r\varphi$ trigger. The *minimum bias* (“MB”) data of the corresponding taking period (being the last part of the whole 1997 data period) offer a possibility to make an independent measurement. In this phase a modified overall trigger setup was applied to the trigger system of H1 using a reduced and simplified set of subtriggers on level 1. Therefore, the Compton channel was recorded by other triggers, especially by inclusive electron subtriggers involving the SpaCal. Thus, an additional Compton selection was carried out on the data of this period under the requirement of the special minimum bias subtriggers

$$s_0^{\text{MB}} = \text{SPCLe_JET}>1 \quad \vee \quad \text{SPCLe_JET_Cen_2}, \quad \text{and} \quad (6.17)$$

$$s_3^{\text{MB}} = \text{SPCLe_JET}>2 \quad \vee \quad \text{SPCLe_JET_Cen_3}. \quad (6.18)$$

Both are purely calorimetric triggers, the thresholds amount to 2 GeV for each of the s_0^{MB} elements, whereas they are 6 GeV for each element in s_3^{MB} . For the event selection the same criteria were applied as for the Compton analysis of the standard period except for specific cuts on run number ranges which are different in minimum bias.

In order to check the trigger response the three highest polar angles of all hadronic final state LAr clusters are calculated for each event of the MB sample. Then the trigger element efficiencies of T_a, T_b, T_c are viewed as function of each of these polar angles $\theta_0, \theta_1, \theta_2$ (sorted decreasingly with the index $0 \dots 2$). The cluster angles are required to match within 0.1 rad at least one polar angle of all CJC-tracks reconstructed in the event. The result is plotted in Figure 6.15. For comparison also efficiencies from a DIS sample in the standard period are superimposed. No *standard* reconstructed vertex must be required in both data samples in order to not bias the track selection. The maximum angle of any LAr cluster is restricted to $\theta_0 < 2.5 \text{ rad}$ in all cases to avoid mixing with one of the Compton clusters or their track pieces in the backward part of CJC, respectively. For the efficiency representation the resulting curves were fit by Fermi-type functions of the form

$$f(\theta) = \frac{p}{1 + \exp\left(-\frac{\theta - \theta_0}{w}\right)} \quad (6.19)$$

The fit results for the plateau p , threshold θ_0 and width w were found to be insensitive to changes of a cut on the minimum HFS cluster energy. In order to exclude noisy LAr cells a cut on the minimum energy was set to 10 MeV per cluster.

In Figure 6.16 the efficiency of the track trigger is shown using the preselected event samples without any detailed cuts applied and comparing Compton data and MC of the standard data acquisition period. As reference also a DIS sample was studied. The histograms show the efficiency of the trigger element T_c as function of the first and third track angle. The principal observation is that data and Monte Carlo do agree nearly perfectly in all distributions, especially the behaviour below and around the efficiency threshold at polar angles of $\approx 30^\circ \dots 50^\circ$.

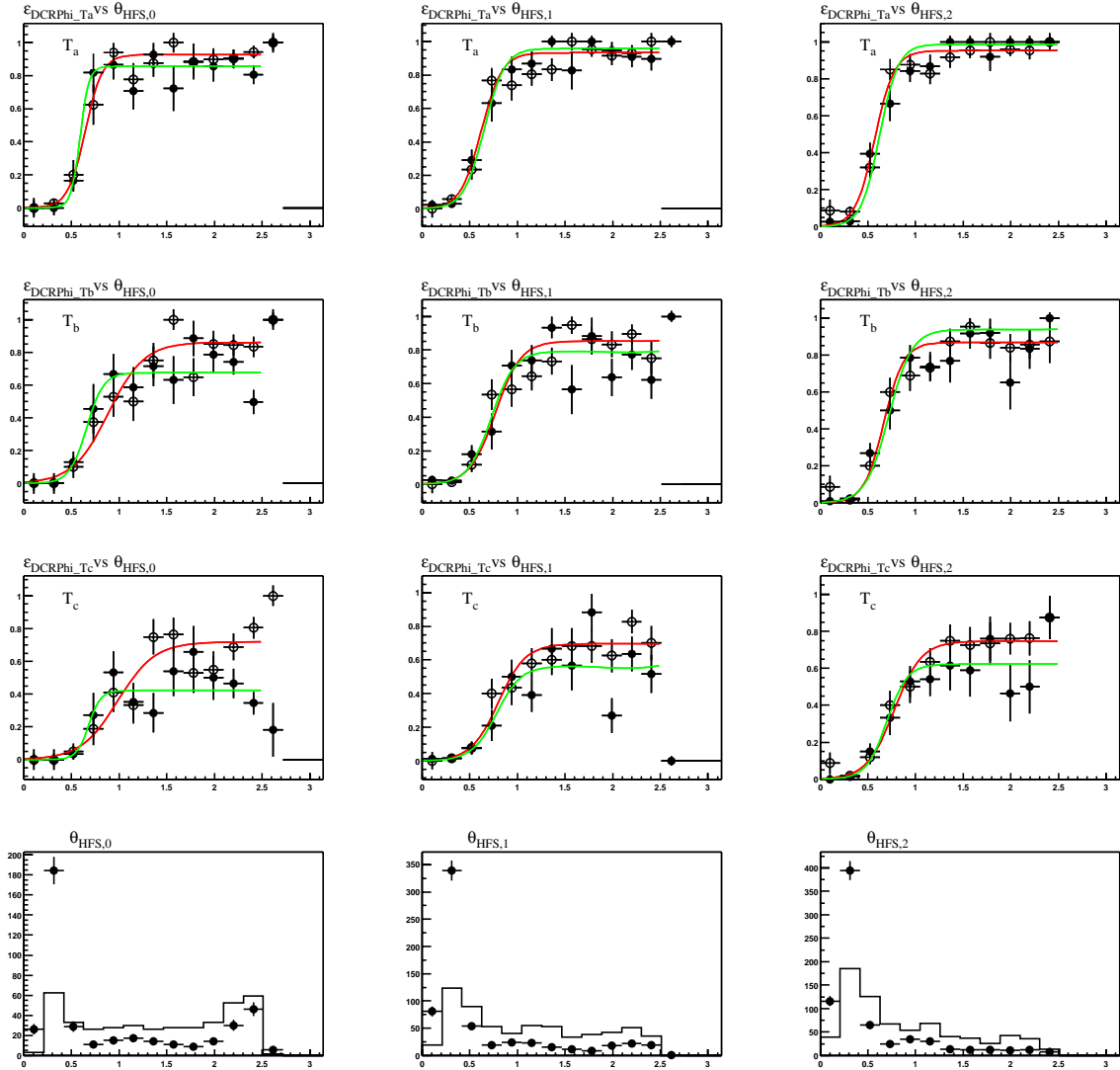


Figure 6.15: Efficiencies of DC $r\varphi$ trigger elements T_a , T_b and T_c using a minimum bias Compton selection (full circles) as function of the θ -sorted LAR clusters (θ_0 , θ_1 and θ_2). DIS selection results (open circles, full line) are shown for comparison. The lowest row displays the (normalized) distributions of $\theta_{0\dots2}$. All angles are measured in rad.

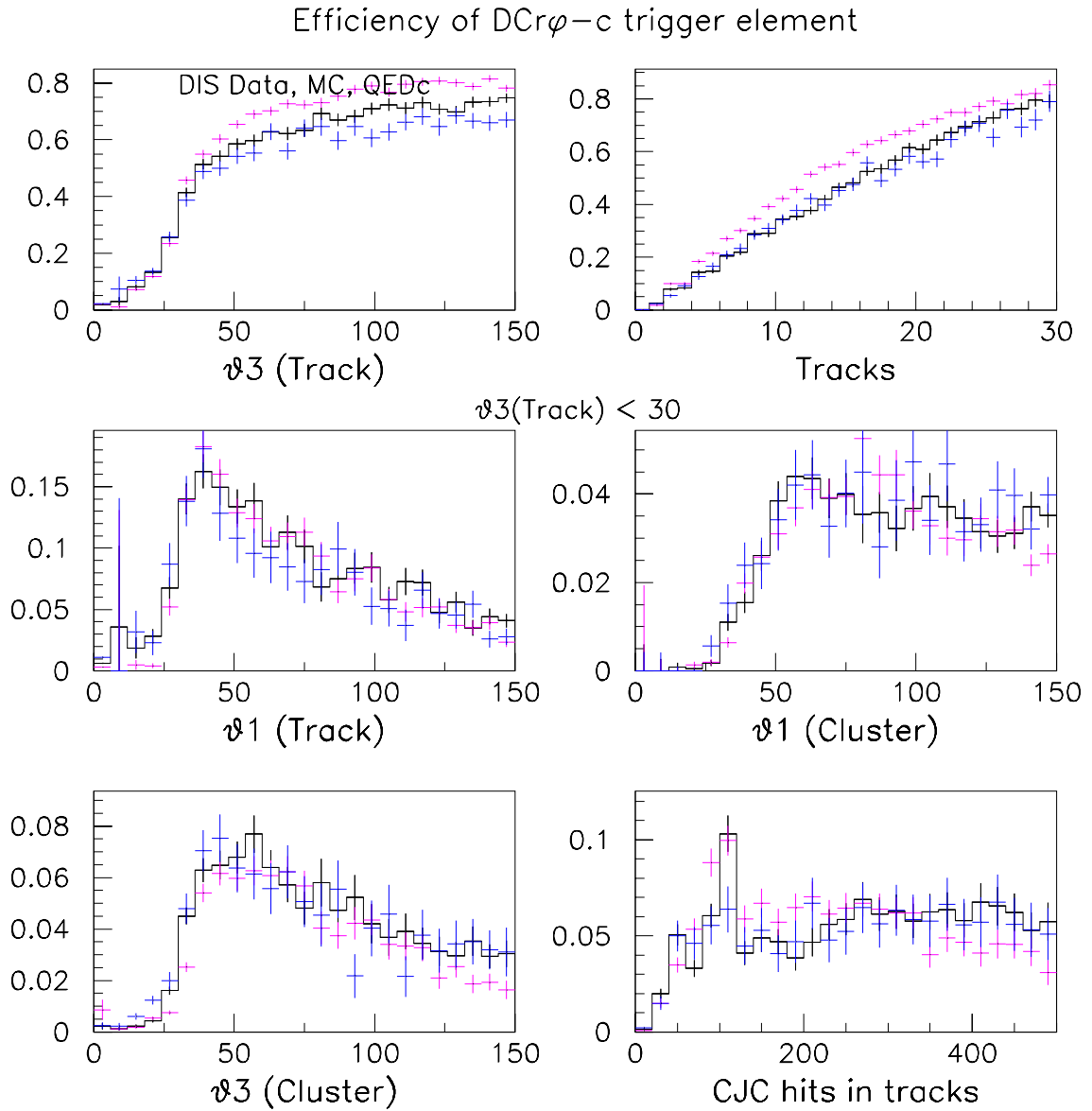


Figure 6.16: Alternative check of the $DCr\phi$ efficiency, trigger element T_c , diagrams using several quantities: ϑ_3 angle of third LAr cluster (all polar angles ϑ measured in $[\circ]$). The T_c -efficiency is also given as function of the total number of central tracks (right top) and number of CJC hits of all tracks (right bottom). No major deviations are observed between Compton data and MC.

6.3.3 Topological trigger on level 2

An additional trigger requirement was set up on the second level of the trigger system to verify that proper Compton events have been selected on level 1. The trigger element responsible for this selection is realized by a special mechanism which is sensitive to the characteristic topology of the Compton acoplanarity. By a well-defined combination of the IET cluster bits the trigger element L2 t18 signals “back-to-back” cluster configurations in the SpaCal plane. For this purpose four different maps of ToF cluster bit-groups had been arranged to form $\approx 90^\circ$ wide areas opposite in azimuth. These areas represent patterns from which the covered active cluster bits are combined (OR-ed) for the trigger-signal formation. The latter requires at least one active cluster bit above one of several energy thresholds in each of the opposite areas. The patterns are oriented in four directions in total by rotation in steps of 45° .

The detailed structure of the cluster bit assignment to each of the resulting configurations depended somewhat on the available hardware resources and, therefore, it was not possible to implement them identically for all areas (s. [61]). This also caused the step-like structures shown in Figure 6.17. But due to the overlapping arrangement and the “soft” edges of each IET trigger bit acceptance holes were avoided.

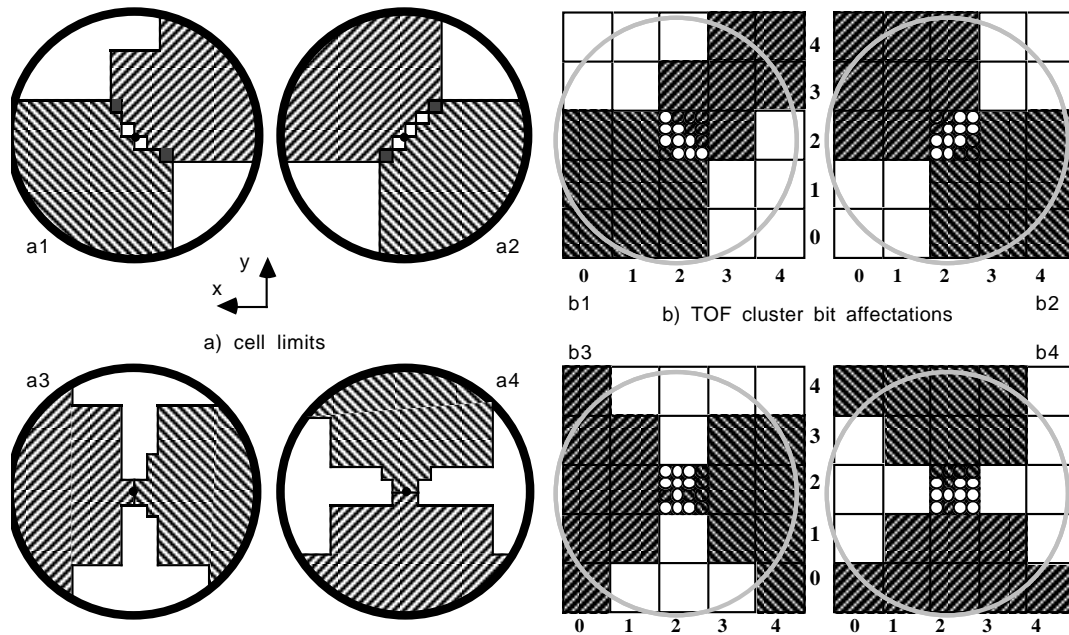


Figure 6.17: Realization of the L2 Topological Trigger element “t18” for the detection of QED Compton events using the SpaCal. The geometrical limits of the calorimeter are represented as big circles. Left, a1-a4: schematic function principle. Right, b1-b4: actual cluster bit sharing realized for the real trigger implementation. Two minimum energy depositions must be detected in two opposite hemispheres (shaded areas) of at least one of the four patterns 1-4. (Taken from [61]).

A test for the appropriate functioning of the level-2 trigger element can be performed using runs where the L2- and L4-filters had been operated in *transparent mode*. In these runs, the event rejection on the trigger stages L2 and L4 was disabled and events were passed through them while they had to be accepted only by subtriggers on L1. The requirement of disabling also the L4-filter is necessary for the efficiency measurement to exclude further event rejection as L4 decides on selection or rejection

of a Compton event by specific conditions as well.

In a special sub-selection of the Compton data sample all non-transparent runs were excluded. Compared to the bulk data set only about 30 runs passed this selection containing ≈ 1800 events in total. These runs are mainly concentrated in the first half of the 1997 standard run range. Further, the trigger phase for these runs was mostly at “1” where generally high prescales are set for the L1 subtriggers (typically 100 for s_{13}) leading to a high suppression of the available statistics. In order to detach the verification mechanism between L1 and L2 (“matrix”) and, thus, avoid further suppression, only the corresponding L2 trigger element, instead of the final L2 subtrigger, will be tested for the following efficiency measurement. Due to the low statistics neither detailed selection cuts nor an explicit electron/photon identification can be applied, which is not necessary anyway as the test aims on the topological sensitivity of the trigger only. Thus, the following simple calorimetric conditions were imposed:

- $|E_{\text{e.m. SpaCal}} - E_1 - E_2| < 1 \text{ GeV}$
- $E_{1,2}^{\text{veto-cells}} < 1 \text{ GeV}$
- $E_{\text{had. SpaCal}} < 1 \text{ GeV}$
- $r_{1,2} > 10 \text{ cm}$,

which correspond to the final selection criteria. About 1250 events remain before the cut on the SpaCal radius and 795 events after it. The resulting efficiency of the trigger element t18 of the topological trigger is shown in Figure 6.18-left versus acoplanarity between the two observed electromagnetic clusters. Up to $|\text{ACO}| \approx 1.8 \text{ rad}$ ($=103^\circ$) the efficiency sustains 100%. With the limit $|\text{ACO}| < 1.5 \text{ rad}$ the efficiency displayed versus the cluster energy sum also shows no losses (same Figure, right). Of these 524 events only one is rejected due to the t18 trigger element, in good agreement with [37].

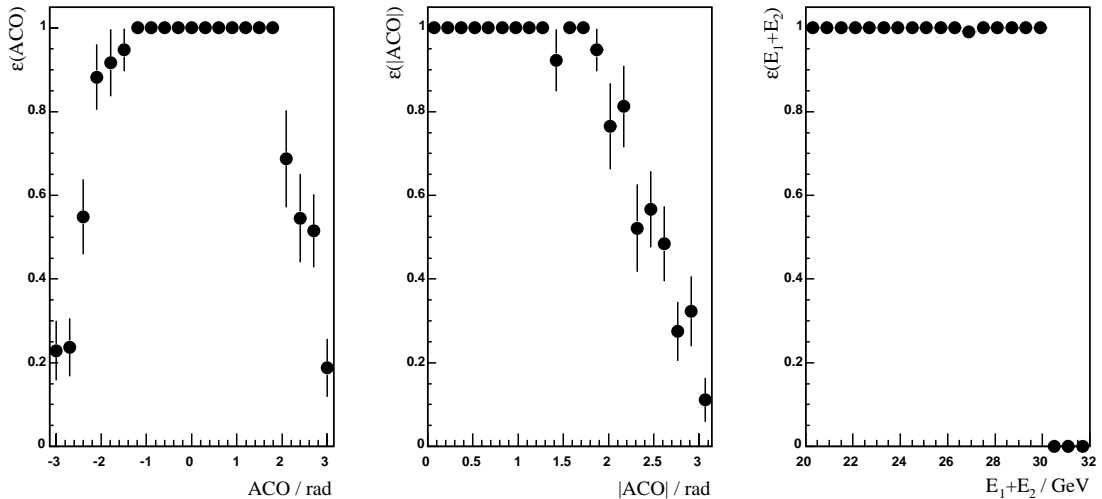


Figure 6.18: Efficiency of the trigger element t18 of the level-2 topological trigger versus acoplanarity (left, middle) and versus energy sum (right) of Compton photon and electron for $|\text{ACO}| < 1.5 \text{ rad}$.

6.4 Vertex weighting

After a consistent Compton vertex measurement in data and simulation has been made, additional z_{vtx} -dependent reweighting factors have to be applied to the simulation. This is necessary to account for slightly different shapes of the vertex distributions in data and MC: since a given event vertex position determines the subdetector acceptance range different fractions of events fall into acceptance (or out of it) in both event sets. A corresponding reweighting function can be calculated as the ratio of the fit functions of the simulated and the measured vertex histograms. To ensure that only the vertex shapes enter the calculation the histograms are normalized first. The fit function is of the form

$$f_{\text{vtx}}(z) = c \exp\left(-\frac{(z - z_0)^2}{2\sigma^2}\right) + b \quad (6.20)$$

where a parameter b is added to a Gaussian to account for the flat base of the distributions, visible especially in the tails of data events. The reweighting function follows then as

$$w_{\text{vtx}}(z) = \frac{f_{\text{vtx}}^{\text{data}}(z)}{f_{\text{vtx}}^{\text{sim}}(z)} \cdot \frac{a_{\text{sim}}}{a_{\text{data}}} \quad (6.21)$$

with the normalization factors $a_{\text{sim}} = \int f_{\text{vtx}}^{\text{sim}}(z) dz$ and $a_{\text{data}} = \int f_{\text{vtx}}^{\text{data}}(z) dz$ in the range $z = -40 \dots +40\text{cm}$. The argument z of the weighting factor w_{vtx} is given by the simulated Compton vertex position. Because the vertex distribution of the Compton data sample has a smaller statistical precision the much larger DIS event selection is used instead as input for $f_{\text{vtx}}^{\text{data}}$, where the same run selection is applied as in the case of Compton data. This is done under the assumption that the Compton data sample is a proper sub-sample of the DIS selection as the same inclusive subtriggers collect both event classes. Thus, the shape of the DIS vertex distribution should well represent the Compton vertex, too. Furthermore, using the DIS reference sample is advantageous because the hadronic final state does not need to be restricted to a maximum polar angle as it is necessary for the Compton selection due to the involved DC $r\varphi$ trigger (see section 6.3.2). This means that the DIS vertex is better defined, in general, because also central tracks with a larger polar angle contribute to the (standard) vertex reconstruction.

The vertex fit functions and the resulting reweighting function w_{vtx} are displayed in Figure 6.19. As can be seen w is of the order of 1 over most of the z -range but steeply rises at the edges. This can be understood from the pure Gaussian simulation where no constant base was added such that the Monte Carlo fit function can assume very small values and the ratio w becomes large. However, only a few Monte Carlo events are affected from higher weights which do not exceed values of 2 within the final vertex range.

The complete vertex distribution displays Figure 6.20. As the histograms show the overall shape of the experimental vertex is well described by the simulation. But the reconstructed vertices in both cases seem to be shifted with respect to each other: the simulated distributions is systematically lower than the data for $z < 0$ and above the data for $z > 0$. This can be attributed to the CIP vertex reconstruction and the problems found in the analysis of the CIP efficiency and pad behaviour around the chamber's wire supports, as described and discussed in Section 5.3.5.

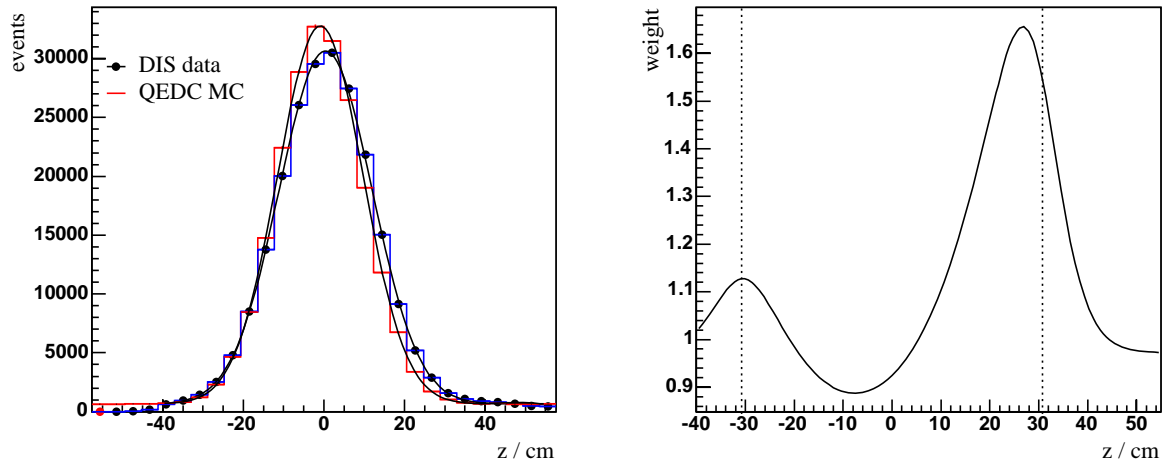


Figure 6.19: Vertex reweighting procedure. Left: input vertex distributions of DIS data sample (dots) and Compton simulation (normalized to data). Right: reweighting function used for final correction of the simulated Compton vertex. The dotted lines indicate the vertex range selected for the final measurement.

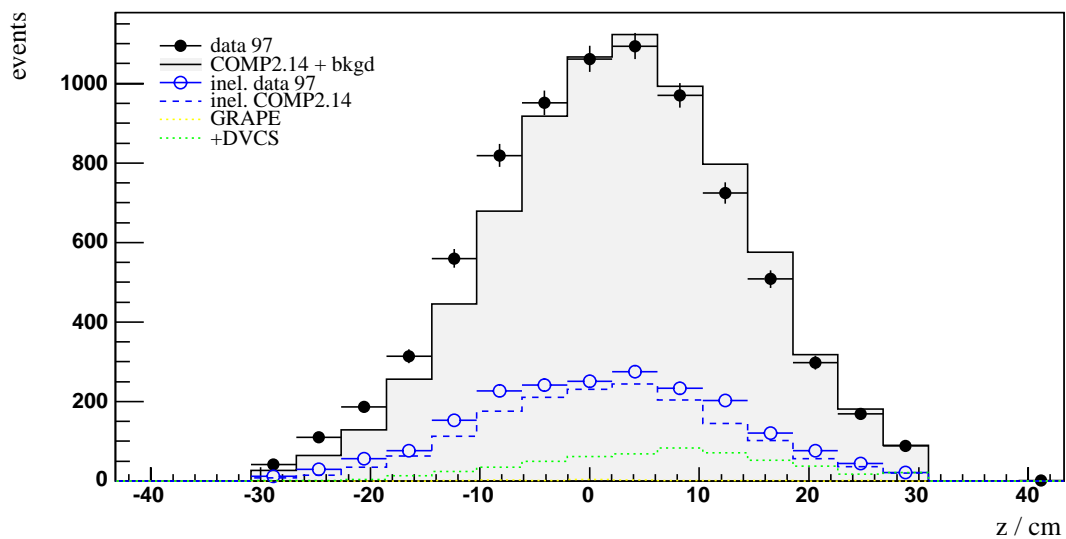


Figure 6.20: Final Compton vertex distribution of data and Monte Carlos (signal and backgrounds). Simulated events are reweighted with their respective inverse luminosities.

7 Cross section

7.1 Definition

The cross section calculation for both data and Monte Carlo follows the same steps from the number of events (sum of weights) accumulated per kinematic bin in x_i and Q_i^2 to the final result. The procedure is given by the formalism for the leading order cross section measurement:

$$\Delta\sigma = \frac{\Delta N - \Delta N_{\text{bg}}}{\mathcal{L}} \cdot \frac{1}{\varepsilon A (1 + \delta)}. \quad (7.1)$$

The double differential cross section is obtained by division of $\Delta\sigma$ with the chosen bin size $\Delta x_i \cdot \Delta Q_i^2$. The numbers ΔN and ΔN_{bg} denote the numbers of events in the data and the added background samples, respectively, in that bin. \mathcal{L} represents the corresponding integrated luminosity excluding all runs and run periods with low data quality or efficiencies as discussed in the preceding sections. The correction factor ε accounts for inefficiency effects which apply for the data sample only in the case the corresponding physical process was not simulated in the MC. The acceptance A represents a normalization factor due to insensitive regions of the experiment and other, geometrical limits (*e.g.* the beam pipe hole). But it also contains all internal inefficiencies of data and MC, which have been studied and brought in line in the analysis. Finally, a correction factor $1/(1 + \delta)$ is applied to account for the effect of higher order radiative corrections:

$$\delta = \frac{\Delta\sigma_{\text{full}}}{\Delta\sigma_{\text{LO}}} - 1, \quad (7.2)$$

where $\Delta\sigma_{\text{full}}$ corresponds to the cross section including the radiative effects and $\Delta\sigma_{\text{LO}}$ the leading order cross section. In addition to the full radiative Monte Carlo sample which has been used throughout the analysis, a second simulation has been carried out in which higher order radiative processes were not allowed during the event generation in order to determine the δ factor. The typical order of magnitude of δ is in the range of a few percent as will be shown in Section 7.5.

7.2 Kinematic range and acceptance

The kinematic range for the present measurement is established according to the preceding analysis in [37] to allow for a consistent comparison of the results. Thus, the lowest bin edge of x_i starts at $1.78 \cdot 10^{-5}$ and advances in steps of $\sqrt{10}$ in four bins, consequently up to a limit of $1.78 \cdot 10^{-3}$. The leptonic Q_i^2 varies in the range given in Table 5.

Using these definitions the acceptance can be calculated from the generated and simulated Compton event sample. The acceptance is generally defined as

$$A = \frac{N_{\text{rec}}}{N_{\text{gen}}}, \quad (7.3)$$

where N_{rec} is the number of all reconstructed events passing the full set of selection cuts, and where N_{gen} is the total number of the generated input events before any of those selection criteria is applied. Especially for N_{gen} it must be ensured already on the MC event selection stage that no event rejection takes place, for example by the cluster search performed within QESCAT. Thus, A will vary in general

Table 5: Binning of the kinematic range in leptonic variables available for the Compton scattering process. The bins in Q_l^2 are of equal width (per x_l range).

x_l	Q_l^2 / GeV^2	binning
1.78 ... 5.63 · 10 ⁻⁵	0.5 ... 4.5	4 × 1.0 GeV
0.563 ... 1.78 · 10 ⁻⁴	1.5 ... 12.0	3 × 3.5 GeV
1.78 ... 5.63 · 10 ⁻⁴	3.0 ... 38.0	3 × 11.7 GeV
0.563 ... 1.78 · 10 ⁻³	10.0 ... 125.0	3 × 38.3 GeV

in the range of 0. . . 1, but in cases with strong migrations from adjacent bins it could also exceed the value of one. For the transition from measured event rates to the cross section it is preferable to avoid large corrections due to very low acceptances since their relative errors directly contribute to the total errors of the final results. The following cuts, which are close to the limits used in the analysis (or given by the detector geometry), are applied to the generated quantities:

$$\begin{aligned}
 \theta_\gamma^{\text{gen}} \text{ and } \theta_e^{\text{gen}} &< 176.5^\circ \\
 \theta_\gamma^{\text{gen}} \text{ and } \theta_e^{\text{gen}} &> 3.5^\circ \\
 E_\gamma^{\text{gen}} \text{ and } E_e^{\text{gen}} &> 4 \text{ GeV} \\
 E_\gamma^{\text{gen}} + E_e^{\text{gen}} &> 20 \text{ GeV}
 \end{aligned} \tag{7.4}$$

The result of the acceptance determination is presented in Figure 7.1 for the whole kinematic range. In agreement with the cited previous analysis there is no visible acceptance in the highest Q_l^2 -bin. Furthermore, for the two outer Q_l^2 -bins at the lowest x_l either the acceptance is very low or the statistical uncertainty is very high, such that they also do not appear appropriate for a reliable cross section measurement.

Purity and stability

The bin widths are required to fit the experimental resolutions in the given quantities in order to reduce bin migrations effects. The level of migration between bins can be estimated and quantified using the simulated sample in which for each physical quantity the reconstructed kinematic bin is related to the true kinematic bin. The *stability* gives the fraction of events which stay in their corresponding kinematic bin i after the reconstruction, it is defined as

$$S = \frac{N_{\text{rec} \wedge \text{gen}}^i}{N_{\text{gen}}^i}, \tag{7.5}$$

while the *purity* measures the fraction of events which were not only reconstructed but also generated in i :

$$P = \frac{N_{\text{rec} \wedge \text{gen}}^i}{N_{\text{rec}}^i}. \tag{7.6}$$

Thus, P and S stand, in some given bin, for the outward and inward migration of events, respectively. Figure 7.1 shows their values over the basic kinematic range, which are typically of the order of 70% to 90%. Only in the spectrum of the lowest x_l -bin the purity drops significantly below the average: in the same distribution the two outer bins show statistical errors of 15% to 30%. Together with the result of the acceptance determination these two bins are regarded as unsuitable for the final measurement.

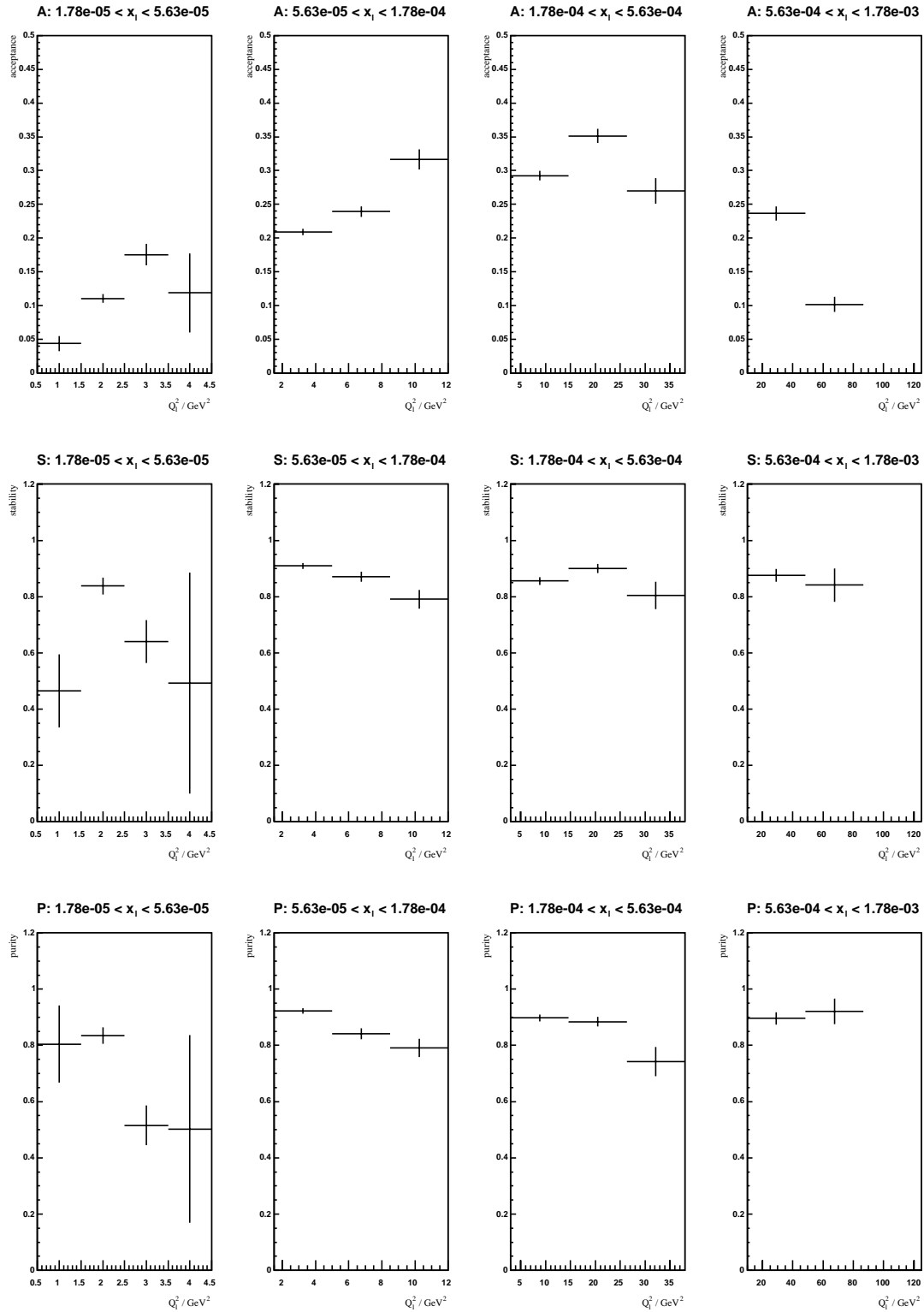


Figure 7.1: Detector acceptance (upper row of histograms, “A”), bin stability (middle row, “S”) and bin purity (lower row, “P”) determined from COMPTON generated and reconstructed events as function of Q_1^2 in different x_1 ranges as denoted. The error bars denote the correlated statistical error of the number ratios given in Eq.s 7.3, 7.5, and 7.6. All values are measured for the full Compton sample, *i.e.* elastic and inelastic contributions.

7.3 Control distributions

Before applying the acceptance corrections and calculating the final results the most important physical properties are discussed. Figure 7.2 shows the distributions of the energy, the SpaCal radial position and the azimuthal angle for the first and the second Compton cluster for which the energy relation $E_1 > E_2$ holds. The background is nearly completely made up of DVCS events, while the di-lepton induced background does not contribute noticeable event rates. Note that the deep inelastic scattering background is not displayed because of its expected low level and the problems of the DJANGO generator in the kinematic range of the QED Compton process (Section 4.1.4). The inelastic channel, defined according to the LAr energy criterion Eq. 4.10, is displayed as sub-sample of the full Compton sample in all histograms for reference; open circles stand for the data, the dashed line histograms for the sum of the simulated inelastic signal and inelastic backgrounds.

The experimental and simulated distributions match smoothly over their respective ranges. The distributions of the SpaCal radial position of the first and the second SpaCal cluster show pronounced drops around the critical value of $r \approx 25$ cm. This is a consequence of the topological selection introduced due to the acceptance transition between BST and CIP in this radial range. The strategy could be modified using less strict acceptance criteria to gather a higher number of events in this region. The azimuthal distributions φ_1, φ_2 are of sine-modulated shape with a peak of the first cluster in direction of the positive x -axis. This effect originates from the tilt of the beams with respect to the H1 coordinate system in combination with the cross section dependence of the scattering angle, sensitively probed by the one Compton cluster which has the higher energy. Using the electron-photon identification, see histograms in Figure 7.3, the azimuth distribution has a flat shape.

Finally, the configuration overview, Figure 7.2-bottom, demonstrates the number of events collected in the different combinations of BST and CIP. The agreement of the normalization between data and Monte Carlo seems to get the better the smaller the involvement of the BST detector is. In c22, where both clusters are located in the outer SpaCal and $e\gamma$ -identified using the CIP, the Compton data and the simulation agree within the statistical errors. In contrast to this the BST-BST configuration shows larger discrepancies which can be explained by the large noise contribution in this silicon detector. In fact, adding the BDC to the particle identification in configuration c00, by the (much stricter) logical “AND” association of BST and BDC track signals, a very good agreement can be achieved in the shape and normalization of the physical distributions in this topology. Interestingly, this observation is in accord with the expectation of the algorithm “III” of the alternative identification schemes, discussed in Section 5.8.2, which predicts a very low mismatching rate in the combination of these two detectors despite the large photon conversion rates just in front of the BDC. On the other hand, this statement can account only for improved distribution shapes, but not for the overall normalization. The data–MC agreement achieved in the case of algorithm “III” might, thus, also indicate an improved rejection power against background and/or noise contributions.

In the control distributions of Figure 7.3 electrons and photons are distinguished. They indicate an overall agreement of the different quantities. A few overshooting data bins in energy, and especially in the azimuth (electron histogram in third row, left), are in contrast to the otherwise good agreement between data and Monte Carlo. As these additional entries are found only in individual φ -bins, it is an indication that again the BST with strong variations of efficiency and noise levels in its φ -sectors (Sections 5.4.1, 5.5) might be responsible for this effect. Note that the chosen approach in this analysis, the direct resimulation of electronic noise for the BST, can be replaced in principle and in practice by explicitly excluding each single noisy channel out of the many thousand in total and apply a corresponding list of all usable BST readout channels in a proper and detailed simulation of the whole silicon detector [50]. However, such a procedure would go beyond the scope of the present analysis.

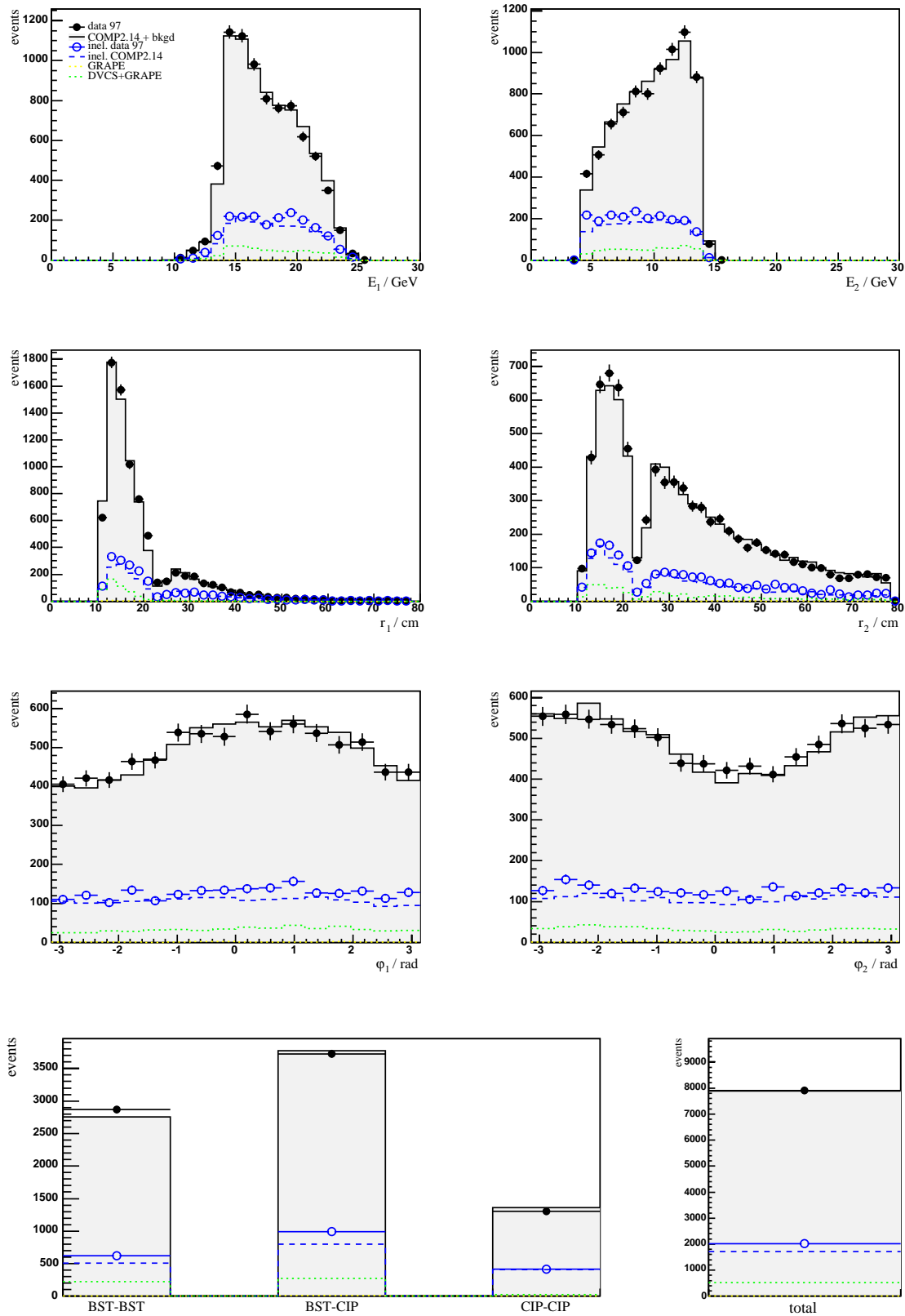


Figure 7.2: QED Compton event distributions of the first and second Compton cluster in energy, SpaCal radial position and azimuth. All Monte Carlo events are reweighted according to their respective integrated sample luminosities. The data (black dots) are represented as actual, unweighted event numbers. The bottom row of histograms displays the event distribution in the separate topological configurations $c00$, $c02$, and $c22$. Error bars represent the statistical error only.

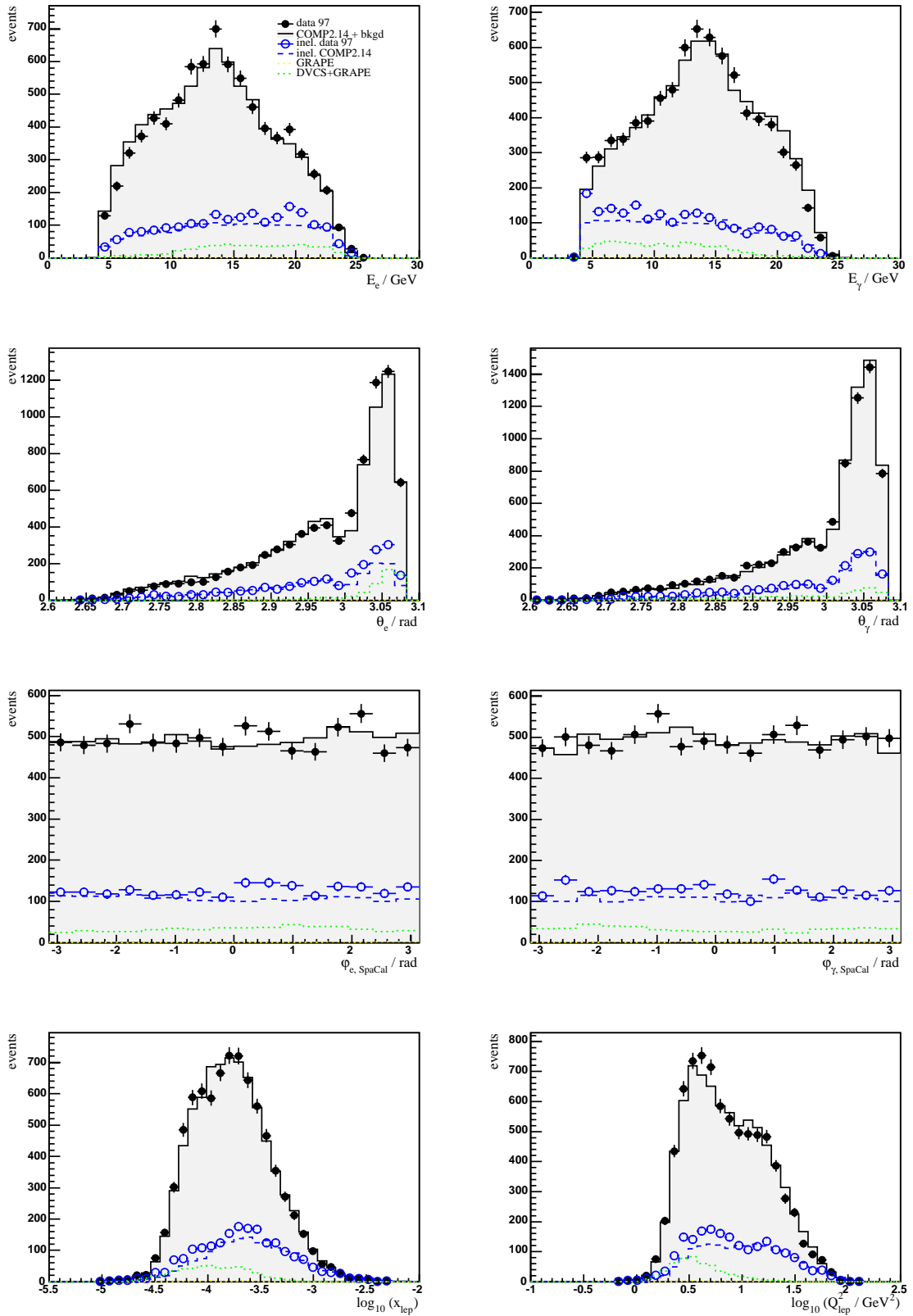


Figure 7.3: QED Compton event distributions of Compton electron and photon in energy, polar angle, azimuth, and the leptonic x_l and Q_l^2 . MC events are reweighted according to their respective integrated sample luminosities. Only the statistical errors are given.

The distributions of the polar angle of electron and photon show that the drops of the corresponding radial position do not appear as strong as in Figure 7.2. Together with the leptonic momentum transfer, see the Q_l^2 distribution in the last row of Figure 7.3, the polar angle distributions underline the observation that additional data entries appear above the Monte Carlo in the acceptance range of BST, namely at high scattering angles θ and/or low Q_l^2 .

7.3.1 Vertex

The Compton event vertex has been presented in the previous Chapter where it was discussed that the experimental and simulated vertex distributions exhibit a significant shift against each other. A more detailed look can be made by separating the vertex distribution into the different cluster configurations. The result is depicted in Figure 7.4 in which the BST-CIP configuration c02 is shown in two sub-samples, one where the electron traverses the BST and another one which contains all those events where the electron produced a pad-cluster in the CIP chamber. While in configurations with only one involved detector (c00, c22) the vertex distributions seem to have more or less matching data and simulation this is not the case in the mixed configuration c02. The vertex distribution seems to be distorted or shifted in c02. The c02-BST reconstructed vertex in *inelastic* events demonstrates (s. Figure) that in this case probably additional background entries contribute to the data distribution as irregular small “spikes” are visible on top of the flat shape of the corresponding simulated vertex distribution. In the other case of c02, with a CIP validated vertex, the vertex distributions appear smooth but with shifted peaks, one at lower z for the data and one at higher z in the simulation. A total normalization difference between data and MC is visible because the surplus of data entries on the negative z -side cannot compensate the lack of data entries on the positive z -side. Both effects can be related to the difficulties of the CIP vertex reconstruction caused by the CIP pad-properties and its influence on the pad-cluster formation. This is demonstrated in the lower histogram of Figure 7.4 in which all those z -coordinates are plotted where the electron trajectory crosses the CIP plane. The pad-cluster formation algorithm appears to be not capable to compensate the efficiency gap of the pad pair 19/20. Because the study on the CIP efficiency revealed no satisfying measure for the simulation to describe the observed efficiency behaviour of the data this result has to be accounted for in the treatment of the systematic errors.

7.4 Systematic errors

The systematic influence on the cross section measurement by the uncertainties of several input quantities is discussed in the following. Typical relative systematic errors of these are estimated either from major differences between the simulation and real data, or, where those are not present, they are judged from their resolution, specific results of their treatment, or other measurements. Then each of the listed relative errors is added in quadrature per kinematic bin to obtain the total relative error which, together with the statistical error, is applied in the end to the result of the cross section calculation. The procedure for a single error source is to vary the respective quantity up and down for each event by its systematic uncertainty. The corresponding variations of the cross section are determined and the average of both relative deviations from the unmodified cross section is regarded as the systematic error.

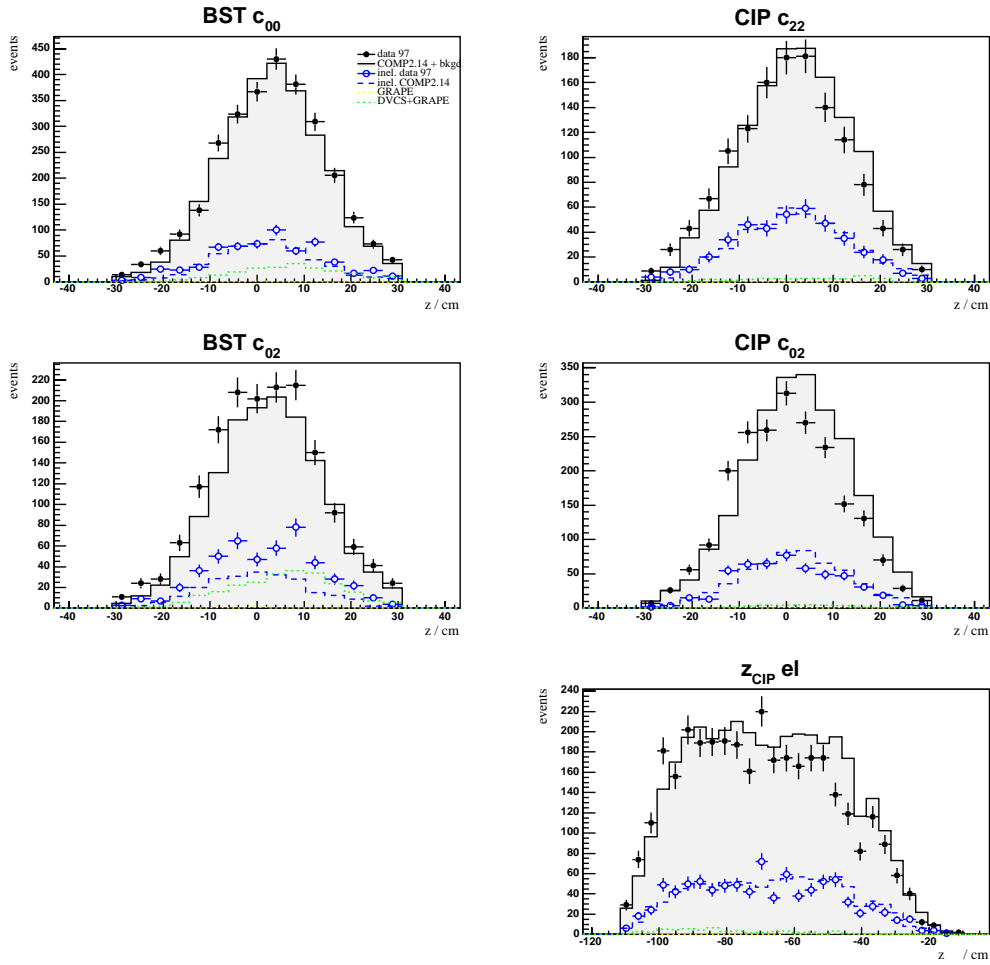


Figure 7.4: QED Compton vertex distributions sub-divided according to cluster configurations c_{00} , c_{02} and c_{22} . In the case of c_{02} (BST-CIP) two cases are distinguished, depending on which detector the electron has crossed. The lowest histogram contains the total z_{CIP} distribution for electrons: the pad-cluster reconstruction problems around the pad pair “19/20” manifest in a corresponding lack of entries at $z \approx -40$ cm.

The precision of the energy levels of the SpaCal and the LAr is estimated, respectively, from the recalibration procedure in the previous section and the typical energy scale precision of corresponding analyses (4%).

The BST and CIP polar angle resolutions are obtained by carrying out the same track reconstruction procedure as used for particle identification in the Compton event sample, but now on the special selection of the DIS event sample where a reference vertex position is available, s. Section 5.6.1. For the BST tracking an average z_{vtx} uncertainty of 0.5 cm is assumed which corresponds to a polar angle error of about 0.3 mrad. While this value is in agreement for example with [37] for the CIP the shape of its corresponding resolution distribution in the data does not match well the simulation. A comparison of the CIP vertex with the DIS vertex based on central tracks position gives a typical data resolution value of about $\sigma_z=2.2$ cm which also matches reasonably the level expected from the CIP pad-cluster size and the underlying pad width in z . Also, there was a significant difference between the reconstructed CIP pad-cluster width in the data and in the simulation. Therefore, the value of α_z

is taken as the systematic uncertainty for the CIP vertex measurement.

The SpaCal polar angle measurement affects (unconverted) photons where no track information can be used. For these cases the calorimeter's spatial resolution has to be considered. A typical value is given by previous SpaCal studies related to clustering algorithms. Here an average cluster position uncertainty in x and y coordinates of 0.3 cm is taken for the systematic variation. The z -position of SpaCal clusters of unconverted photons has turned out to be an unclear issue in the context of the energy calibration procedure (in contrast to other measurements).

Systematic background simulation errors are based on and estimated from their theoretical uncertainty. In the case of the DVCS process the error has to be set to 50% to account for the fact that an inelastic event generation is so far not available. Following [37] and [40] this error assumption is of the same size as found in diffractive vector meson production. The complete generation of the DVCS process is under development ([63]).

Table 6: Relative systematic errors ε_{sys} of important quantities affecting the Compton cross section measurement. The values are given as percentages for each of the kinematic bins listed in Table 5. In the lowest row the total error is calculated as the sum of all individual errors per column added in quadrature.

Source of error	ε_{sys} (in %) in kinematic ranges											
	$\Delta x_{l,1}, \Delta Q_{l,i}^2$				$\Delta x_{l,2}, \Delta Q_{l,j}^2$			$\Delta x_{l,3}, \Delta Q_{l,k}^2$			$\Delta x_{l,4}, \Delta Q_{l,m}^2$	
energy, SpaCal	7.5	6.8	5.3	10.6	0.3	1.7	2.8	2.4	1.3	0.4	5.4	2.8
BST θ	12.5	2.8	3.2	10.6	0.3	1.0	0.3	1.1	0.0	0.4	0.3	0.0
CIP $z(\text{pad})$	0.0	0.0	1.6	10.6	0.5	10.6	2.3	1.7	6.3	10.1	5.7	8.5
SpaCal θ	7.5	0.7	2.4	21.3	0.3	0.4	1.9	0.6	0.5	0.8	1.0	1.1
energy, LAr	2.5	0.7	0.4	0.0	0.7	0.4	0.5	0.5	0.4	0.8	0.6	0.0
DVCS bkgd.	25.0	9.5	4.2	3.2	5.7	2.2	0.8	5.2	0.5	0.8	1.0	0.5
GRAPE bkgd.	5.0	0.7	0.0	0.0	0.5	0.4	0.3	0.6	0.3	0.8	1.0	0.0
DJANGO bkgd.	5.0	0.7	0.0	0.0	0.5	0.4	0.3	1.3	0.7	0.8	1.8	0.0
total	30.9	12.1	8.0	28.4	5.8	11.0	4.3	6.3	6.6	10.2	8.2	9.1

7.5 Cross section

Once the acceptances are applied, the cross section measurement still needs to be corrected for radiative effects according to Eq. 7.1. The non-radiative Monte Carlo simulation together with the standard simulation yields the correction values within the present kinematic binning as listed in Table 7. The δ values range within a few percent of $\approx +0.6\% \dots -6\%$ whereas the maximum is found to be at -9.8% in the third x_l bin. They are applied to the reconstructed cross section values of the data and the (full radiative) COMPTON Monte Carlo to obtain the double differential Born level cross section $d^2\sigma/dx_l dQ_l^2$ of the QED Compton scattering process. The resulting numbers are listed in Table 8 and displayed as histograms in Figure 7.6. As an additional information also the contribution of the inelastic Compton events is displayed as a sub-sample in the corresponding kinematic bins for comparison with the total Compton cross section histograms. The inelastic channel's own acceptance was applied bin by bin analogous to the full cross section; in addition the corresponding bin-wise radiative

Table 7: Radiative corrections for the calculation of the leading order QED Compton cross section, determined from two MC simulations. The numbers are given in percentages; note that according to Eq. 7.1 negative values of δ lead to increased cross section values compared to the measured σ . Values in parentheses are affected by too low statistics or missing acceptance, respectively (see Section 7.2).

kinematic range	$\delta = \sigma/\sigma_{\text{LO}} - 1$ (in %)			
$\Delta x_{l,1}, \Delta Q_{l,i}^2$	(+92.3)	+0.6	-8.3	(-13.6)
$\Delta x_{l,2}, \Delta Q_{l,j}^2$		+0.1	-3.8	-5.2
$\Delta x_{l,3}, \Delta Q_{l,k}^2$		-2.6	-6.4	-9.8
$\Delta x_{l,4}, \Delta Q_{l,m}^2$		-2.9	-5.8	(0.0)

corrections were used. But especially in the lowest (x_l, Q_l^2) bins of the inelastic part the acceptance is too low ($\approx 5\%$) and the relative statistical error is too high ($\approx 50\%$) for a reliable measurement. The low acceptance is a consequence of the limitation of the maximum polar angle of the hadronic final state in inelastic events.

For comparison purposes with previous analyses (as in [37]) the double differential cross section and its errors are also given without bin size division in Table 9. The lower four diagrams of Figure 7.5 show the corresponding histograms together with the inelastic channel. The upper four diagrams show the original QED Compton event rate (number of events normalized with luminosity of the data) with all considered background contributions added to the Compton Monte Carlo.

Table 8: Double differential QED Compton cross sections (Born level) in their individual kinematic bins. All cross section values are valid for the kinematic cuts given by Eq. 7.4.

kinematic range		cross sections [nb/GeV ²]					
x_l	Q_l^2 [GeV ²]	σ_{data}	$\Delta\sigma_{\text{data}}^{\text{stat}}$	$\Delta\sigma_{\text{data}}^{\text{sys}}$	$\Delta\sigma_{\text{data}}^{\text{tot}}$	σ_{MC}	$\Delta\sigma_{\text{MC}}^{\text{stat}}$
1.78e-05 ... 5.63e-05	0.5 ... 1.5	660.3	326.5	203.7	384.8	488.5	140.1
" ... "	1.5 ... 2.5	7534.8	702.7	910.5	1150.1	7071.2	449.7
" ... "	2.5 ... 3.5	2126.3	290.9	170.3	337.0	1717.5	178.9
" ... "	3.5 ... 4.5	126.7	90.2	35.9	97.1	98.0	54.9
5.63e-05 ... 1.78e-04	1.5 ... 5.0	1835.5	69.3	106.3	126.9	1745.4	46.8
" ... "	5.0 ... 8.5	768.6	39.4	84.6	93.3	804.5	29.8
" ... "	8.5 ... 12.0	237.7	18.2	10.1	20.8	261.6	14.3
1.78e-04 ... 5.63e-04	3.0 ... 14.7	99.3	4.0	6.2	7.4	100.1	2.8
" ... "	14.7 ... 26.3	57.7	2.7	3.8	4.6	53.1	1.9
" ... "	26.3 ... 38.0	12.1	1.4	1.2	1.9	14.6	1.2
5.63e-04 ... 1.78e-03	10.0 ... 48.3	3.7	0.3	0.3	0.4	3.9	0.2
" ... "	48.3 ... 86.7	2.1	0.3	0.2	0.4	1.8	0.2

Table 9: The double differential QED Compton cross section is listed here without bin-size division for comparison with other measurements, such as [37]. The cross sections are valid for the kinematic cuts given in Eq. 7.4.

kinematic range		cross sections [pb]					
x_l	Q_l^2	σ_{data}	$\Delta\sigma_{\text{data}}^{\text{stat}}$	$\Delta\sigma_{\text{data}}^{\text{sys}}$	$\Delta\sigma_{\text{data}}^{\text{tot}}$	σ_{MC}	$\Delta\sigma_{\text{MC}}^{\text{stat}}$
1.78e-05 ... 5.63e-05	0.5 ... 1.5	25.4	12.6	7.8	14.8	18.8	5.4
" ... "	1.5 ... 2.5	290.0	27.0	35.0	44.3	272.2	17.3
" ... "	2.5 ... 3.5	81.8	11.2	6.6	13.0	66.1	6.9
" ... "	3.5 ... 4.5	4.9	3.5	1.4	3.7	3.8	2.1
5.63e-05 ... 1.78e-04	1.5 ... 5.0	781.9	29.5	45.3	54.0	743.5	19.9
" ... "	5.0 ... 8.5	327.4	16.8	36.0	39.8	342.7	12.7
" ... "	8.5 ... 12.0	101.3	7.7	4.3	8.9	111.4	6.1
1.78e-04 ... 5.63e-04	3.0 ... 14.7	445.9	18.1	27.9	33.3	449.5	12.7
" ... "	14.7 ... 26.3	259.1	12.1	17.0	20.9	238.6	8.4
" ... "	26.3 ... 38.0	54.3	6.2	5.6	8.3	65.5	5.3
5.63e-04 ... 1.78e-03	10.0 ... 48.3	172.7	11.9	14.2	18.5	182.6	9.3
" ... "	48.3 ... 86.7	97.8	15.0	8.9	17.4	85.3	10.5

7.6 Summary and prospects

In the present work a measurement of the double differential QED Compton cross section in ep scattering at HERA was performed on the basis of the 1997 standard data set. The cross section was calculated in leptonic kinematic variables x_l , Q_l^2 and compared to the result of the event generator COMPTON2.14. The analysis included a detailed inspection of the subdetectors relevant for the chosen phase space in Compton scattering, namely the Backward Silicon Tracker and the Central Inner Proportional Chamber of the H1 experiment. The performance of both devices was checked by using an independent event selection of deep inelastic scattered electrons of the same data taking period. This DIS sample allowed to monitor and to determine efficiency variations in time and in different subdetector parts, as well as the level of electronic noise. Further, the rate of conversion in front of the used tracking detectors was measured with the Compton event samples containing the photons necessary for this purpose. In addition the Compton selections allowed the application of several important calibration measures as, for instance, detector alignment and corrections to particle energies. An optimum particle identification was achieved by demonstrating that the involvement of the BDC detector into the signal analysis degrades the quality of the identification by increased mismatch probabilities.

The leptonic cross section measurement in QED Compton turned out to be consistent with the results of [37] within the statistical and systematic errors, both of comparable order. The statistical errors of the cross sections are increased through the low acceptances which are affected by the particle identification as a substantial factor. This is again due to the high photon conversion rate in general found in the backward part of the H1 detector. The systematic errors are dominated firstly by the uncertainties of the background contributions, most importantly by the Deeply Virtual Compton Scattering process. And secondly by the difficult procedure of track reconstruction using the CIP subdetector, mainly due to the fact that only two sensitive layers are available and no other track information was used, and also due to the unexpected problems imposed by the electronic performance around the first CIP wire-support within the backward part of this device. A further consequence

is that the resolution of the CIP vertex reconstruction cannot be very much better than the pad size in z . The differences of the pad-cluster sizes, reconstructed in data and simulation, show that an improvement might be possible by reconsidering the details of the chamber simulation.

Concerning further calibration aspects the position reconstruction quality of the barycenter of Compton photon clusters in the backward calorimeter remains unclear. The study in this field indicated that part of the energy calibration can be improved by assuming a systematic radial displacement introduced by the electromagnetic cluster reconstruction, visible in the case of unconverted photons where no other spatial information but the one from the calorimeter is available. At last it was found that subdetector alignment constants are close to former measurements. The particle identification performed in the present analysis allows azimuthal corrections of the magnetic deflection and offers an improved resolution, due to the narrower acoplanarity peak, compared to standard methods of earlier strategies which also used the Compton channel for this purpose but did not exploit the particle identification.

The overall agreement between experimental and simulated Compton data as seen in control and cross section results must be carefully interpreted. Splitting the full event sample into sub-selections identical to the different topological configurations, named as c00, c02 and c22, where one of the cluster is either in the acceptance of BST or CIP, shows a *mutual* changing quality among the control distributions, *i.e.* for example energy, radial cluster position and the event z -vertex distribution, between the individual configurations. These “internal” discrepancies can be partly correlated with the complex resimulation sequence of subdetector efficiencies, electronic noise and the conversion effects. Because this treatment is performed on a semi-phenomenological level, *i.e.* not all detector properties are resimulated on the level of elementary physics processes, it could be one reason for some of the remaining systematic disagreements between Compton data and the simulation.

Prospects

Several options still exist to extend the kinematic range and improve the quality of the cross section measurement. One of the major difficulties of this analysis was to deal with the track reconstruction in the backward region of the experiment where only particle trajectories of high polar angles can be observed. Extending the kinematic range into the LAr system would offer the possibility to make use of the central tracking devices in order to precisely determine electron tracks or anti-validate photon clusters. Further, the use of higher statistics data samples would allow not only a reduction of statistical errors but also support the understanding of statistics-limited studies such as the conversion rate measurement which represents a part of the overall calibration process. This measurement can only be carried out by using the Compton sample. The upgrade of the backward tracking device BST to BST-2 in later H1 data taking periods offers the possibility of an much improved signal-to-noise ratio by four additional silicon sensor planes. Other technical possibilities still exist, as for example the use of CJC or CIZ reconstructed track elements for a further improvement of track reconstruction quality in the backward area.

From the physics point of view the measurement of the structure function F_2 in ep scattering at very low Q_h^2 is the main objective. Such a step requires, in addition to the aspects discussed in this analysis, an understanding of the hadronic final state in inelastic QED Compton scattering as already attempted in [38]. The present analysis provides a control towards the detailed understanding of the leptonic side of the Compton process in terms of particle identification, calibration and normalization of data and Monte Carlo. With improved versions of the DVCS event generator the most important background estimation will also become more reliable in the future.

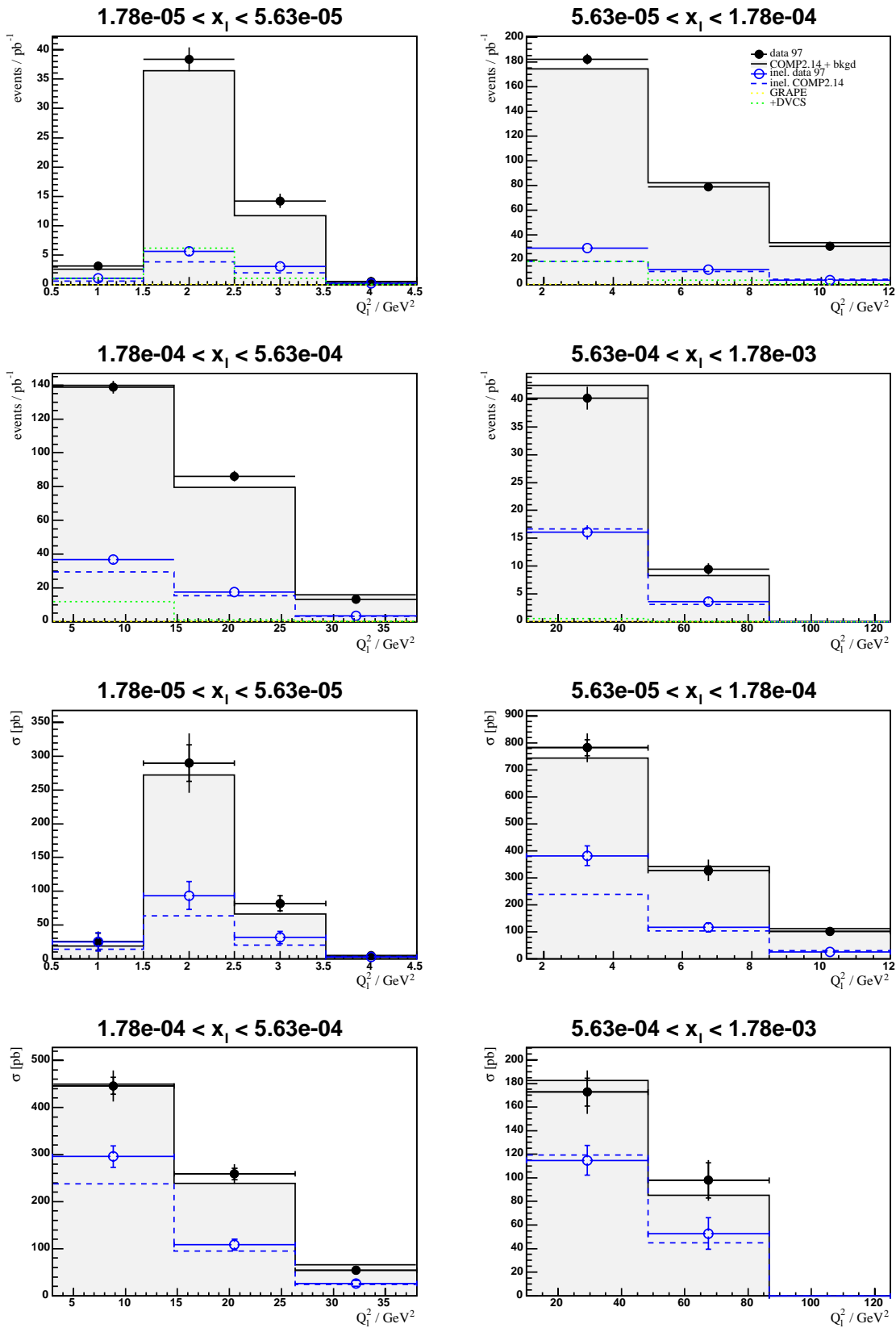


Figure 7.5: QED Compton event rates and cross section. Upper four histograms: rate as number of events normalized to luminosity. The backgrounds are denoted in the upper right histogram. Lower four plots: cross section after background subtraction and acceptance correction. For the QED Compton cross section (sum elastic plus inelastic) statistical (inner error bars) and systematic errors are added in quadrature (outer bars).

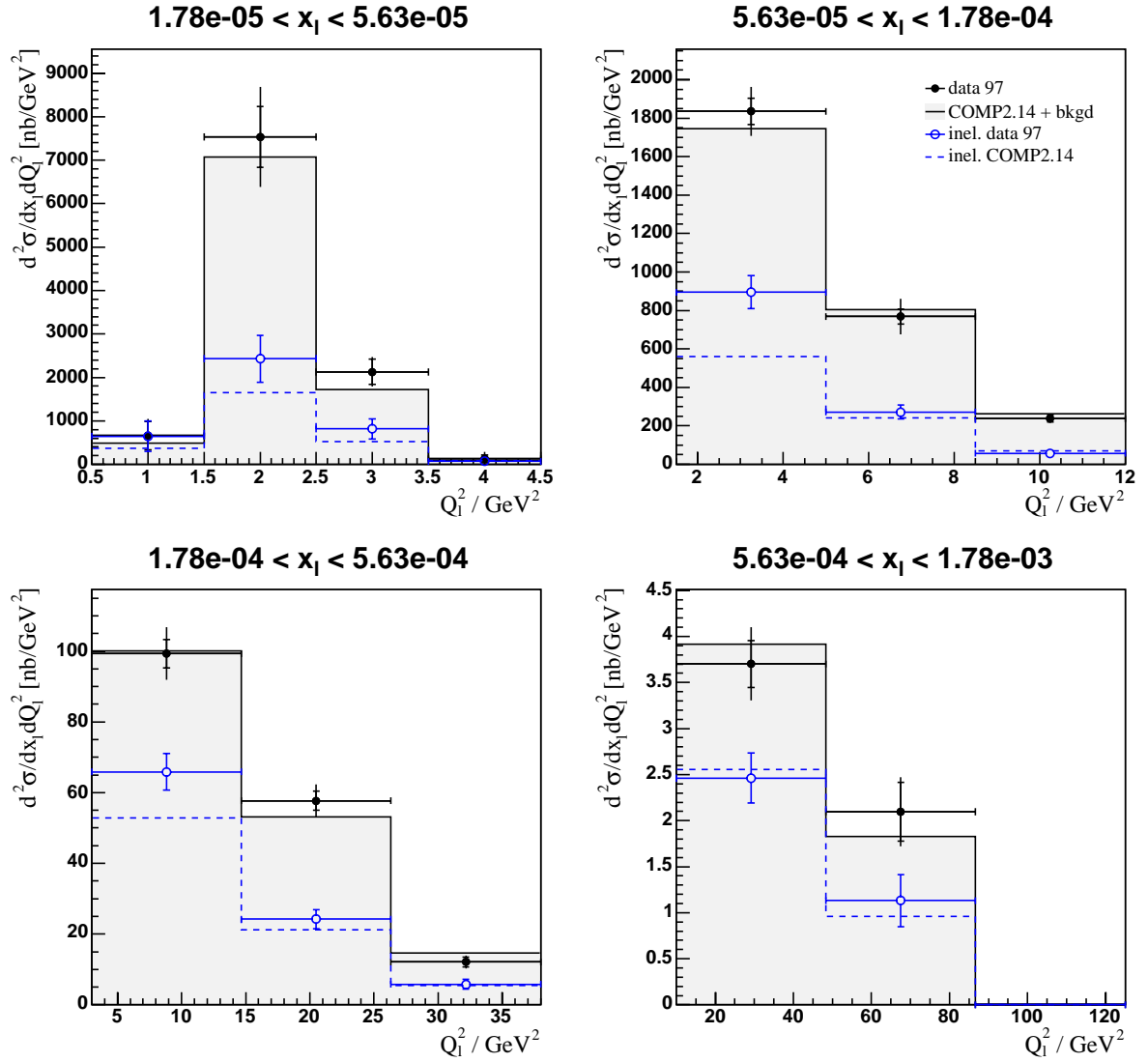


Figure 7.6: The QED Compton double differential cross section as measured according to the kinematic range of the MC event generation given by the limits of Eq. 7.4. The inelastic selection is shown for comparison with dashed lines for MC and with open dots for the data. The inner error bars show the statistical errors, the full error bars denote the statistical and systematic error added in quadrature; for the inelastic sub-selection only the statistical errors are given.

A Appendix

This appendix gives further information about different analysis aspects like the acoplanarity determination as well as technical data for run selections and alignment constants. Finally, the central part of the encoding of the algorithm applied in the CIP pad-cluster formation is shown. They are all used for the study of event data and efficiencies, and they are presented as reference for other analyses and comparison purposes.

A.1 Computation of acoplanarity

The following describes briefly the determination of the signed acoplanarity as used throughout this analysis. As defined in Section 2.1.2 the acoplanarity $A = 180^\circ - \Delta\varphi$, using the azimuthal angle difference of two particles 1 and 2, takes into account the relative azimuthal position of both particles. Although it is, in principle, sufficient to view only the absolute value of the acoplanarity, $|A|$, as done in other works, here the sign of the deviation is preserved in order to be more sensitive in detecting possible asymmetries in the lower and upper tail distributions of A . Especially in the case that particle 1 (2) represents the Compton-electron (-photon) the symmetry of $A_{e\gamma}$ can be distorted by systematic effects introduced by inaccurate particle identification or insufficient compensation of the electron magnetic deflection. For further details and discussion s. Chapter 5 and also Section 6.1.2. Without any further treatment the raw distribution of

$$\Delta\varphi = \varphi_1 - \varphi_2 \quad \text{with } \varphi_1, \varphi_2 \in [-\pi, \pi]$$

is characterized by two peaks around the values $+\pi$ and $-\pi$, respectively, with the tails ranging within $[-2\pi, 2\pi]$ in total. The acoplanarity follows in two steps. First, by an interval reduction of $\Delta\varphi$:

$$\Delta\varphi \begin{cases} > +\pi : & \Delta\varphi' = \Delta\varphi - 2\pi \\ < -\pi : & \Delta\varphi' = \Delta\varphi + 2\pi \end{cases} \quad \text{where } \Delta\varphi' \in [-\pi, \pi].$$

The $\Delta\varphi'$ distribution features two “half” peaks sharply limited at the lowest and highest interval borders without any tails beyond them. The second step merges these peaks into the final signed acoplanarity A_{12} :

$$\Delta\varphi' \begin{cases} > 0 : & A_{12} = \Delta\varphi' - \pi \\ \leq 0 : & A_{12} = \Delta\varphi' + \pi \end{cases} \quad \text{such that } A_{12} \in [-\pi, \pi].$$

Positive (negative) acoplanarities mean that the second cluster is closer in azimuth to the first cluster in the direction equal to the positive (negative) rotation sense. Thus, the case example of Figure 2.2 has a positive acoplanarity.

A.2 Run selection

Table 10: List of rejected run numbers for the Standard and Minimum Bias data which was taken in 1997 [46].

Run number range	Comment
177920 ... 180958	startup instabilities
188581 ... 188637	general trigger problems
191512 ... 191694 194783 ... 194785 194832 ... 194835	MWPC problems
194166 ... 194255	L2 problems
191749 ... 192008 192759 ... 192906 193065 ... 193235 193433 ... 193462 193502 ... 193526 195932 ... 196377 198826 ... 198884 198826 ... 198884	IET1 problems L2 problems related to subtrigger 1 and 3
198345 ... 198440	timing problems, LAr trigger experiments
201320 ... 201383 191730 191984 192914 193315 195512 196374 ... 196375 197036	Minimum Bias runs - new L4-2000 scheme for fills 1593-1594
192864 194521 194527 193139 193163	double run numbers
200445	Strange L5 weights
201141	lumi platform mistakenly moved
201281 201282 ... 201283 201293 201439 201441 201445 201470 ... 201473 201475 ... 201476 201478 ... 201479 201481 201220	BST readout problem Last of BST surely broken Pretest for L4 scheme 2000

Table 11: *List of run numbers with inactive trigger stages L2 and L4, as used for the measurement of the efficiency of the L2 topological Compton trigger element.*

Run numbers
180061
180064
180068
180069
180070
180072
180074
181003
181135
181401
181759
181876
182798
182990
184596
184602
184690
185722
185724
185725
185727
185729
185731
185732
185734
185735
185736
185748
185749
186006
192496

A.3 BST parameters

Table 12: *BST alignment parameters, as to be used as program steering bank “BSTA”, taken from [32]. The first five numbers in the upper row represent the external alignment parameters, i.e. shifts along the x, y, z axes (in cm) and the two tilt parameters of the principal BST cylinder axis. All other numbers represent relative positions of the internal silicon detectors.*

.129	-1.38	-0.275	0.0062	0.00036			
37.23	-76.77	-68.10	-89.56	-41.41	-72.12	-69.42	-75.28
715.59	478.29	536.49	403.06	-31.92	41.33	8.66	36.95
-79.18	-227.93	-208.34	-109.05	-287.32	-315.39	-343.94	-349.34
-124.94	-156.23	-197.77	-14.12	146.22	134.20	140.58	283.10
383.04	-7.58	-105.12	-44.38	59.09	76.61	131.27	90.18
255.17	297.74	249.91	233.16	13.25	138.40	94.43	105.83
-120.04	-4.43	-7.47	17.91	-143.37	22.83	20.64	27.01
-392.28	-118.22	-208.20	-119.83	-237.11	-281.38	-258.66	-175.56

A.4 Encoding of the CIP cluster algorithm

The commented code excerpt below illustrates the implementation of the CIP pad-cluster algorithm as developed for this analysis. The resimulation of the individual pad efficiency and of the wire-spacer effect take place before the actual pad-cluster formation. The routine is run for each detected electromagnetic Compton cluster candidate per event.

```
[Initialisation]
[In Monte Carlo: individual pad resimulation of efficiencies and of the spacer effect]

//--- Author: Nicolas Keller
//-----
//--- Removal of single active pads
//-----

for ( j=0; j<30; j++) //--- Scan all pads of CIP from chamber -z end
  { //--- towards vertex.
    if ( p1[j] ) //--- In layer 1 (outer CIP)
      { //--- check for single active pads and
        if ( j<29 && !( p1[j+1] || p0[j] || p0[j+1] ) //--- their relative geometrical positions,
          || //---
            j==29 && ! p0[j] )
          { //--- remove them from list.
            p1[j] = kFALSE;
          }
      }
    if ( p0[j] ) //--- Do the same for layer 0 (inner CIP):
      { //--- also using pad-information <p1> (layer 1).
        if ( j> 0 && !( p1[j] || p1[j-1] || p0[j-1] ) //---
          || //---
            j==0 && ! p1[j] )
          {
            p0[j] = kFALSE;
          }
      }
  }

//-----
//--- Find contiguous pad series, form half clusters,
//--- fill matching pads into arrays <c10> and <c11>:
//-----

j = ip0 = ip1 = ic = 0; //--- Reset counters, j: pad start index.
//--- ip0/1: offsets to j.

for ( k=0; k<10; k++)
  { //--- Reset list entry counter.
    n10[k] = n11[k] = 0; //---
    for ( m=0; m<10; m++) c10[k][m] = c11[k][m] = 0; //--- Reset c10/1 lists.
  }

while ( j<30 ) //--- Start to find all possible pad-clusters:
  {
    if ( j+ip1<30 )
      { //--- Scan outer layer
        while ( p1[j+ip1] ) //---
          { //--- Add pad <j+ip1> of layer 1 to cluster <ic>.
            c11[ic][ip1] = j+ip1;
            ip1++;
          }
      }
    k = 0;
    while ( !p0[j+k] ) k++; //--- Find starter pad for inner layer.
    if ( j+ip0+k<30 ) //--- Require index range validity
      { //--- Scan inner layer...
        while ( p0[j+ip0+k] ) //---
          { //--- ... and add active pads to half cluster.
            c10[ic][ip0] = j+ip0+k;
            ip0++;
          }
      }
    if ( ip1>0 && ip0>0 ) //--- At least one pad in each layer/half cluster:
      { //--- = full cluster found!
        n10[ic] = ip0; //--- Store number of pads inner layer.
        n11[ic] = ip1; //--- Store number of pads outer layer.
        j = max( c10[ic][ip0-1], c11[ic][ip1-1] )+1; //--- Set new starter pad for next cluster-search
        //--- (last pad of previous cluster).
        ic++; //--- Count this cluster.
        ip1 = 0;
        ip0 = 0;
      }
    else j++; //--- No cluster found: continue layer scanning.
  }

[Calculate cluster properties]
[Return to event calculation]
```


Tables

1	Radiative processes	7
2	Performance of the particle identification algorithms	83
3	Particle mismatch rates using BST and CIP	84
4	Elements of Compton level-1 trigger	103
5	Kinematic binning of the leptonic variables	113
6	Relative systematic errors	120
7	Radiative corrections	121
8	QED Compton double differential, leptonic cross section	121
9	QED Compton double differential, leptonic cross section (no bin size normalization)	122
10	Default list of rejected runs	129
11	List of runs transparent for level-2 & 4	130
12	BST alignment constants	131

Figures

2.1	Feynman graph in radiative ep scattering	7
2.2	Definition of the acoplanarity	9
2.3	Comparison of Feynman graphs in DIS and QED Compton	12
2.4	Photon radiation from a quark	15
2.5	Gluon radiation from a quark	15
2.6	Comparison of gluon- and photon-density evolution	16
2.7	Distributions of x_l and x_γ in Monte Carlo	17
2.8	Kinematic plane for HERA including QED Compton	18
3.1	The electron-proton storage ring HERA	20
3.2	FTS model	21
3.3	View into the H1 detector	22
3.4	The H1 backward calorimeter SpaCal	24
3.5	Radial view of the Central Tracking Devices	26
3.6	Structure of the Central Inner Proportional Chamber	27
3.7	Wire arrangement of the BDC	28
3.8	The Backward Silicon Tracker	29
3.9	Schematic of the H1 Trigger components	31
3.10	Luminosity measurement principle	32
4.1	Kinematic range of QED Compton events in hadronic variables	34
4.2	F_2 parameterisation in the COMPTON generator	35
4.3	Initial State Radiation in QED Compton	36
4.4	Feynman graph DVCS	37
4.5	Feynman graph di-lepton scattering	38
4.6	Feynman graph π^0 backward scattering in DIS	38
4.7	Reconstructed cluster energies in Monte Carlo	41
4.8	Detector display of an elastic QED Compton event	43
5.1	BDC radial track distribution	46
5.2	Vertex reconstruction with the CIP	47
5.3	The CIP pad-cluster algorithm	49
5.4	Width of CIP pad-clusters	49
5.5	Reconstruction of charged tracks with the BST	50
5.6	Acceptance of the BST	55
5.7	Time dependent stability of the BST	57
5.8	Hit bank loss of the BST	57
5.9	Radial BST efficiency	58
5.10	Radial CIP acceptance	59
5.11	Time dependent stability of the CIP	59
5.12	Radial CIP efficiency	60
5.13	CIP efficiency as function of pad number and z -coordinate	61
5.14	Correlated pad efficiencies of the CIP	62
5.15	Radial BDC efficiency	64
5.16	Time dependent stability of the BDC	64
5.17	Principle of the noise measurement	65
5.18	Noise rates in BST and CIP	67
5.19	Overall subdetector noise rates	68
5.20	Azimuthal efficiency of the BST	69
5.21	Resimulation of sector-wise BST inefficiency	70

5.22	Resimulation of sector-wise BST noise level	70
5.23	z -vertex difference between both Compton clusters	71
5.24	Resolution of the z -vertex position	72
5.25	Backward region of H1 as technical drawing with map of BDC charge deposition	74
5.26	Photon conversion in front of the BST	77
5.27	Photon conversion CIP	77
5.28	Photon conversion between backward subdetectors	78
6.1	Acoplanarity with and without particle identification	87
6.2	Correction of the electron azimuth	88
6.3	Alignment of the SpaCal	90
6.4	Control of the SpaCal alignment	90
6.5	Acoplanarity of first and second cluster	91
6.6	Acoplanarity of electron and photon	91
6.7	Misalignment of the BDC	92
6.8	Control of the BDC alignment	92
6.9	Alignment of the BST	93
6.10	Measured energies and double angle energies	95
6.11	Non-linearity of the energy measurement	97
6.12	Non-linearity of Monte Carlo energies	98
6.13	Correction of the photon polar angle	100
6.14	QED Compton cluster energy sum	102
6.15	Efficiencies of the DC $r\varphi$ trigger elements	106
6.16	DC $r\varphi$ trigger versus central track properties	107
6.17	Realization scheme of the L2TT trigger	108
6.18	Efficiency of the L2TT element t-18	109
6.19	Reweighting of the z -vertex distribution	111
6.20	Final z -vertex	111
7.1	Acceptance, stability and purity in bins of x_t and Q_t^2	114
7.2	Control distributions of first and second cluster	116
7.3	Control distributions of electron and photon	117
7.4	z -vertex distributions in different event topologies	119
7.5	QED Compton event rates and leptonic cross section	124
7.6	QED Compton double differential, leptonic cross section	125

References

- [1] E. Rutherford, *The Scattering of α and β Particles by Matter and the Structure of the Atom*, University of Manchester, Phil. Mag. **21** (1911) 669.
- [2] R. Frisch, O. Stern, *Über die magnetische Ablenkung von Wasserstoffmolekülen und das magnetische Moment des Protons. I.*, Z. Phys. **85** (1933) 4.
- [3] R. Hofstadter, Nobel Lectures Physics 1942-1962, Elsevier Publishing Company, Amsterdam, pp. 560-581.
- [4] M.N. Rosenbluth, Phys. Rev. **79** (1950) 615.
- [5] R.K. Ellis, W.J. Sterling and B.R. Webber, QCD and Collider Physics, 1996.
- [6] Yu.L. Dokshitzer, Sov. Phys. JETP **46** (1977) 641.
- [7] V.N. Gribov, L.N. Lipatov, Yad. Fiz. **15** (1972) 781 and 1218 / Sov. J. Nucl. Phys. **15** (1972) 438 and 675.
- [8] G. Altarelli, G. Parisi, Nucl. Phys. **B 126** (1977) 298.
- [9] A. Courau and P. Kessler, "QED Compton scattering in high-energy electron-proton collisions", Phys. Rev. **D 46** (1992) 177.
- [10] A. De Rújula and W. Vogelsang, "On the photon constituency of protons", CERN-TH/98-377, hep-ph/9812231 (1998).
- [11] M. Glück, E. Reya, and A. Vogt, Eur. Phys. J. **C 5** (1998) 461.
- [12] C.F. von Weizsäcker, Z. Phys. **88** (1934) 612.
- [13] E.J. Williams, Phys. Rev. **45** (1934) 729.
- [14] M. Glück, M. Stratmann, W. Vogelsang, "The inelastic photon content of the proton", Phys. Lett. **B 343** (1995) 399.
- [15] M. Drees, R.M. Godbole, M. Nowakowski and S.D. Rindani, Phys. Rev. **D 50** (1994) 2335, referenced in [14].
- [16] J. Blümlein, G. Levman, and H. Spiesberger, "On the Measurement of the Proton Structure at Small Q^2 ", DESY report 93-097 (1993); also in: Proceedings of the Durham Workshop 'Physics at HERA', Durham, UK, March 1993.
- [17] L.W. Mo and Y.S. Tsai, Rev. Mod. Phys. **41** (1969) 205 (referenced in [16]).
- [18] B.A. Kniehl, Phys. Lett. **B 254** (1991) 267.
- [19] S. Kermiche, Ph.D. Thesis, University of Paris-Sud, LAL Orsay, 1994.
- [20] R. Kajantie and R. Raitio, Nucl. Phys. **B 139** (1978) 72.
- [21] H. Abramowicz and A. Levy, DESY 97-251 (Dec 1997); hep-ph/9712415 (1997).
- [22] T. Ahmed *et al.* (H1 Collaboration), Z. Phys. **C 66** (1995) 529.

- [23] T. Abe, Computer Physics Communications **136** I-II (2001) 126-147, hep-ph/0012029 (2000).
- [24] F.W. Brasse, W. Flauger, J. Gayler, S.P. Poel, R. Haidan, M. Merkwitz, H. Wriedt, Nucl. Phys. **B 100** (1976) 413.
- [25] R. Poeschl, Diploma Thesis, Dortmund 1996.
- [26] Z. Zhang, A. Antmann, and T. Constant, H1 internal note H1-10/96-495.
- [27] K. Hagiwara *et al.* (The Particle Data Group), Phys. Rev. **D 66**, 010001 (2002).
- [28] C. Carimalo, G. Cochard, P. Kessler, J. Parisi, and B. Roehner, Phys. Rev. **D 10**, 1561 (1974).
- [29] J. Drees, Springer Tracts in Modern Physics, Springer 1971, Vol. 60, 106.
- [30] E. Etim, G. Pancheri, and B. Touschek, Nuovo Cimento, **51 B** (1967) 276; G. Pancheri, *ibid.* **60 A** (1969) 321.
- [31] Desy internal report, DESY-H1-96-01, March 1996, published in Nucl. Instr. and Meth. **A 386** (1997) 310.
- [32] V.V. Arkadov, "Measurement of the Deep-Inelastic ep Scattering Cross Section using the Backward Silicon Tracker at the H1 Detector at HERA", Ph.D. Thesis, Humboldt-Universität Berlin, 2000.
- [33] M. Vorobiev, FTS illustration, ITEP Moscow.
- [34] H. Henschel, BST illustration, IfH Zeuthen.
- [35] The H1 Trigger, referenced in [31], pp. 19-30.
- [36] V. Lendermann, H1 internal note H1-08/99-575, 1999.
- [37] V. Lendermann, Ph.D. Thesis, University Dortmund 2001.
- [38] H1 Collaboration, "Measurement of F_2 at low Q^2 in QED Compton Scattering at HERA", Contributed Paper to International Europhysics Conference on High Energy Physics (EPS 2003), Aachen, Germany, 17.-23.07.2003, Abstract 084.
- [39] R. Stamen, Diploma Thesis, University Dortmund 1998.
- [40] R. Stamen, Ph.D. Thesis, University Dortmund 2001.
- [41] C. Adloff *et al.* (H1 Collaboration), Phys. Lett. **B 517** (2001) 47.
- [42] H. Drumm *et al.*, Nucl. Instr. and Meth. **A 176** (1980) 333.
- [43] S. Egli *et al.*, Nucl. Instr. and Meth. **A 283** (1988) 487.
- [44] P. Sievers, Diploma Thesis, Ruprecht-Karls-Universität Heidelberg 1999.
- [45] J. Marks, "QESCAT – Electron identification software in H1PHAN", talk at H1 meeting on 16 July 1996.
- [46] H1 ELAN working group, T. Kurca, H1 internal compilation of low quality runs in H1 for 1997 data taking, 1997.

-
- [47] H1 ELAN working group.
- [48] R. Maraček, Ph.D. Thesis, IEP Slovak Academy of Sciences, Košice 1998.
- [49] M. Dirkmann, K. Pfeiffer, H1 internal note H1-01/97-512.
- [50] T. Laštovička, private communication.
- [51] J.P. Pharabod, A. Semenov, V. Shekelyan, D. VanDenPlas, A. Walther, and A. Zhokin, H1 internal note H1-03/96-474.
- [52] H.P. Beck, “Measurement of the Total Photoproduction Cross Section at the Electron Proton Collider HERA at $W_{\gamma p}$ of 200 GeV”, Inaugural-Dissertation, Universität Zürich 1996.
- [53] H.P. Beck, H1 internal note H1-05/96-479, 1996.
- [54] K. Müller *et al.*, “Construction and performance of a thin cylindrical multiwire proportional chamber with cathode pad readout for the H1-experiment”, Nucl. Instr. and Meth. **A 312** (1992) 457-488.
- [55] B. Schwab, Ph.D. Thesis, Ruprecht-Karls-Universität Heidelberg, 1996.
- [56] J. Katzy, Ph.D. Thesis, Ruprecht-Karls-Universität Heidelberg, 1997.
- [57] S. Glazov and R. Wallny, Talk presented by S. Glazov at H1 Group Meeting (DESY), January 1998.
- [58] A. Meyer, Ph.D. Thesis, Universität Hamburg, 1997.
- [59] R. Wallny, “The BDC 25 cm problem” (co-work with S.Glazov), talk presented at H1 Data Quality Meeting (DESY), February 3rd, 1998.
- [60] N. Keller *et al.*, H1 internal note H1-08/98-550, August 1998.
- [61] J.C. Bizot, M. Jacquet, L. Görlich, J. Martinyak, S. Mikocki, G. Nowak, D. Hoffmann, “SpaCal-based L2TT trigger elements”, H1 internal note H1-04/98-538, April 1998.
- [62] R. Bernet, “Production of $D^{*\pm}$ Mesons Measured with the H1 Detector at HERA”, Ph.D. Thesis, ETH Zürich, 1995.
- [63] E. Perez, private communication.

Acknowledgement

Conducting and maintaining a complex experiment like H1, as well as the analysis of its physics data is a challenging task for all involved people. I had the opportunity to explore and experience both fields during the last years, for which I would like to thank those who shared the joint efforts.

I would like to thank Prof. Dr. Ulrich Straumann for making this work possible by his support during the operation of the Backward Drift Chamber, first at the University of Heidelberg and then at the University of Zürich, as well as for his advice in detail questions of this study of QED Compton events. Finally, I would like to thank him for his general practical support, his patience and humour.

Thanks Ueli!

I would like to thank Dr. Katharina Müller for her continuous interest, advice and support for the Compton analysis. She contributed her valuable expert knowledge about handling the data of the Central Inner Proportional Chamber, innumerable hints and many discussions, and helped with her experience solving many details and questions of principle.

Also thanks to Victor Lendermann, for his important insight to many details of the Compton scattering process, the extension of the COMPTON Monte Carlo generator, making available useful Backward Silicon Tracker code, and many discussions.

Thanks to Tomáš Laštovička for discussions, and to Jörg Gayler for proofreading and discussions.

Thanks to Rainer Wallny for introduction to the experiment and especially to the operation of the BDC, vital BDC cable numbering, and for his untamed commitment in the north-hall. In doing so he offered an unequaled example.

Alvaro de Rújula for being a disputatious man of science.

Thanks to the ever ready but not so well known technicians of the H1 experimental hall, and those of the institutes' workshops in Heidelberg and Zürich. Representative for them I would like to thank Torsten Külper (DESY) who offered essential help to keep the Backward Drift Chamber running during its last months of operation.

Thanks to the secretaries of the Physik Institut/Zürich M. Stöcklin, R. Salzmann, and U. Wolf.

Finally, I would like to thank very much my sister Julia, Andreas and Michael, Heinrich, Marcus, Kristine and Stefan, Thayani, Matthew Siegler, Hanika and Framus, as well as Arno, Franca and Sabine.

Lebenslauf

Name: Keller
Vorname: Nicolas
Geboren am: 9. Oktober 1970 in Bensheim, Deutschland

Ausbildung:

1977 - 1981 Joseph-Heckler Grundschule Bensheim
1981 - 1990 Goethe-Gymnasium Bensheim
1990 Abitur
1990 - 1992 Physik-Studium an der Technischen Hochschule Darmstadt
1992 Vordiplom (30.9.1992)
1992 - 1996 Physik-Studium an der Ruprecht-Karls-Universität Heidelberg
1995 - 1996 Diplomarbeit in Experimentalphysik, Betreuung durch Prof. Dr. W. Siebert
“Inklusive Produktion der Hyperonresonanz $\Xi(1530)^0$ in Σ^- -N-Reaktionen”
(WA89-Experiment/CERN)
1996 Diplom der Physik (3.12.1996)
1997 - 1999 Physikalisches Institut der Universität Heidelberg
1999 - 2003 Physik Institut der Universität Zürich
1997 - 2003 Wissenschaftliche Mitarbeit am H1-Experiment/DESY,
Wartung der BDC Driftkammer, sowie
Promotion bei Prof. Dr. U. Straumann, Uni Zürich